Department of Energy
Office of Civilian Radioactive Waste Management
Yucca Mountain Site Characterization Office
P.O. Box 364629
North Las Vegas, NV 89036-8629

QA: N/A

JUL 02 2002

OVERNIGHT MAIL

Janet R. Schlueter, Chief
High-Level Waste Branch
Division of Waste Management
Office of Nuclear Materials Safety
and Safeguards
U.S. Nuclear Regulatory Commission
Two White Flint North
Rockville, MD 20852

TRANSMITTAL OF INFORMATION ADDRESSING KEY TECHNICAL ISSUE (KTI) AGREEMENT ITEMS RADIONUCLIDE TRANSPORT (RT) 3.09 AND UNSATURATED AND SATURATED ZONE FLOW UNDER ISOTHERMAL CONDITIONS (USFIC) 6.04

This letter transmits a hard copy (enclosure 1) and a CD (enclosure 2) of a report entitled *C-Wells Hydraulic and Tracer Testing* which satisfies the subject agreements. These KTI agreements are as follows:

> RT 3.09 – "Provide the documentation for the C-wells testing. Use the field test data or provide justification that the data from the laboratory tests is consistent with the data from the field tests."
> "DOE will provide the C-wells test documentation and will either use the test data or provide a justified reconciliation of the lab and field test data in the C-wells AMR available in October 2001."
>
> USFIC 6.04 – "Provide the documentation for the C-wells testing. Use the field test data or provide justification that the data from the laboratory tests is consistent with the data from the field tests."
> "DOE will provide the C-wells test documentation and will either use the test data or provide a justified reconciliation of the lab and field test data in the C-wells document(s) available in October 2001."

The enclosures comprise a detailed discussion of the results of the testing program at the C-Wells Complex, including hydraulic properties and tracer transport testing. The results are also discussed in terms of limitations, uncertainties, and the conceptual model. Where available, the U.S. Department of Energy (DOE) will use data from the field tests. Where field test data are not available, DOE will use data from laboratory tests that are shown to be consistent with, or conservative relative to, field test data.

YMP-5

While the agreement for RT 3.09 stated that these test results would be provided in an Analysis and Model Report, the information has been provided in this report as discussed at the April 15-16, 2002, U.S. Nuclear Regulatory Commission (NRC)/DOE Technical Exchange and Management Meeting on KTIs.

This letter contains no new regulatory commitments. Please direct any questions concerning this letter and its enclosures to Drew H. Coleman at (702) 794-5537 or Timothy C. Gunter at (702) 794-1343.

Joseph D. Ziegler
Acting Assistant Manager, Office of Licensing
and Regulatory Compliance

OL&RC:TCG-1352

Enclosures:
1. Hard copy of *C-Wells Hydraulic and Tracer Testing*
2. CD copy of Enclosure 1

cc w/encl 2:
J. W. Andersen, NRC, Rockville, MD
N. M. Coleman, NRC, Rockville, MD
D. D. Chamberlain, NRC, Arlington, TX
R. M. Latta, NRC, Las Vegas, NV
B. J. Garrick, ACNW, Rockville, MD
Richard Major, ACNW, Rockville, MD
W. D. Barnard, NWTRB, Arlington, VA
Budhi Sagar, CNWRA, San Antonio, TX
W. C. Patrick, CNWRA, San Antonio, TX
S. H. Hanauer, DOE/HQ (RW-2), Las Vegas, NV
Steve Kraft, NEI, Washington, DC
J. H. Kessler, EPRI, Palo Alto, CA
J. R. Egan, Egan & Associates, McLean, VA
R. R. Loux, State of Nevada, Carson City, NV
John Meder, State of Nevada, Carson City, NV
Alan Kalt, Churchill County, Fallon, NV
Irene Navis, Clark County, Las Vegas, NV
George McCorkell, Esmeralda County, Goldfield, NV
Leonard Fiorenzi, Eureka County, Eureka, NV
Andrew Remus, Inyo County, Independence, CA
Michael King, Inyo County, Edmonds, WA
Mickey Yarbro, Lander County, Battle Mountain, NV

cc w/encl 2: (continued)
Lola Stark, Lincoln County, Caliente, NV
L. W. Bradshaw, Nye County, Pahrump, NV
David Chavez, Nye County, Tonopah, NV
Josie Larson, White Pine County, Ely, NV
Arlo Funk, Mineral County, Hawthorne, NV
R. I. Holden, National Congress of American Indians, Washington, DC
Allen Ambler, Nevada Indian Environmental Coalition, Fallon, NV
CMS Coordinator, BSC, Las Vegas, NV

cc w/o encls:
N. K. Stablein, NRC, Rockville, MD
L. L. Campbell, NRC, Rockville, MD
C. W. Reamer, NRC, Rockville, MD
S. L. Wastler, NRC, Rockville, MD
Margaret Chu, DOE/HQ (RW-1), FORS
A. B. Brownstein, DOE/HQ (RW-52), FORS
R. A. Milner, DOE/HQ (RW-2), FORS
S. E. Gomberg, DOE/HQ (RW-2), FORS
N. H. Slater-Thompson, DOE/HQ (RW-52), FORS
R. B. Murthy, DOE/OQA (RW-3), Las Vegas, NV
E. P. Opelski, NQS, Las Vegas, NV
N. H. Williams, BSC, Las Vegas, NV
S. J. Cereghino, BSC, Las Vegas, NV
Donald Beckman, BSC, Las Vegas, NV
K. M. Cline, MTS, Las Vegas, NV
R. B. Bradbury, MTS, Las Vegas, NV
R. P. Gamble, MTS, Las Vegas, NV
R. C. Murray, MTS, Las Vegas, NV
R. D. Rogers, MTS, Las Vegas, NV
Richard Goffi, BAH, Washington, DC
J. R. Dyer, DOE/YMSCO, Las Vegas, NV
D. G. Horton, DOE/YMSCO, Las Vegas, NV
G. W. Hellstrom, DOE/YMSCO, Las Vegas, NV
S. P. Mellington, DOE/YMSCO, Las Vegas, NV
R. E. Spence, DOE/YMSCO, Las Vegas, NV
J. D. Ziegler, DOE/YMSCO, Las Vegas, NV
W. J. Boyle, DOE/YMSCO, Las Vegas, NV
C. M. Newbury, DOE/YMSCO, Las Vegas, NV
T. C. Gunter, DOE/YMSCO, Las Vegas, NV
E. T. Smistad, DOE/YMSCO, Las Vegas, NV
D. H. Coleman, DOE/YMSCO, Las Vegas, NV
C. L. Hanlon, DOE/YMSCO, Las Vegas, NV

cc w/o encls: (continued)
M. C. Tynan, DOE/YMSCO, Las Vegas, NV
J. T. Sullivan, DOE/YMSCO, Las Vegas, NV
G. L. Smith, DOE/YMSCO, Las Vegas, NV
C. A. Kouts, DOE/YMSCO (RW-2), FORS
R. N. Wells, DOE/YMSCO (RW-60), Las Vegas, NV
OL&RC Library
Records Processing Center = "8"
(ENCLS = READILY AVAILABLE)

SATURATED ZONE C-WELLS HYDRAULIC AND TRACER TESTING

June 2002

Preparation:

P.W. Reimus, Saturated Zone Testing, Principal Investigator — Date 6/5/02

M.J. Umari, Saturated Zone Testing, Principal Investigator — Date 6/5/02

Checked by:

S.M. Kelkar, Los Alamos National Laboratory — Date 6/5/02

Approval:

A.A. Eddebbarh, Department Manager, Saturated Zone — Date 6/5/02

P.R. Dixon, Subproject Manager, Natural Systems — Date 6/5/02

Reviewed by:

Thom Booth, License Application Project — Date 6/11/02

ENCLOSURE 1

KEY TECHNICAL ISSUE (KTI) AGREEMENTS RADIONUCLIDE TRANSPORT (RT) 3.09 AND UNSATURATED AND SATURATED ZONE FLOW UNDER ISOTHERMAL CONDITIONS (USFIC) 6.04

C-WELLS HYDRAULIC AND TRACER TESTING

YUCCA MOUNTAIN PROJECT

This report contains discussion of data including: 1) qualified data that have been incorporated in the Bechtel/SAIC Company's (BSC) Technical Data Management System (TDMS), and 2) in-process or raw data that are not yet incorporated but for which data management activities are ongoing. Accordingly, Data Tracking Numbers (DTNs) are currently available for some of the data, although no DTNs are provided in the report. More important, all of the data presented in this report will be incorporated in the TDMS and published in a planned Analysis/Model Report (AMR) that will support the License Application.

TABLE OF CONTENTS

TABLE OF CONTENTS (continued)

Page

TABLE OF CONTENTS (continued)

Page

LIST OF FIGURES

Page

LIST OF FIGURES (continued)

Page

LIST OF FIGURES (continued)

Page

LIST OF FIGURES (continued)

Page

LIST OF FIGURES (continued)

Page

LIST OF TABLES

LIST OF TABLES (continued)

Page

ACRONYMS AND ABBREVIATIONS

1-D	one-dimensional
2-D	two-dimensional
2,6 DFBA	2,6 difluorobenzoic acid
BTC	breakthrough curve
CEC	cation exchange capacity
CML	carboxylate-modified latex
CRW	constant-rate withdrawal
C#1	UE-25 c#1
C#2	UE-25 c#2
C#3	UE-25 c#3
EDTA	ethylenediamine tetraacetic acid
FBA	fluorinated benzoate
HPLC	high-pressure liquid chromatograph
H-4	USW H-4
ICP-AES	inductively-coupled-plasma, atomic-emission-spectroscopy
KTI	key technical issue
LANL	Los Alamos National Laboratory
LBNL	Lawrence Berkeley National Laboratory
MULTRAN	multicomponent transport
NTS	Nevada Test Site
ONC-1	UE-25 ONC-1
PC	personal computer
PEST	parameter estimation software
PFBA	pentafluorobenzoate
Pyridone	3-carbamoyl-2-pyridone
p#1	UE-25 p#1
QXRD	quantitative x-ray diffraction
RELAP	REactive transport LAPlace transform inversion computer code
RTV	room-temperature vulcanizing

ACRONYMS AND ABBREVIATIONS (Continued)

TeFBA	2,3,4,5 tetrafluorobenzoic acid
TFBA	2,4,5 trifluorobenzoic acid
USGS	U.S. Geological Survey
UV	ultraviolet
WT#3	UE-25 WT#3
WT#14	UE-25 WT#14

1. INTRODUCTION

The saturated zone near Yucca Mountain along potential flow paths from the potential repository to the accessible environment can be divided into two regimes: (1) fractured tuffs that underlie the potential repository and that extend for several kilometers (km) to the south of Yucca Mountain (in the general direction of flow), and (2) valley-fill or alluvium deposits that the water table transitions into several kilometers before the current ~18-km performance compliance boundary (40 CFR 197, 2001). Radionuclides released from the potential repository would first have to travel through the saturated fractured tuffs and then through the saturated alluvium to reach the compliance boundary. To support the characterization of the saturated fractured tuffs, several hydraulic and tracer tests were conducted at a three-well complex (UE-25 c#1, UE-25 c#2, and UE-25 c#3) known as the C-wells, which is located approximately 2 km southeast of the potential repository footprint. Hydraulic tests conducted at the C-wells are discussed in Section 2 of this report, and tracer tests at the C-wells are discussed in Section 3. In addition to presenting the results and interpretations of field tracer testing conducted at the C-wells, this report also presents the results and interpretations of laboratory transport tests conducted to help support the interpretation of field tracer tests (Section 2).

1.1 HYDROGEOLOGIC SETTINGS OF C-WELLS

Figure 1 shows the location and surface layout of the C-wells. The wells were drilled on a two-tiered drill pad in a channel of an ephemeral stream that cuts through Bow Ridge, a spur of Yucca Mountain. The lower tier of the pad, in which borehole UE-25 c#1 (C#1) was drilled, is at an altitude of 1,130.5 m above sea level. The upper tier, in which boreholes UE-25 c#2 (C#2) and UE-25 c#3 (C#3) were drilled, is at an altitude of 1,132.3 m. The C-wells are 30.4 to 76.6 m apart at the land surface, but they deviate substantially at depth (Geldon 1993) (Figure 1 and Table 1).

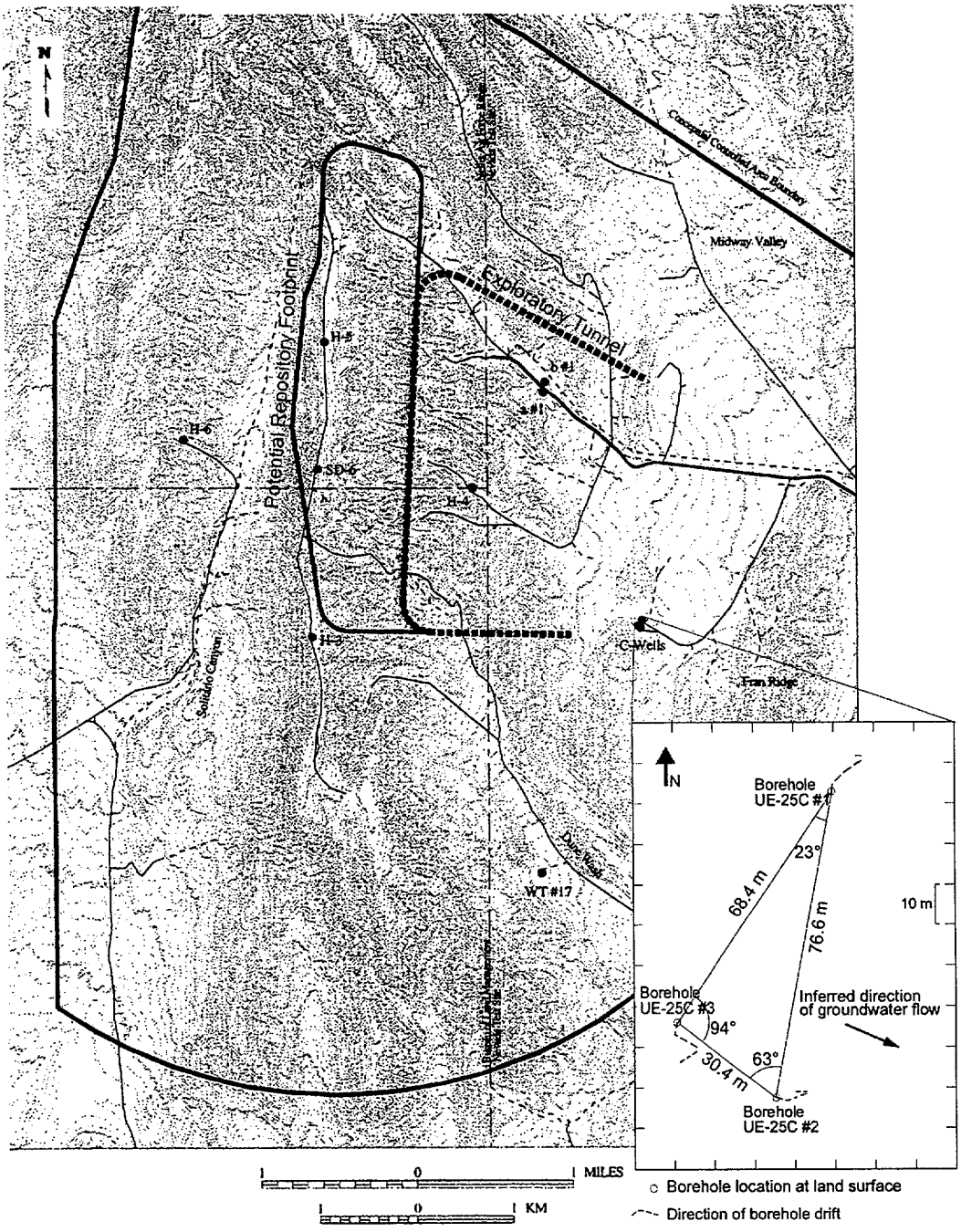

Figure 1. Location and Surface Layout of the C-wells Complex

Table 1. Approximate Interborehole Distances at the Midpoints of Hydrogeologic Intervals as Monitored During Hydraulic Tests at the C-wells Complex, August 1995 to April 1996

	Borehole Data			Interborehole Distances	
	C#1	C#2	C#3	C#1 – C#3	C#2 – C#3
Calico Hills					
Top depth (m)	418	416	417	78.6	29.0
Bottom depth (m)	547	531	540		
Midpoint depth (m)	483	474	478		
North coordinate (m)	230,771	230,691	230,703		
East coordinate (m)	173,646	173,633	173,607		
Distance north/south from C#3 (m)	68.3	12.2	—		
Distance east/west from C#3 (m)	39.3	26.2	—		
Prow Pass					
Top depth (m)	549	533	542	81.1	28.6
Bottom depth (m)	605	606	610		
Midpoint depth (m)	577	569	576		
North coordinate (m)	230,772	230,691	230,702		
East coordinate (m)	173,648	173,634	173,607		
Distance north/south from C#3 (m)	70.4	11.0	—		
Distance east/west from C#3 (m)	40.2	26.5	—		
Upper Bullfrog					
Top depth (m)	607	607	612	83.2	28.6
Bottom depth (m)	698	696	695		
Midpoint depth (m)	653	652	653		
North coordinate (m)	230,773	230,691	230,701		
East coordinate (m)	173,648	173,634	173,607		
Distance north/south from C#3 (m)	72.2	9.75	—		
Distance east/west from C#3 (m)	41.4	26.8	—		
Lower Bullfrog					
Top depth (m)	700	698	697	85.6	29.3
Bottom depth (m)	797	792	813		
Midpoint depth (m)	749	745	755		
North coordinate (m)	230,774	230,692	230,700		
East coordinate (m)	173,649	173,633	173,606		
Distance north/south from C#3 (m)	73.8	8.84	—		
Distance east/west from C#3 (m)	43.3	27.7	—		

NOTE: C#1, C#2, and C#3 are abbreviations for boreholes UE-25 c#1, UE-25 c#2, and UE-25 c#3, respectively. North and south are referenced to Nevada State Zone 2 coordinates. Depths in UE-25 c#3 and interborehole distances changed slightly in April 1996 when instrumentation in UE-25 c#3 was reconfigured.

Table 1 (continued). Approximate Interborehole Distances at the Midpoints of Hydrogeologic Intervals as Monitored During Hydraulic Tests at the C-wells Complex, August 1995 to April 1996

	Borehole Data			Interborehole Distances	
	C#1	C#2	C#3	C#1 – C#3	C#2 – C#3
Upper Tram					
Top depth (m)	799	794	814	86.9	29.6
Bottom depth (m)	870	870	878		
Midpoint depth (m)	834	832	846		
North coordinate (m)	230,774	230,691	230,700		
East coordinate (m)	173,648	173,632	173,604		
Distance north/south from C#3 (m)	74.7	8.53	—		
Distance east/west from C#3 (m)	44.2	28.3	—		
Lower Tram					
Top depth (m)	872	871	879	87.2	29.9
Bottom depth (m)	898	903	900		
Midpoint depth (m)	885	887	890		
North coordinate (m)	230,774	230,691	230,700		
East coordinate (m)	173,648	173,632	173,603		
Distance north/south from C#3 (m)	74.7	8.23	—		
Distance east/west from C#3 (m)	44.8	28.6	—		

NOTE: C#1, C#2, and C#3 are abbreviations for boreholes UE-25 c#1, UE-25 c#2, and UE-25 c#3, respectively. North and south are referenced to Nevada State Zone 2 coordinates. Depths in UE-25 c#3 and interborehole distances changed slightly in April 1996 when instrumentation in UE-25 c#3 was reconfigured.

The C-wells were completed to a depth of 914 m below land surface in Miocene tuffaceous rocks, mainly of the Paintbrush Group, the Calico Hills Formation, and the Crater Flat Group (Table 2), which are overlain by 0 to 24 m of Quaternary alluvium. The geology below the water table at the C-wells is depicted in Figure 2, along with fracture densities and estimated average matrix porosities in each unit. The tuffaceous rocks are estimated to be 1,040 to 1,590 m thick in the vicinity of the C-wells complex, where they consist of nonwelded to densely welded ash-flow tuff with intervals of ash-fall tuff and volcaniclastic rocks (e.g., Geldon 1993; Geldon et al. 1998). The tuffaceous rocks have pervasive tectonic and cooling fractures that strike predominantly north-northeast to north-northwest and dip westward at angles of 50° to 87° (e.g., Geldon 1996). Several thousand meters of Paleozoic limestone and dolomite likely underlie the tuffaceous rocks about 455 m below the bottom of the C-wells or ~1370 m below land surface (based on extrapolations from relations in borehole UE-25 p#1 presented by Carr et al. 1986).

Table 2. Stratigraphy of Miocene Tuffaceous Rocks in the C-wells Area

Geologic Unit	Depth Below Land Surface (m)				
	USW H-4	UE-25 c#1	UE-25 c#2	UE-25 c#3	UE-25 p#1
Timber Mountain Group					
Rainier Mesa Tuff	not present	not present	not present	not present	39–55
Paintbrush Group					
Tiva Canyon Tuff	0–65	0–96	21–88	24–88	55–81
Topopah Spring Tuff	65–400	96–406	88–401	88–396	81–381
Calico Hills Formation	400–496	406–516	401–510	396–496	381–436
Crater Flat Group					
Prow Pass Tuff	496–693	516–656	510–652	496–644	436–558
Bullfrog Tuff	693–812	656–828	652–829	644–814	558–691
Tram Tuff	812–1,164	828–914+	829–914+	814–914+	691–873
Lithic Ridge Tuff	1,164–1,219+	not reached	not reached	not reached	873–1,068

Source: Geldon et al. (1998).

In the vicinity of the C-wells complex, northerly and northwesterly trending, high-angle faults, such as the Paintbrush Canyon, Midway Valley, and Bow Ridge faults, have brecciated, offset, and tilted the tuffaceous rocks (Day et al. 1998; Dickerson and Drake 1998). Figure 3 shows major faults and structural features in the vicinity of Yucca Mountain. The dip of the tuffaceous rocks increases from 5° to 10° eastward at the crest of Yucca Mountain to about 20° eastward at the C-wells complex (Frizzell and Shulters 1990). At the C-wells complex, the north-striking Midway Valley or Paintbrush Canyon fault dropped Miocene tuffaceous rocks down to the west. Those rocks later were dropped to the northeast by a northwest-striking fault that cuts through Bow Ridge (Figure 3).

Hydrogeologic data and numerical modeling indicate that groundwater recharge in the Yucca Mountain area discharges mostly to Carson Slough, Ash Meadows, Alkali Flat, the lower Amargosa River Valley, and Death Valley (D'Agnese et al. 1997). Locally, groundwater flows mainly through Tertiary volcanic rocks and Quaternary and Tertiary alluvium and lacustrine deposits. Controlled largely by faults and related fractures, groundwater flows from basin to basin, mainly through deeper Paleozoic carbonate rocks (Faunt 1997). Cohen et al. (1996) demonstrated by two-dimensional (2-D) numerical modeling that water in Miocene rocks at the C-wells complex could be derived from the Paleozoic carbonate rocks by upward flow along the Paintbrush Canyon, Midway Valley, or Bow Ridge faults. Geldon et al. (1998) concluded that a northwest-trending zone of discontinuous faults between Bow Ridge and Antler Wash also transmits groundwater.

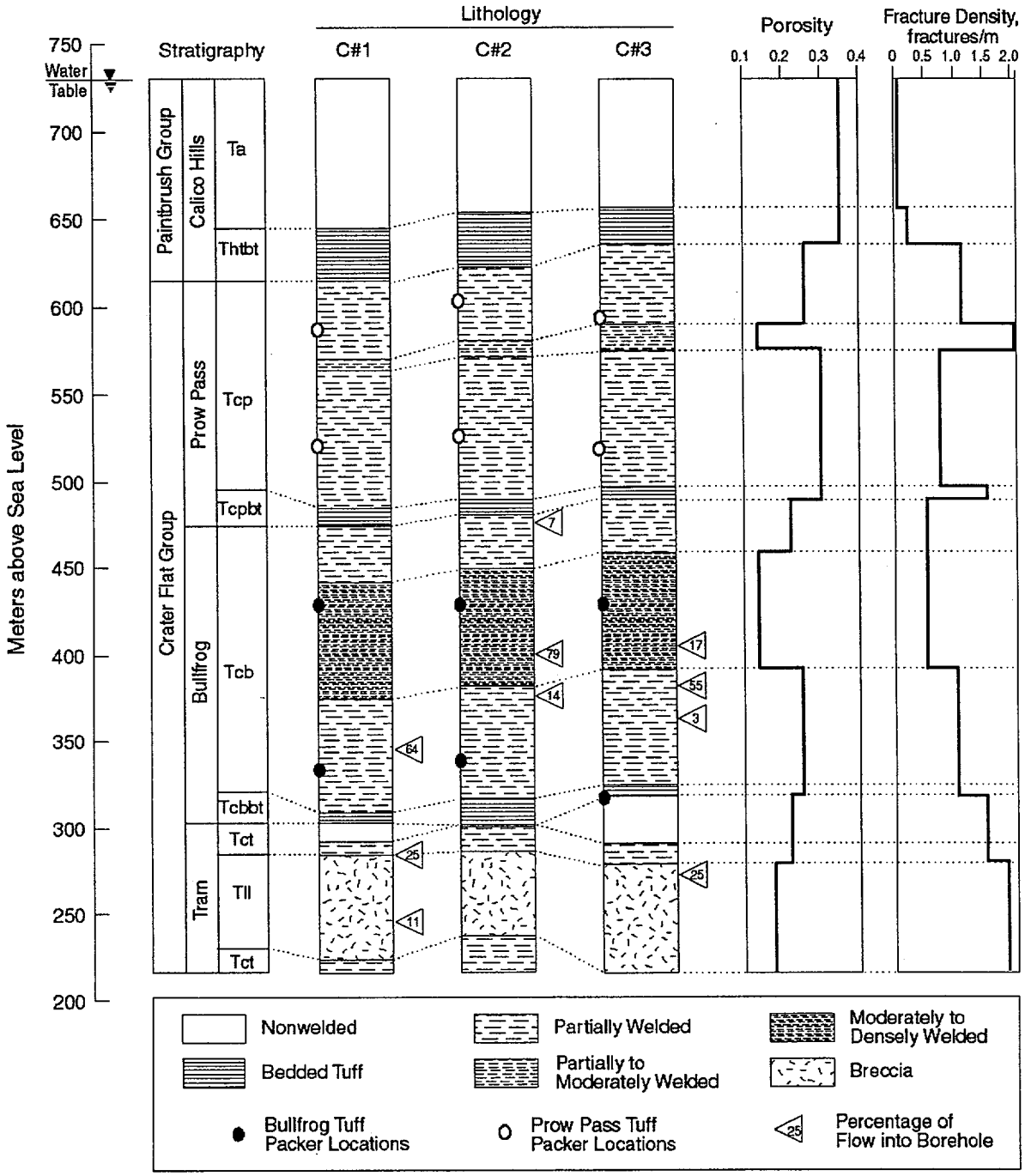

NOTE: Packer locations indicate intervals in which tracer tests described in this paper were conducted at Los Alamos (note that the tracer tests were conducted between UE-25 c#2 and c#3).

Figure 2. Stratigraphy, Lithology, Matrix Porosity, Fracture Density, and Inflow From Open-Hole Flow Surveys at the C-wells

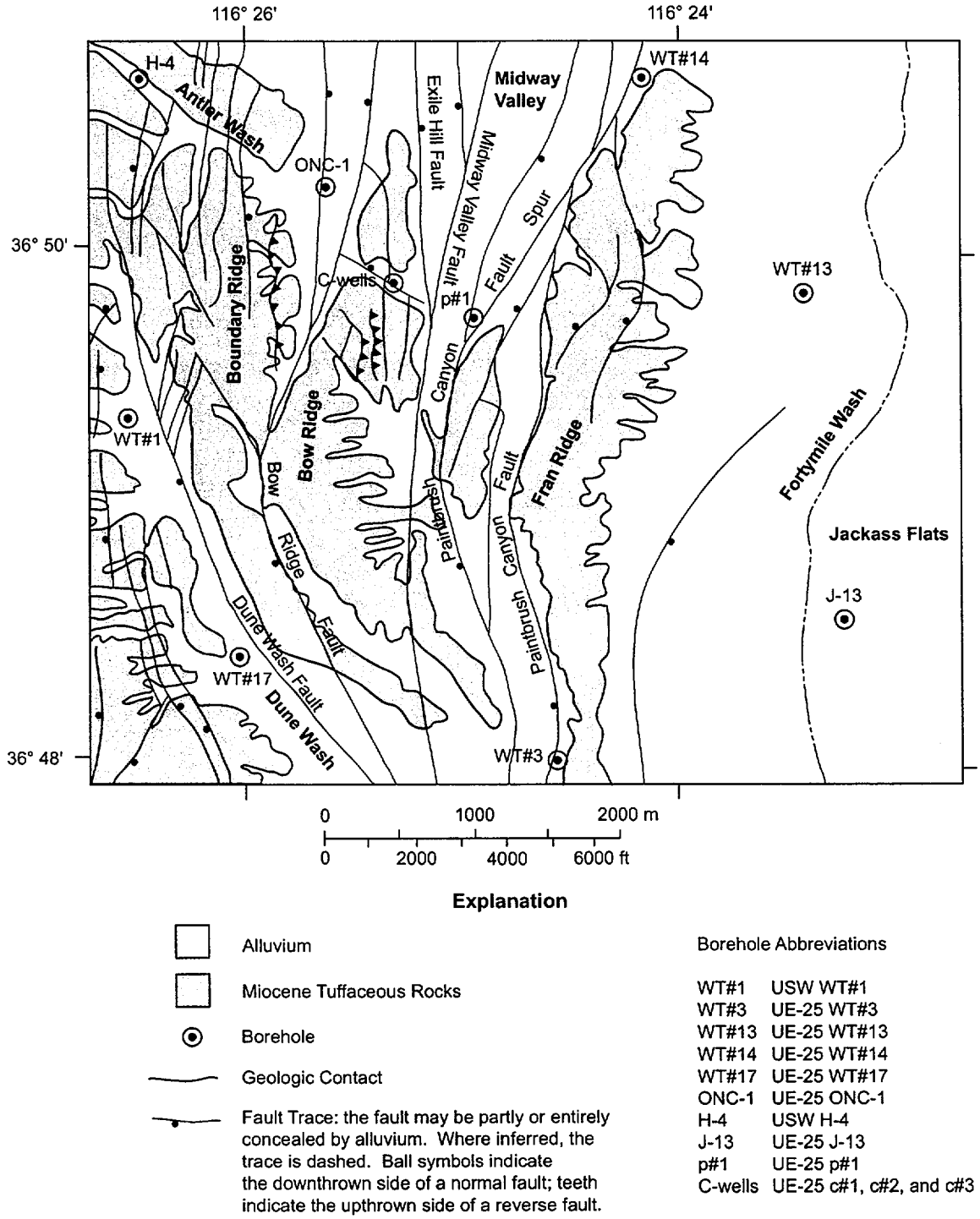

Source: Geology modified from Day et al. (1998).

Figure 3. Generalized Geologic Map Showing the Location of the C-wells Complex and Nearby Boreholes

The water table in the Miocene tuffaceous rocks at Yucca Mountain in the vicinity of the C-wells complex ranges from about 335 to 520 m below land surface (O'Brien et al. 1995) and in the C-wells from 400 to 402 m. These depths all correspond to a water table elevation of approximately 730 m above mean sea level in the vicinity of the C-wells. Water in the tuffaceous rocks generally flows southeasterly (Ervin et al. 1994; Tucci and Burkhardt 1995), but flow patterns are disrupted by faults acting as conduits or barriers to flow. Water-level data are sparse in the vicinity of the C-wells complex, but the Paintbrush Canyon, Bow Ridge, and other faults apparently created a groundwater divide centered on Bow Ridge and Boundary Ridge that directs flow southward to Dune Wash, northward to Midway Valley, and eastward to Fortymile Wash (Figure 4). Flow from the west into the area of the C-wells is inhibited by the north-striking Solitario Canyon fault (shown in Figure 3; Tucci and Burkhardt 1995). The Solitario Canyon fault is interpreted to be a constant-head boundary, whereas discharge areas north, east, and south of the C-wells complex are interpreted to be head-dependent flux boundaries.

The Miocene tuffs near the C-wells complex behave as a single dual-permeability aquifer, in which the volume and direction of groundwater flow are controlled mainly by proximity to faults, fracture zones, and partings (Geldon et al. 1998). Fractures in transmissive intervals have no preferred orientation, and fracture density appears unrelated to the extent of welding and permeability. Matrix permeability of the Calico Hills Formation and the Crater Flat Group within 5 km of the C-wells complex reaches 20 mDarcy. On the basis of barometric efficiency and specific storage, the average effective porosity of the Calico Hills Formation near the water table in the C-wells was determined to be 36 percent (Geldon et al. 1997b). The Crater Flat Group is much less porous than the Calico Hills Formation. The average porosity of those geologic units in the C-wells is 21 percent (computed from porosity values reported by Geldon 1993). Despite the influence of fractures, rock within about 3 km of the C-wells complex consistently responds to hydraulic tests as an equivalent porous medium.

Borehole flow surveys in combination with geophysical logs and aquifer tests show that flow within the tuffs at the C-wells complex comes primarily from discrete intervals (Figure 2). The total thickness of transmissive intervals identified in individual boreholes ranges from 165 to 274 m (Geldon 1996). Hydraulic tests conducted in 1984 indicated that those intervals have layered heterogeneity (Geldon 1996). Figure 5 is a depiction of the hydrogeologic intervals identified in the C-wells during hydraulic and tracer testing from 1995 to 1997 (Geldon 1996).

1.2 SEQUENCE OF HYDRAULIC AND TRACER TESTS

Figure 6 is a graphical timeline showing the sequence of hydraulic and tracer tests conducted at the C-wells since May 1995. Each of the tests is described in detail in Sections 2 and 3. In this report, the C-wells tracer tests are split into two general categories: (1) tests involving only conservative (nonsorbing) solute tracers and (2) tests involving combinations of conservative and reactive solute tracers and colloid tracers (polystyrene microspheres). The former tests were conducted and interpreted primarily by the U.S. Geological Survey (USGS), and the latter were conducted and interpreted primarily by the Los Alamos National Laboratory (LANL). Los Alamos also conducted two conservative solute-only tracer tests to prepare for a multiple tracer test in the Lower Bullfrog Tuff, but these tests were not quantitatively interpreted.

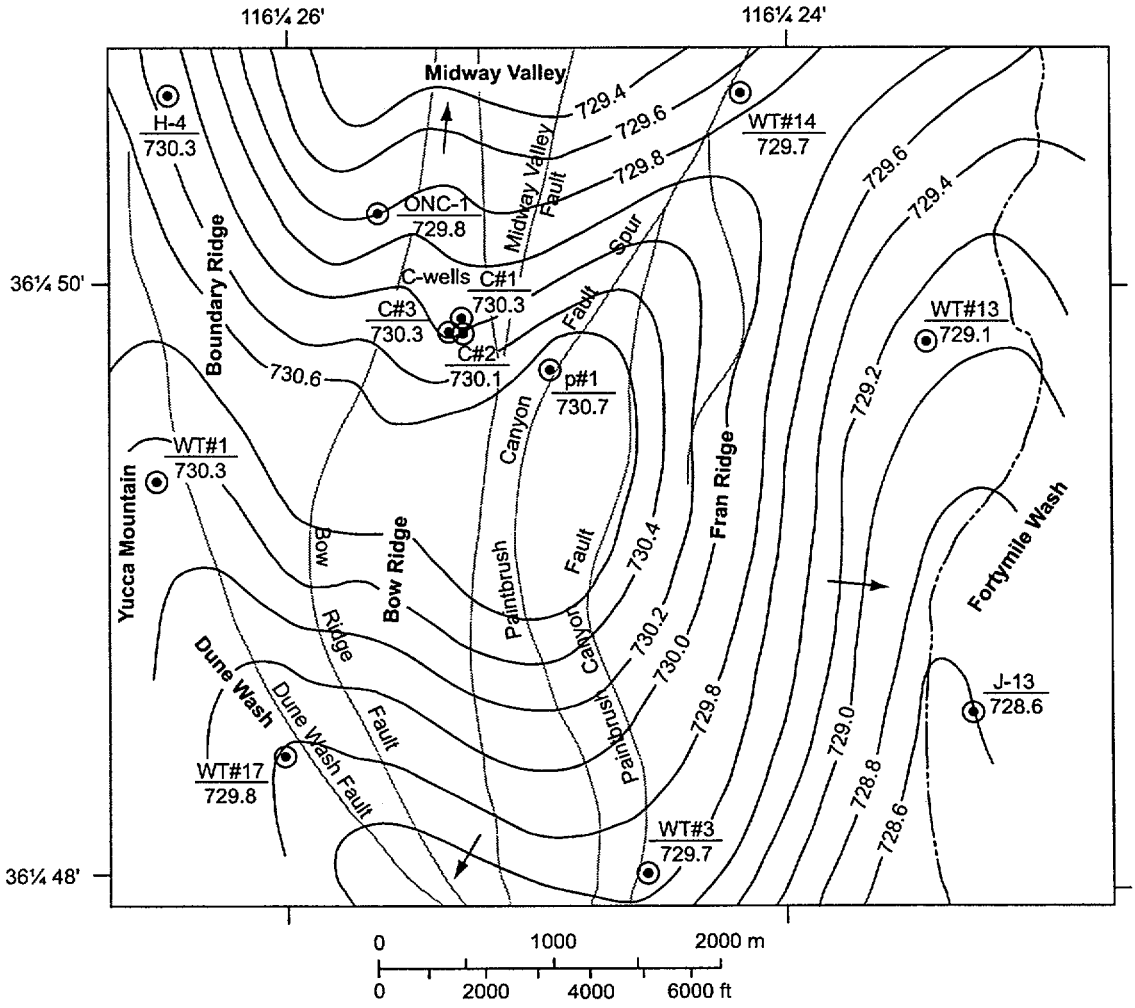

Explanation

H-4 / 730.3 — **Borehole.** The circle indicates the position of the borehole; the numbers show the borehole number (above the line) and the water level altitude, in meters above NGVD of 1929 (below the line). Complete borehole designations are listed in Figure 3.

730.0 — **Potentiometric Surface.** The contours give the altitude above NGVD of 1929 at which water would have stood in tightly cased wells completed in the Miocene tuffaceous rocks in May 1995. The water-level altitude in UE-25 p#1 is estimated from the measured hydraulic head of Paleozoic carbonate rocks and the vertical head gradient between the Paleozoic carbonate rocks and Miocine tuffaceous rocks in the borehole. The arrows on the contour lines indicate the approximate direction of groundwater flow. The countour interval is 0.2 m.

Fault Trace.

Source: Water-level altitudes from Graves et al. (1997); Geldon et al. (1998).

Figure 4. Potentiometric Surface of the Miocene Tuffaceous Rocks in the Vicinity of the C-wells Complex, May 1995

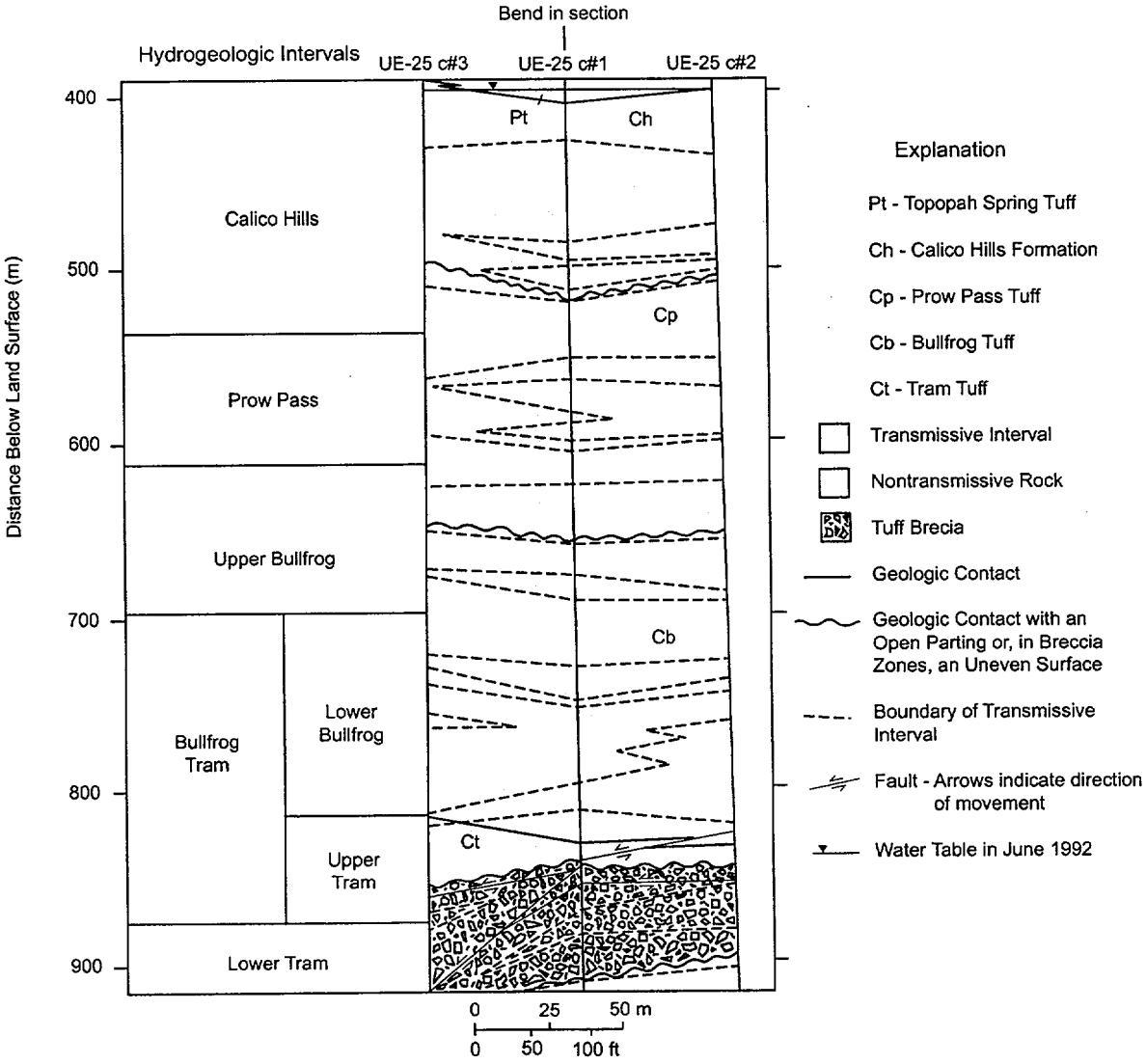

Source: Modified from Geldon (1996).

Figure 5. Hydrogeologic Intervals in the C-wells Identified During Hydraulic and Tracer Testing from 1995 to 1997

The distinction between the conservative and the multiple tracer tests is important because the two organizations, while working closely together, took different approaches to interpreting the tracer tests. These different approaches result in different transport parameter estimates derived from the tracer responses (see Section 3.6 for a discussion of these differences and how they affect uncertainty). Both approaches are presented so that readers can gain an appreciation for the uncertainties in parameter estimation associated with the different methods and assumptions and can also make informed decisions about which approach they may want to give more weight when determining parameter distributions for performance assessments.

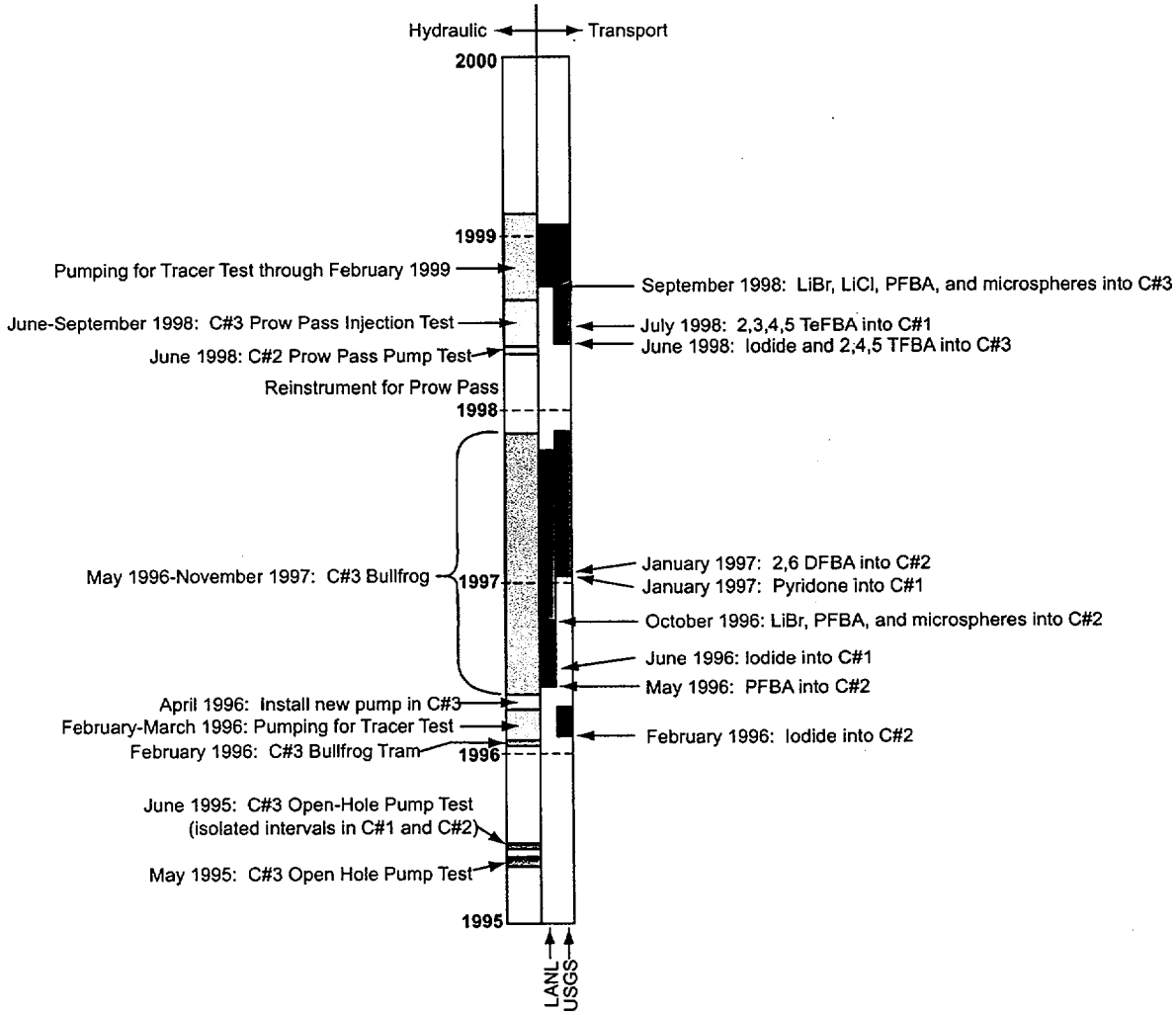

Figure 6. Timeline for C-wells Hydraulic and Tracer Tests

2. HYDROLOGIC PROPERTIES OF FRACTURED TUFFS (C-WELLS COMPLEX)

The hydrologic properties of the fractured tuffs at Yucca Mountain were tested as part of on-going investigations of the hydrologic and geologic suitability of Yucca Mountain as a potential high-level nuclear waste repository by the USGS in cooperation with the U.S. Department of Energy under Interagency Agreement DE-AI08-97NV12033. Four cross-hole hydraulic tests, some in conjunction with tracer tests, were conducted by the USGS at the C-wells complex in May and June 1995, February 1996, and from May 1996 to November 1997. The first test is documented in Geldon et al. (1998), and the others are described in this report.

This section of the report has three prongs. It describes the hydraulic tests conducted, the changes in water levels in monitoring wells as a result of pumping, and analyses performed on the test data. It also evaluates the uncertainties associated with the test data, analyses, and values of hydraulic properties determined from test analyses. Finally, it extrapolates test results to interpret groundwater flow paths in Miocene tuffaceous rocks beyond the immediate vicinity of the C-wells complex.

2.1 STUDIES CONDUCTED BEFORE LATE JUNE 1995

Before the in-situ testing of the fractured tuffs at Yucca Mountain began in May 1995, studies were conducted to determine hydrogeologic intervals of the rocks, flow patterns, geologic influences, geologic properties of the rocks, and the hydraulic results of an open-hole test in one of the C-wells. Most of these studies have been published and are referred to in this section. Hydrogeologic intervals discussed in this report were identified by Geldon (1996) on the basis of borehole geophysical logs, borehole flow surveys, cross-hole seismic tomography, and aquifer tests. Geophysical logs run in the C-wells include caliper, borehole-deviation, temperature, resistivity, gamma-gamma, acoustic, epithermal neutron, acoustic televiewer, and television logs (Geldon 1993). Flow surveys run in the C-wells include tracejector, heat-pulse flowmeter, spinner, and oxygen-activation surveys (Geldon 1993; 1996). Tracejector surveys using radioactive iodide were run in the C-wells during hydraulic tests conducted in 1983 and 1984. Heat-pulse flowmeter surveys were run in 1991 without the boreholes being pumped. Spinner and oxygen-activation surveys were run in borehole C#3 during a hydraulic test in June 1995. In 1993, a seismic tomogram was conducted between boreholes C#2 and C#3 by Lawrence Berkeley National Laboratory (LBNL) for the USGS (Majer 1993, written communication). That tomogram showed many of the hydrogeologic details evident from borehole lithologic and geophysical logs and flow surveys.

Hydraulic properties of the intervals in the C-wells and the manner in which they transmit water were determined provisionally by Geldon (1996) from geophysical logs, laboratory analyses, and aquifer tests. A matrix-porosity profile for the C-wells was developed from a gamma-gamma log and nine values of core porosity obtained from C#1 in 1983 (Geldon 1993). Geldon (1996) developed a matrix-permeability profile for the C-wells from permeameter tests on 89 core samples obtained from the C-wells and four nearby boreholes between 1980 and 1984. Geldon (1996) developed a hydraulic-conductivity profile for the C-wells by analyzing falling-head and pressure-injection tests done in C#1 in 1983. Transmissivity, hydraulic conductivity, and storativity of discrete intervals within the Calico Hills Formation and the Crater Flat Group were determined (Geldon 1996) from analyses of a constant-flux injection test in C#2 and three

hydraulic tests in C#2 and C#3 performed in 1984. From May 22 to June 12, 1995, an open-hole hydraulic test was conducted in borehole C#3. Simultaneous monitoring of water-level and atmospheric-pressure fluctuations in 1993 established the barometric efficiency of the C-wells (Geldon et al. 1997b). The open-hole hydraulic test determined the transmissivity, hydraulic conductivity, and storativity of the composite saturated thickness of Miocene tuffaceous rocks at the C-wells complex; lateral variations in hydraulic properties within a 3.2-km radius of the C-wells complex; and possible hydraulic connection between the tuffaceous rocks and the underlying regional aquifer composed of Paleozoic carbonate rocks (Geldon et al. 1998).

An hydraulic test conducted at the C-wells complex from May 22 to June 12, 1995, indicated that the composite section of tuffaceous rocks in the vicinity of the C-wells has a transmissivity of 2,300 m^2/d (square meters per day) and a storativity of 0.003 (Geldon et al. 1998). That test also indicated transmissivity values of 1,600 to 3,200 m^2/d and storativity values of 0.001 to 0.003 for the rocks in individual boreholes (C#1, C#2, UE-25 ONC-1, and USW H-4).

Hydraulic tests conducted in 1984 indicated that those intervals have layered heterogeneity (Geldon 1996). An hydraulic test conducted at the C-wells complex from May 22 to June 12, 1995, indicated that the composite section of tuffaceous rocks in the vicinity of the C-wells has a transmissivity of 2,300 m^2/d and a storativity of 0.003 (Geldon et al. 1998). That test also indicated transmissivity values of 1,600 to 3,200 m^2/d and storativity values of 0.001 to 0.003 for the rocks in individual boreholes (C#1, C#2, UE-25 ONC-1, and USW H-4).

2.2 INSTRUMENTATION USED IN C-WELLS HYDRAULIC TESTING

Principal components of the equipment installed at the C-wells complex to conduct hydraulic tests from 1995 to 1997 are available commercially, but much of this hardware and software has not been used extensively because of its relatively recent development. Consequently, all of the equipment received extensive performance evaluation during prototype hydraulic tests conducted jointly with LBNL from 1992 to 1994 at a research site near Raymond, California. Modifications to system components and their assembly were made to address problems encountered during prototype testing and after the equipment was installed and initially used at the C-wells complex. With few exceptions (discussed below), most system components performed remarkably well, despite being operated almost continuously for more than two years.

2.2.1 Packers

Dual-mandrel packers, manufactured by TAM International, Inc., were installed in C#1 and C#2 throughout the tests and in C#3 after August 1995. The packers are about 1.83 m long and have a deflated diameter of about 21.6 centimeters (cm) (see Geldon et al. 1998, Figure 6, for detailed drawing). Suspended on 7.30-cm-diameter tubing, each packer contains 12 pass-through tubes to allow packer-inflation lines and electrical cable to be installed in the borehole. The packers are inflated individually by injection of argon gas through 0.64-cm, stainless-steel tubing. Inflation pressures, which are about 1,034 kPa above hydrostatic pressure, range from about 2,758 to 5,861 kPa at the depths at which packers were set in the C-wells from 1995 to 1997. Packer depths from 1995 to 1997, as measured from the land surface, are listed in Table 3.

Table 3. Location of Packers Emplaced in the C-wells Complex for Hydraulic Tests, 1995 to 1997

Packer Number	Packer Depth (m below land surface)			
	UE-25 c#1	UE-25 c#2	UE-25 c#3	
			8/95–4/96	4/96–11/97
1	547.4–549.3	531.3–533.1	540.4–542.2	None
2	605.3–607.2	605.6–607.5	609.9–611.7	None
3	698.3–700.1	696.5–698.3	695.0–696.8	694.6–696.5
4	797.1–798.9	791.9–793.7	812.6–814.4	812.9–814.7
5	869.9–871.7	869.6–871.4	877.5–879.4	878.1–880.0

NOTE: There were no packers in UE-25 c#3 before August 1995.

2.2.2 Transducers

Continuous records of pressures and temperatures in packed-off intervals during hydraulic tests were obtained using absolute pressure transducers (manufactured by Paroscientific, Inc), which record water pressure plus atmospheric pressure. The transducers used in the C-wells were strapped into brackets welded onto the 7.30-cm-diameter tubing on which the packers were suspended. Field determinations indicated a precision of 0.30 cm under pumping conditions and 0.061 cm under non-pumping conditions.

Although transducers were installed in all hydrogeologic intervals, several of the transducers failed after installation. Transducers that were operative during some or all of the hydraulic tests conducted from 1995 to 1997 and the locations of those transducers, as determined by subtracting recorded pressure heads from static water-level altitudes, are listed in Table 4. Listed transducer altitudes have an accuracy of ±0.3 m.

2.2.3 Barometers

A nonsubmersible, temperature-compensated pressure transducer, manufactured by Paroscientific, Inc., was used as a barometer during the 1995 to 1997 hydraulic tests. The barometer operated in a temperature-controlled office trailer at the C-wells complex. The factory-calibrated accuracy of this barometer is ±0.005 percent of its full operating range (103 kPa). The barometer was checked periodically against another barometer of the same type in the same office trailer.

2.2.4 Pumps

A 37-stage, 25.2- liters per second (L/s) capacity, Centrilift submersible pump was used during the hydraulic test in June 1995. The pump was suspended in borehole C#3 on 13.9-cm-diameter tubing. The pump intake depth was 450.1 m (48.0 m below the water-level altitude prior to pumping). The pump was powered by a 250-KW generator, and its frequency was regulated by a variable-speed controller. Water discharged by the pump was transported by a 15-cm-diameter pipeline to a leachfield in Fortymile Wash, about 8 km from the C-wells complex.

Table 4. Operative Transducers in the C-wells, 1995 to 1997

Borehole	Interval	Transducer		
		Number	Depth (m)	Altitude (m)
UE-25 c#1	Prow Pass	2	552.09	578.51
	Upper Bullfrog	3	610.03	520.57
	Lower Bullfrog[a]	4	703.04	427.56
UE-25 c#2	Calico Hills	1	519.83	612.36
	Prow Pass	2	536.28	595.91
	Upper Bullfrog	3	610.70	521.49
	Lower Bullfrog[a]	4	701.58	430.61
UE-25 c#3	Calico Hills[b]	1	533.81	598.62
	Upper Bullfrog	3	614.49	517.93
	Lower Bullfrog[c]	4	708.93	423.49
	Upper Tram[d]	5	817.68	314.75

NOTE: (a) Monitored Lower Bullfrog and Upper Tram together, February to March 1996.

(b) Listed transducer locations are for August 1995 to March 1996. Prior to August 1995, a single transducer was installed in the Calico Hills interval at a depth of 441.12 m (altitude = 691.30 m) to monitor the composite geologic section in UE-25 c#3. After April 1996, a new transducer was installed at a depth of 691.31 m (altitude = 441.11 m) to monitor the Calico Hills, Prow Pass, and Upper Bullfrog intervals combined.

(c) Operative after April 1996.

(d) Monitored Lower Bullfrog and Upper Tram together in February and March 1996; replaced in April 1996 by a transducer at a depth of 819.32 m (altitude = 313.11 m).

The original pump was replaced in August 1995 by a 43-stage, 12.6 L/s-capacity, Centrilift submersible pump. That pump, enclosed in a protective shroud, was offset from the main part of the 7.30-cm-diameter tubing on which the packers were suspended by a 22.9-m-long "Y-block" assembly (see Geldon et al. 1998, Figure 7, for detailed drawing). The Y-block assembly was designed to allow wireline tool access past the pump for opening and closing sliding sleeves (screens installed to allow water movement to or from test intervals) and for placing a plug in the tubing to prevent recirculation of water through the pump shroud.

Although the Y-block assembly facilitated operations, its placement in the instrument string created problems that eventually caused pump performance to degrade beyond an acceptable level during hydraulic and tracer tests conducted in February and March 1996. Because the combined diameter of the Y-block assembly and main section of the instrument tubing (24.7 cm) was about the same as the borehole diameter below a depth of 463.4 m, the pump intake had to be set about 247 m above the top of the slotted section of pipe open in the test interval. Frictional head losses produced by water flowing through small openings (slots) in the intake tubing and through the tubing from the test interval to the pump intake caused the pump to operate at the limit of its designed performance range. Consequently, discharge decreased from 8.77 L/s when pumping started on February 8, 1996, to 6.18 L/s when pumping was terminated on March 29, 1996.

In April 1996, the pump-performance problem was addressed by (1) discarding the Y-block; (2) suspending a 72-stage, 12.6 L/s-capacity Centrilift pump enclosed in a narrower shroud directly on the 7.30-cm-diameter tubing; (3) lowering the pump to within about 47 m of the interval to be tested; and (4) adding 6.1 m of slotted pipe in the test interval. From May 1996 to March 1997, the reconfigured pump assembly performed without major problems and sustained a relatively constant discharge of 9.34 to 9.84 L/s. Problems with one of the generators providing power to the pump caused the pump to operate erratically between March 26 and May 8, 1997, but the pump performed adequately again after the generator problem was resolved.

2.2.5 Flowmeters

A McCrometer turbine-type flowmeter was used during the hydraulic test in June 1995. Subsequently, the primary device used for monitoring discharge was a differential switched capacitor, vortex flowmeter, manufactured by Endress and Hauser, measuring vortex frequency past a bluff body, with signal output converted to voltage output across a temperature-controlled resistor.

The flowmeter signal was recorded at user-specified intervals by monitoring software installed on a personal computer (PC) in the office trailer at the C-wells complex (see Section 2.2.6). The software program used a regression equation developed on the basis of the flowmeter calibration to convert the voltage signal from the flowmeter to a discharge rate. Periodically, discharge recorded by the PC was checked against total volume pumped (recorded at the wellhead) divided by the duration of pumping. Good agreement was maintained between recorded and computed discharge rates.

2.2.6 Data Acquisition and Instrument Control

Data acquisition from and control of the transducers, barometer, flowmeter, and an automatic water sampler used for tracer tests was accomplished with a commercially available, graphic-language software program called LabView (Johnson 1995). Installed on the PC in the office trailer, LabView made the PC monitor screen look and act like an instrument panel.

Two separate programs were written for data acquisition and instrument control. One program communicated with the transducers, barometer, and flowmeter; the other program communicated with the automated water sampler during tracer tests. The two programs ran simultaneously. Small utility "transfer programs" were written to transfer information back and forth between the two main programs to facilitate synchronization of the automated sampler operation with data acquisition from the transducers, barometer, and flowmeter.

2.3 RESULTS AND INTERPRETATIONS OF HYDRAULIC TESTS

The results and interpretations of the hydraulic tests discussed below include the conceptual models considered and tested.

2.3.1 Hydraulic Tests Conducted between June 1995 and November 1997

Three hydraulic tests were conducted at the C-wells complex from June 1995 to November 1997 (see timeline in Figure 6). During June 12 to June 22, 1995, well C#3 was pumped, without

packers installed, and drawdown and recovery were measured in six hydrogeologic intervals in C#1 and C#2 that were separated by packers (see Figure 5 and Table 3). From February 8 to February 13, 1996, C#3 was pumped, with packers inflated to isolate the Bullfrog Tram interval, to establish a steady-state hydraulic gradient for a tracer test in the Bullfrog Tram interval that continued until March 29, 1996. Drawdown was analyzed in the Bullfrog Tram interval and in all other packed-off intervals of C#1 and C#2 that responded to pumping during the hydraulic test.

In the third hydraulic test, with packers inflated to isolate the Lower Bullfrog Tuff interval, C#3 was pumped for 553 days, from May 8, 1996 to November 12, 1997, before and during a series of tracer tests in the Lower Bullfrog interval. Drawdown was analyzed in this interval and in all other intervals of C#1 and C#2 that responded to pumping before mechanical problems developed on March 26, 1997. Drawdown was analyzed in UE-25 ONC-1 (ONC-1), USW H-4 (H-4), UE-25 WT#14 (WT#14), and UE-25 WT#3 (WT#3) for periods from 7 to 18 months to evaluate heterogeneity and scale effects in the Miocene tuffaceous rocks. Water levels in UE-25 p#1 (p#1), completed in Paleozoic carbonate rocks, were measured to detect a hydraulic connection between the Miocene tuffaceous rocks and the Paleozoic carbonate rocks in the vicinity of the C- wells.

2.3.1.1 Analytical Methods

Although rock at the C-wells complex is fractured pervasively, hydrogeologic intervals respond to pumping as an equivalent porous medium (Geldon 1996; Geldon et al. 1998). Because the water table occurs at or near the top of the Calico Hills interval in the vicinity of the C-wells complex, that interval typically responds to pumping as an anisotropic, unconfined aquifer. With pervasive fracturing that apparently extends to the water table, the Prow Pass and Upper Bullfrog intervals respond to pumping as either an unconfined, fissure-block, or confined aquifer. Isolated by intervals of nonfractured rock, the Lower Bullfrog interval typically responds to pumping as a confined aquifer. Recharged by flow from fractures related to faults (identified on lithologic logs prepared by Richard W. Spengler and included in a report by Geldon (1993)), the Upper Tram interval typically responds to pumping as a leaky, confined aquifer without confining bed storage.

Analytical methods used for hydraulic tests discussed in this section are those of Theis (1935) and Cooper and Jacob (1946), for infinite, homogeneous, isotropic, confined aquifers; Neuman (1975), for infinite, homogeneous, anisotropic, unconfined aquifers; and Streltsova-Adams (1978), for fissure-block aquifers. Geldon (1996) discusses assumptions, equations, and application of these analytical methods in hydraulic tests at the C-wells complex. Analysis of drawdown in this study was restricted to observation wells because drawdown in pumping wells at the C-wells complex typically is too large and rapid to be explained solely by hydraulic properties of the pumped interval (Geldon 1996). This observation can be illustrated by looking at the drawdown in C#3 at 464,000 minutes (322.22 days) after pumping began on May 8, 1996. That drawdown was 599 cm. With hydraulic properties computed for the Lower Bullfrog interval in C#1 and C#2 inserted into an approximation of the Theis (1935) equation as given by Lohman (1979), the drawdown in C#3 attributable to aquifer characteristics should have been no more than 69 to 72 cm after 322.22 days of pumping, or 12 percent of the actual recorded drawdown. Most of the drawdown in C#3 probably can be attributed to frictional head loss or

"borehole skin." Therefore, calculation of hydraulic properties from that drawdown is not reliable.

All of the analytical methods used in this study, except for the Neuman (1975) method, assume radial flow to the pumping well, and, therefore, ignore vertical flow (application of the Neuman fully-penetrating-well solution, as was done in this report, to cases where pumping was in one interval and the analyzed drawdown response was in another, also ignores vertical flow). However, in hydraulic tests of the Bullfrog-Tram interval (February 1996) and the Lower Bullfrog interval (May 1996 to March 1997), drawdown was observed in the Calico Hills, Prow Pass, and Upper Bullfrog intervals, even though the sliding sleeves allowing direct communication between those intervals and the flow intake piping were not open. For water to reach the pumping well from the intervals that did not have open sliding sleeves, a downward component of flow must have occurred. The downward flow was assumed to be much less than radial flow to the pumping well in order to analyze the drawdown from the non-open intervals by the methods outlined in this section. Hydraulic properties calculated under this assumption have a high level of confidence because they generally are consistent with quantitative results of the hydraulic test conducted in June 1995, which was designed such that flow from hydrogeologic intervals in C#1 and C#2 to C#3 would be largely radial.

2.3.1.2 Earth Tides and Barometric Effects

Previous monitoring of water levels in observation wells before, during, and after hydraulic tests conducted in the C-wells indicated that all of those boreholes respond to Earth tides and atmospheric pressure changes. With frequencies of 0.9 to 2.0 cycles per day (Galloway and Rojstaczer 1988), Earth tides caused water-level altitudes in the C-wells to fluctuate as much as 12 cm during a 10-day hydraulic test conducted at the C-wells complex from May to June 1995 (Geldon et al. 1998). Consequently, in the hydraulic testing described here, Earth-tide effects were removed from water levels, and cycles of the same frequency as Earth tides were removed from simultaneously recorded atmospheric pressures before computing the barometric efficiency of most borehole intervals. Earth-tide effects also were removed from the records of observation wells in which drawdown caused by pumping was expected to be obscured by Earth tides (boreholes H-4, WT#14, WT#3, and p#1). The boreholes requiring an Earth-tide correction to water-level records were completed in Miocene tuffaceous rocks more than 1,500 m from C#3 or were completed in a different aquifer than that of the C-wells complex (i.e., in the Paleozoic carbonate rocks). Earth-tide effects were removed from records of water levels, and cycles of the same frequency as Earth tides were removed from simultaneously recorded atmospheric pressure by applying a low-pass filter with a cutoff frequency of 0.8 cycles/day to those records. As shown in Figure 7, this filtering removes semi-diurnal changes in water levels while preserving longer-term trends.

Changes in atmospheric pressure in the vicinity of the C-wells complex typically produce synchronous (but opposite) changes in water levels in boreholes (Figure 8). The slope of a line fit to a plot of water-level change as a function of atmospheric-pressure change is called the barometric efficiency. Determination of the barometric efficiency of the Lower Bullfrog interval in C#2 is shown in Figure 9. Barometric efficiency values of borehole intervals for which drawdown was computed during this study ranged from 0.75 to 0.99 (Table 5). To compute barometrically corrected drawdown, barometric effects were removed from borehole records by

subtracting the product of atmospheric-pressure change and barometric efficiency from the change in water level.

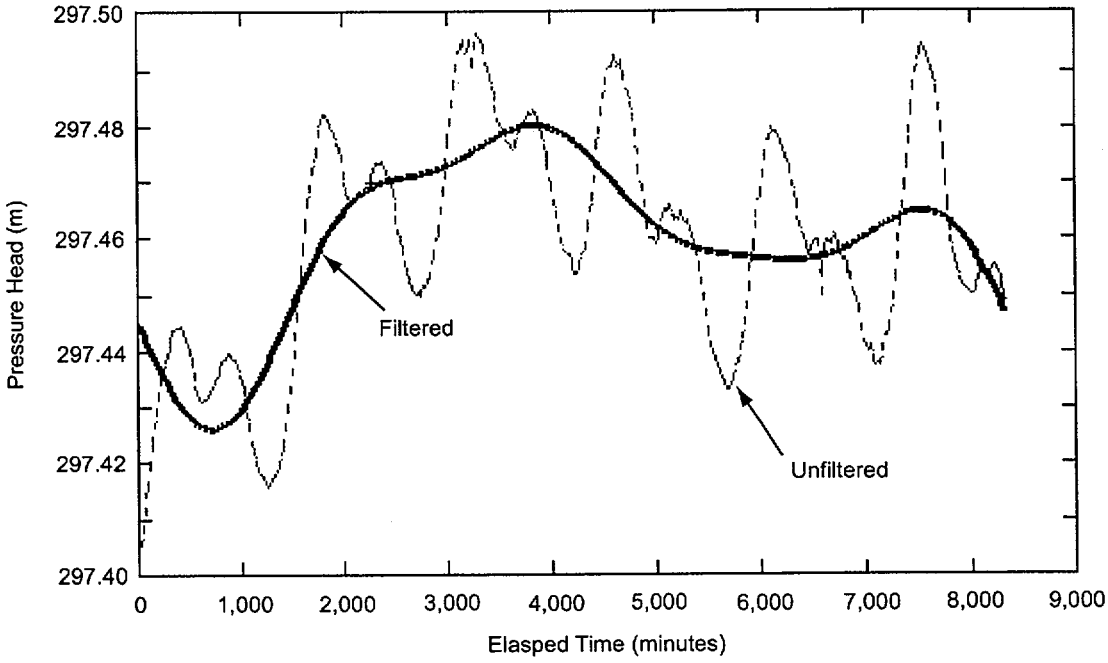

Figure 7. Result of Filtering Out Earth Tides on UE-25 C#2 Lower Bullfrog Interval Pressure Heads, June 23–29, 1995

2.3.1.3 Flow Distribution in the C-wells

During hydraulic tests conducted in the C-wells in February 1996 and from May 1996 to November 1997, all hydrogeologic intervals in the C-wells that were being monitored responded to pumping, regardless of the interval being pumped. Leakage around packers could have occurred, although the packers were seated in non-rugose, sparsely fractured zones, but it is extremely unlikely that all packers failed to seal properly. A more reasonable interpretation is that fractures beyond borehole walls are so interconnected that packers emplaced in the C-wells do not isolate the interval being pumped from other transmissive intervals within the volume of aquifer stressed by the pumping.

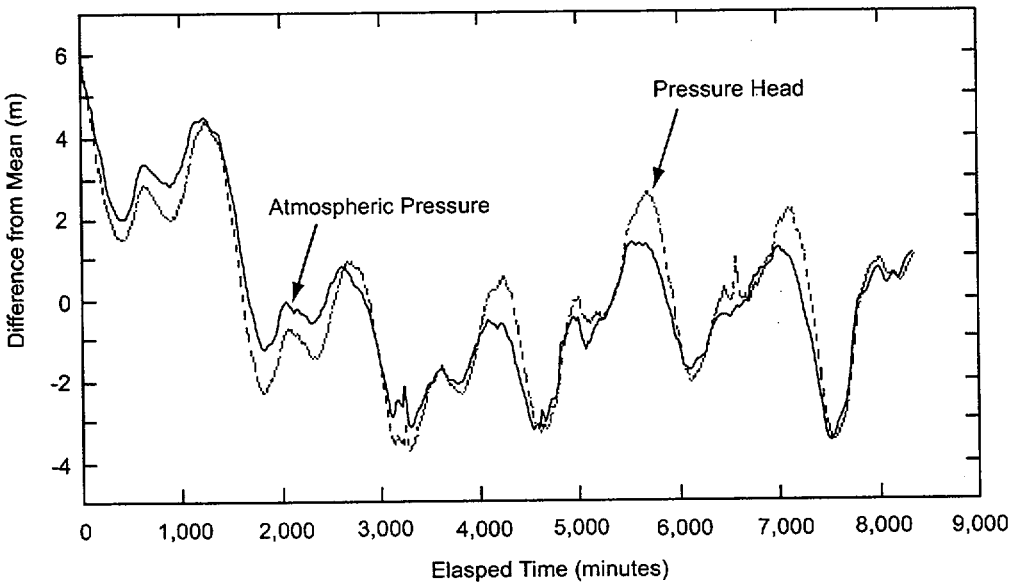

Figure 8. Difference from Mean Pressure Head in UE-25 c#2 Lower Bullfrog Interval and Atmospheric Pressure at the C-wells Complex, June 23-29, 1995

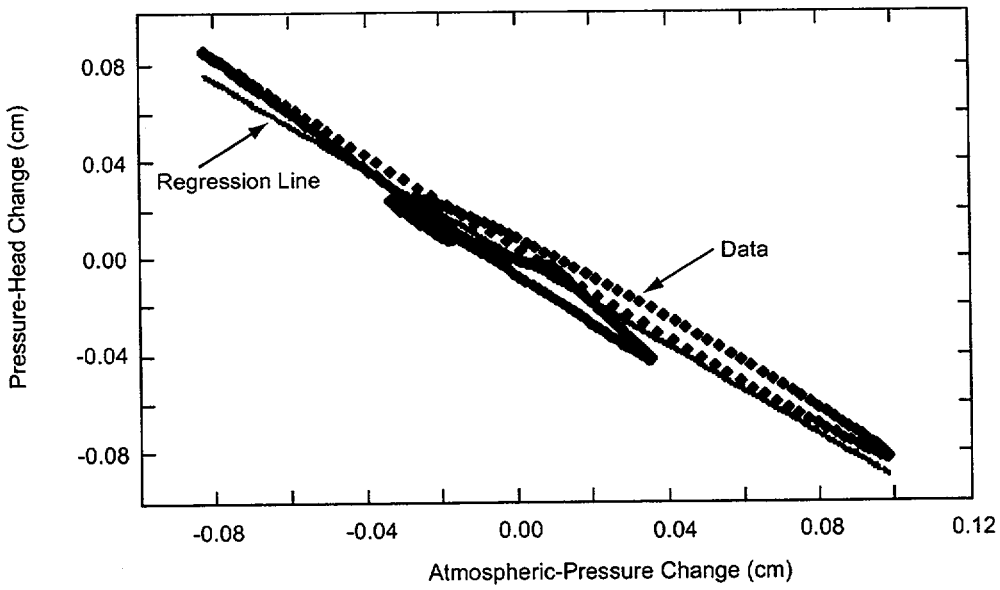

Figure 9. Filtered Pressure-head Change in UE-25 c#2 Lower Bullfrog Interval as a Function of Filtered Atmospheric-Pressure Change at the C-wells Complex, June 23–29, 1995

Table 5. Barometric Efficiency Values Determined for Borehole Intervals Monitored at the C-wells Complex, May 1996 to December 1997

Borehole	Interval	Barometer Location	Period of Record	Barometric Efficiency	Regression Coefficient
UE-25 c#1	Prow Pass	C-wells	June 23–29, 1995	0.96	0.98
	Upper Bullfrog	C-wells	June 24–29, 1995	0.99	0.97
	Lower Bullfrog[a]	C-wells	June 23–29, 1995	0.97	0.98
UE-25 c#2	Calico Hills	C-wells	June 23–29, 1995	0.93	0.94
	Prow Pass	C-wells	June 23–29, 1995	0.93	0.97
	Upper Bullfrog	C-wells	June 23–29, 1995	0.93	0.97
	Lower Bullfrog[a]	C-wells	June 23–29, 1995	0.91	0.96
UE-25 c#3	Calico Hills[b]	C-wells	February 7–8, 1996	0.83	0.89
	Lower Bullfrog	C-wells	May 9–13, 1996	0.87	0.92
	Bullfrog-Tram	C-wells	Not applicable	0.94[c]	Not applicable
UE-25 ONC-1	Prow Pass	ONC-1	July 1–Sept. 13,1995	0.99	0.90
USW H-4	Prow Pass to Lithic Ridge	ONC-1	June 8–12, 1995	0.91	0.87
UE-25 WT#14	Calico Hills	C-wells	June 4–12, 1995	0.89	0.94
UE-25 WT#3	Lower Bullfrog	C-wells	June 4–12, 1995	0.91	0.82
UE-25 p#1	Paleozoic carbonates	C-wells	Jan. 1–June 20, 1986	0.75	Not applicable

NOTES: (a) Barometric efficiency of Lower Bullfrog used, also, for Bullfrog-Tram in hydraulic test February 8–13, 1996.

(b) Barometric efficiency of Calico Hills used, also, for Calico Hills-Upper Bullfrog in hydraulic test February 8–13, 1996.

(c) Barometric efficiency estimated from values for Bullfrog-Tram in UE-25 c#1 and UE-25 c#2.

Spinner and oxygen-activation flow surveys (Figure 10) were run in C#3 during the hydraulic test in June 1995 to determine the flow distribution in the C-wells under pumping conditions. However, those flow surveys failed to detect flow from the Prow Pass interval that was indicated by heat-pulse flowmeter surveys conducted without pumping in the C-wells in 1991 (Geldon 1996). Results of the 1991 and 1995 flow surveys were combined algebraically to estimate a flow distribution during the hydraulic test in June 1995 (Table 6). That flow distribution was adjusted for the hydraulic tests conducted in February 1996 and May 1996 to November 1997 (Table 6) by inserting discharge and drawdown values recorded at the same elapsed time in the three hydraulic tests into the following equation:

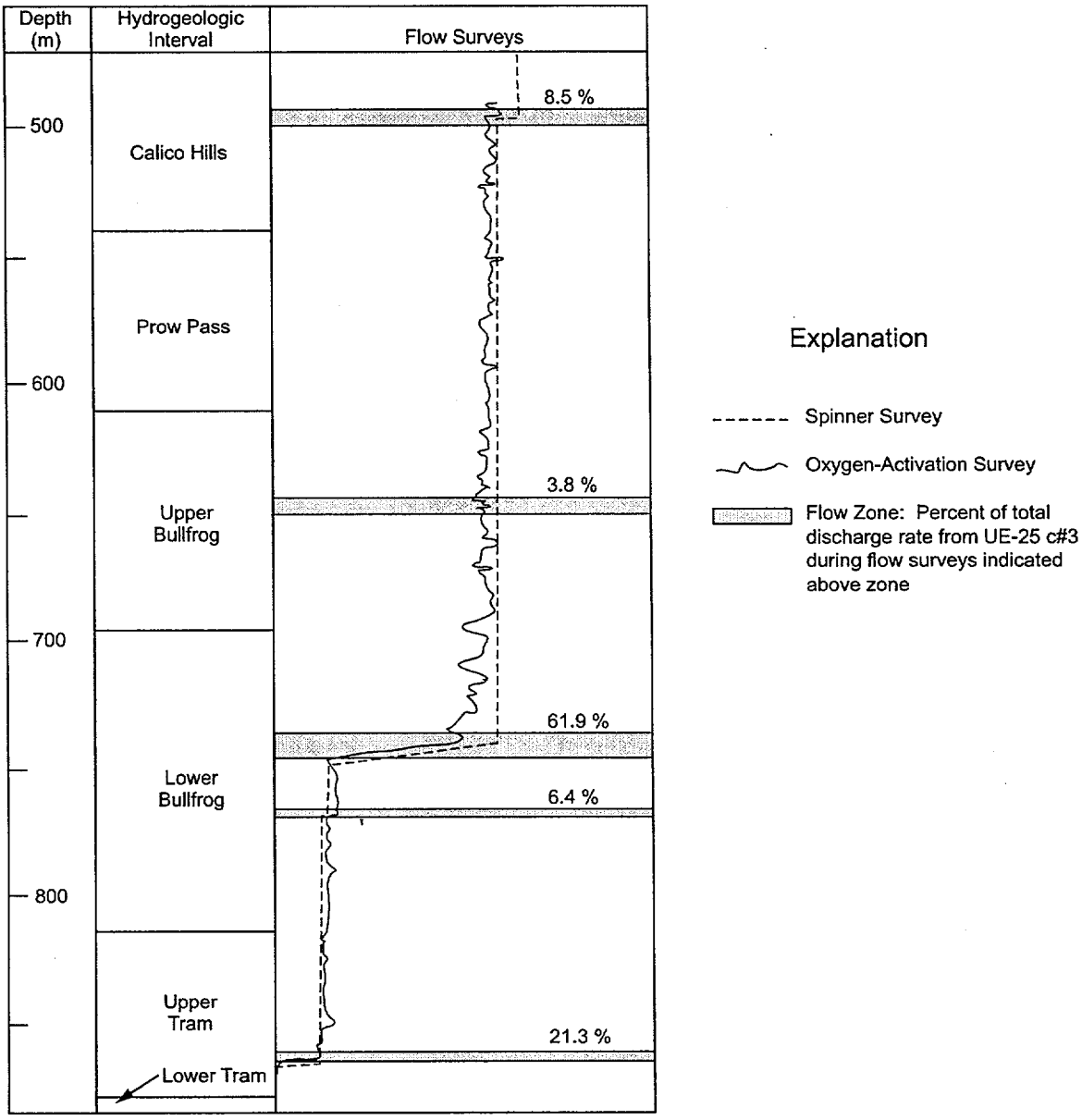

Figure 10. Flow Surveys in UE-25 c#3 During Hydraulic Testing in June 1995

Table 6. Interval Discharges 5,800 Minutes After Pumping Started in Hydraulic Tests in UE-25 c#3, June 1995 to November 1997

Hydro-geologic Unit	June 1995			February 1996			May 1996 to November 1997		
	Dis-charge (L/s)	Draw-down (cm)	Flow %	Dis-charge (L/s)	Draw-down (cm)	Flow %	Dis-charge (L/s)	Draw-down (cm)	Flow %
UE-25 c#1									
Calico Hills	22.5	No data	3.8	8.45	No data	0.5 (est)	9.72	No data	1.1 (est)
Prow Pass	22.5	43.0	2.9	8.45	14.0	2.5	9.72	14.9	2.3
Upper Bullfrog	22.5	52.1	3.9	8.45	21.6	4.3	9.72	19.2	3.3
Lower Bullfrog	22.5	49.7	68.3	8.45	No data	No data	9.72	21.0	66.8
Bullfrog-Tram	22.5	No data	89.4	8.45	19.5	92.7	9.72	N/A	N/A
Upper Tram	22.5	No data	21.1	8.45	No data	No data	9.72	No data	26.5
Lower Tram	22.5	No data	trace	8.45	No data	trace	9.72	No data	trace
UE-25 c#2									
Calico Hills	22.5	351.7	3.8	8.45	16.4	0.5	9.72	43.0	1.1
Prow Pass	22.5	75.6	2.9	8.45	14.6	1.5	9.72	22.2	2.0
Upper Bullfrog	22.5	62.2	3.9	8.45	25.0	4.2	9.72	26.5	3.8
Lower Bullfrog	22.5	49.4	68.3	8.45	No data	No data	9.72	21.9	70.2
Bullfrog-Tram	22.5	No data	89.4	8.45	21.0	93.8	9.72	N/A	N/A
Upper Tram	22.5	283.2	21.1	8.45	No data	No data	9.72	No data	22.9
Lower Tram	22.5	239.6	trace	8.45	No data	trace	9.72	No data	trace

NOTE: Flow proportion for the Bullfrog-Tram interval shown in June 1995 is the sum of values for the Lower Bullfrog and Upper Tram intervals. est = estimated; N/A = not applicable

$$P_2 = Q_1 P_1 s_2 / Q_2 s_1 \qquad \text{(Eq. 1)}$$

where

P_1 = the proportion of flow determined for a hydrogeologic interval during the hydraulic test in June 1995

P_2 = the proportion of flow determined for a hydrogeologic interval during a hydraulic test in either February 1996 or May 1996 to November 1997, as appropriate

Q_1 = the average discharge during the hydraulic test in June 1995

Q_2 = the average discharge during a hydraulic test in February 1996 or May 1996 to November 1997, as appropriate

s_1 = the drawdown in a hydrogeologic interval during the hydraulic test in June 1995

s_2 = the drawdown in a hydrogeologic interval during a hydraulic test in either February 1996 or May 1996 to November 1997, as appropriate.

In the three hydraulic tests discussed in this report, the Lower Bullfrog interval consistently contributed about 70 percent of the flow from observation wells to the pumping well at the C-wells complex; the Upper Tram interval consistently contributed about 20 percent of that flow; and all other intervals combined contributed about 10 percent of the total flow. To analyze the drawdown in any hydrogeologic interval, the total discharge from C#3 first was multiplied by the percentage of flow contributed by the interval being analyzed to avoid calculating erroneously large values of transmissivity and storativity (both of which are directly proportional to discharge).

2.3.1.4 Monitoring Network

The monitoring network at the C-wells complex was selected after borehole C#3 was chosen as the pumping well for all hydraulic tests conducted from 1995 to 1997 on the basis of its successful performance during two hydraulic tests conducted in 1984. Boreholes C#1 and C#2 were used as observation wells for the hydraulic tests conducted in June 1995 and February 1996. Boreholes ONC-1, H-4, WT#14, WT#3, and p#1 also were used as observation wells for the longer-term hydraulic test conducted from May 1996 to November 1997. Recording barometers were located at the C-wells complex during all hydraulic tests; a barometer located at borehole ONC-1 also was used during the third hydraulic test.

Borehole C#3 is 900.4 m deep (Geldon et al. 1997a). The borehole is cased and grouted to a depth of 417.0 m, just below the water table. During the hydraulic test in June 1995, C#3 did not contain packers and was open from the Calico Hills Formation to the Lower Tram interval. After packers were emplaced in August 1995, manipulation of the packers, sliding sleeves, and slotted casing allowed selective hydraulic communication with only the Lower Bullfrog and Upper Tram intervals during hydraulic and tracer tests in February and March 1996 and with only the Lower Bullfrog interval from May 1996 to December 1997.

Borehole C#2 is 30.4 m from C#3 at the land surface and 910.1 m deep (Geldon et al. 1997a). It is cased and grouted to a depth of 416.0 m. Five dual-mandrel packers, suspended on 7.30-cm-diameter tubing, were emplaced in the borehole to isolate hydrogeologic intervals throughout the period of testing discussed in this report. Manipulation of packers and sliding sleeves allowed hydraulic communication with six separate hydrogeologic intervals (Figure 5 and Table 3) in June 1995, with the Lower Bullfrog and Upper Tram intervals in February and March 1996, and with the Lower Bullfrog interval from May 1996 to December 1997.

Borehole C#1 is 68.4 m from C#3 at the land surface and is 897.6 m deep (Geldon et al. 1997a). It is cased and grouted to a depth of 417.9 m. Five dual-mandrel packers, suspended on 7.30-cm-diameter tubing, were emplaced in the borehole to isolate hydrogeologic intervals throughout the period of testing discussed in this report. Manipulation of packers and sliding sleeves allowed hydraulic communication with the Calico Hills, Prow Pass, Upper Bullfrog, and Lower Bullfrog intervals in June 1995, with the Lower Bullfrog and Upper Tram intervals in February and March 1996 and with the Lower Bullfrog interval from May 1996 to December 1997.

Borehole ONC-1 is 842.8 m from borehole C#3 at the land surface and is 469.4 m deep (extending about 36.3 m below the water level in the borehole) (Nye County Nuclear Waste Repository Project Office 1995). The borehole is telescoped downward and has a diameter of

about 13 cm in the saturated zone. Seven packers inflated between the bottom of the casing and a depth of 410 m separate the unsaturated and saturated zones; another packer emplaced at a depth of 452 m divides the saturated zone into two intervals. The upper of the saturated-zone intervals is open in the Calico Hills Formation and the Prow Pass Tuff; the lower of those intervals is open in the Prow Pass Tuff. Absolute transducers, installed in all packed-off intervals, transmitted total (atmospheric plus hydraulic) pressures to a data logger every 15 to 20 minutes during the tests reported here. Data from the lowermost transducer, positioned at a depth of 458 m, were converted to pressure heads for analysis.

Borehole H-4, which is 2,245 m from borehole C#3 at the land surface, is 1,219 m deep (Graves et al. 1997). The borehole diameter is 37.5 cm to a depth of 564 m and 22.2 cm below 564 m. Casing extends to a depth of 561 m; it is perforated below the water level, which was at an average depth of 518.3 m from 1985 to 1995. A packer emplaced at a depth of 1,181 m separates the Prow Pass, Bullfrog, and Tram Tuffs and the upper part of the Lithic Ridge Tuff from the lower part of the Lithic Ridge Tuff in the borehole. A 48-mm-diameter piezometer tube is installed in the upper part of the borehole, and a 62-mm-diameter piezometer tube is installed in the lower part of the borehole. Differential transducers emplaced in the two monitored intervals transmitted hydraulic pressures to a data logger every 15 minutes during this study. Only the data from the upper interval were used.

Borehole WT#14, which is 2,249 m from borehole C#3 at the land surface, is 399 m deep (Graves et al. 1997). The borehole has a diameter of 22.2 cm below the water table, which was at an average depth of 346.4 m from 1985 to 1995. The borehole is cased to a depth of 37 m and is open in the Topopah Spring Tuff and Calico Hills Formation. A 62-mm-diameter piezometer tube is installed in the borehole. A differential transducer emplaced in the piezometer tube transmitted hydraulic pressures to a data logger every 15 minutes during this study.

Borehole WT#3, which is 3,526 m from borehole C#3 at the land surface, is 348 m deep (Graves et al. 1997). The borehole has a diameter of 22.2 cm below the water table, which was at an average depth of 300.5 m from 1985 to 1995. The borehole is cased to a depth of 12 m and is open in the Bullfrog Tuff. A 62-mm-diameter piezometer tube is installed in the borehole. A differential transducer emplaced in the piezometer tube transmitted hydraulic pressures to a data logger every 15 minutes during this study.

Borehole p#1, which is 630 m from borehole C#3 at the land surface, is 1,805 m deep (Graves et al. 1997). The borehole diameter decreases from 37.5 to 15.6 cm with depth. Casing and cement emplaced to a depth of 1,297 m isolate the Miocene tuffaceous rocks in the upper part of the borehole from Paleozoic carbonate rocks in the lower part of the borehole. The water-level altitude for the Paleozoic carbonate rocks in p#1 was monitored through a 38-mm-diameter piezometer tube. The average depth to water in the piezometer tube was 361.8 m from 1985 to 1995. A differential transducer emplaced in the piezometer tube transmitted hydraulic pressures to a data logger every 60 minutes during this study.

2.3.1.5 Description of Tests

An hydraulic test was conducted in June 1995 to determine hydraulic properties of six hydrogeologic intervals at the C-wells complex (Figure 5 and Table 3). The six intervals were isolated by packers in boreholes C#1 and C#2. Sliding sleeves open in the packed-off intervals of the observation wells allowed hydraulic communication with the pumping well C#3, which was uncased and contained no packers to isolate intervals. Because of malfunctioning transducers, analyzable data were obtained only from the Prow Pass, Upper Bullfrog, and Lower Bullfrog intervals of C#1 and from the Calico Hills, Prow Pass, Upper Bullfrog, and Lower Bullfrog intervals of C#2.

The hydraulic test began on June 12 and ended on June 16, after 4.03 days of pumping. (Note that data were collected over thousands of elapsed minutes, the measure of time used by data-acquisition software and needed for hydraulic calculations. For the summarizing discussions here, those time intervals are expressed in hours and days.) Recovery was monitored until June 29, by which date it appeared to be complete in all intervals. At an average discharge rate of 22.5 L/s, drawdown in C#3 rapidly increased to a maximum of 10.9 m (Figure 11). The pumping in C#3 produced drawdown ranging from 43.0 to 52.1 cm in intervals of C#1 (Figure 12) and from 49.4 to 352 cm in intervals of C#2 (Figure 13).

The most permeable interval identified in the hydraulic test conducted in June 1995, the Lower Bullfrog interval, was chosen for subsequent tracer tests at the C-wells complex to increase the chance of successful transport of tracers between the injection and recovery wells. Because the transducer in the Lower Bullfrog interval of C#3 was not working, the packers between the Lower Bullfrog and Upper Tram intervals in all three of the C-wells were deflated, and the combined Lower Bullfrog and Upper Tram intervals (shown in Figure 5 as the Bullfrog Tram interval) became the test interval for the following series of tests.

After testing pump performance in January 1996 and allowing water levels in the C-wells to recover, pumping began on February 8, 1996, to establish a steep, quasi-steady-state hydraulic gradient between C#2 (the injection well) and C#3 (the recovery well) for a conservative tracer test. Tracer injection on February 13 disturbed the hydraulic pressure in the injection interval for 12.5 hours and effectively terminated the analyzable drawdown record. The 4.85 days of drawdown recorded between the start of pumping and the injection of tracer on February 13 (when the hydraulic pressure in the injection interval was disturbed) were analyzed as an hydraulic test.

During the hydraulic test in February 1996, operation of the pump outside its optimal performance range caused discharge to decrease steadily, despite an adjustment of the pump speed on February 12, some 5,640 minutes (3.917 days) after pumping started. Prior to that adjustment, discharge decreased from 8.78 to 8.21 L/s. Adjusting the pump speed restored the discharge to 8.75 L/s, but discharge immediately began to decrease and was at 8.57 L/s when the tracer test started on February 13 (Figure 14). Although average discharge after adjusting the pump speed was 0.10 L/s larger than before that adjustment, deviation from the average discharge of 8.49 L/s was just 3 percent for the entire period of pumping.

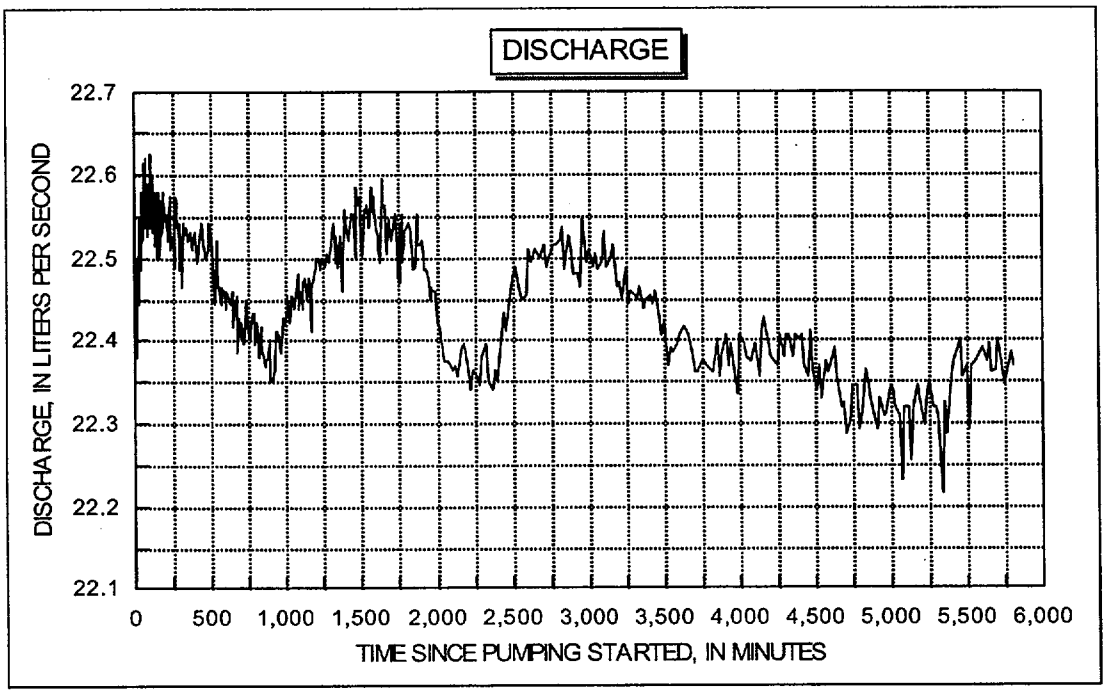

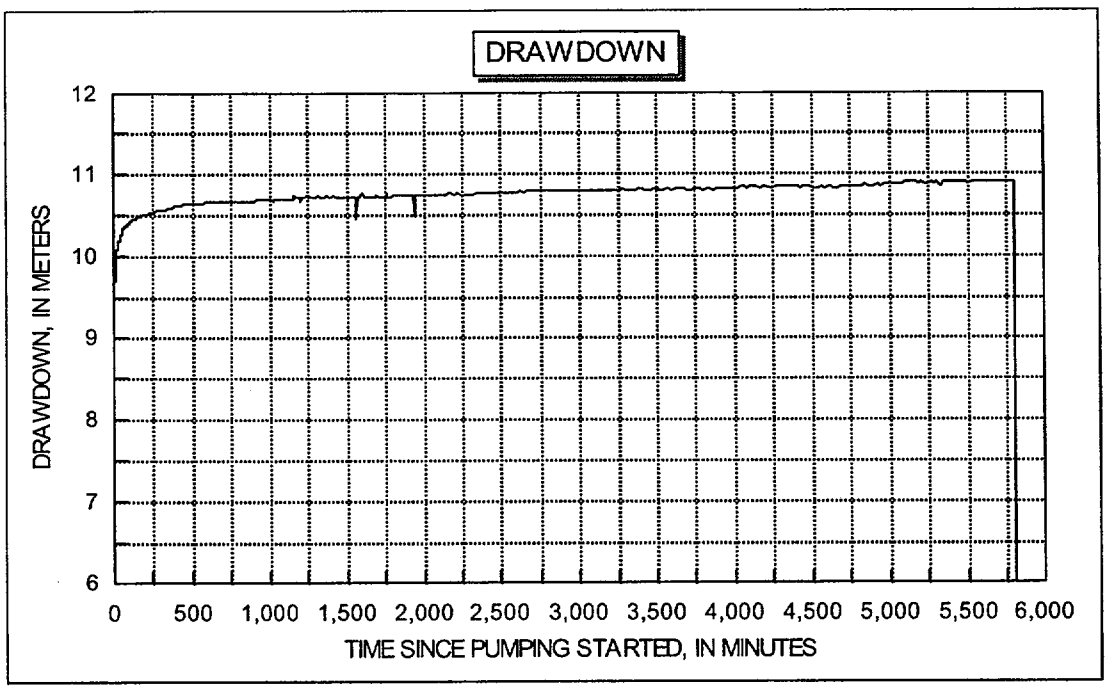

Figure 11. UE-25 c#3 Discharge and Drawdown, June 12, 1995 (~0 minutes), to June 16, 1995 (~5,800 minutes)

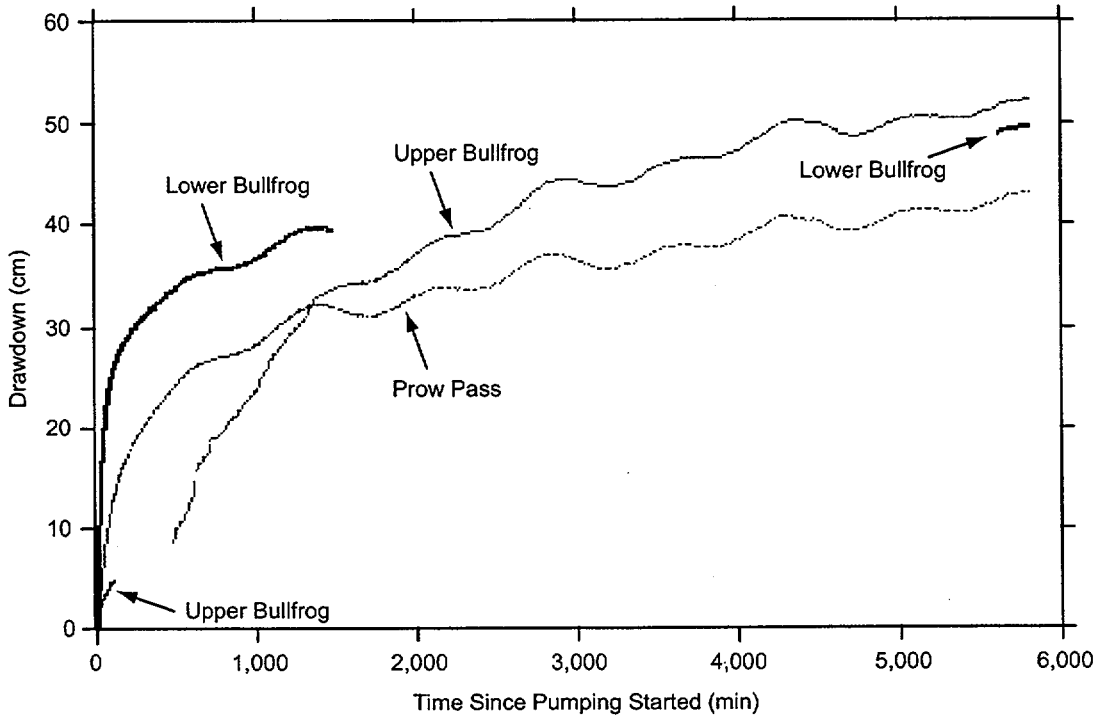

Figure 12. UE-25 c#1 Drawdown

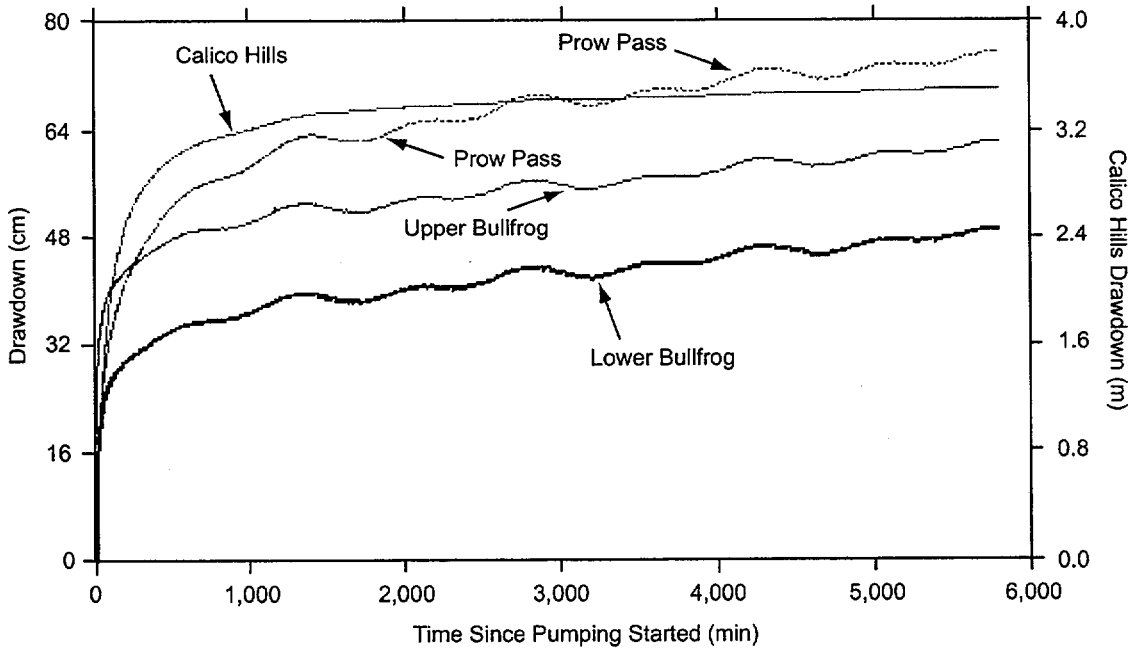

Figure 13. UE-25 c#2 Drawdown

As shown in Figure 14, the pumping produced as much as 2.86 m of drawdown in the Bullfrog Tram interval of C#3 (96 percent of which occurred in the first 10 minutes). Adjustment of the pump speed caused a step-like increase of 0.19 m in C#3 drawdown, but it had no discernible effect on drawdown in the other C wells. Although oscillatory, drawdown in C#1 steadily increased and ranged from 14.3 to 22.1 cm in the Prow Pass, Upper Bullfrog, and Bullfrog Tram intervals (Figure 15). Likewise oscillatory, drawdown in C#2 steadily increased and ranged from 14.9 to 25.3 cm in the Calico Hills, Prow Pass, Upper Bullfrog, and Bullfrog Tram intervals (Figure 16). Steady increases in observation-well drawdown together with small deviations from the average discharge enabled the observation-well drawdown for the entire period before tracer injection to be analyzable.

After the tracer test in the Bullfrog Tram interval ended in March 1996, a new transducer was installed in the Lower Bullfrog interval of C#3, and packers in the borehole were reconfigured. Subsequently, it was possible to conduct hydraulic and tracer tests in the isolated Lower Bullfrog interval. With nearly continuous pumping, a series of tracer tests was conducted in that interval by the USGS and by LANL from May 1996 to November 1997. Pumping in C#3 to establish a steep, quasi-steady-state hydraulic gradient for tracer tests in the Lower Bullfrog interval began May 8, 1996. From May 24, 1996, to March 26, 1997, the pump shut off 11 times because of problems with the generators that provided power to the site. Between March 26 and May 8, 1997, the pump operated erratically because of continued problems with one of the generators. Problems with the power supply caused the pump to shut off intermittently between May 30 and September 29, 1997, and at least once a day between October 15 and November 12, 1997. Pumping was terminated on November 12, 1997, 553.24 days after pumping started, and recovery was monitored until December 31, 1997.

Discharge between May 8, 1996, and March 26, 1997, initially oscillated between 9.6 and 9.8 L/s, eventually stabilized at about 9.4 L/s, and averaged 9.53 L/s (Figure 17). After generator problems were resolved on May 8, 1997, discharge decreased steadily from 9.3 to 8.9 L/s on November 12, 1997, and averaged 9.01 L/s. The volume of water withdrawn between May 8, 1996, and November 12, 1997, was 440.2 million L, equivalent to an average discharge of 9.21 L/s.

As in previous hydraulic tests, drawdown in the pumped well was large and reached steady-state conditions rapidly (Figure 17). Drawdown in the Lower Bullfrog interval of C#3 reached 4.8 m in 60 minutes and remained at 4.85 to 5.0 m until October 16, 1996, 161.11 days (232,000 minutes) after pumping started. For unknown reasons, drawdown then began increasing steadily and was 5.98 m on March 26, 1997, 322.22 days (464,000 minutes) after pumping started. After March 26, the frequent pump shutoffs kept drawdown less than 5.9 m, except during the process of restarting the pump. Pump shutoffs typically caused rapid and complete or nearly complete recovery in C#3, but those effects were reversed just as rapidly when the pump was restarted. Tracer-test operations affected drawdown in the pumped well minimally. Recovery from pumping on December 12, 1997, approximately 30 days (42,965 minutes) after pumping stopped, was 99 percent of antecedent drawdown. The prolonged period of unsteady pump discharge after March 26, 1997, effectively ended the drawdown record that could be analyzed as an hydraulic test for all observation wells except ONC-1. The analyzable drawdown record from

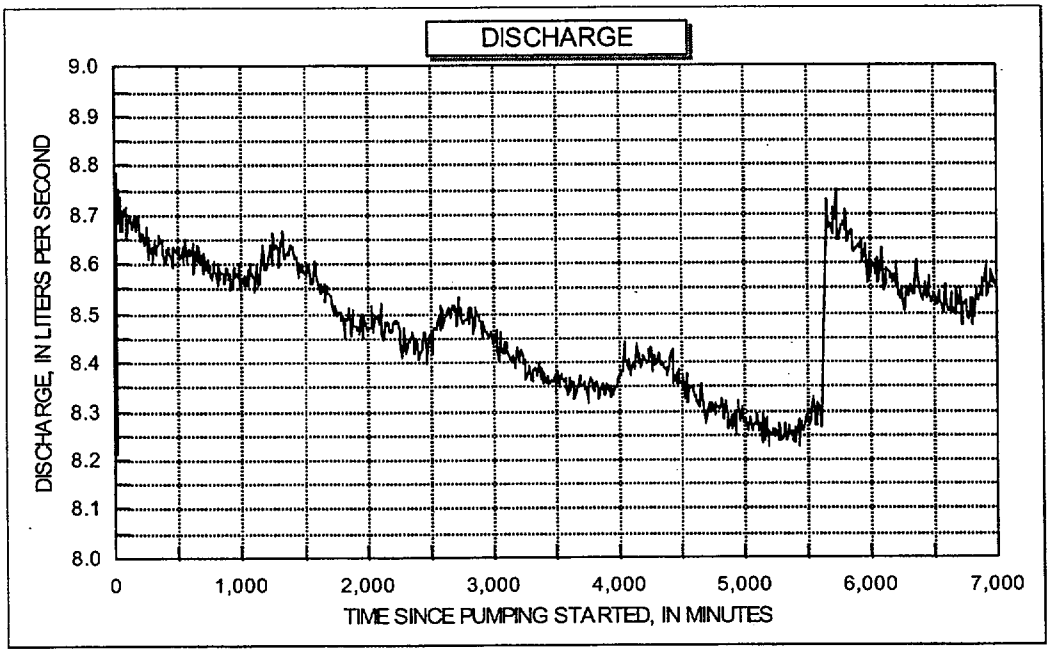

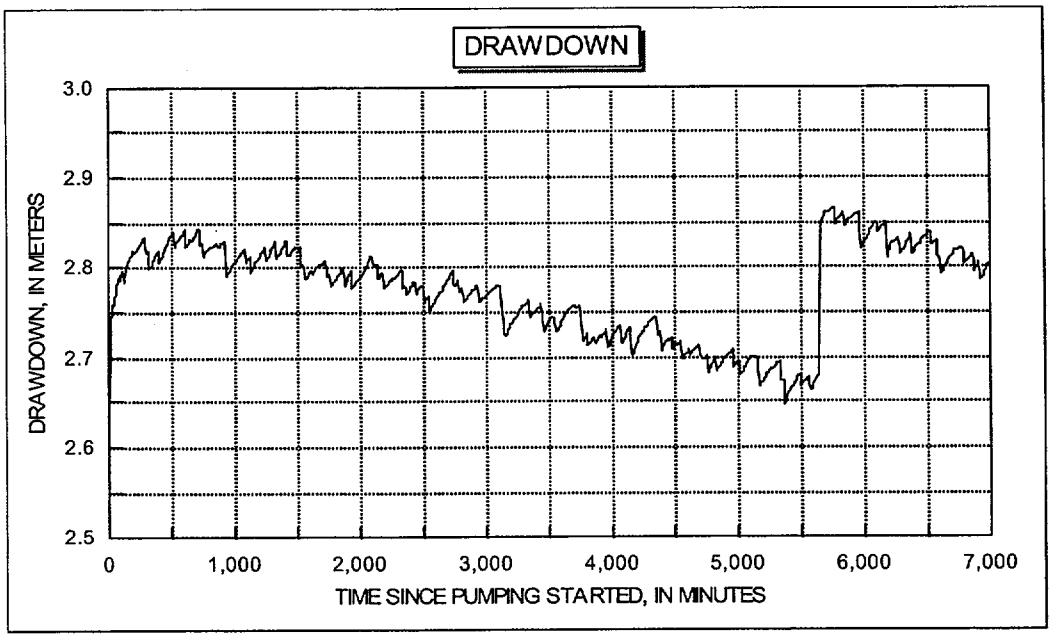

Figure 14. UE-25 c#3 Discharge and Drawdown, February 8, 1996 (~0 minutes), to February 13, 1996 (~7,000 minutes)

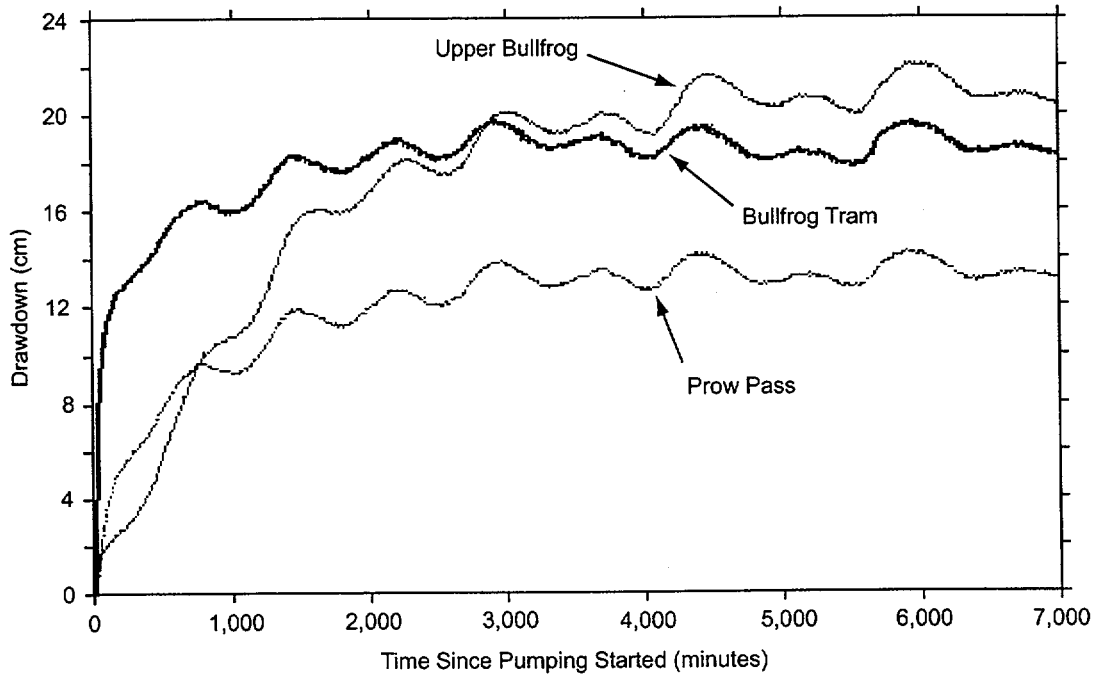

Figure 15. UE-25 c#1 Drawdown, February 8, 1996 (~0 minutes), to February 13, 1996 (~7,000 minutes)

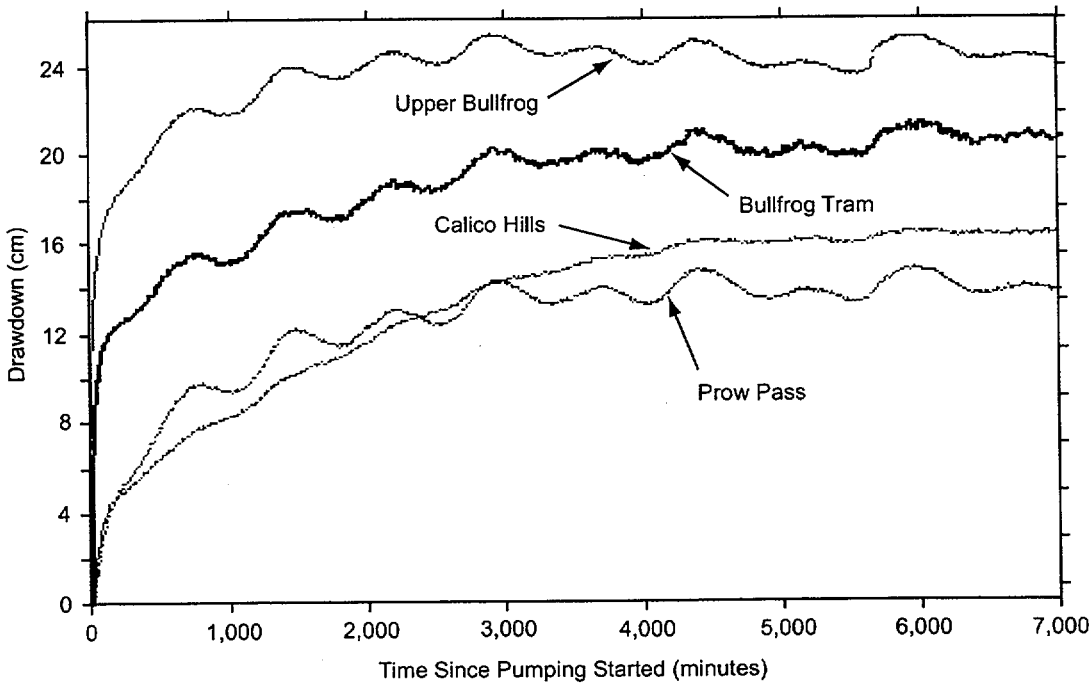

Figure 16. UE-25 c#2 Drawdown, February 8, 1996 (~0 minutes), to February 13, 1996 (~7,000 minutes)

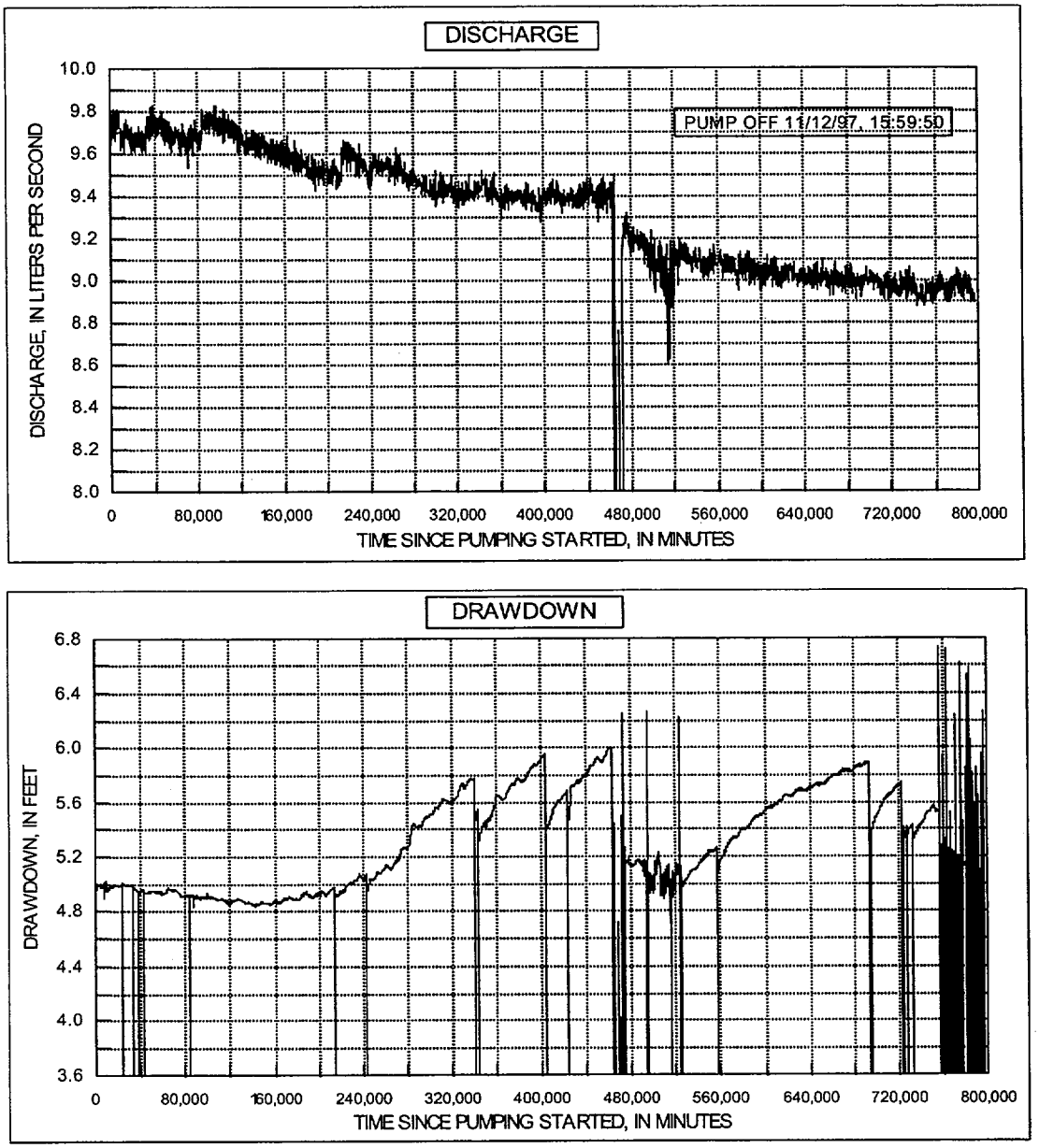

Figure 17. UE-25 c#3 Discharge and Drawdown, May 8, 1996 (~0 minutes), to November 12, 1997 (~800,000 minutes)

May 8, 1996, to March 26, 1997, is 322.32 days in duration. With 11 down times ranging from 2 to 185 minutes, the pump was off for 10.82 hours (649 minutes), about 0.1 percent of the time, during that period.

Drawdown in response to pumping the Lower Bullfrog interval of C#3 is known to have occurred in the Prow Pass, Upper Bullfrog, and Lower Bullfrog intervals of C#1 and in the Calico Hills, Prow Pass, Upper Bullfrog, and Lower Bullfrog intervals of C#2. Drawdown in all intervals of these boreholes generally increased steadily but was very oscillatory. Peak drawdown by March 26, 1997, ranged from about 36 to 42 cm in intervals of C#1 (Figure 18) and from about 35 to 51 cm in intervals of C#2 (Figure 19).

Disruptions of drawdown in the Lower Bullfrog and other intervals of C#1 and C#2 occurred from pump shutoffs 11 times between May 1996 and March 1997. Pump shutoffs (most of the unlabeled downward spikes in Figures 18 and 19) generally resulted in 20 to 50 percent recovery of water levels. However, these effects dissipated 50 to 500 minutes after the pump was restarted and did not affect analysis of the drawdown.

Recirculation of water during tracer tests conducted between May and November 1996 generally caused small decreases in drawdown in the Lower Bullfrog interval of C#1 or decreases followed by increases in drawdown in the Lower Bullfrog interval of C#2 at the start and end of recirculation, which generally lasted 70 to 560 minutes. However, recirculation of water in C#1 from June 17 to July 3, 1996, to facilitate transport of iodide tracer between the injection and recovery wells, caused drawdown in the Lower Bullfrog interval of C#1 to decrease in steps for 23,350 minutes (Figures 18 and 20A). Pumping water into C#1 faster than it could drain probably caused the drawdown to decrease. Periodic increases in the injection pump rate caused this decrease to occur in steps.

Tracer injection during four tests that were conducted between May 1996 and November 1997 caused increased drawdown in the Lower Bullfrog interval of C#1 or C#2 that generally lasted 180 to 750 minutes. However, following injection of 2,6 difluorobenzoic acid tracer into C#2 on January 10, 1997, drawdown in the Lower Bullfrog interval of C#2 remained high for 8,360 minutes (Figures 19 and 20B). Increased drawdown could have resulted from opening fractures within an unknown (probably small) radius of the injection well; enlarged fractures would have allowed water to drain from the well faster. Changes in hydraulic head associated with the dense tracer injection solution also could have produced the observed water-level changes in C#2.

Hypotheses regarding disturbances from tracer-test operations cannot be tested and, therefore, are presented only for consideration. It is important to note that (1) tracer-test operations conducted in one borehole generally did not affect drawdown in other boreholes and (2) disturbances from tracer-test operations did not affect analyses of drawdown in C#1 and C#2.

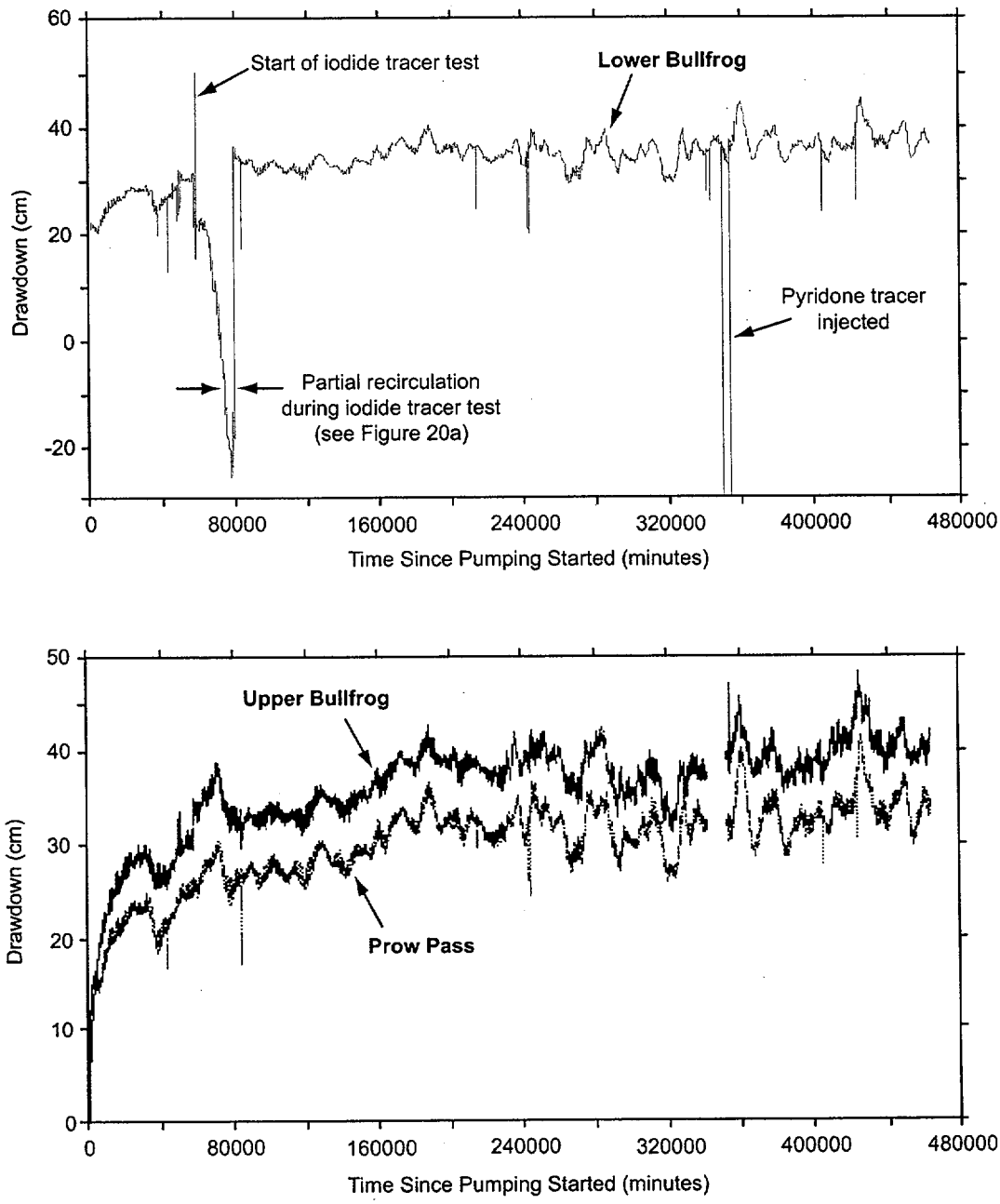

Figure 18. UE-25 c#1 Drawdown, May 8, 1996 (~0 minutes), to March 26, 1997 (~470,000 minutes)

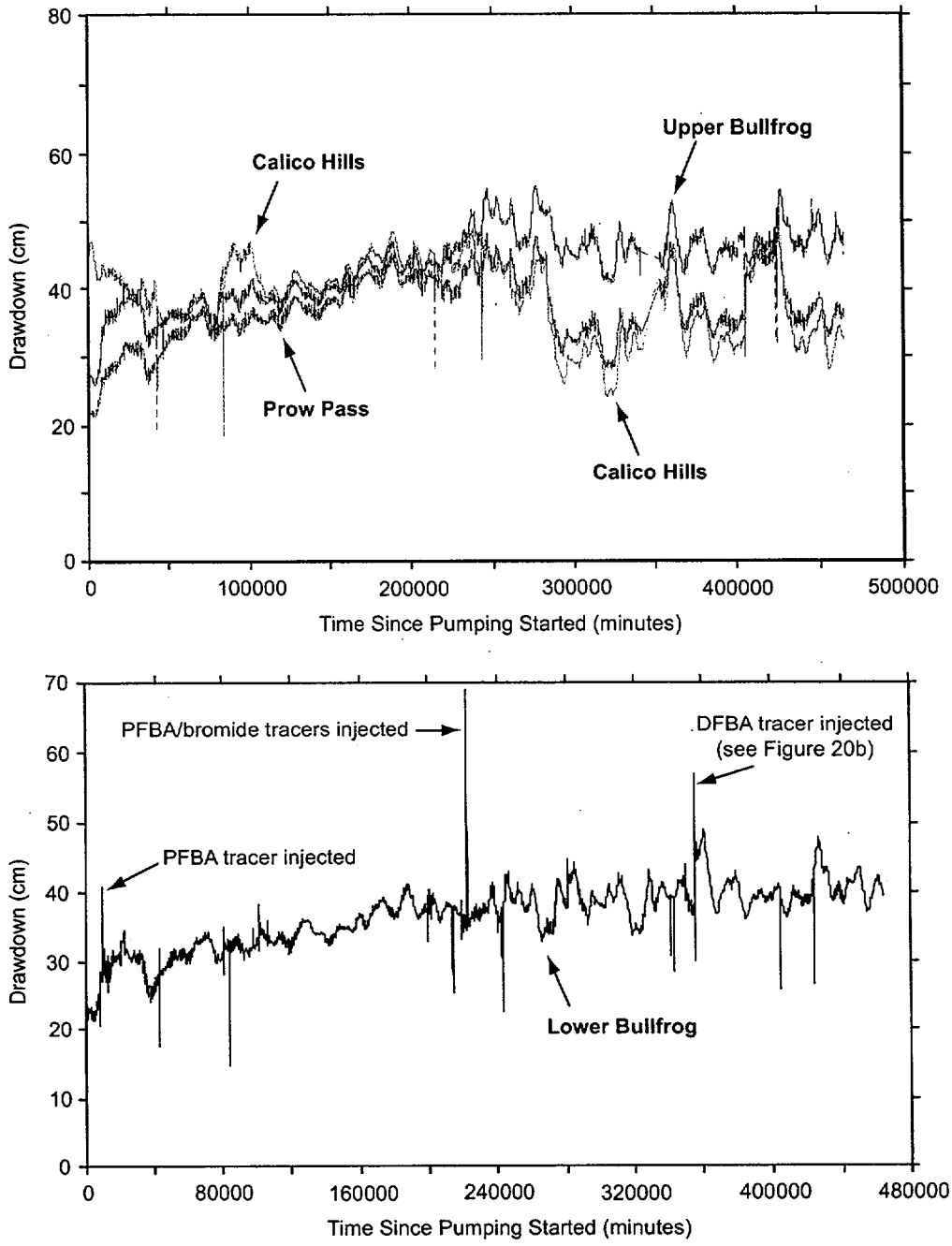

NOTE: PFBA: Pentafluorobenzoic acid; DFBA: 2,6 difluorobenzoic acid.

Figure 19. UE-25 c#2 Drawdown, May 8, 1996 (~0 minutes), to March 26, 1997 (~470,000 minutes)

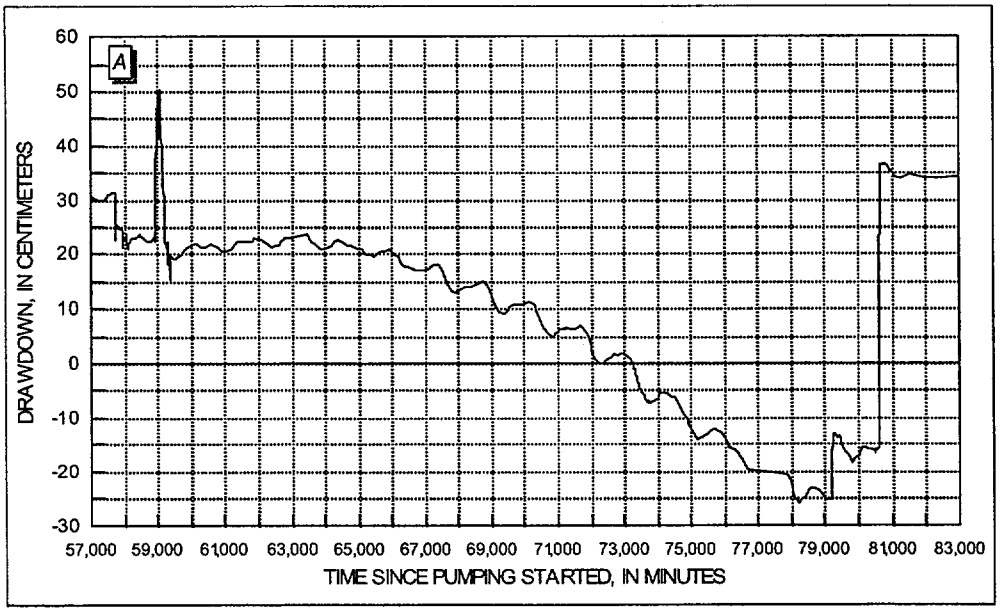

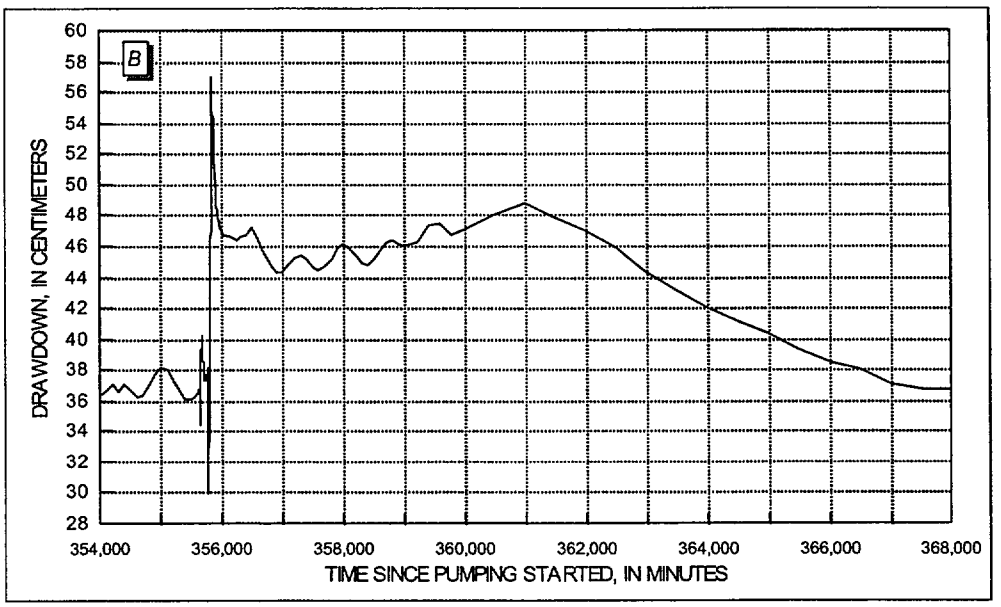

NOTES: A: Iodide tracer test in UE-25 c#1, June 17, 1996 (~57,000 minutes), to July 5, 1996 (~83,000 minutes).

B: 2,6 DFBA tracer test in UE-25 c#2, January 9, 1997 (~354,000 minutes), to January 18, 1997 (~368,000 minutes).

2,6 DFBA: 2,6 Difluorobenzoic acid.

Figure 20. Disturbance of Drawdown in Lower Bullfrog Interval of UE-25 c#1 and UE-25 c#2 by Tracer Tests in 1996 and 1997

Events of unknown, possibly human, origin caused hydraulic heads in the Lower Bullfrog interval of C#1 and C#2 to rise 5 to 8 cm from June 1 to June 11, 1996 (a period of 14,800 minutes) and from November 6 to November 14, 1996 (a period of 11,900 minutes). Because six observation wells within 3.5 km of C#3 showed similar rises in hydraulic head, the events that produced these disturbances could not have been local in scale.

Shutting off the pump in C#3 on November 12, 1997, caused erratic responses in the Lower Bullfrog intervals of C#2 and C#1 that are not analyzable. Recovery in the Lower Bullfrog interval of C#1 reached a plateau from 8,000 to 38,500 minutes after pumping stopped, after which it began increasing cyclically. On December 29, 1997, 46.53 days (67,000 minutes) after pumping stopped, recovery in the Lower Bullfrog interval of C#1 was about 95 percent of the antecedent drawdown (Figure 21). The transducer in the Lower Bullfrog interval of C#2 was removed on December 9, 1997, at a time when readings from the transducer were erratic, and recovery was only about 70 percent of the antecedent drawdown.

Pumping in the Lower Bullfrog interval of C#3 from May 1996 to March 1997 caused drawdown in all four of the observation wells beyond the C-wells complex that are completed in Miocene tuffaceous rocks. As in C#1 and C#2, drawdown in the four outlying observation wells was very oscillatory. Drawdown in these wells was not affected by pump shutoffs or tracer test operations.

Drawdown in ONC-1, the nearest observation well to the C-wells, was detected 200 minutes after pumping started and increased steadily thereafter (Figure 22). Peak drawdown by March 26, 1997, was about 28 to 30 cm. Peak drawdown when pumping ended on November 12, 1997, was about 36 to 37 cm. Recovery in ONC-1 followed a pattern similar to the Lower Bullfrog interval in C#1 (Figure 21). On December 29, 1997, 46.875 days (67,500 minutes) after pumping stopped, recovery in ONC-1 was about 76 percent of the antecedent drawdown.

Borehole WT#3, the farthest observation well from the C-wells, responded like the C-wells and ONC-1 to the pumping in C#3 that began on May 8, 1996. Drawdown in WT#3 was detected 6.34 days (9,130 minutes) after pumping started (Figure 23). Peak drawdown by March 26, 1997, was about 14 to 16 cm. Drawdown in WT#3 was more oscillatory than in the other observation wells after 166.67 days (240,000 minutes) of pumping. This behavior was possibly because (1) WT#3 was much farther from the pumping well than the other observation wells and affected by environmental stresses that did not extend to the other wells and (2) pumping-related water-level changes in WT#3 were much smaller than in the other observation wells and, therefore, harder to separate from barometric and Earth-tide effects.

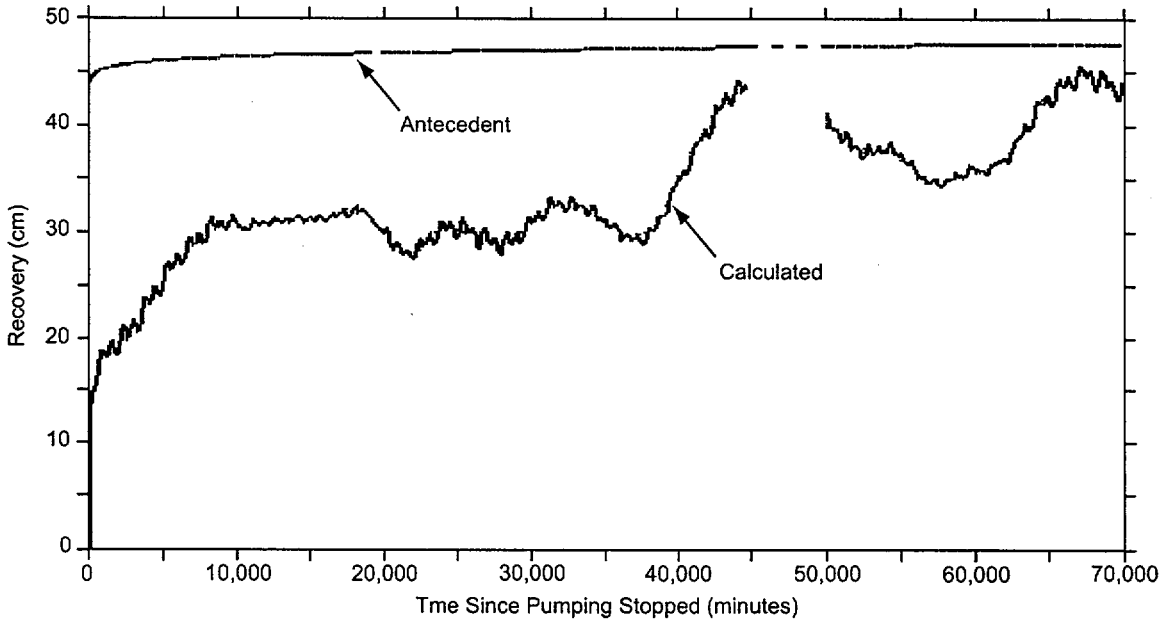

NOTE: Pump was turned off 11/12/97 at 15:59:50 PST.

Figure 21. UE-25 c#1 Lower Bullfrog Recovery, November 12, 1997 (~0 minutes), to December 31, 1997 (~70,000 minutes)

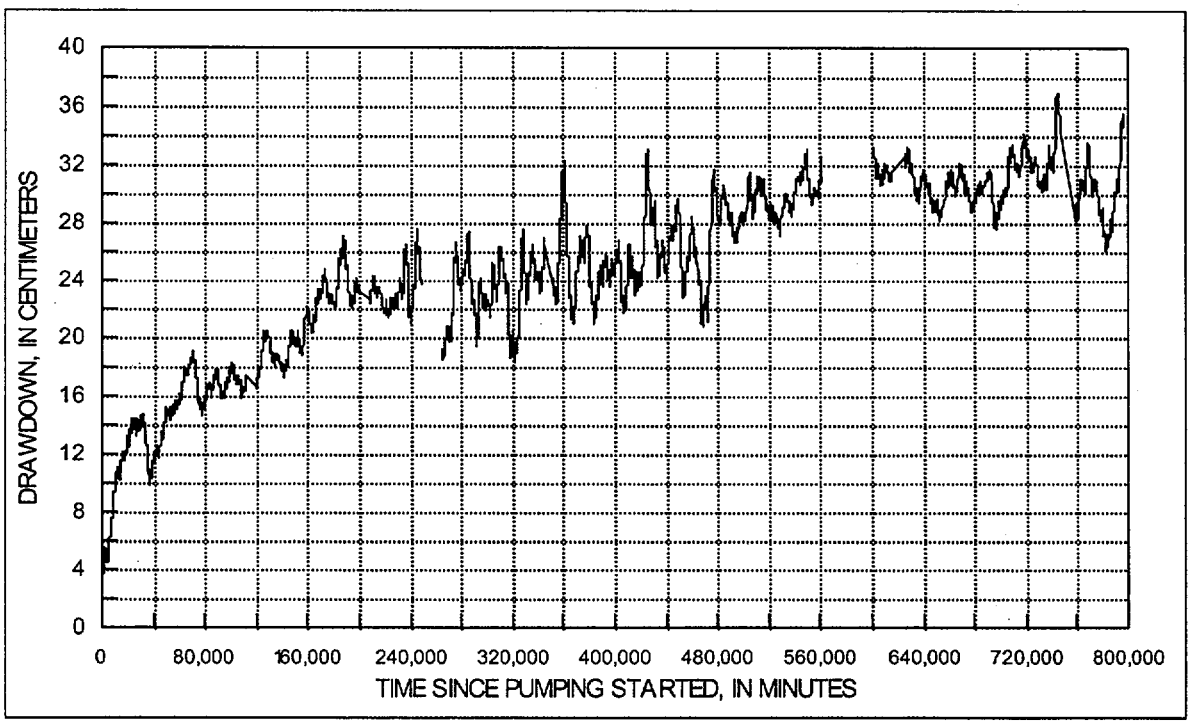

Figure 22. Drawdown in UE-25 ONC-1, May 8, 1996 (~0 minutes), to November 12, 1997 (~800,000 minutes)

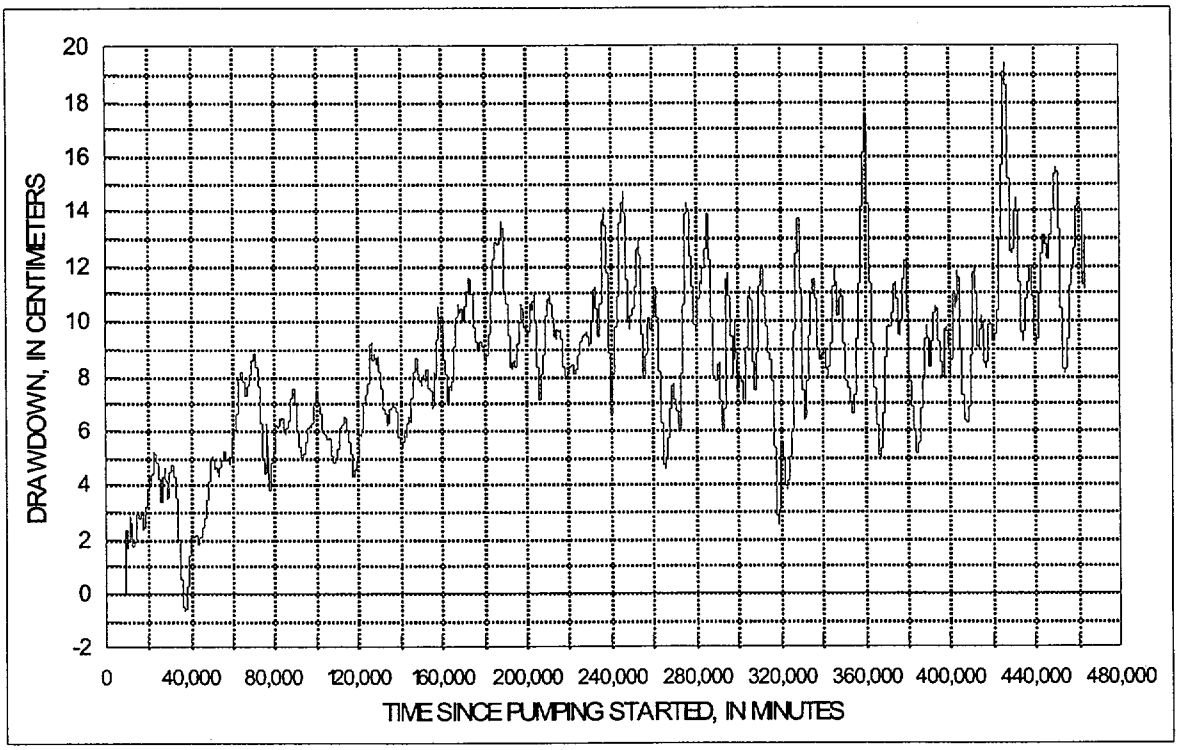

Figure 23. Drawdown in UE-25 WT#3, May 8, 1996 (~0 minutes), to March 26, 1997 (~480,000 minutes)

Unlike other observation wells monitored during the hydraulic test that began in May 1996, H-4 and WT#14 exhibited steady-state drawdown as pumping progressed (Figure 24). Drawdown in both boreholes was delayed for about 5,000 minutes after pumping started, although very small, oscillatory water-level changes, possibly caused by borehole-storage release, occurred during this time. Between 5,000 and 72,000 minutes after pumping started, drawdown increased steadily in response to pumping. Drawdown in H-4 peaked at about 22 cm; drawdown in WT#14 peaked at about 15 cm. After about 50 days (72,000 minutes) of pumping, fluxes from recharge boundaries prevented further drawdown. As in a hydraulic test of the Tram interval in C#1 conducted in 1984 (Geldon 1996), recharge boundaries affecting H-4 and WT#14 are inferred to be faults present near the observation wells. Numerous faults are located near H-4 (Day et al. 1998), and several segments of the Paintbrush Canyon Fault are located near WT#14 (Dickerson and Drake 1998). Conversely, there are no known changes in stratigraphy or lithology between the C-wells and either H-4 or WT#14 that might be interpreted to create an hydraulic boundary.

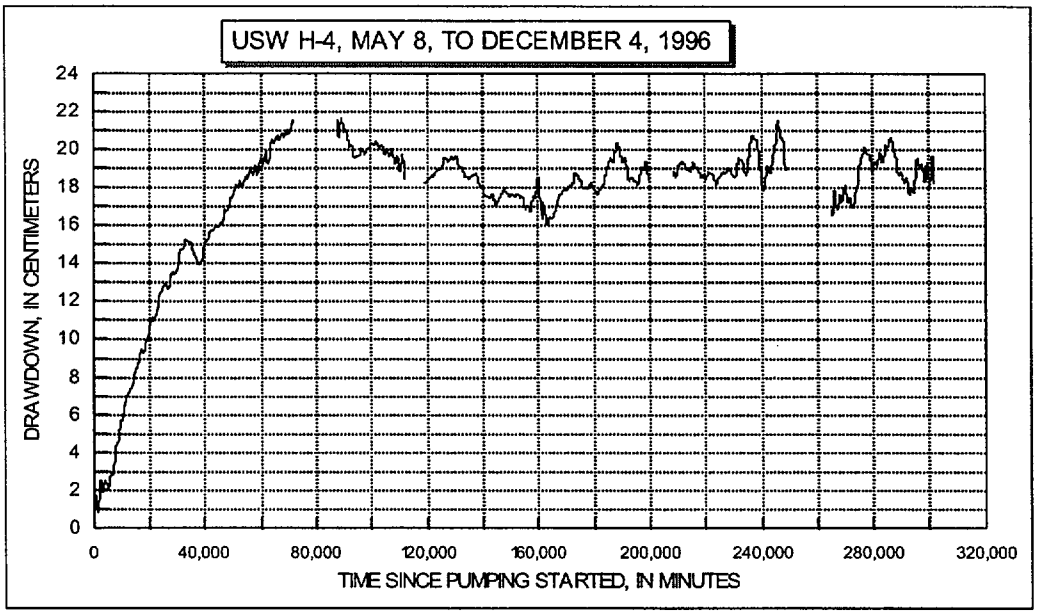

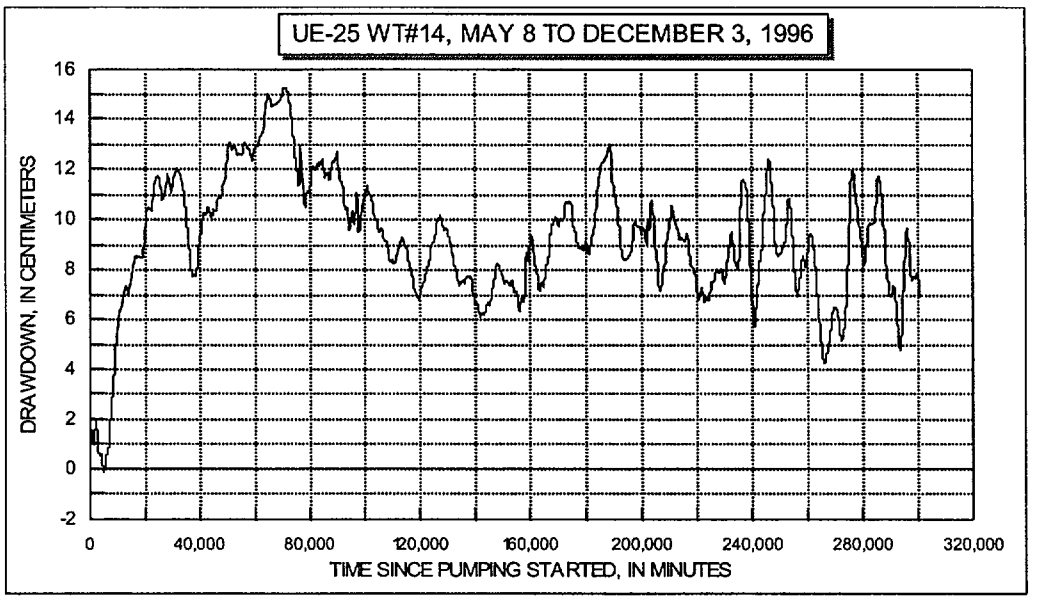

Figure 24. Drawdown in USW H-4 and UE-25 WT#14, May 8, 1996 (~0 minutes), to December 4, 1996 (~300,000 minutes)

2.3.2 Hydraulic Tests Conducted in 1998 and 1999 (Prow Pass Interval)

Pumping in C#2 to create a forced hydraulic gradient for tracer tests in the Prow Pass interval at the C-wells complex began June 2, 1998, and continued uninterrupted until September 22, 1998. The pump in C#2 shut off for 70 minutes on September 22 as one of two packers at the bottom of the Prow Pass interval (number 3) was being deflated. Injection of water into C#3 to expedite tracer transport began June 11 and continued without interruption until September 2. The injection pump was off briefly on September 2 and 3 while injection tubing was removed from C#3. Tracers were injected into C#3 on June 17 and into C#1 on July 31.

Responses of C#1, C#3, and ONC#1 to pumping June 2 to June 11, in advance of the tracer tests, were analyzed as a constant-rate withdrawal test. After water injection into C#3 began on June 11, the superimposed effects of pumping water from C#2, injecting water into C#3, injecting tracers into C#3 and C#1, operating a mixing pump in C#3 intermittently, and mechanical problems that affected pumping and injection rates made it difficult to analyze data from the C-wells quantitatively. However, ONC#1 was far enough away from the pumping and injection wells that a water-level rise in ONC#1 resulting from injecting water into C#3 clearly could be separated from relatively minor drawdown in the well caused by pumping C#2. The water-level rise in ONC#1 from June 11 to September 1 was analyzed as a constant-rate injection test.

2.3.2.1 Performance Tests

Hydraulic and tracer tests in the Prow Pass interval were preceded by pump-performance, step-drawdown, and 1-day hydraulic tests conducted in C#2 and C#3 from April 21 to May 29, 1998. These tests were designed primarily to determine whether C#2 could be used as a pumping well for tracer tests and what the optimum pumping rate should be. These tests also were analyzed to determine values of hydraulic properties that would be expected from a longer hydraulic test that was planned to precede tracer tests in the Prow Pass interval. Fluctuations in water and atmospheric pressures between performance tests indicated barometric efficiency values (Table 7) for the C-wells and ONC#1 that were used to analyze hydraulic tests in the Prow Pass interval.

Table 7. Barometric Efficiency in the C-wells and UE-25 ONC#1

Interval	UE-25 c#1	UE-25 c#2	UE-25 c#3	UE-25 ONC#1
Calico Hills	N/A	0.93	0.94	N/A
Prow Pass	0.96	0.93	1.0	0.99
Upper Bullfrog	0.99	0.93	≅1.0	N/A
Lower Bullfrog	0.97	N/A	N/A	N/A

NOTE: N/A: not applicable.

2.3.2.2 Analytical Methods

Analytical solutions were used to analyze data from hydraulic tests in the Prow Pass interval. Most of the data were analyzed using the method of Streltsova-Adams (1978) for a fissure-block aquifer. The method of Cooper and Jacob (1946) for an infinite, homogeneous, isotropic, confined aquifer was used to analyze drawdown in observation wells as a function of distance from the pumping well. Analysis of data in this study was restricted to observation wells because most water-level changes in pumping wells at the C-wells complex are too large and rapid to be explained solely by hydraulic properties of the pumped interval (Geldon 1996).

2.3.2.3 Constant-Rate Withdrawal Test

A constant-rate withdrawal (CRW) test in the Prow Pass interval started June 2, 1998. The pumping well for this test was C#2, and the observation wells for the test were C#1, C#3, and ONC#1.

Prior to starting the test, the packer in C#2 between the Prow Pass and Calico Hills intervals was deflated, and the two intervals, together, were pumped for 37 minutes at a rate of 0.57 L/s to fill tubing in the pumping well to the level of the flowmeter. After pumping stopped, the packer in C#2 between the Prow Pass and Calico Hills intervals was reinflated. With slight residual effects from the pre-test pumping (which were removed to analyze the test), pumping for the CRW test in the Prow Pass began at 16:00 hours on June 2. Discharge averaged 0.33 L/s between June 2 and 11, a period of 12,500 minutes. Pumping water into C#1 on June 5 to attempt a tracer test, injecting argon gas into C#1 on June 9 to blow sediment out of the tracer injection valve, and testing the downhole mixing pump in C#3 on June 10 briefly disturbed discharge from C#2 as well as pressures in C#1 and C#3. The CRW test was terminated on June 11, 1998, at 08:19 when operations began for a tracer test between C#3 and C#2.

The pumping in C#2 caused 135 m of drawdown in the Prow Pass interval of C#2 three minutes after pumping started. However, the water level rebounded 22 m in the next nine minutes. Subsequently, drawdown increased steadily but slowly and was about 128 m after 12,500 minutes of pumping. On the basis of values of transmissivity and storativity determined in this and previous tests in which the drawdown in the Prow Pass in observation wells was analyzed, only 1.04 percent of the 128-m drawdown in the Prow Pass of the pumped well C#2, namely 1.34 m, is estimated to have resulted from stressing the aquifer. The remainder of the drawdown is attributed to head losses.

The pumping in C#2 caused oscillatory drawdown in the Prow Pass interval of the observation wells. After 12,500 minutes of pumping, this drawdown was 54 cm in C#3 (Figure 25), 12 cm in C#1 (Figure 26), and 0.9 cm in ONC#1. Plotted on log-log scales, drawdown in the Prow Pass interval of C#1 and C#3 indicated delayed yield that is characteristic of a fissure-block aquifer (Streltsova-Adams 1978).

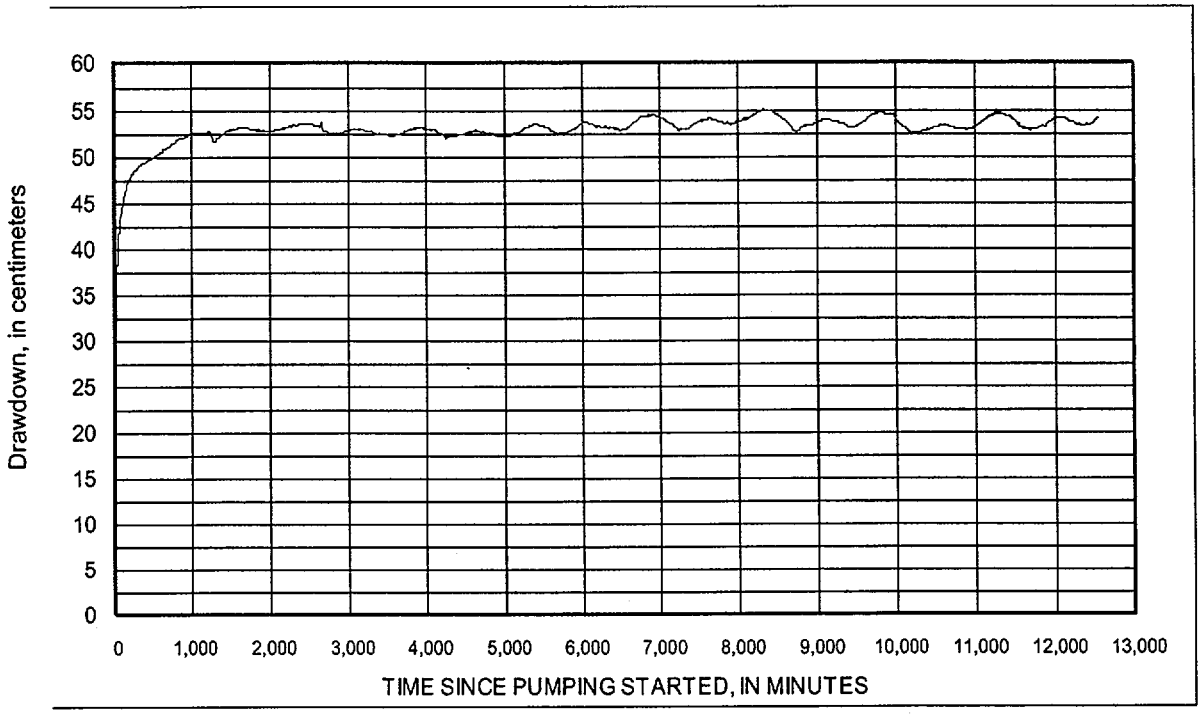

Figure 25. UE-25 c#3 Prow Pass Drawdown, June 2, 1998 (~0 minutes), to June 11, 1998 (~12,800 minutes)

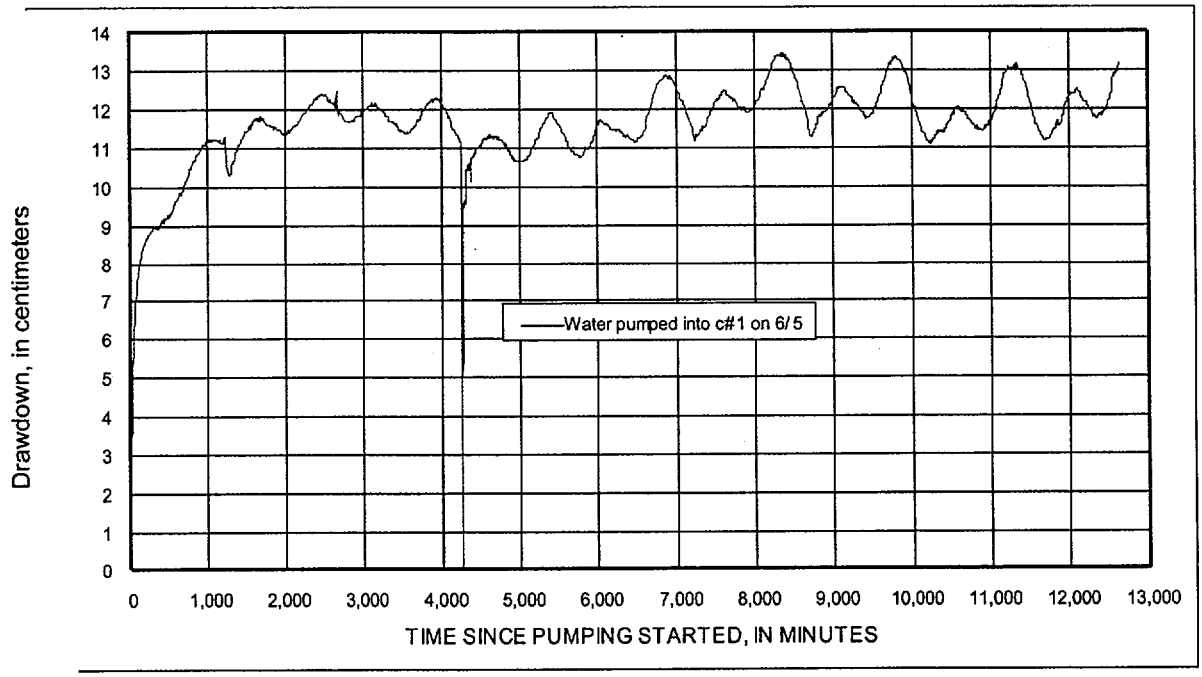

Figure 26. UE-25 c#1 Prow Pass Drawdown, June 2, 1998 (~0 minutes), to June 11, 1998 (~12,800 minutes)

The pumping in C#2 indicated that the Calico Hills and Prow Pass intervals are connected by fractures beyond borehole walls because the Calico Hills responded to pumping in the Prow Pass wherever it was monitored. During the CRW test, the water level in the Calico Hills interval was drawn down as much as 19 cm in C#2 and 12 cm in C#3. In contrast, no drawdown was observed below the Prow Pass interval in C#2 and C#3 and below the Upper Bullfrog interval in C#1 during this test. The Upper Bullfrog drawdown in C#1 was 55 cm. The general lack of a response to pumping below the Prow Pass probably indicates that the highly permeable Lower Bullfrog and Upper Tram intervals in the C-wells were isolated from the Prow Pass interval during the CRW test.

The responses of the Calico Hills in the C-wells and the Upper Bullfrog in C#1 during pumping of the Prow Pass interval in C#2 made it necessary to apportion flow among the responding intervals to determine hydraulic properties. Lacking a flow survey for the test conditions, interval flow was determined by solving analytical equations simultaneously for interval discharge and transmissivity. To make the number of equations equal to the number of unknowns, it was assumed that (1) transmissivity values for the Calico Hills and Prow Pass intervals in the C-wells are constant, (2) the transmissivity of the Calico Hills is 5.6 m^2/d (on the basis of previous hydraulic tests), and (3) flow laterally and vertically within the Calico Hills interval was the same in each of the C-wells during the test. These assumptions were based on analyses and interpretations of previous hydraulic tests, borehole flow surveys, borehole geophysical logs, and other information, which are discussed in reports by Geldon (1996) and Geldon et al. (1997a).

Calculations indicated that the Prow Pass interval contributed 94 percent of the total flow in C#2 and C#3 but only 24 percent of the flow in C#1. The substantially different flow from the Prow Pass in C#1 does not seem reasonable because lithologic changes that might account for variable flow do not occur in the Prow Pass interval at the C-wells complex. It is more likely that flow from the Calico Hills interval or the transmissivity of either or both the Prow Pass and Calico Hills intervals is not constant throughout the C-wells complex. Unquantifiable uncertainty results from failure to apportion flow satisfactorily.

Hydraulic properties of the Prow Pass interval determined from analyses of drawdown during the CRW test are summarized in Table 8.

2.3.2.4 Constant-Rate Injection Test

From June 11 to September 1, 1998, a period of 118,159 minutes, 676,973 L of water was pumped into C#3 to conduct tracer tests. The injection rate ranged from 0.032 to 0.16 L/s before tracers were injected into C#3 on June 17, but it subsequently was stabilized by periodic valve adjustments. From June 11 to September 1, the injection rate averaged 0.095 L/s.

As water was being injected into C#3 from June 11 to September 1, 2,311,290 L of water were withdrawn from C#2 at an average rate of 0.33 L/s. Injecting water into C#3 caused the discharge from C#2 to oscillate wildly within a range of 0.05 L/s. The discharge from C#2 ranged from 0.30 to 0.35 L/s after water injection into C#3 started. Lowering the frequency of the pump in C#2 and increasing backpressure on it between August 3 and 31 decreased the discharge from C#2 to a range of 0.28 to 0.33 L/s after August 31.

Table 8. Hydraulic Properties of the Prow Pass Interval in the C-wells

Borehole	UE-25 c#1	UE-25 c#3
Test dates	June 2–11, 1998	June 2–11,1998
Period of record (min)	12,500	12,500
Analyzed data	Drawdown	Drawdown
Transmissivity (m^2/d)	30	30
Hydraulic conductivity, fractures (m/d)	1	0.8
Hydraulic conductivity, matrix (m/d)	0.000003	0.0002
Hydraulic conductivity (m/d)	No Data	No Data
Storativity, fractures	0.00004	0.00004
Storativity, matrix	0.0003	0.0004
Storativity	0.0004	0.0004

Water levels in the Prow Pass interval of C#2 oscillated as much as 10 m between readings due to injection of water into C#3. Although the water injection into C#3 caused drawdown in the Prow Pass interval of C#2 to decrease from 128 to 115 m in the first 11 days after it began, pumping in C#2 eventually predominated over the superimposed effects of the water injection. From June 22 to September 1, the range in C#2 drawdown increased from 115–125 m to 130–143 m (Figure 27).

Drawdown in the Prow Pass interval of C#3 decreased from +0.58 m to a range typically between -25 and -30 m between June 11 and September 1 (the period of continuous injection of water into C#3 [Figure 28]). This pronounced water-level rise was affected slightly by periodically adjusting the injection rate. Drawdown fluctuated markedly from +87 to -32 m while tracers were injected into C#3 on June 17 and 18.

Drawdown in the Prow Pass interval of C#1 was disturbed significantly by tracer-test operations in C#3 and C#1 from June 11 to September 1. Injection of water into C#3 decreased drawdown in C#1 from 13 to 2.8 cm between June 11 and July 27, but drawdown subsequently increased and ranged from 4.0 to 7.9 cm by September 1 (Figure 29). Injection of tracers into C#3 on June 17 increased drawdown from 8.9 cm to as much as 13 cm, whereas tracer injection in C#1 on July 31 decreased drawdown from +5.9 to -174 cm and then increased it to +10 cm. Removal of injection tubing from C#1 on June 26 to replace a cracking valve increased drawdown from 10 to 217 cm and then decreased it to -16 cm. Reinstallation of the tubing on July 13 increased drawdown from 5.5 to 10 cm and then decreased it to -1,150 cm.

Drawdown in ONC#1 decreased irregularly from +1.1 to -2.3 cm between June 11 and September 1 (Figure 30). Sharply increased drawdown about 9,000 minutes after injection of water into C#3 began may be related to tracer injection into C#3 on June 17, although the timing of this spike does not correlate precisely with the timing of tracer injection in C#3.

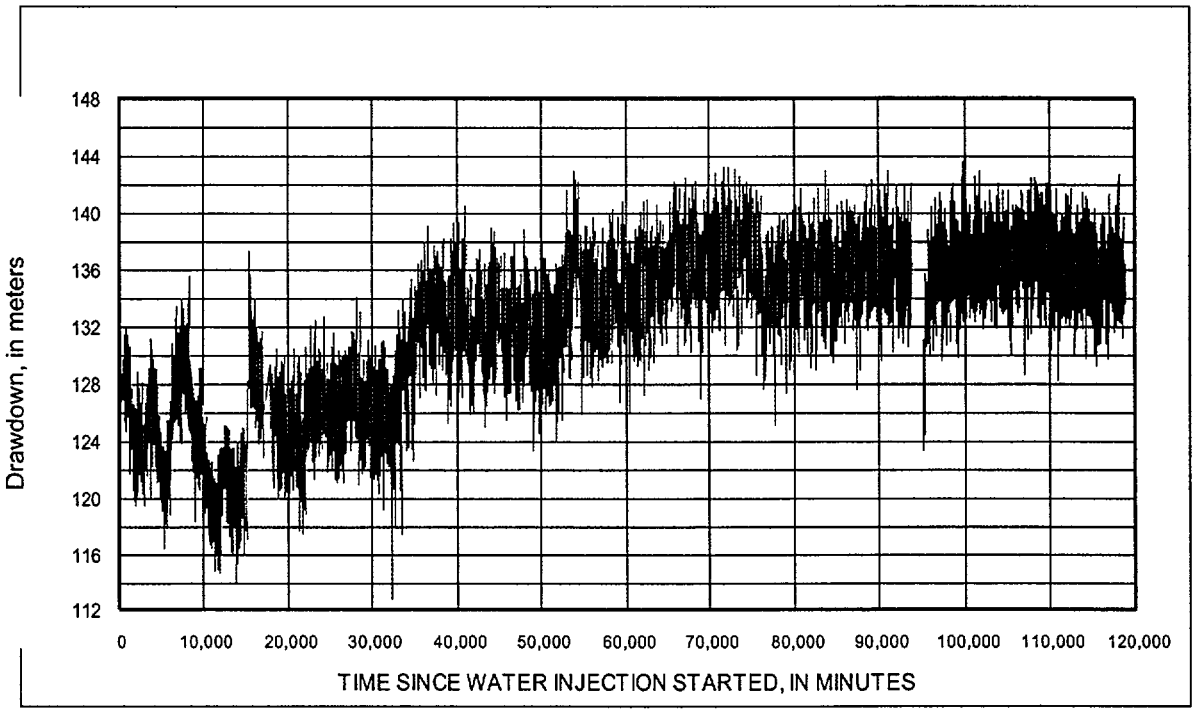

Figure 27. UE-25 c#2 Prow Pass Drawdown, June 11, 1998 (~0 minutes) to September 1, 1998 (~120,000 minutes)

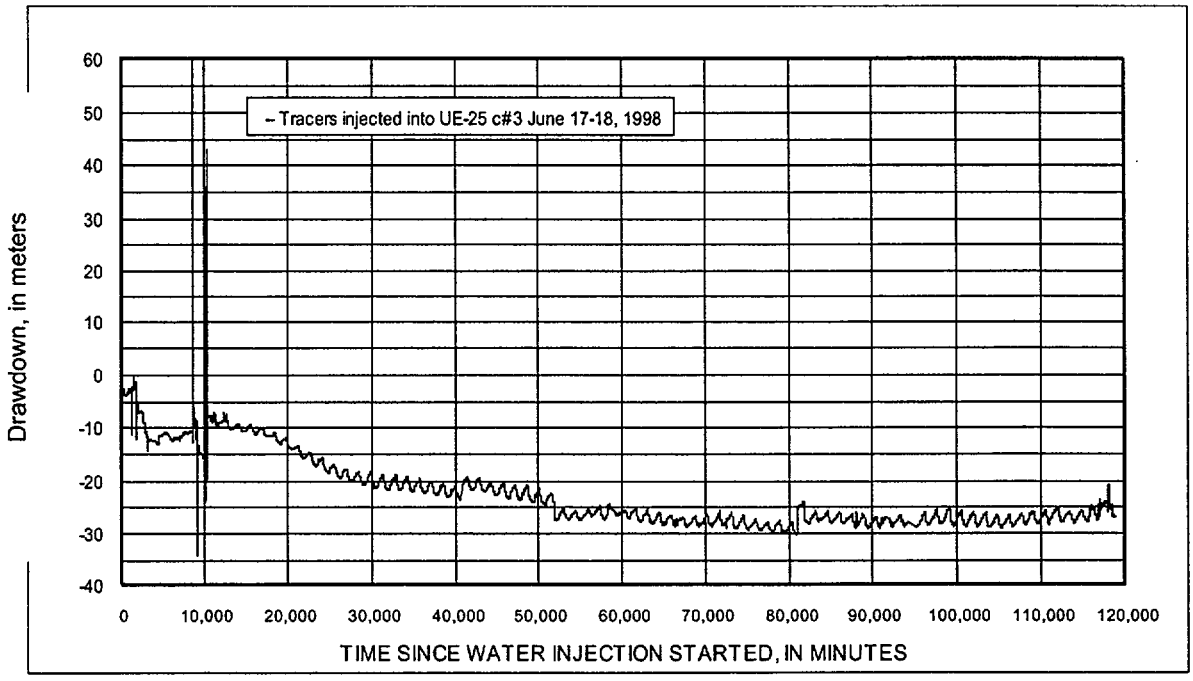

Figure 28. UE-25 c#3 Prow Pass Drawdown, June 11, 1998 (~0 minutes), to September 1, 1998 (~120,000 minutes)

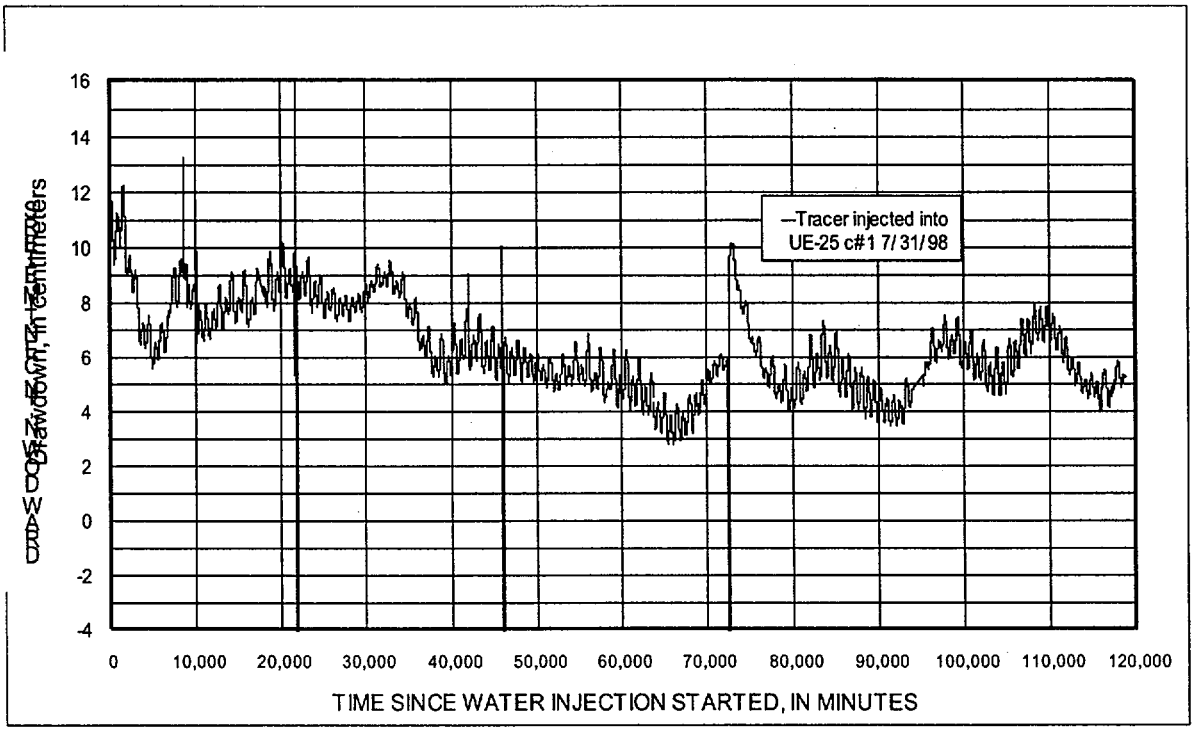

Figure 29. UE-25 c#1 Prow Pass Drawdown, June 11, 1998 (~0 minutes), to September 1, 1998 (~120,000 minutes)

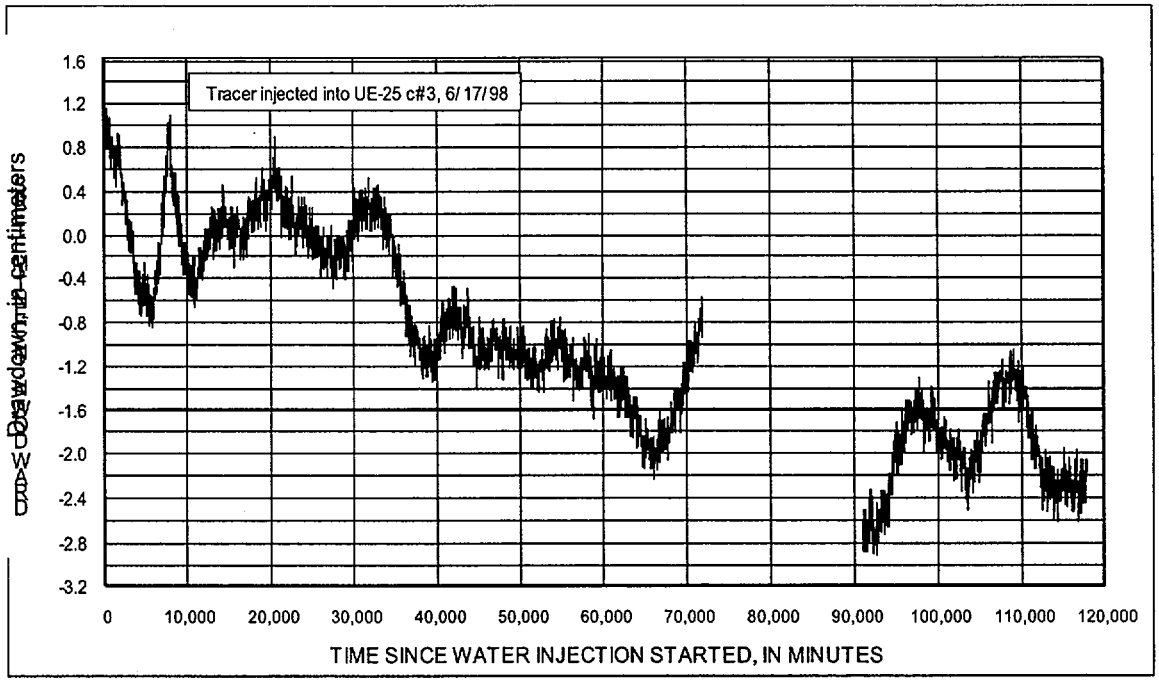

Figure 30. UE-25 ONC#1 Prow Pass Drawdown, June 11, 1998 (~0 minutes), to September 1, 1998 (~120,000 minutes)

Water-level rises in the C-wells from June 11 to September 1, 1998, were very irregular and too disturbed by tracer-test operations to be analyzed quantitatively. However, the water-level rise in ONC#1 during this period (with superimposed drawdown from pumping C#2 removed) could be matched to the type curves of Streltsova-Adams (1978) for a fissure-block aquifer. This analysis indicated a transmissivity of 30 m^2/d, a fracture hydraulic conductivity of 2 m/d, insignificant matrix hydraulic conductivity, and a storativity of 0.002 (90 percent of which is in the matrix). The Prow Pass interval in ONC#1 and the C-wells have equally low permeability, but storativity is an order of magnitude larger between ONC#1 and the C-wells than at the C-wells complex.

2.4 HYDRAULIC PROPERTIES

Hydraulic tests conducted at the C-wells complex from 1995 to 1997 revealed much about the ability of hydrogeologic intervals in the C-wells and the Miocene tuffaceous rocks in the vicinity to store and transmit water. However, it must be emphasized that hydraulic properties computed from these tests pertain only to the structural setting in which the tests were conducted. The Lower Bullfrog interval is the most permeable interval in the C-wells because it is located in these boreholes where two intersecting faults have caused intense fracturing. The Calico Hills interval is the least permeable interval in the C-wells because it is the farthest interval vertically from faults that intersect these boreholes. In a different structural setting, the Lower Bullfrog, Calico Hills, and other intervals of the Miocene tuffaceous rocks would be expected to have different hydraulic properties than indicated at the C-wells complex. For example, the Bullfrog Tuff yielded very little of the water produced from the Miocene tuffaceous rocks during a tracejector flow survey of p#1 (Craig and Robison 1984), and the Calico Hills Formation yielded 32 percent of the water produced from the Miocene tuffaceous rocks during a tracejector flow survey of b#1 (Lahoud et al. 1984).

Hydraulic properties for the various hydrogeologic intervals at the C-wells are discussed in the following subsections. With the exception of the Prow Pass interval, all of the hydraulic properties were derived from testing conducted prior to 1998. Properties of the Prow Pass interval were derived from testing conducted both prior to and during 1998. The 1998 testing involved pumping of only the Prow Pass interval.

2.4.1 Calico Hills Interval

The Calico Hills interval responded in most hydraulic tests, including one conducted from May to June 1984 (Geldon 1996), as an unconfined aquifer. In four tests conducted from 1984 to 1997, the Calico Hills interval consistently was determined to be the least permeable interval in the C-wells (Table 9). The hydraulic test in May and June 1984 indicated that the Calico Hills interval in C#1 has a transmissivity of 9 m^2/d, a horizontal hydraulic conductivity of 0.2 m/d, a vertical hydraulic conductivity of 0.3 m/d, and a specific yield of 0.003 (Geldon 1996). The hydraulic test in June 1995 indicated that the Calico Hills interval in C#2 has a transmissivity of 6 m^2/d, a horizontal hydraulic conductivity of 0.1 m/d, and a storativity of 0.0002. Hydraulic

Table 9. Results of Hydraulic Tests in Borehole UE-25 c#3, June 1995 to November 1997

Starting Date	06/12/95	02/08/96	02/08/96 UE-25 c#1	05/08/96	05/08/96	06/12/95	02/08/96 UE-25 c#2	05/08/96	05/08/96
Calico Hills									
Analyzed data	None	None	N/A	None	N/A	Drawdown	Drawdown	Drawdown	N/A
Period of record (min)	N/A	N/A	N/A	N/A	N/A	5,800	7,000	464,100	N/A
Aquifer type	Unconfined	Unconfined	N/A	Unconfined	N/A	Unconfined	Confined	Unconfined	N/A
Transmissive thickness (m)	60.4	60.4	N/A	60.4	N/A	45.4	45.4	45.4	N/A
Distance from pumping well (m)	78.3	78.3	N/A	78.3	N/A	29.0	29.0	29.0	N/A
Average discharge (L/s)	0.85	0.042	N/A	0.10	N/A	0.85	0.042	0.10	N/A
Transmissivity (m^2/day)	9(est)	9(est)	N/A	9(est)	N/A	6	10	4	N/A
Horizontal hydraulic conductivity (m/day)	0.2(est)	0.2(est)	N/A	0.2(est)	N/A	0.1	0.2	0.08	N/A
Vertical hydraulic conductivity (m/day)	0.3(est)	0.3(est)	N/A	0.3(est)	N/A	ND	ND	0.01	N/A
Storativity (dimensionless)	ND	ND	N/A	ND	N/A	0.0002	0.0006	0.0003	N/A
Specific yield (dimensionless)	0.003(est)	0.003(est)	N/A	0.003(est)	N/A	ND	ND	0.4	N/A
Prow Pass									
Analyzed data	Drawdown	Drawdown	Drawdown	Drawdown	N/A	Drawdown	Drawdown	Drawdown	N/A
Period of record (min)	5,800	7,000	7,000	464,100	N/A	5,800	7,000	464,100	N/A
Aquifer type	Confined	Unconfined	Confined	Confined	N/A	Confined	Confined	Confined	N/A
Transmissive thickness (m)	18.9	18.9	18.9	18.9	N/A	23.8	23.8	23.8	N/A
Distance from pumping well (m)	81.1	81.1	81.1	81.1	N/A	28.6	28.6	28.6	N/A
Average discharge (L/s)	0.65	0.21	0.21	0.22	N/A	0.65	0.13	0.19	N/A
Transmissivity (m^2/day)	60	50	60	50	N/A	40	30	30	N/A
Horizontal hydraulic conductivity (m/day)	3	3	3	3	N/A	2	1	1	N/A
Vertical hydraulic conductivity (m/day)	ND	0.0001	ND	ND	N/A	ND	ND	ND	N/A
Storativity (dimensionless)	0.0003	0.0003	0.0004	0.0002	N/A	0.0004	0.003	0.0008	N/A
Specific yield (dimensionless)	ND	ND	ND	ND	N/A	ND	ND	ND	N/A

NOTE: *First number is for fractures; second is for matrix. ND: no data; N/A: not applicable; est: estimated to be the same as values obtained from an hydraulic test in May 1984.

Table 9 (continued). Results of Hydraulic Tests in Borehole UE-25 c#3, June 1995 to November 1997

Starting Date	06/12/95	02/08/96	02/08/96 UE-25 c#1	05/08/96	05/08/96	06/12/95	02/08/96 UE-25 c#2	05/08/96	05/08/96
Upper Bullfrog									
Analyzed data	Recovery	Drawdown	N/A	Drawdown	N/A	Drawdown	Drawdown	Drawdown	N/A
Period of record (min)	5,700	7,000	N/A	464,100	N/A	5,800	7,000	464,100	N/A
Aquifer type	Confined	Unconfined	N/A	Fissure-block	N/A	Confined	Confined	Confined	N/A
Transmissive thickness (m)	46.0	46.0	N/A	46.0	N/A	24.1	24.1	24.1	N/A
Distance from pumping well (m)	83.2	83.2	N/A	82.3	N/A	28.6	28.6	28.6	N/A
Average discharge (L/s)	0.88	0.37	N/A	0.32	N/A	0.88	0.36	0.36	N/A
Transmissivity (m^2/day)	90	40	N/A	50	N/A	100	100	80	N/A
Horizontal hydraulic conductivity (m/day)	2	0.8	N/A	1/0.00002*	N/A	4	4	3	N/A
Vertical hydraulic conductivity (m/day)	ND	0.5	N/A	ND	N/A	ND	ND	ND	N/A
Storativity (dimensionless)	0.00006	0.0009	N/A	0.0001/0.0009*	N/A	0.00003	0.00002	0.00002	N/A
Specific yield (dimensionless)	ND	0.002	N/A	ND	N/A	ND	ND	ND	N/A
Bullfrog-Tram									
Analyzed data	N/A	Drawdown	N/A	N/A	N/A	N/A	Drawdown	N/A	N/A
Period of record (min)	N/A	7,000	N/A	N/A	N/A	N/A	7,000	N/A	N/A
Aquifer type	N/A	Confined	N/A	N/A	N/A	N/A	Confined	N/A	N/A
Transmissive thickness (m)	N/A	112	N/A	N/A	N/A	N/A	51.2	N/A	N/A
Distance from pumping well (m)	N/A	86.3	N/A	N/A	N/A	N/A	29	N/A	N/A
Average discharge (L/s)	N/A	7.84	N/A	N/A	N/A	N/A	7.93	N/A	N/A
Transmissivity (m^2/day)	N/A	2,500	N/A	N/A	N/A	N/A	2,500	N/A	N/A
Horizontal hydraulic conductivity (m/day)	N/A	20	N/A	N/A	N/A	N/A	50	N/A	N/A
Vertical hydraulic conductivity (m/day)	N/A	ND	N/A	N/A	N/A	N/A	ND	N/A	N/A
Storativity (dimensionless)	N/A	0.0003	N/A	N/A	N/A	N/A	0.002	N/A	N/A
Specific yield (dimensionless)	N/A	ND	N/A	N/A	N/A	N/A	ND	N/A	N/A

NOTE: *First number is for fractures; second is for matrix. ND: no data; N/A: not applicable; est: estimated to be the same as values obtained from a hydraulic test in May 1984.

Table 9 (continued). Results of Hydraulic Tests in Borehole UE-25 c#3, June 1995 to November 1997

Starting date	06/12/95	02/08/96	02/08/96 UE-25 c#1	05/08/96	05/08/96	06/12/95	02/08/96 UE-25 c#2	05/08/96	05/08/96
Lower Bullfrog									
Analyzed data	Recovery	None	N/A	Drawdown	Drawdown	Drawdown	None	Drawdown	Drawdown
Period of record (min)	6,300	N/A	N/A	464,100	464,100	5,800	N/A	464,100	464,100
Aquifer type	Confined	Confined	N/A	Confined	Fissure-block	Confined	Confined	Confined	Fissure-block
Transmissive thickness (m)	62.8	62.8	N/A	62.8	62.8	29.9	29.9	29.9	29.9
Distance from pumping well (m)	85.6	85.6	N/A	85.6	85.6	29.3	29.3	29.3	29.3
Average discharge (L/s)	15.3	ND	N/A	6.37	6.37	15.3	ND	6.69	6.69
Transmissivity (m^2/day)	1,800	ND	N/A	1,600	1,300	1,900	ND	1,600	1,300
Horizontal hydraulic conductivity (m/day)	30	ND	N/A	30	20/0.0004*	60	ND	50	40/0.001*
Vertical hydraulic conductivity (m/day)	ND	ND	N/A	ND	ND	ND	ND	ND	ND
Storativity (dimensionless)	0.0004	ND	N/A	0.0002	0.0002/0.002*	0.003	ND	0.001	0.002/0.02*
Specific yield (dimensionless)	ND	ND	N/A	ND	ND	ND	ND	ND	ND
Upper Tram									
Analyzed data	None	None	N/A	None	N/A	None	None	None	N/A
Period of record (min)	N/A	N/A	N/A	N/A	N/A	N/A	N/A	N/A	N/A
Aquifer type	Leaky	Leaky	N/A	Leaky	N/A	Leaky	Leaky	Leaky	N/A
Transmissive thickness (m)	49.7	49.7	N/A	49.7	N/A	21.3	21.3	21.3	N/A
Distance from pumping well (m)	86.9	86.9	N/A	86.9	N/A	29.6	29.6	29.6	N/A
Average discharge (L/s)	4.74	ND	N/A	2.52	N/A	4.74	ND	2.18	N/A
Transmissivity (m^2/day)	ND	ND	N/A	800	N/A	ND	ND	900	N/A
Horizontal hydraulic conductivity (m/day)	ND	ND	N/A	20	N/A	ND	ND	40	N/A
Vertical hydraulic conductivity (m/day)	ND	ND	N/A	ND	N/A	ND	ND	ND	N/A
Storativity (dimensionless)	ND	ND	N/A	0.0001	N/A	ND	ND	0.001	N/A
Specific yield (dimensionless)	ND	ND	N/A	ND	N/A	ND	ND	ND	N/A

NOTE: *First number is for fractures; second is for matrix. ND: no data; N/A: not applicable; est: estimated to be the same as values obtained from a hydraulic test in May 1984.

tests conducted in February 1996 and from May 1996 to November 1997 generally supported the previous analyses. A representative plot indicating a match between the data and one of the type curves of Neuman (1975) for an unconfined, anisotropic aquifer is shown in Figure 31.

2.4.2 Prow Pass Interval

The Prow Pass interval generally responded to hydraulic tests conducted from June 1995 to November 1997 as a confined aquifer (Table 9). The hydraulic test in June 1995 indicated that the Prow Pass interval in C#1 had a transmissivity of 60 m^2/d, a hydraulic conductivity of 3 m/d, and a storativity of 0.0003. The same hydraulic test indicated that the Prow Pass interval in C#2 has a transmissivity of 40 m^2/d, a hydraulic conductivity of 2 m/d, and a storativity of 0.0004. Hydraulic tests conducted in February 1996 and from May 1996 to March 1997 generally supported the previous analyses. A representative plot indicates a match between the data and the type curve of Theis (1935) for a confined aquifer (Figure 32).

Hydraulic testing of the Prow Pass interval conducted in 1998 by pumping C#2 indicated a transmissivity of 30 m^2/d in both C#1 and C#3. Fracture hydraulic conductivities derived from responses in C#1 and C#3 were 1 m/d and 0.8 m/d, respectively. Matrix hydraulic conductivities were negligible, and overall storativity was 0.0004, with most of that being attributed to the matrix. These parameter estimates are in good agreement with those derived from earlier testing in which the Prow Pass interval was not pumped directly (above). This result instills confidence in the ability to estimate hydraulic parameters for intervals that are not pumped directly but that respond to pumping other intervals.

2.4.3 Upper Bullfrog Interval

The Upper Bullfrog interval in C#2 responded to all hydraulic tests as a confined aquifer (Table 9). Those tests consistently indicated a transmissivity of 80 to 100 m^2/d, a hydraulic conductivity of 3 to 4 m/d, and a storativity of 0.00002 to 0.00003. A representative plot indicates a match between the data and the type curve of Theis (1935) for a confined aquifer (Figure 33).

The hydraulic test in June 1995 produced results for the Upper Bullfrog interval in C#1 that were consistent with results for that interval in C#2 (Table 9). During longer tests conducted in February 1996 and May 1996, sufficient time elapsed to reveal the effects of fractures on flow between the Upper Bullfrog interval in C#1 and open intervals in the pumping well. Analyses of drawdown (complicated by downward flow through fractures) indicated smaller values of transmissivity and hydraulic conductivity and larger values of storativity than analyses of drawdown in which the effects of fractures were not evident (Table 9). Hydraulic properties determined from hydraulic tests conducted in 1996 and 1997 are less reliable than properties determined from the hydraulic test in June 1995 because of the sliding sleeve placement in the observation and pumping wells in the later tests.

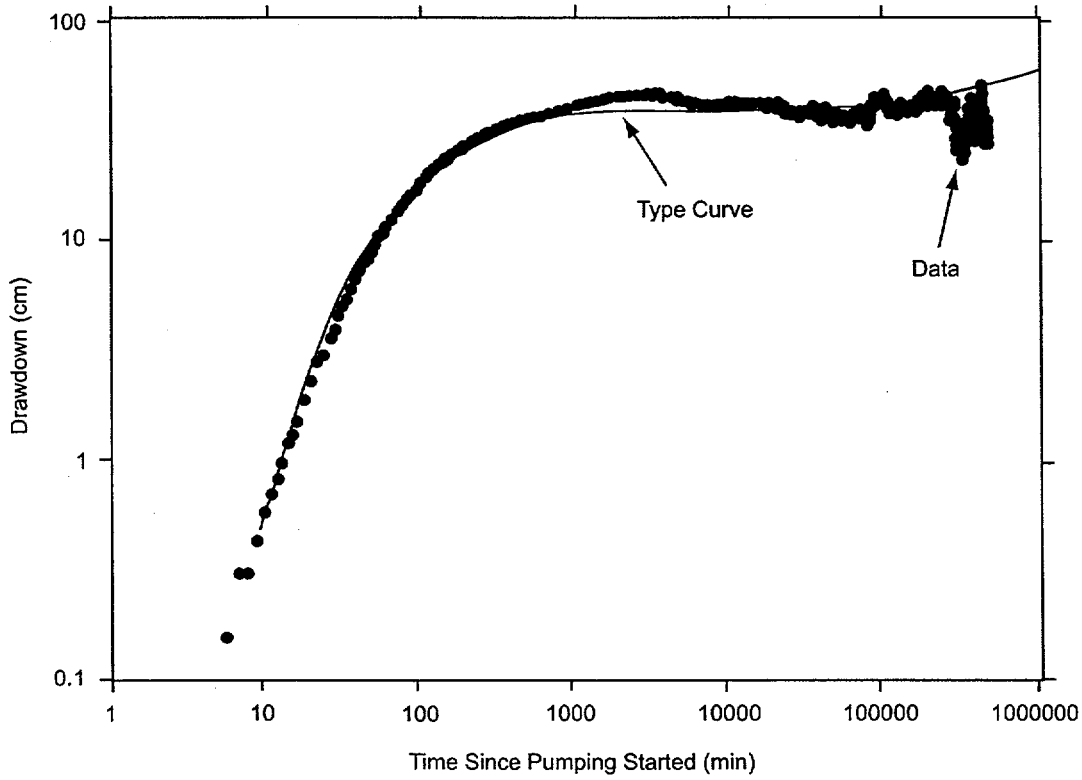

Source: Neuman (1975), analysis method.

Figure 31. Analysis of Drawdown in the Calico Hills Interval of UE-25 c#2, May 8, 1996 (~0 minutes), to March 26, 1997 (~470,000 minutes), by the Method of Neuman

2.4.4 Lower Bullfrog Interval

Undisturbed drawdown in the Lower Bullfrog interval of C#1 and C#2 during the hydraulic test conducted from May 1996 to November 1997 can be interpreted in several ways that were not evident from previous hydraulic tests of much shorter duration. Although previous tests indicated a confined-aquifer response, the test beginning in May 1996 progressed long enough to develop a double-humped drawdown curve characteristic of a fissure-block aquifer. From 158,000 minutes (110 days) after pumping started in May 1996 to the end of the analyzed record (464,100 minutes [312 days] after pumping started), drawdown in C#1 and C#2 was greater than anticipated on the basis of extrapolating the earlier drawdown for long periods (using the equation of Theis (1935), to extrapolate drawdown). The oscillatory pattern of drawdown in the C-wells after 158,000 minutes (110 days) of pumping can be interpreted to indicate that the spreading cone of depression encompassed volumes of the Lower Bullfrog interval that alternately were less transmissive or as transmissive as the Lower Bullfrog in the C-wells.

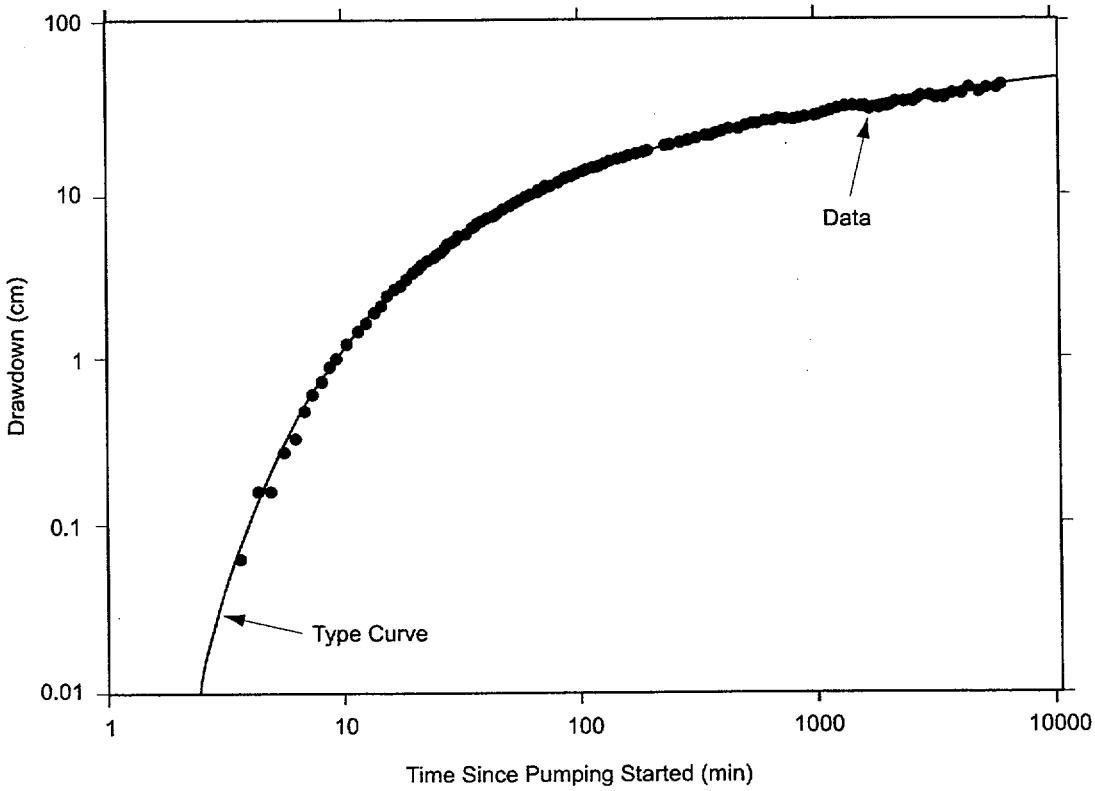

Source: Theis (1935), analysis method.

Figure 32. Analysis of Drawdown in the Prow Pass Interval of UE-25 c#1, June 12–16, 1995, by the Method of Theis

Values of transmissivity computed for the Lower Bullfrog interval are significantly different depending on whether the interval is considered a confined aquifer or a fissure-block aquifer (Table 9). In C#1 and C#2, transmissivity is 1,600 m^2/d if the Lower Bullfrog is analyzed as a confined aquifer (Figure 34), and it is 1,300 m^2/d if the Lower Bullfrog is analyzed as a fissure-block aquifer (Figure 35). Although the two analytical solutions produced equally plausible results, the fissure-block aquifer solution is consistent with a tracer test conducted from February to March 1996 that indicated dual porosity in the Bullfrog-Tram interval (Fahy 1997). Also, the longer pumping required for the fissure-block aquifer response to develop and the lower transmissivity value determined from that response can be interpreted to confirm that less-transmissive rocks were reached as the cone of depression spread to increasingly distant areas during the hydraulic test that began in May 1996.

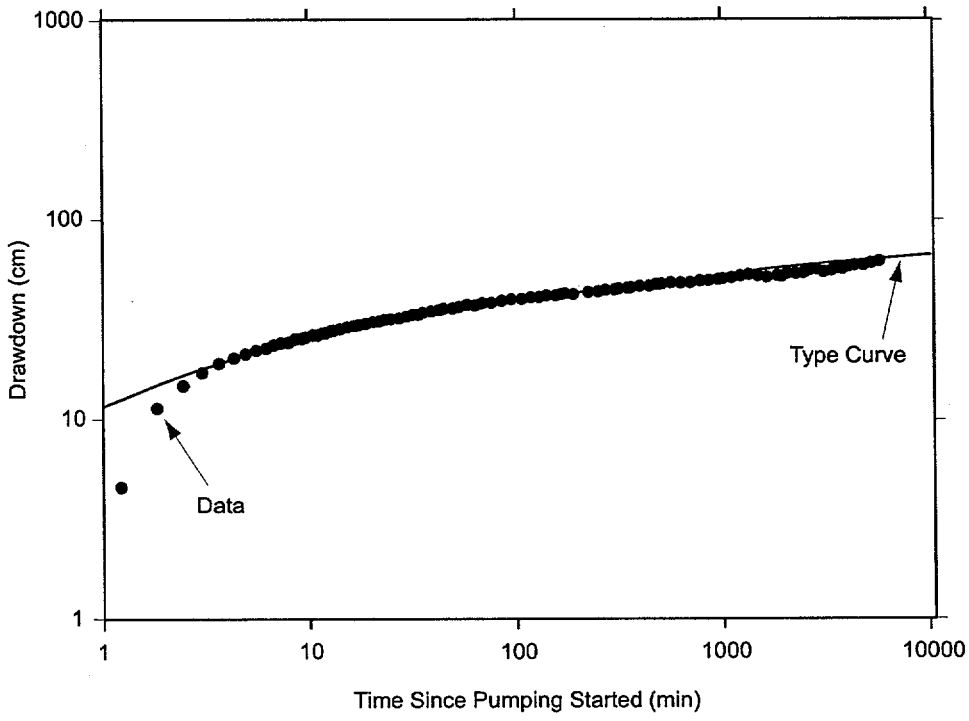

Source: Theis (1935), analysis method.

Figure 33. Analysis of Drawdown in UE-25 c#2 Upper Bullfrog Interval, June 12–16, 1995, by the Method of Theis

Values of hydraulic conductivity and storativity are considerably larger in the rock mass between C#2 and C#3 than in the rock mass between C#1 and C#3. When analyzed as a confined aquifer, the hydraulic conductivity of the Lower Bullfrog interval is 50 m/d in C#2 and 30 m/d in C#1, and its storativity is 0.001 in C#2 and 0.0002 in C#1. (These hydraulic conductivities and storativities of the interval in both boreholes are about the same as those of the fractures in the interval in both boreholes obtained when the Lower Bullfrog is analyzed as a fissure-block aquifer; see Table 9.)

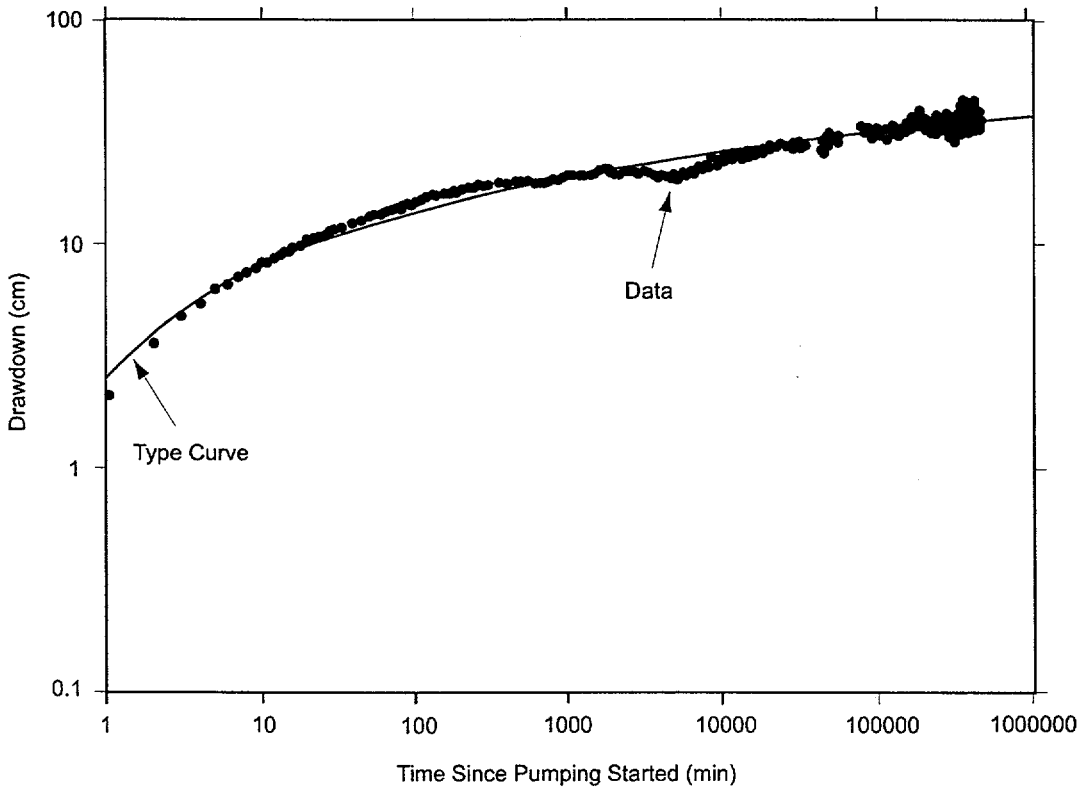

Source: Theis (1935), analysis method.

Figure 34. Analysis of Drawdown in UE-25 c#1 Lower Bullfrog Interval, May 8, 1996, to March 26, 1997, by the Method of Theis

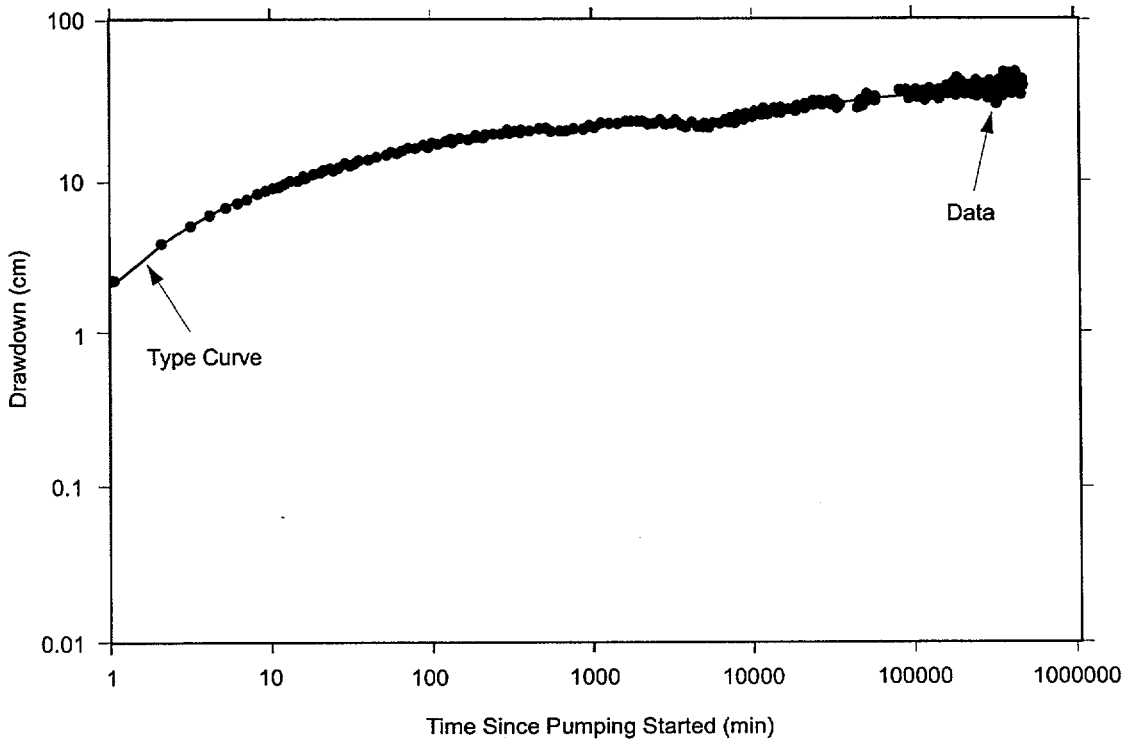

Source: Streltsova-Adams (1978); analysis method.

NOTE: For the analysis curve, the parameter$\tau/B = 0.05$.

Figure 35. Analysis of Drawdown in UE-25 c#1 Lower Bullfrog Interval, May 8, 1996, to March 26, 1997, by Method of Streltsova-Adams

2.4.5 Upper Tram Interval

The Upper Tram interval was known from earlier hydraulic tests (conducted in 1984) to respond to pumping as a leaky aquifer without confining bed storage because of recharge from faults that intersect the C-wells in that interval (Geldon 1996). Although hydraulic properties of the Upper Tram (UT) interval could not be determined directly from hydraulic tests conducted during this study (because of transducer malfunction), they could be estimated by subtracting values of hydraulic properties determined for the Lower Bullfrog (LB) interval from those determined for the Bullfrog-Tram (BT) interval. This is deemed acceptable based on the assumption that flow during the Bullfrog-Tram test and the Lower Bullfrog test was radial in an equivalent porous medium that is homogeneous and isotropic, composed of interconnected fractures. The following equations were used (Geldon 1996):

$$T_{UT} = T_{BT} - T_{LB} \quad \text{(Eq. 2)}$$

$$S_{UT} = S_{BT} - S_{LB} \quad \text{(Eq. 3)}$$

$$K_{UT} = (K_{BT} \times b_{BT} - K_{LB} \times b_{LB})/b_{UT} \quad \text{(Eq. 4)}$$

where

T = transmissivity (L^2/T)
S = storativity (dimensionless)
K = hydraulic conductivity (L/T)
b = thickness (L).

Only hydraulic properties of the Lower Bullfrog interval determined by the Theis (1935) solution were used in these calculations because hydraulic properties of the Bullfrog-Tram interval (which includes the Lower Bullfrog) were determined by this method. These calculations indicated a transmissivity of 800 m^2/d, a hydraulic conductivity of 20 ft/d, and a storativity of 0.0001 for the Upper Tram interval in C#1 and a transmissivity of 900 m^2/d, a hydraulic conductivity of 40 m/d, and a storativity of 0.001 for the Upper Tram interval in C#2 (Table 9).

2.4.6 Miocene Tuffaceous Rocks: Hydraulic Properties and Large-scale Horizontal Anisotropy

Indicative of hydraulic connection through a highly developed fracture network, diverse intervals of the Miocene tuffaceous rocks in six observation wells responded to the pumping in C#3 from May 1995 to November 1997 (Table 10). The C-wells, ONC-1, and H-4 appear to be connected hydraulically through a northwest-trending zone of discontinuous faults that extends from Bow Ridge to Antler Wash (Geldon et al. 1998). The Paintbrush Canyon and related faults that intersect WT#14 and the C-wells probably enhance hydraulic communication between those boreholes. Hydraulic communication between the C-wells and WT#3 probably is enabled both stratigraphically and structurally because those boreholes were open during hydraulic tests in the same geologic unit (the Bullfrog Tuff) and are cut by the same faults (the Paintbrush Canyon and related faults).

Analyses of the drawdown in individual observation wells (Figures 36 to 39) provide hydraulic properties of the rock mass at the scale of the distance between those boreholes and C#3 (Table 10). Analyses of drawdown in multiple observation wells, either as a function of time (normalized by dividing by the square of the distance between the observation and pumping wells) or as a function of distance at a specified time, allow computation of hydraulic properties of the tuffaceous rock mass in which all of the included observation wells are located.

Table 10. Hydraulic Properties Computed from Observation Well Responses to Pumping in UE-25 c#3, May 1995 to November 1997

Borehole	UE-25 c#2	UE-25 c#2	UE-25 c#1	UE-25 c#1
Starting date of hydraulic test	05/22/95	05/08/96	05/22/95	05/08/96
Period of record (min)	14,400	464,100	11,400	464,100
Analyzed data	Drawdown	Drawdown	Recovery	Drawdown
Geologic units in monitored interval	Calico Hills to Tram	Calico Hills to Tram	Calico Hills to Tram	Calico Hills to Tram
Aquifer type	Unconfined	Variable	Unconfined	Variable
Transmissive thickness (m)	165	144	252	238
Distance from pumping well (m)	29.0	29.0	82.6	82.9
Average discharge (L/s)	17.9	9.53	17.9	9.53
Transmissivity (m^2/day)	2,100	2,400–2,600	1,800	2,200–2,600
Horizontal hydraulic conductivity (m/day)	13	16–18	7	9–11
Vertical hydraulic conductivity (m/day)	1.7	Unknown	0.3	Unknown
Storativity (dimensionless)	0.003	0.003–0.004	0.001	0.002
Specific yield (dimensionless)	0.2	Unknown	0.01	Unknown

Borehole	UE-25 ONC-1	USW H-4	UE-25 WT#14	UE-25 WT#3
Starting date of hydraulic test	05/08/96	05/08/96	05/08/96	05/08/96
Period of record (min)	796,663	72,000	72,000	463,500
Analyzed data	Drawdown	Drawdown	Drawdown	Drawdown
Geologic units in monitored interval	Prow Pass	Prow Pass to Lithic Ridge	Topopah Spring and Calico Hills	Bullfrog
Aquifer type	Fissure-block	Confined	Confined	Confined
Transmissive thickness (m)	193 (est)	276	Unknown	47.5 (est)
Distance from pumping well (m)	843	2,245	2,249	3,526
Average discharge (L/s)	9.21	9.72	9.72	9.59
Transmissivity (m^2/day)	1,000	700	1,300	2,600
Horizontal hydraulic conductivity (m/day)	5/.002*	2	Unknown	56
Storativity (dimensionless)	0.001/0.01*	0.002	0.002	0.002

NOTES: est: estimated

*First number is for fractures; second is for matrix (values of transmissivity and hydraulic conductivity listed for UE-25 ONC-1 and USW H-4 differ from those obtained from a hydraulic test conducted from May 22 to June 1, 1995, but the values determined from the longer test beginning in May 1996 are considered more reliable).

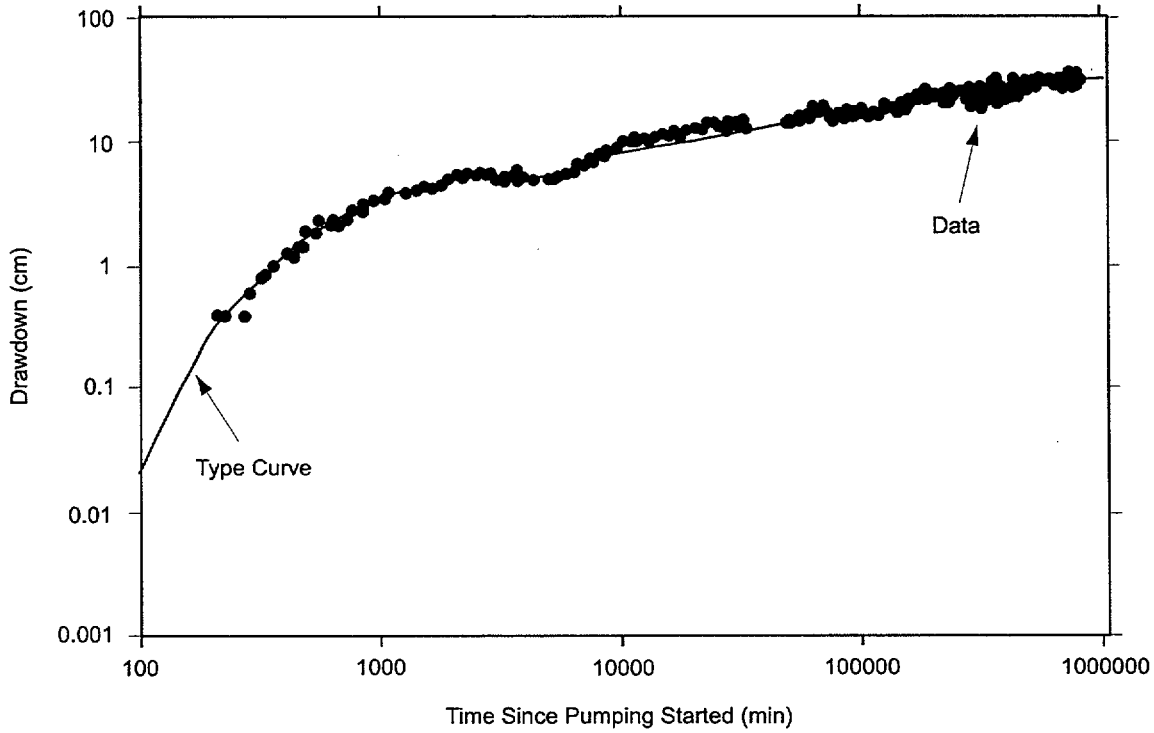

Source: Streltsova-Adams (1978); analysis method.

NOTE: For the analysis curve, the parameter $\tau/B = 0.05$.

Figure 36. Analysis of Drawdown in UE-25 ONC-1, May 8, 1996, to November 12, 1997, by the Method of Streltsova-Adams

Observation wells showed clear responses to the pumping, allowing computation of hydraulic parameters. Despite being 843 m from C#3, ONC-1 responded to pumping after only 200 minutes because it is in the same structural block as the C-wells (between the Bow Ridge and Paintbrush Canyon faults) and is connected by fractures related to northwest-striking faults. That fracture connection is reflected in a characteristic fissure-block aquifer response. From 200 to 2,000 minutes (1.4 days), flow from fractures caused drawdown to increase as a function of log time. From 2,000 to 6,000 minutes (1.4 days to 4 days), drawdown remained relatively constant as flow occurred from the rock matrix into fractures. After 6,000 minutes (4 days), drawdown increased again as a function of log time as flow from both the fractures and matrix occurred. Drawdown conformed to the type curve of Streltsova-Adams (1978; see Figure 36). Transmissivity computed from the type-curve match equals 1,000 m^2/d. If the transmissive thickness between the C-wells complex and ONC-1 is assumed to vary linearly between known thicknesses in C#2 and H-4, then it can be estimated to be about 193 m in ONC-1. Dividing transmissivity by the estimated transmissive thickness indicates a fracture hydraulic conductivity of 5 m/d. In comparison, the hydraulic conductivity of the matrix (Table 10) is insignificant. Computed storativity for the fractures in ONC-1 is 0.001, which is a tenth of the computed storativity of the matrix.

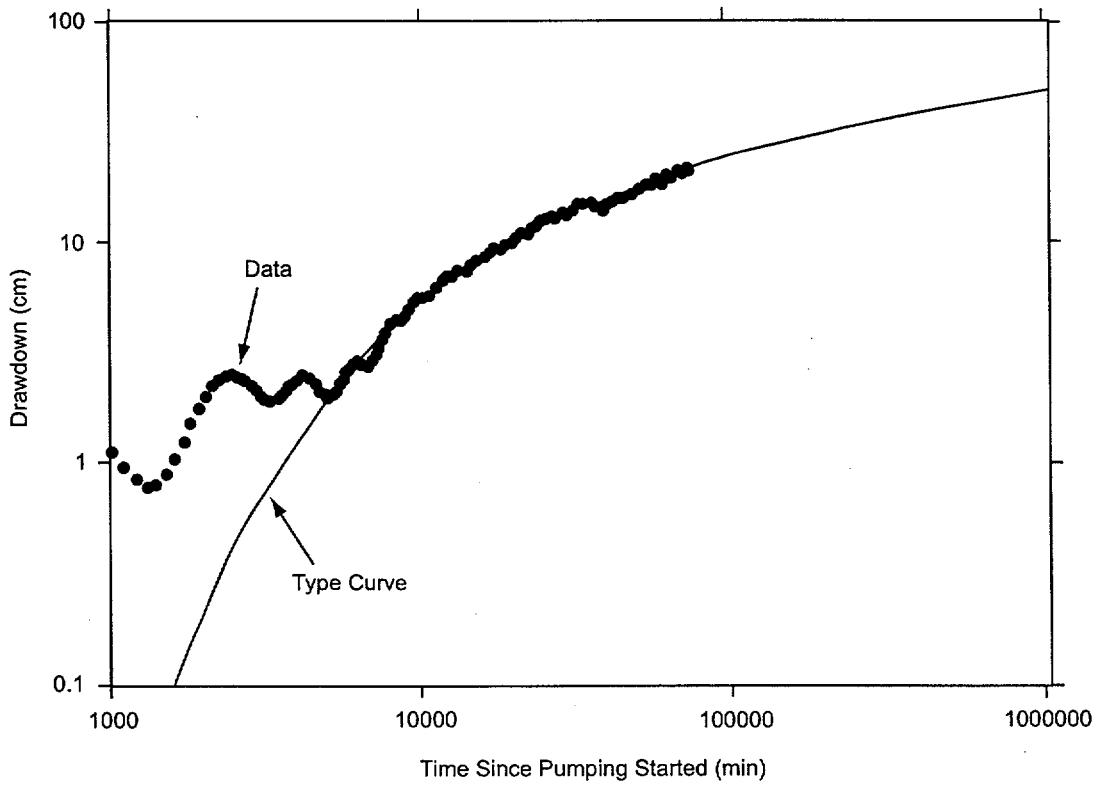

Source: Theis (1935), analysis method.

Figure 37. Analysis of Drawdown in USW H-4, May 8, 1996, to June 27, 1996, by the Method of Theis

Because of its location 2,245 m from C#3, borehole H-4 took 5,000 minutes (3.5 days) to respond to pumping. From 5,000 to 72,000 minutes (3.5 to 50 days) after pumping started, drawdown in H-4 conformed to the type curve of Theis (1935) for a confined aquifer (Figure 37). After 72,000 minutes (50 days), drawdown became relatively constant, probably in response to flux from a nearby fault boundary. The pre-boundary drawdown indicated transmissivity of 700 m^2/d and storativity of 0.002 (Table 10). Dividing transmissivity by the transmissive thickness obtained from a flow survey (Whitfield et al. 1984) indicated an hydraulic conductivity of 2 m/d. The location of the recharge boundary could not be ascertained because only H-4 was affected by that boundary, and the analytical solution to determine the location of a boundary (Lohman 1979) requires that at least two wells be affected by the same boundary.

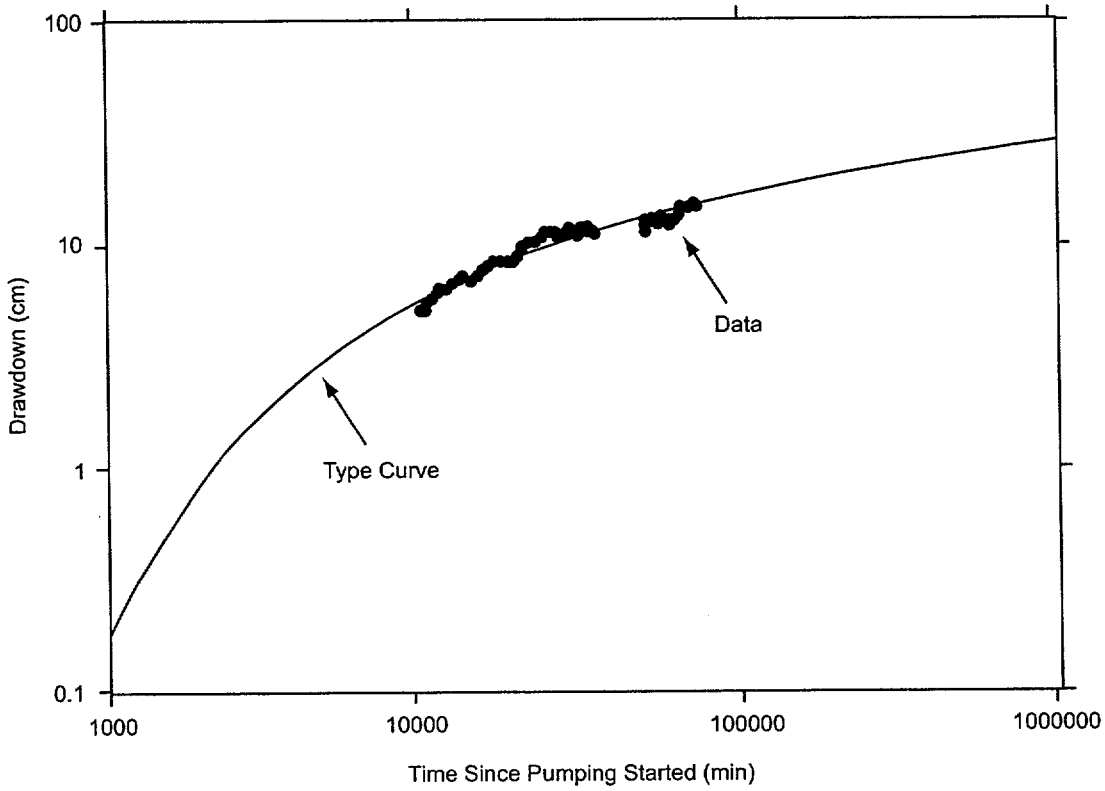

Source: Theis (1935), analysis method.

Figure 38. Analysis of Drawdown in UE-25 WT#14, May 8, 1996, to June 27, 1996, by the Method of Theis

Located a nearly identical distance (2,249 m) from C#3, borehole WT#14 took slightly longer (5,250 minutes or 3.7 days) to respond to pumping. From 3.7 days to just over 6 days (5,250 to 9,000 minutes), a transition from borehole-storage release to release of water from the aquifer occurred. From 6 to 50 days (9,000 to 72,000 minutes) after pumping started, drawdown in WT#14 conformed to the type curve of Theis (1935) for a confined aquifer (Figure 38). After that time, drawdown became strongly oscillatory, but those broad oscillations in the data deviated about a relatively constant value. The late-time data are interpreted to represent less-than-ideal response to a recharge boundary. The pre-boundary drawdown indicates transmissivity of 1,300 m^2/d and storativity of 0.002 (Table 10). Hydraulic conductivity and the location of the boundary could not be determined because of insufficient data.

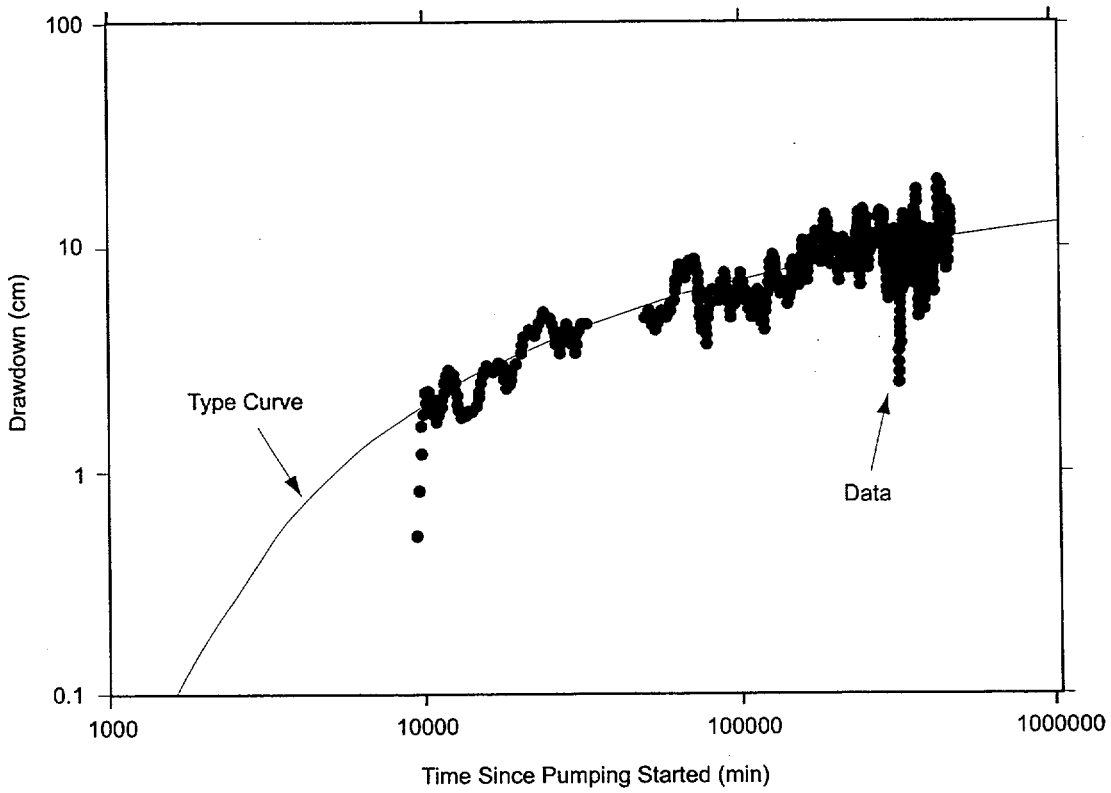

Source: Theis (1935), analysis method.

Figure 39. Analysis of Drawdown in UE-25 WT#3, May 8, 1996, to March 26, 1997, by the Method of Theis

Borehole WT#3 is located 3,526 m from C#3 and took more than 6 days (9,130 minutes) to respond to pumping. Thereafter, drawdown in WT#3 was oscillatory, but the data could be fit to the type curve of Theis (1935) for a confined aquifer (Figure 39). The solution indicated a transmissivity of 2,600 m^2/d and a storativity of 0.002 (Table 10). Dividing transmissivity by the length of the open interval in WT#3 (47.5 m) indicated a hydraulic conductivity of 56 m/d. Actual hydraulic conductivity probably is smaller than the calculated value because the thickness of transmissive rock between the C-wells complex and WT#3 probably exceeds the length of the open interval.

The transmissivity of the Miocene tuffaceous rocks appears to decrease northwestward in the area containing the observation wells used in the hydraulic test that began in May 1996. Depending on the analytical solutions used, transmissivity could be interpreted to decrease from 2,600 m^2/d in the vicinity of WT#3 to about 2,000 m^2/d in the vicinity of the C-wells. The transmissivity of the Miocene tuffs is 1,300 m^2/d in the vicinity of WT#14, 1,000 m^2/d in the vicinity of ONC-1, and 700 m^2/d in the vicinity of H-4.

The distribution of hydraulic conductivity in the tuffs in the vicinity of the C-wells complex appears to be structurally controlled. Hydraulic conductivity in C#2 decreases sharply from a range of 20 to 60 m/d in the Upper Tram and Lower Bullfrog intervals to a range of 0.08 to 0.2 m/d in the Calico Hills interval as the vertical distance from faults that intersect the boreholes increases (Table 9). Average hydraulic conductivity of the Miocene tuffaceous rocks in C#2 is twice that of C#1 (Table 10), possibly because C#2 is located nearer to the subsurface intersection of the north-striking Paintbrush Canyon or Midway Valley faults and a northwest-striking fault (shown in Figure 3) that underlies the gap through the northern part of Bow Ridge. If spatial relations between faults and hydraulic conductivity at the C-wells complex are combined with values of hydraulic conductivity determined from analyses of drawdown in ONC-1, WT#3, and H-4 (Table 10), then a possible distribution of hydraulic conductivity for the Miocene tuffaceous rocks in the vicinity of the C-wells can be inferred (Figure 40).

In the 21-km^2 area encompassed by observation wells used in hydraulic tests at the C-wells complex from 1995 to 1997, the storativity of Miocene tuffaceous rocks in those observation wells uniformly is 0.001 to 0.003 (Table 10). Analysis of drawdown in observation wells not affected by boundaries as a function of the time divided by the square of the distance from the pumping well (Figure 41) indicates that the average storativity of the tuffs in the observation area is 0.002. This same analysis indicates that the average transmissivity of the Miocene tuffaceous rocks in the area is 2,200 m^2/d. Derivation of a single analytical solution for C#1, C#2, ONC-1, and WT#3 confirms that the Miocene tuffaceous rocks, at least as far north as lower Midway Valley in the structural block delineated by the Paintbrush Canyon, Bow Ridge, and Dune Wash faults, are a single aquifer in which flow is influenced by the same structural and stratigraphic factors.

Plots of drawdown in observation wells as a function of distance 30,000, 100,000, 200,000, 305,000, and 463,000 minutes (21, 69, 139, 212, and 322 days) after pumping started in May 1996 (drawdown contours at 30,000 and 463,000 minutes shown in Figure 42) confirm an ovoid pattern of drawdown aligned with faults extending from Bow Ridge to Antler Wash that was detected during the hydraulic test conducted from May 22 to June 1, 1995 (Geldon et al. 1998). Analyzed by the method of Cooper and Jacob (1946), plots of drawdown as a function of distance (Figure 43) indicate values of transmissivity ranging from 2,100 to 2,600 m^2/d and values of storativity ranging from 0.0005 to 0.002 (Table 11). In comparison, the same type of analysis of drawdown in observation wells as a function of distance 10 days (14,000 minutes) after pumping started in May 1995 had indicated a transmissivity of 2,300 m^2/d and storativity of 0.003 (Geldon et al. 1998). Distance-drawdown and time-drawdown analyses discussed in this section converge on similar solutions.

The ovoid pattern of drawdown aligned with faults extending from Bow Ridge to Antler Wash that was detected during the hydraulic test conducted from May 22 to June 1, 1995 (Geldon et al. 1998) and confirmed in this study (Figure 42) indicates large-scale anisotropy caused by heterogeneity and structure. Large-scale transmissivity is higher in the direction of the long axis of the ovoid and lower in the direction perpendicular to it.

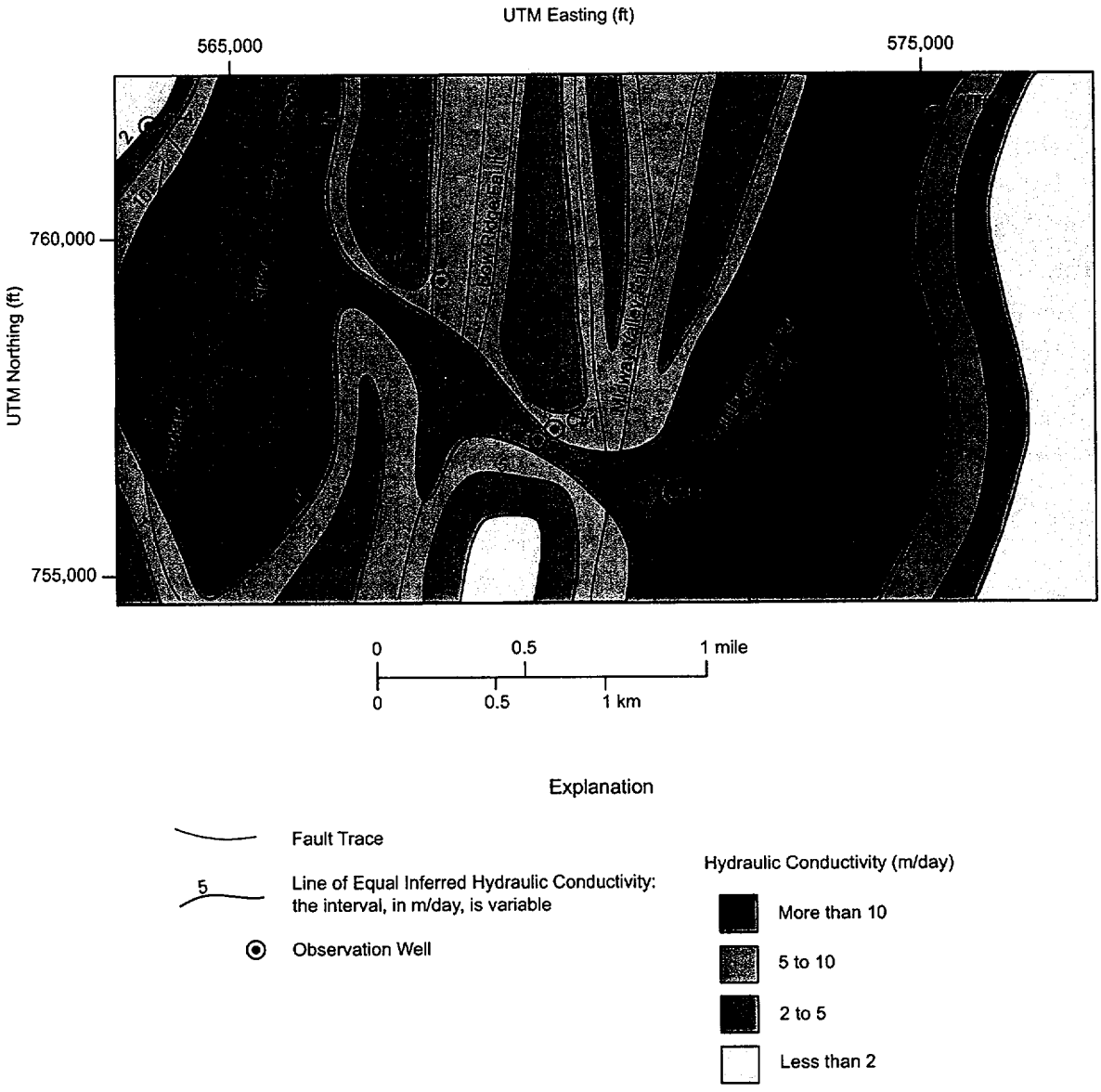

Figure 40. Inferred Distribution of Hydraulic Conductivity of Miocene Tuffaceous Rocks in the Vicinity of the C-wells

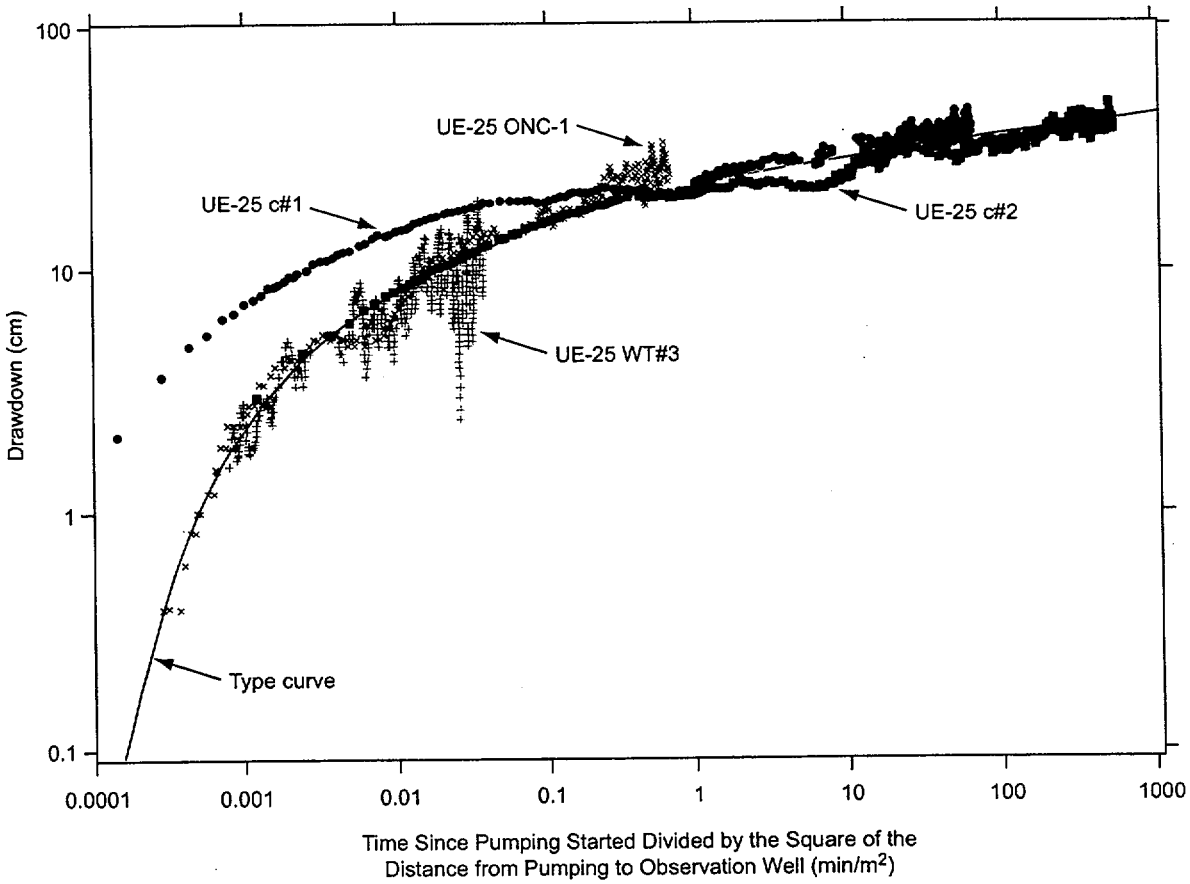

Figure 41. Analysis of Drawdown in Observation Wells as a Function of Time Divided by the Square of the Distance from the Pumping Well, UE-25 c#3

2.4.7 Paleozoic Carbonate Rocks

Borehole p#1 was monitored during hydraulic tests in 1995 and 1996 to detect hydraulic connection between the Miocene tuffaceous rocks and Paleozoic carbonate rocks in the vicinity of the C-wells. Hydraulic connection previously had been indicated by hydraulic head measurements in p#1 and by borehole flow surveys in the C-wells. Measurements made as p#1 was being drilled in 1983 detected a 22-m difference in hydraulic heads for the Paleozoic carbonate rocks and Miocene tuffaceous rocks in p#1 (Craig and Robison 1984), which indicated a potential for water to flow from the lower to the upper of those hydrogeologic units. Flow surveys conducted in the C-wells in 1991 detected upward flow in the lower parts of those boreholes (Geldon 1996) that most likely originated in the Paleozoic carbonate rocks, because the intervening tuffaceous rocks generally behave as a confining unit (Luckey et al. 1996).

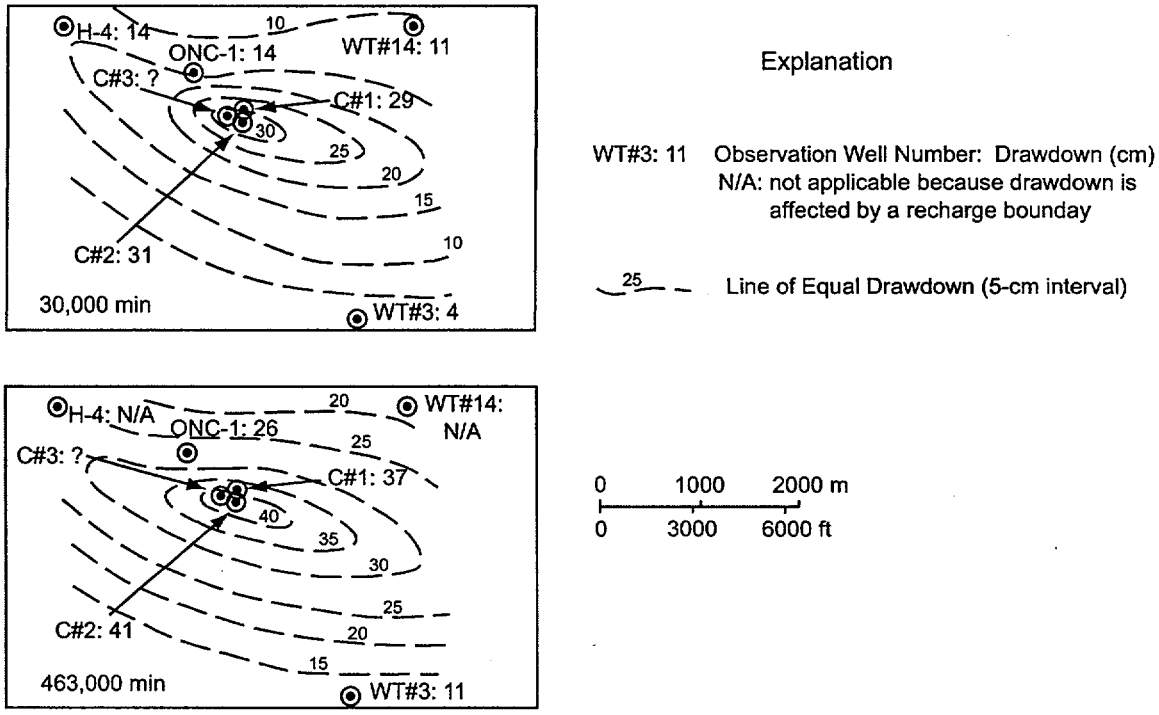

NOTE: The upper panel shows the drawdown distribution 30,000 minutes (20.8 days) after pumping started; the lower panel shows the distribution 463,000 minutes (321.5 days) after pumping started.

Figure 42. Distribution of Drawdown in Observation Wells at Two Times After Pumping Started in UE-25 c#3 on May 8, 1996

Although p#1 was monitored for 10 days (14,400 minutes) after pumping started in May 1995 (Geldon et al. 1998) and for about 180 days (256,200 minutes) after pumping started in May 1996, drawdown in the Paleozoic carbonate rocks was not detected (Figure 44). This lack of drawdown could indicate that the water being pumped was drawn laterally from the Miocene tuffaceous rocks. Alternatively, the water could have been drawn upward from Paleozoic carbonate rocks without causing drawdown in the underlying aquifer if the Paleozoic rocks have a large storage capacity. Hydraulic connection between the Miocene tuffaceous rocks and Paleozoic carbonate rocks could not be confirmed or refuted by monitoring water levels in p#1 during the study reported here.

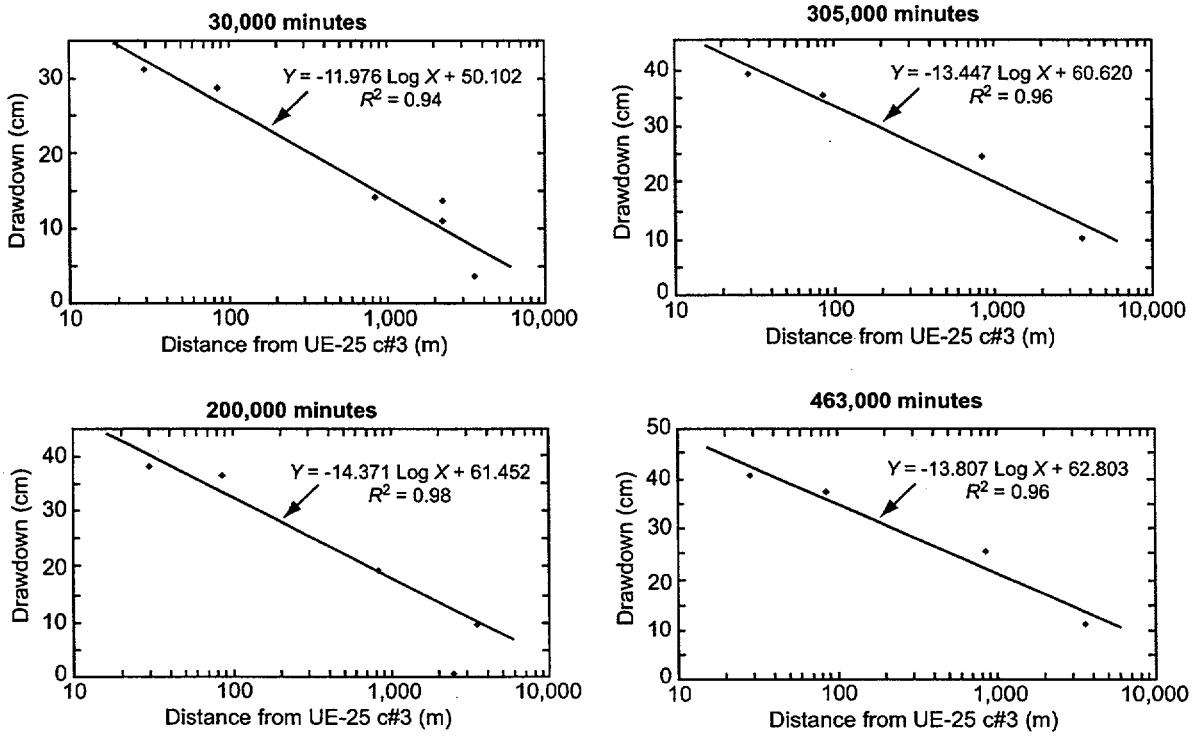

NOTE: The panels show the drawdown analyses at 30,000 (upper left), 200,000 (lower left), 305,000 (upper right), and 463,000 (lower right) minutes after pumping started.

Figure 43. Analyses of Drawdown in Observation Wells as a Function of Distance from the Pumping Well at Various Times After Pumping Started in UE-25 c#3

Table 11. Hydraulic Properties Determined from Drawdown in Observation Wells as a Function of Distance From the Pumping Well UE-25 c#3, May 1996 to November 1997

Time Since Pumping Started (min)	Transmissivity (m^2/day)	Storativity
30,000	2,600	0.0005
100,000	2,500	0.0009
200,000	2,100	0.002
305,000	2,300	0.001
402,000	2,200	0.001
463,000	2,200	0.001

2.5 LIMITATIONS AND UNCERTAINTIES

All analytical methods used in this study to determine hydraulic properties from drawdown or recovery responses assume that the aquifer is an equivalent porous medium. Although the flow system consists of a fracture network rather than a porous medium, the pressure responses conform quite well to type curves derived for either porous media or uniformly fractured media (Strelsova-Adams 1978). Thus, the fracture network at the C-wells is apparently interconnected in such a way that the fractured tuffs respond to pumping as "an equivalent porous medium." Another fundamental assumption is that flow to the pumping well is derived from an aquifer of infinite extent. The many faults near the C-wells complex that potentially function as either recharge or barrier boundaries make the concept of an infinite aquifer difficult to support. However, only observation wells that lay between faults bounding the structural block in which the C-wells are located were considered in the analyses, so boundary effects, while not completely eliminated, should have been minimized. Drawdown in H-4 and WT#14 obviously was affected by recharge boundaries.

All of the analytical methods used in this study, except for the Neuman (1975) method, assume radial flow to the pumping well, and, therefore, ignore vertical flow (application of the Neuman fully-penetrating-well solution, as was done in this report, to cases where pumping was in one interval and the analyzed drawdown response was in another, also ignores vertical flow). The flow from intervals other than the one being pumped that was detected during hydraulic tests in February 1996 and May 1996 to November 1997 indicates that flow during those tests actually was three-dimensional or spherical. Ignoring the vertical component of flow seems to have been justified by the generally good agreement between results of the hydraulic test in June 1995 (in which flow between observation and pumping wells was radial) and results for most intervals monitored in subsequent tests. Nevertheless, there is some inaccuracy involved in analyzing the flow from intervals that did not have open sliding sleeves above or below the pumped interval by techniques developed only for analyzing flow from the pumped interval.

The most commonly applied analytical method in this study, that of Theis (1935), assumes flow from an infinite, homogeneous, isotropic, confined aquifer. Transected by numerous faults and variably welded, the Miocene tuffs in the vicinity of the C-wells complex are neither homogeneous nor isotropic. As a result, hydraulic gradients toward the pumping well vary directionally, a situation ignored by the mathematics of the Theis (1935) solution. Disregarding a nonuniform hydraulic gradient seemingly would result in inaccurate computations of hydraulic properties. Consistent calculations, however, of hydraulic properties for individual intervals and the composite section of Miocene tuffaceous rocks (from test to test, from well to well, or from use of multiple observation wells in time-drawdown or distance-drawdown analyses) indicate that errors are at least being made consistently. That consistency provides confidence that calculated values approximate actual values of hydraulic properties, despite simplification of structural and lithologic complexities.

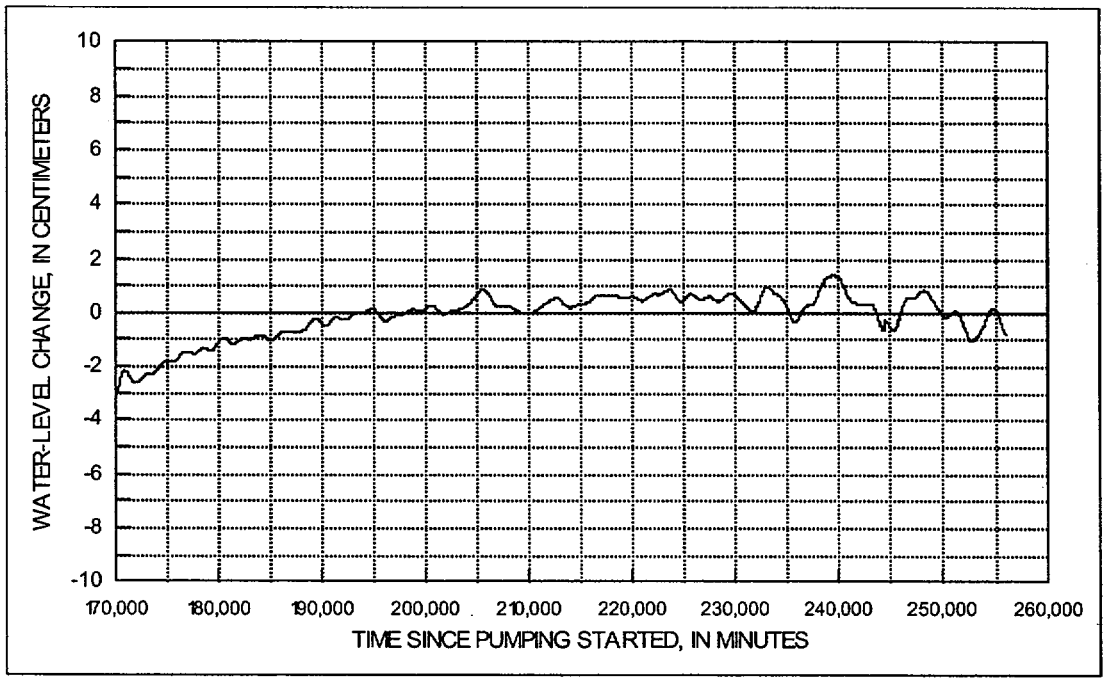

Figure 44. Water-level Changes in UE-25 p#1, September 3 to November 2, 1996

All of the analytical techniques used in this study required input parameters that had to be determined or approximated for hydrogeologic intervals or boreholes in which drawdown was monitored. Included in those parameters are the distance of the interval or borehole from the pumping well, the transmissive thickness of the interval or borehole, the barometric efficiency of the interval or borehole, the proportion of flow from a given hydrogeologic interval, and the fracture spacing within a hydrogeologic interval. Errors in deriving any of those input parameters could have changed calculated hydraulic properties considerably.

Values of transmissivity and storativity determined in this study are estimated to be accurate to one significant figure, but reported values of hydraulic conductivity are more uncertain. Hydraulic conductivity can be calculated by dividing the transmissivity by either the known thickness of transmissive intervals within a test interval, the entire thickness of the test interval, or an assumed thickness of transmissive rock between the observation and pumping wells. Because the transmissive thickness was unknown, it was impossible to determine hydraulic conductivity in many analyses. Even where hydraulic conductivity could be determined, it was done with limited confidence. For example, it is impossible to know whether the hydraulic conductivity of the Lower Bullfrog interval in C#1 really is about half that in C#2 or whether these calculated hydraulic conductivity values result from dividing approximately the same transmissivity in each borehole by an assumed transmissive thickness that is twice as large in C#1 as in C#2.

2.6 SUMMARY OF CONCEPTUAL MODELS AND PARAMETERS

Hydraulic tests conducted by the USGS in Miocene tuffaceous rocks at the C-wells complex, Yucca Mountain, Nevada, between May 1995 and November 1997 determined flow characteristics in six saturated-zone hydrogeologic intervals. North- and northwest-striking faults intersect boreholes of the C-wells complex, defining hydrogeologic intervals by spatially related faults and fracture zones. Flow within those intervals comes from diversely oriented fractures and from the interstices of variably welded ash-flow, ash-fall, and reworked tuff. The tuffs act as a single aquifer. About 70 percent of flow seen in hydraulic tests was contributed by the Lower Bullfrog interval, and another 20 percent came from the Upper Tram interval. Identified hydrogeologic units, and related hydraulic properties, cannot be extended far beyond the immediate vicinity of the C-wells complex due to control of those intervals by fault and fracture zones.

In several hydraulic tests from 1995 to 1997, borehole C#3 of the C-wells complex was used as the pumping well. Boreholes C#1 and C#2 (tens of meters distant) were used as observation wells. Each of the wells of the complex is about 900 m deep, and all are open below surface casings to the penetrated formations. Additional boreholes were used as observation wells in some of the hydraulic tests, including ONC-1, H-4, WT #14, WT#3, and p#1. The observation wells were completed in various intervals seen also in the holes of the C-wells complex; p#1 was completed in Paleozoic carbonate rocks. Those observation wells were sited 630 to 3,526 m from C#3, allowing some extrapolation of hydraulic characteristics from the C-wells location. The hydraulic tests were conducted to determine: (1) properties of the composite saturated-zone section in the C-wells; (2) hydraulic properties of the six intervals in those holes; and (3) heterogeneity in the tuffs, including the influence of faults. Monitoring in borehole p#1 was intended to establish whether the tuffs are connected hydraulically to the Paleozoic carbonate rocks (a regional aquifer), estimated to lie some 455 m below the C-wells.

The series of hydraulic tests began with short-term test episodes. The 10-day test of May 1995 pumped borehole C#3 at an average rate of 17.9 L/s and produced pumping-well drawdown of 7.76 m. Drawdown in observation wells ranged from 0 to 42 cm. The June 1995 test lasted four days and used packers to isolate the six saturated-zone hydrogeologic intervals of the C-wells complex. After pumping at a rate of 22.5 L/s, drawdown in the pumping well was 10.9 m, and drawdown in monitored intervals of observation wells C#1 and C#2 ranged from 43 to 352 cm. The five-day test of February 1996 used packers to isolate and pump the Lower Bullfrog and Upper Tram intervals at a rate of 8.5 L/s. All monitored intervals responded to that pumping. Drawdown in the pumping well was 2.86 m, and drawdown in C#2 and C#1 ranged from 14 to 25 cm.

A long-term test in which the Lower Bullfrog interval was isolated was conducted over more than 550 days starting in May 1996. All monitored intervals again responded to pumping (at a rate of 9.2 L/s). Drawdown reached nearly 6 m by late March 1997 when some disruption due to pump shutoffs occurred. Drawdown in all observation wells was strongly oscillatory, with peak drawdown in the C-wells complex observation holes of 35 to 51 cm. Drawdown in distant observation wells began after hours to days of pumping and ranged from 15 to 37 cm. No drawdown had been observed in p#1 (completed in the carbonate aquifer) by December 1996.

In all of these tests, significant, rapid drawdown and recovery in the pumping well far exceeded amounts that could be predicted from hydraulic properties calculated from observation-well drawdown in the same tests. Much of that excess likely can be attributed to frictional head loss ("borehole skin") in the pumping well. Because the pumping-well drawdown largely is independent of aquifer properties, analyses of that drawdown result in misleadingly small values of transmissivity and hydraulic conductivity. Hydraulic tests at the C-wells complex imply that analyses of pumping-well drawdown throughout the Yucca Mountain area are not reliable.

Hydrogeologic intervals in the C-wells exhibit layered heterogeneity. The Calico Hills interval is unconfined; the Prow Pass and Upper Bullfrog intervals are confined; the Lower Bullfrog interval is a fissure-block aquifer; and the Upper Tram interval received flow from cross-cutting faults in response to pumping. Transmissivity increases downhole from a range of 4 to 10 m^2/d in the Calico Hills interval to a range of 1300 to 1600 m^2/d in the Lower Bullfrog interval. This trend is reversed near the bottom of the wells: i.e., in the Upper Tram Interval, transmissivity is 800 to 900 m^2/d. Likewise, hydraulic conductivity increases downhole from about 0.2 m/d in the Calico Hills interval to a range of 20 to 50 m/d in the Lower Bullfrog and Upper Tram intervals. Storativity generally increases downhole; for example, in C#2 it increases from a range of about 0.0002 to 0.0004 in the Calico Hills and Prow Pass intervals to a range of 0.001 to 0.002 in the Lower Bullfrog and Upper Tram intervals. Order-of-magnitude differences, though, are evident between wells of the C-wells complex and nearby observation wells. These vertical distributions of hydraulic properties reflect the greater influence of faults and related fractures toward the bottom of the boreholes.

During hydraulic tests at the C-wells complex, drawdown occurred in all monitored intervals of those holes and in observation wells, regardless of the interval being pumped. That hydraulic connection across lithostratigraphic contacts likely results from interconnected faults, fractures, and intervals with large matrix permeability. The Miocene tuffaceous rocks thereby act as a single aquifer within a portion of the structural block bounded by the Paintbrush Canyon and Dune Wash faults as well as by faults cutting Boundary Ridge (extending at least as far north as lower Midway Valley). This aquifer encompasses a 21-km^2 area surrounding the C-wells complex. These hydraulic results indicate that the formal designation of multiple aquifers and confining units within the tuffaceous sequence at Yucca Mountain may not be justified.

Drawdown data from monitored wells during the long-term hydraulic test matched the type curve for a confined aquifer and indicated a transmissivity of 2,200 m^2/d and a storativity of 0.002 for the tuffs in the region around the C-wells complex. Plots of drawdown in observation wells as a function of distance during the same test showed a transmissivity of 2,100 to 2,600 m^2/d and a storativity of 0.0005 to 0.002. Analyses of drawdown in the C-wells and in outlying observation wells indicated a northwestward decrease in transmissivity from 2,600 m^2/d in WT#3 to about 2,000 m^2/d at the C-wells and, eventually, to 700 m^2/d in USW H-4. (Hydraulic conductivity is smallest toward the crest of Yucca Mountain and toward Jackass Flats.) Distributions of drawdown likewise were influenced strongly by northwest- and north-striking faults, as was hydraulic conductivity. Drawdown in observation well ONC-1 showed a fissure-block aquifer response during the long-term test, possibly due to a northwesterly zone of discontinuous faults that extends beneath Bow Ridge and Antler Wash. Drawdown in other observation wells reached a steady state after some 50 days of pumping, again likely in response to faults and fracture zones. Hydraulic conductivity ranges areally from less than 2 to more than

10 m/d and is largest where prominent north-striking faults are closely spaced or intersected by northwest-striking faults. Relatively large hydraulic conductivity occurs beneath Fran Ridge, Bow Ridge, and Boundary Ridge.

3. TRANSPORT PROPERTIES OF FRACTURED TUFFS

3.1 CONSERVATIVE TRACER TESTS AT THE C-WELLS

Conservative tracer tests conducted at the C-wells complex included: (1) iodide injection into the combined Bullfrog-Tram interval; (2) injection of iodide into the Lower Bullfrog interval; (3) injection of 2,6 Difluorobenzoic acid (DFBA) into the Lower Bullfrog interval; (4) injection of 3-carbamoyl-2-pyridone (Pyridone) into the Lower Bullfrog interval; (5) injection of iodide and 2,4,5 trifluorobenzoic acid (TFBA) into the Prow Pass formation; and (6) injection of 2,3,4,5 tetrafluorobenzoic acid (TeFBA) into the Prow Pass formation. Additionally, penta-fluorobenzoic acid (PFBA) was injected into the Lower Bullfrog interval; this test is discussed in Section 3.2. The sequence of testing is illustrated in Figure 6.

The purpose of testing with conservative tracers was to obtain estimates of flow porosity and longitudinal dispersivity of the Bullfrog and the Prow Pass Tuffs. The approach to developing parameters was to conduct multiple tests in a cross-hole system and use different solutions to interpret the results. Consequently, uncertainties and the sensitivity of the system were better understood.

Iodide, benzoic acids (including DFBA, TFBA, TeFBA, and PFBA), and pyridone can be analyzed by high-pressure liquid chromatography (HPLC) with either ultraviolet (UV) absorbance detection or fluorescence detection (pyridone). This method was selected not only because it is precise and sensitive but also because the groundwater samples can be injected directly into the instrument, allowing analyses to be conducted easily in the field for immediate test results.

All conservative tracer tests were analyzed by the Moench (1989; 1995) single- and dual-porosity analytical solutions to the advection-dispersion equation or by superposition of these solutions. The input parameters required by the Moench single-porosity solution and the dual-porosity solution are:

- pumping rate, q_o.
- distance from the pumping to injection well, r_L
- aquifer thickness, h
- radius of pumping well, r_w; and injection well, r_i
- thickness where mixing occurs in the pumping well, h_w
- thickness where mixing occurs in the injection well, h_I

- mass of tracer injected, M
- volume of water in which the mass of tracer is dissolved prior to entering the aquifer, V
- time for the tracer slug to enter the aquifer, t_{inj}
- flow porosity, ϕ_f and matrix porosity, ϕ (matrix porosity is also referred to, interchangeably, as "storage porosity" in Section 2).
- longitudinal dispersivity, α_L in the form of a Peclet number ($Pe = r_L/\alpha_L$)
- retardation coefficients representing linear, reversible adsorption R in the fractures and R' in the matrix
- dimensionless diffusion coefficient, Gamma, which is a function of the effective coefficient of diffusion from the fractures into the matrix, D', and of h, ϕ_f, R, q_o, and the radius, b', of theoretical sphere-shaped matrix blocks of the dual-porosity aquifer
- dimensionless storage parameter, Sigma, which is a function of ϕ_f, ϕ, R, and R'
- dimensionless skin parameter, SK, which is a function of the mass transfer coefficient, k_s, representing the continuity of diffusive flux across the "skin" (such as mineral fracture-surface coatings separating fractures from matrix blocks), and of D' and b'.

In a radially-convergent flow field, the volume of interest is a cylinder centered at the pumping borehole and extending to the injection borehole. To approximate the effects of mixing in the injection borehole, Moench (1989) used the hypothesis that the average value of the tracer concentration over this large cylindrical surface equals the tracer concentration in the injection borehole.

Radially-convergent, flow-type curves were generated for a range of Peclet numbers. These single-porosity and dual-porosity type curves are in the form of log-log plots of dimensionless concentration, C_d, versus dimensionless time, t_d. The observed recovery data are presented in the form of log-log plots of normalized concentration, C/C_{max} (where the concentration is normalized by the maximum observed concentration), versus time since injection. By overlaying the type curve and dimensionless recovery curve and fitting the rising portions of the two curves, an estimate of the advective travel time, t_a, is obtained when the match point ($C_d = 1$, $t_d = 1$) is projected onto the log-time axis of the observed data plot (e.g., Figure 45, which shows this process for the tracer test described in Section 3.1.1.1). In addition, because dimensionless time is defined as the ratio of time since injection to the advective travel time, the value of t_a is equal to the time since injection, indicated on the time axis of the recovery curve, corresponding to $t_d = 1$. The Peclet number is also estimated based on the type curve fit. In the dual-porosity solution, diffusion is minimal on the rising limb of the breakthrough curve, but it was calculated on the falling limb. The tail of the observed data was fitted to a theoretical dual-porosity breakthrough curve (BTC) with diffusion processes in which the controlling parameters include the Gamma and Sigma terms. The physical parameters that are estimated are the matrix porosity, ϕ, and the dimensionless diffusion coefficient, Gamma.

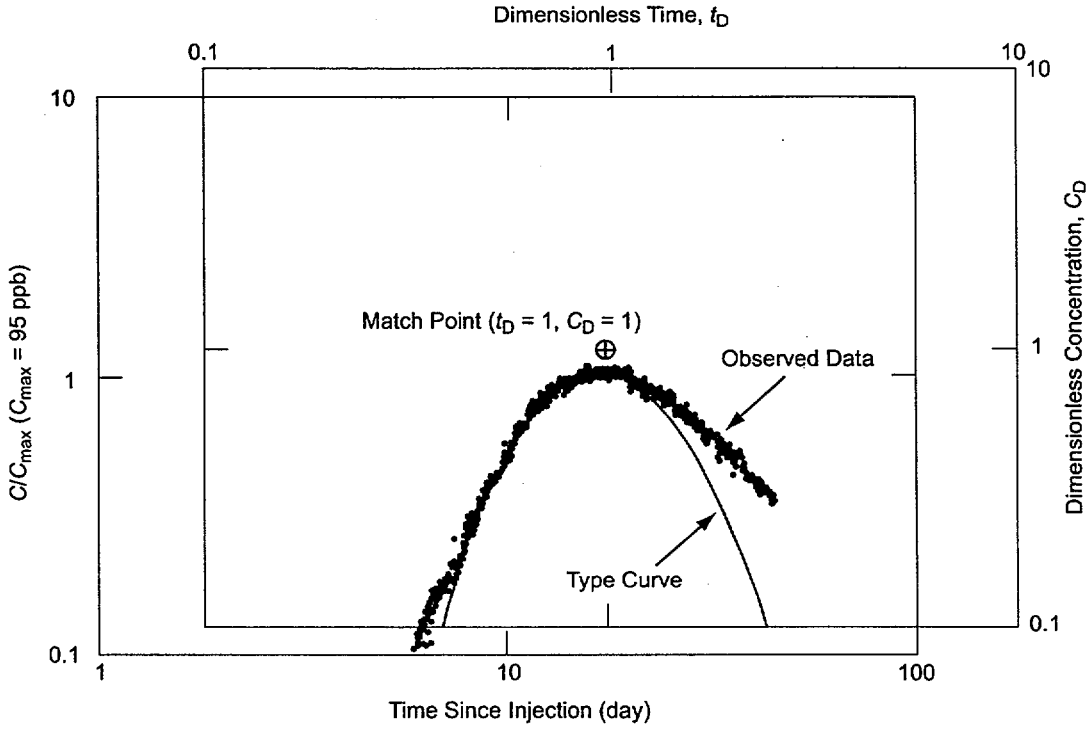

NOTES: The Peclet number Pe = 11.

Figure 45. Type-Curve Fit for Iodide Injection into UE-25 c#2

Some of the analyses of conservative tracer tests in this report used the single-porosity Moench solution, some used the dual-porosity solution, and some used a combination of both, depending on the type of test. This was done to explore the effectiveness of a particular solution method in fitting a particular set of data. When both the single- and dual-porosity solutions were used, the t_a and Peclet number were first obtained from the fit of the single-porosity type curves to the rising limb of the data curve; then Moench's dual-porosity solution was used to obtain estimates of Gamma and Sigma by fitting to the whole data curve.

To constrain the range of parameter values (such as of flow porosity) that can result from various possible interpretations of tracer tests, the fracture characteristics of the formations in which tracer testing was conducted should be considered. Fracture orientations in the Lower Bullfrog were based on televiewer data reported in Geldon (1996) and obtained in the 1980's when the boreholes were drilled. Two orientations are statistically significant. The dip and strike of the fracture planes are: 77/167 and 78/191 (the two orientations are shown in Figure 46, relative to the sides of the C-wells triangle). The fractures at the C-wells complex are moderately to steeply inclined, trend in a northerly direction, and have a probable nonuniform spacing. If transport is along fractures and faults, then the orientation data represent the possible directions of transport that may be occurring at the small scale in any interpretation.

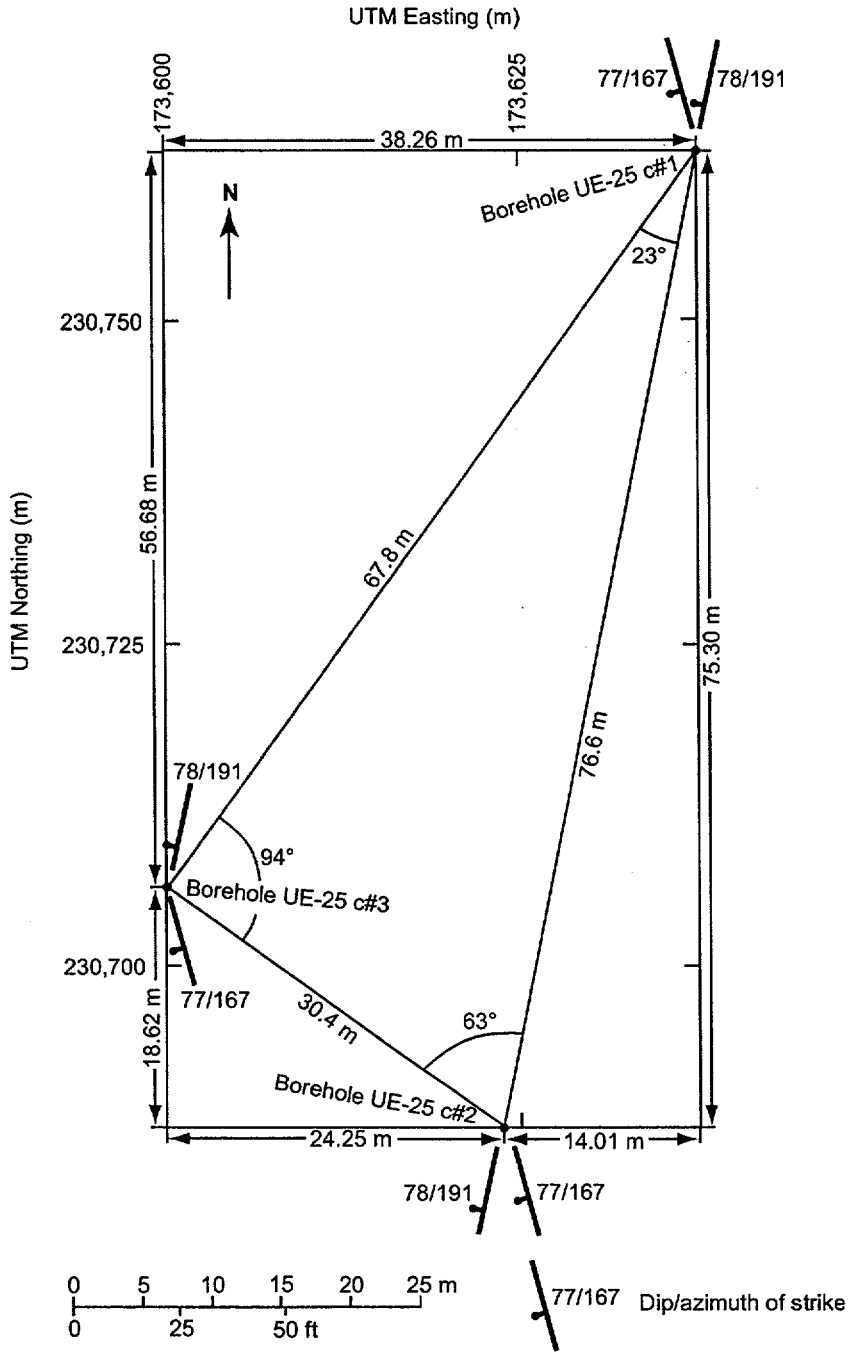

Source: Geldon 1993.

Figure 46. Dominant Bullfrog Tuff Fracture Sets in Each of the C-wells

3.1.1 Results and Interpretations of Conservative Tracer Tests: Bullfrog and Tram Formations

3.1.1.1 Iodide Tracer Test in the (Lower Bullfrog/Upper Tram) Interval

Following establishment of a quasi-steady-state hydraulic gradient by pumping the recovery borehole (C#3) for about 7,000 minutes, the first convergent tracer test at the C-wells complex was initiated in the Bullfrog-Tram Tuff interval on February 13, 1996, under convergent flow field conditions. Tracer solution was injected into the Bullfrog Tram interval of borehole C#2 for 28 minutes at an average rate of 0.41 (liters per second (L/s)) (6.5 gallons per minute (gpm)). This test was conducted in the most transmissive interval in the C-wells (the Bullfrog Tram interval), over the shortest interborehole distance (from borehole C#2 to borehole C#3), and using the simplest flow field (a convergent flow field) to enhance the possibility of successful tracer recovery.

The tracer solution consisted of 5.9 kilograms (kg) of sodium iodide (of which 5 kg were iodide) dissolved in 500 liters (L) (132 gallons) of water from borehole C#3. The tracer solution was chased with 182 L (48 gallons) of water, which was pumped into borehole C#2 to ensure evacuation of the injection string.

The chemical constituent used as a tracer was iodide with a concentration of 10,200 parts per million (ppm). The iodide injection from C#2 on February 13, 1996, has been discussed by Fahy (1997). The field-determined detection limit for iodide was 3 µg/L. The accuracy of the HPLC analytical technique, calculated as the difference between the prepared and measured concentrations of standards divided by the prepared concentration, was 3.47 percent for field analyses and 2.67 percent for laboratory analyses. The precision of the technique, as determined by comparing replicate analyses, was 2.3 percent for the field-determined concentrations and 1.61 percent for laboratory-determined concentrations.

Iodide concentrations in water sampled during the tracer test were obtained by a reverse-phase, HPLC in conjunction with an ultraviolet (UV)-absorption detector (Stetzenbach and Thompson 1983). Breakthrough occurred 5.07 days after injection. The peak concentration occurred 17.75 days after injection. The test was terminated 45.1 days after injection. The iodide mass recovered was estimated as 2.347 kg, 47 percent of the injected mass (Fahy 1997, written communication).

The tracer test was complicated by progressively decreasing discharge from the recovery well, which was caused by a mechanically failing pump. The pump discharge decreased from 8.5 L/s (134.7 gpm) on February 13, 1996, to 6.2 L/s (98.3 gpm) on March 29, 1996. For analysis, the median value of 7.4 L/s (117.3 gpm) was used as the discharge rate. Despite these problems, a recovery curve, with breakthrough and peak arrival times readily discernible, clearly was established by March 29, 1996.

3.1.1.1.1 Interpretation of Test

Both the single- and dual-porosity Moench solutions were used to interpret the iodide test in the Bullfrog-Tram interval. The rising limb was first analyzed using the single-porosity solution, as

presented in Figure 45, to obtain the flow porosity and Peclet number. The dual porosity solution was then used with these parameter values to fit the whole curve and obtain the matrix porosity. Input parameters and results are the following.

- Discharge equal to the median value of 7.4 L/s (117.3 gpm)
- Aquifer thickness equal to the transmissive thickness of the Bullfrog Tram interval between boreholes C#2 and C#3
- Peclet number of 11 to 12
- Advection travel time of 17.75 days (calculated from peak concentration; Figure 45)
- The flow porosity, ϕ_f, was estimated as 8.6%. This porosity estimate is high if only fractures are considered as the flow pathways. Typical fracture porosities are of the order of 1% maximum (Streltsova 1988).
- The complete curve fit (Figure 47) results in an estimate of the matrix porosity of 19 percent.

The high-flow porosity values above indicate that a composite pathway occurs for the iodide; that is, the fracture network is not well-connected at the scale of the test. The solute travels through a connected-fracture-network segment, then through a segment of matrix until it reaches the next connected-fracture-network segment. The matrix porosity estimated is reasonable, based on geophysical logging conducted at the C-wells complex (Geldon 1996).

The software program PEST (Parameter Estimation; [Watermark Computing 1994]) was used to corroborate tracer solution results and to obtain optimal parameter values based on the iodide test results. The PEST optimization started with the visual graphical fit to the BTC presented in Figure 47 for which *Pe* = 11.0, Sigma = 2.0, and Gamma = 0.04. Three PEST runs were conducted with each of these parameters changed from the above values while the others were held constant. In the first run, PEST was given *Pe* = 11, Sigma = 1.0 (intentionally "perturbed" from its good-visual-fit value of 2.0), and Gamma = 0.04; PEST was allowed to change only Sigma. At the end of this run, PEST converged on an optimal value of Sigma = 1.7175 and an associated confidence interval for Sigma. In the second run, PEST was given the values *Pe* = 8 (intentionally perturbed from its good-visual-fit value of 11.0), Sigma = 1.7175, and Gamma = 0.04; PEST was allowed to change only *Pe*. At the end of this run, PEST converged on an optimal value of *Pe* = 11.478 and an associated confidence interval for *Pe*. In the third run, PEST was given the values *Pe* = 11.478, Sigma = 1.7175, and Gamma = 1.0 (intentionally perturbed from its good-visual-fit value of 0.04); PEST was allowed to change only Gamma. At the end of this run, PEST converged on an optimal value of Gamma = 0.03565 and an associated confidence interval for Gamma. The above optimal values, their associated confidence intervals, and the fit to the actual BTC that they produce are presented in Figure 48.

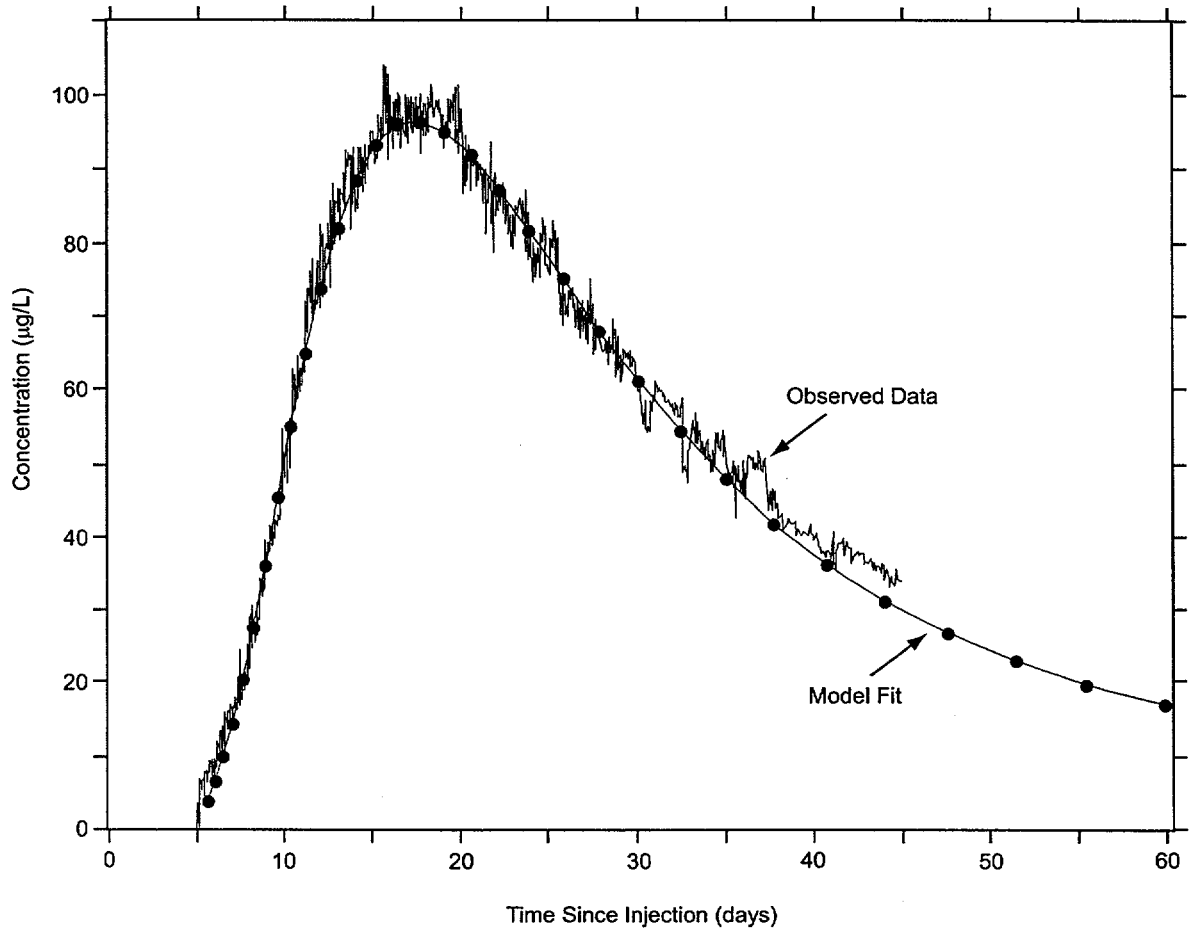

NOTE: Estimated parameters are Peclet number Pe = 11, dispersivity α_L = 2.6 m (8.64 ft), flow porosity ϕ_f = 8.6%, and matrix porosity ϕ = 19%.

Figure 47. Preliminary Moench Analytical Model for Iodide Injection in UE-25 c#2

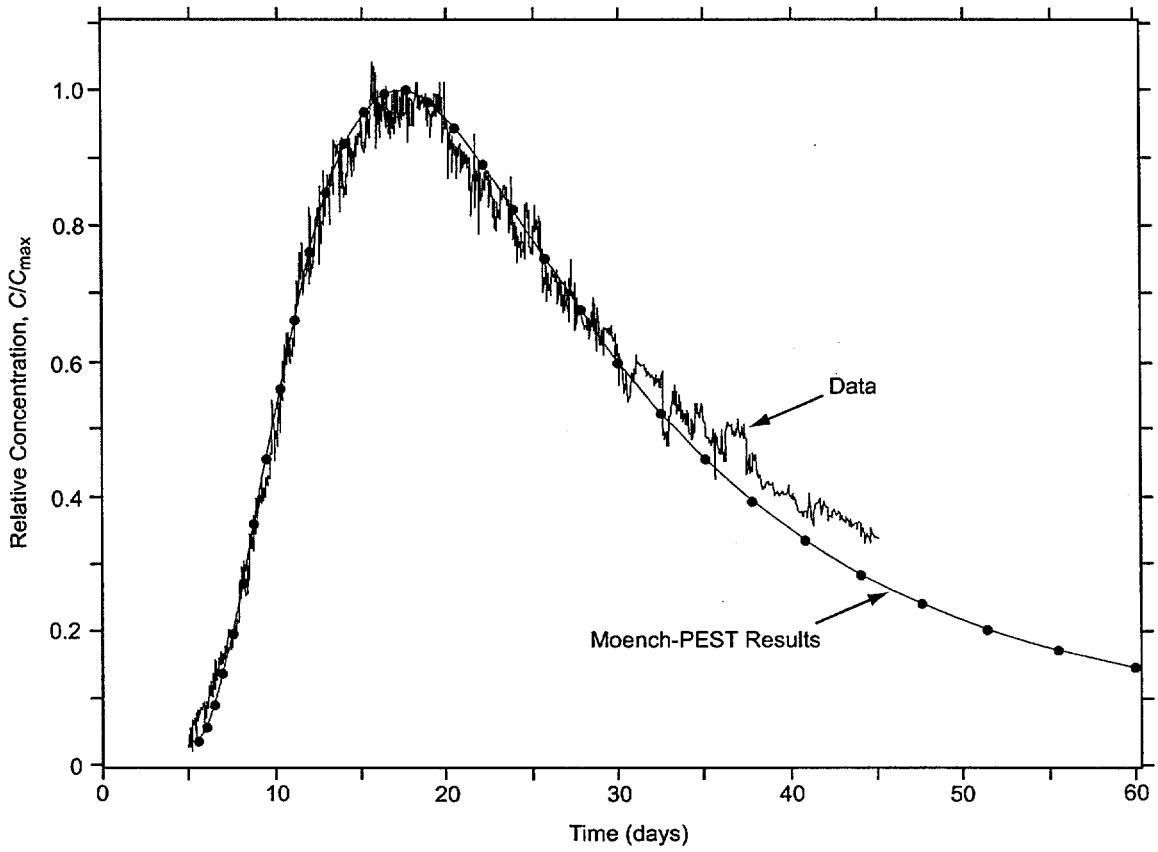

NOTE: The breakthrough curve was matched by the PEST program with initial estimates from a manual match. The optimal PEST results, with 95% confidence intervals in parentheses, are Pe = 11.478 (11.2276–11.7284), R = 1.0, σ = 1.71746 (1.4353–1.99962), and γ = 0.0356464 (0–0.12744), and the other estimated parameters are dispersivity α_L = 2.52 m (8.28 ft), flow porosity ϕ_f = 8.66%, and matrix porosity ϕ = 16.3%.

Figure 48. Breakthrough Curve for February 13, 1996, Iodide Tracer Test

The visual graphical fit and the optimized PEST parameters are in good agreement. The Peclet number and dispersivity estimates vary by approximately 4 percent. The flow porosity estimates vary by less than 1 percent. The visual-graphical-fit matrix-porosity estimate is 19 percent, and the PEST estimate is 16.3 percent.

The difference in values is attributed to the different weights assigned to fitting portions of the BTC. The rising limb is used exclusively in the visual graphical fit to estimate the Peclet number and the advective travel time, and then the advective travel time is used to estimate the flow porosity. The PEST approach uses all of the data, both rising- and falling-limb, and optimizes the fit to these data. This results in a slightly different fit than the visual graphical fit. Tables 17 and 18 in Section 3.4 (summary section) show the parameter values obtained from all of the conservative tracer testing described in Section 3.1.

3.1.1.2 Difluorobenzoic Acid Tracer Test in the Lower Bullfrog Interval

On January 10, 1997, approximately 11.35 kg of 2,6-difluorobenzoic acid (2,6 DFBA) mixed with 795 L (210 gallons) of C#3 water were injected into the Lower Bullfrog Tuff in borehole C#2, followed by 238 L (62.9 gallons) of chase water. A total of 1798 L (475 gallons) of fluid was injected, the first portion of which was the fluid in the injection string preceding the injectate solution. The average injection rate was 0.52 L/s (8.2 gpm), with a range of 0.48 to 0.55 L/s (7.6 to 8.8 gpm). The average progressive-cavity pump (injection pump) pressure, measured at the surface, was 223.6 psi, with a range of 215 to 230 psi. The chemical constituent used as a tracer in this test was 2,6 DFBA. Chemical analysis indicated that the 2,6 DFBA injectate-solution had a concentration of 15,560 mg/L. The field-determined detection limit for DFBA was 40 µg/L. The accuracy of the HPLC analytical technique, calculated as the difference between the nominal and measured concentrations of standards divided by the nominal concentration, was ±10 percent. The precision of the technique, as determined by comparing replicate analyses, was ±10 percent.

Breakthrough occurred on January 15, 1997, 5.07 days after injection. The peak concentration occurred 13.5 days after injection. The mass recovered is estimated as 7.6 kg, which is approximately 67 percent of the injected mass (Fahy 1997, written communication).

3.1.1.2.1 Interpretation of Test

Interpretation of the DFBA test using the Moench (1989) single-porosity analytical solution for radially convergent flow produced the following results.

- Peclet number between 12 and 15 (Figures 49, 50, and 51)
- Advection travel time between 16.5 and 12 days
- Flow porosity between 9.9 and 7.2 percent (Figures 50 and 51)
- Matrix porosity between 8.8 and 13.2 percent, and a longitudinal dispersivity value between 2.43 m (7.96 feet) and 1.94 m (6.37 feet): (Figures 50 and 51).

The range of values reflects two philosophies for the complete curve fit. The Peclet number of 12, flow porosity of 9.9 percent, matrix porosity of 8.8 percent, and a dispersivity of 2.43 m (7.96 feet) reflect fitting the rising limb of the BTC and honor the initial decline closely (Figure 50). At longer times, the data and the fit diverge, possibly indicating secondary arrivals. The alternative is to fit the rising limb of the BTC and reasonably fit the complete declining portion of the curve (Figure 51).

The program PEST was applied to the DFBA test results by starting with the visual graphical fit to the BTC presented in Figure 51, for which Pe = 15.0, Sigma = 1.7, and Gamma = 0.12.

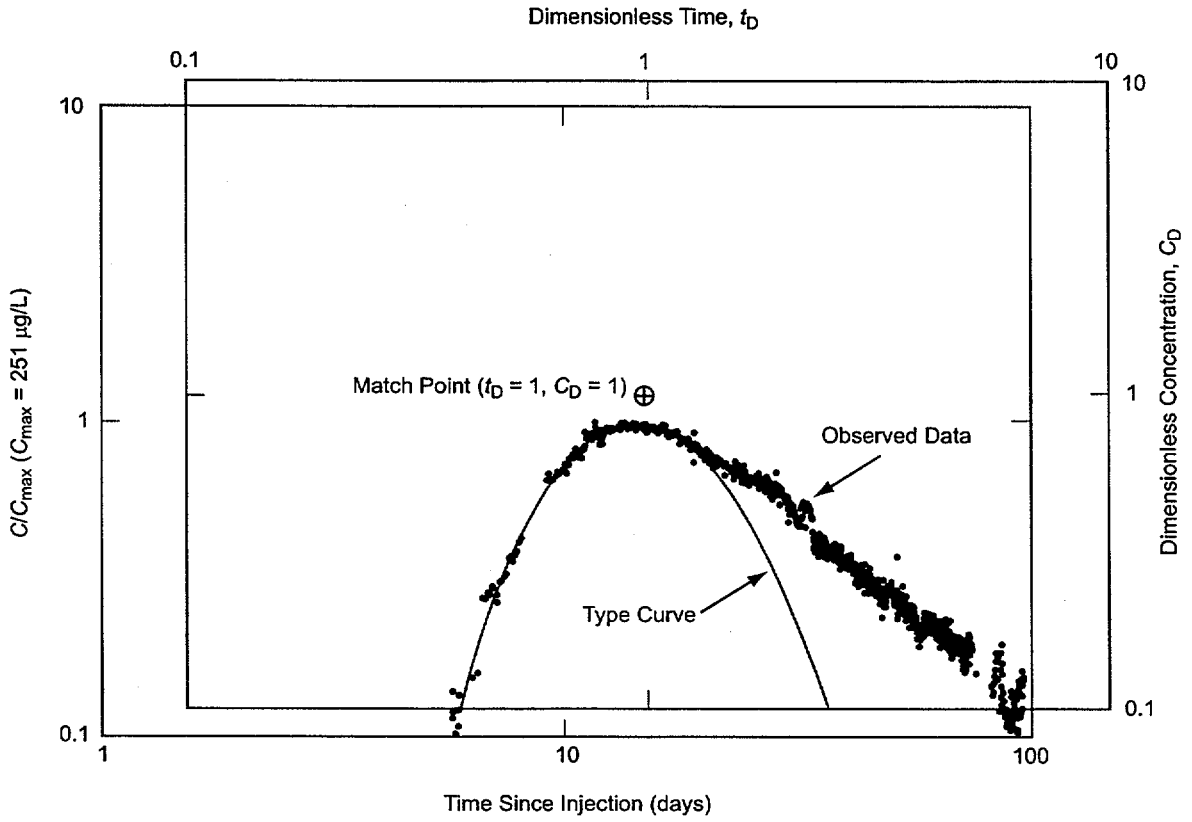

NOTE: The Peclet number *Pe* = 12. Only the rising limb of the observed data was fit because the falling limb could be the result of secondary arrivals.

Figure 49. Type Curve Fit for 2,6 DFBA Injection in UE-25 c#2

Three PEST runs were conducted, each with one of these parameters changed from the above values while the other parameters were held constant. In the first run, PEST was given *Pe* = 15, Sigma = 3.0 (intentionally "perturbed" from its good-visual-fit value of 1.7), and Gamma = 0.12; PEST was allowed to change only Sigma. At the end of this run, PEST converged on an optimal value of Sigma = 1.8776 and an associated confidence interval for Sigma. In the second run, PEST was given the values *Pe* = 8 (intentionally "perturbed" from its good-visual-fit value of 15.0), Sigma = 1.8776, and Gamma = 0.12; PEST was allowed to change only *Pe*. At the end of this run, PEST converged on an optimal value of *Pe* = 15.8 and an associated confidence interval for *Pe*. In the third run, PEST was given the values *Pe* = 15.8, Sigma = 1.8776, and Gamma = 1.0 (intentionally perturbed from its good-visual-fit value of 0.12); PEST was allowed to change only Gamma. At the end of this run, PEST converged on an optimal value of Gamma = 0.11793 and an associated confidence interval for Gamma. The above optimal values, their associated confidence intervals, and the fit to the actual BTC that they produce are presented in Figure 52.

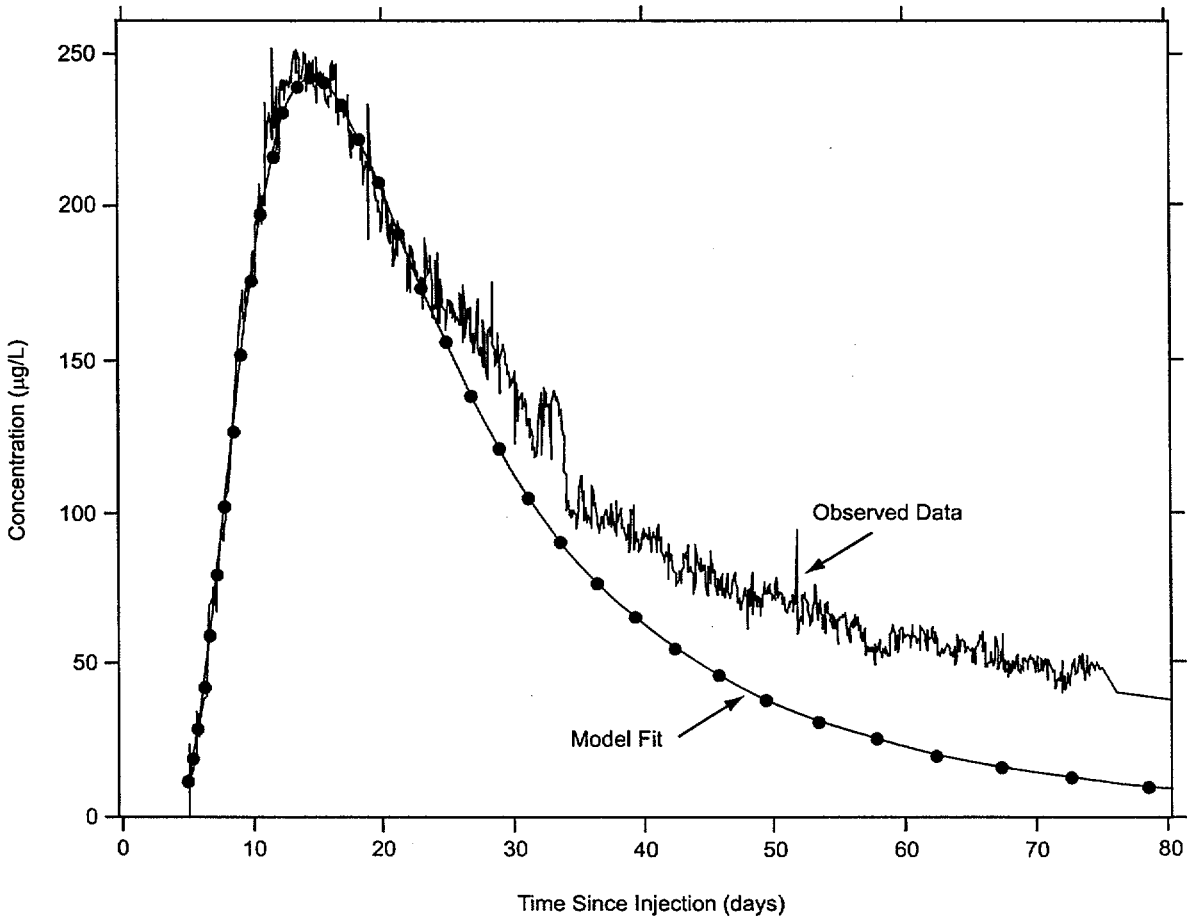

NOTE: The Fit 1 estimated parameters are Peclet number Pe = 12, dispersivity α_L = 2.4 m (7.96 ft), flow porosity ϕ_f = 9.9%, and matrix porosity ϕ' = 8.8%. Only the rising limb of the observed data was fit because the falling limb could be the result of secondary arrivals.

Figure 50. Fit 1 Preliminary Moench Analytical Model for 2,6 DFBA Injection in UE-25 c#2

The visual-graphical fit and the optimized PEST parameters are in good agreement. The Peclet number and dispersivity estimates vary by approximately 5 percent. The flow porosity estimates are identical. The visual-graphical-fit matrix porosity estimate is 13.2 percent, and the PEST estimate is 14.6 percent.

3.1.1.3 Pyridone Tracer Test in the Lower Bullfrog Interval

On January 9, 1997, approximately 3.018 kg of 3-carbamoyl-2-pyridone (pyridone), mixed with 795 L (210 gallons) of borehole C#3 water, was injected into borehole C#1, followed by 252 L (66.6 gallons) of chase water to test the Lower Bullfrog interval. This injection was made

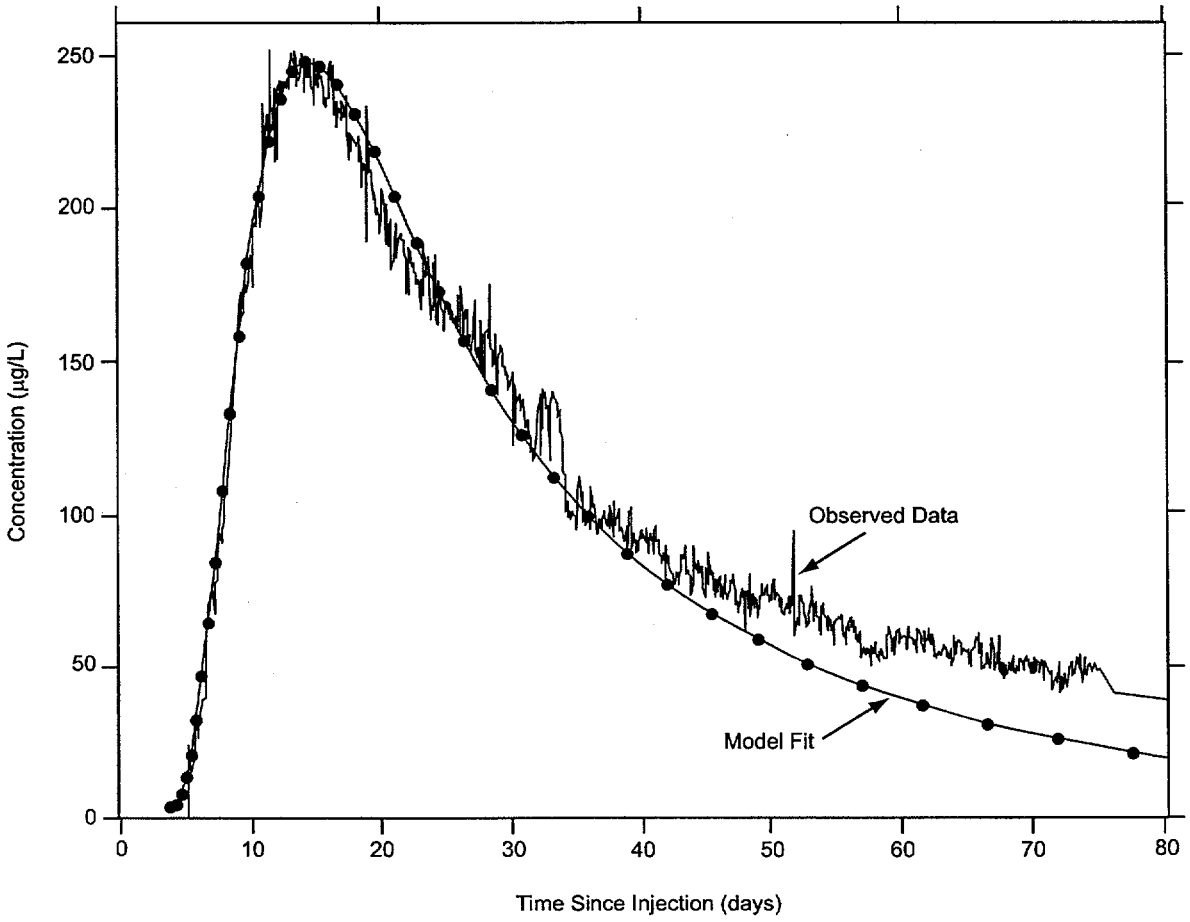

NOTE: The Fit 2 estimated parameters are Peclet number Pe = 15, dispersivity α_L = 1.9 m (6.37 ft), flow porosity ϕ_f = 7.2%, and matrix porosity ϕ' = 13.2%.

Figure 51. Fit 2 Preliminary Moench Analytical Model for 2,6 DFBA Injection in UE-25 c#2

while C#3 was being pumped at an average rate of 9.53 L/s (151.1 gpm). A total of 2,082 L (550 gallons) of fluid were injected, the first portion of which was the fluid in the injection string preceding the injectate solution. The average injection rate was 0.38 L/s (6.1 gpm), with a range of 0.28 to 0.62 L/s (4.4 to 9.8 gpm). The average progressive-cavity pump (injection pump) pressure, measured at the surface, was 252.8 psi, with a range of 50 to 300 psi. Chemical analysis indicated that the pyridone injectate solution had an average concentration of 2,998 mg/L. The field-determined detection limit for pyridone was 0.1 µg/L. The accuracy of the HPLC/fluorometry analytical technique, calculated as the difference between the nominal and measured concentrations of standards, divided by the nominal concentration, was ± 7 percent. The precision of the technique, as determined by comparing replicate analyses, was ± 10 percent.

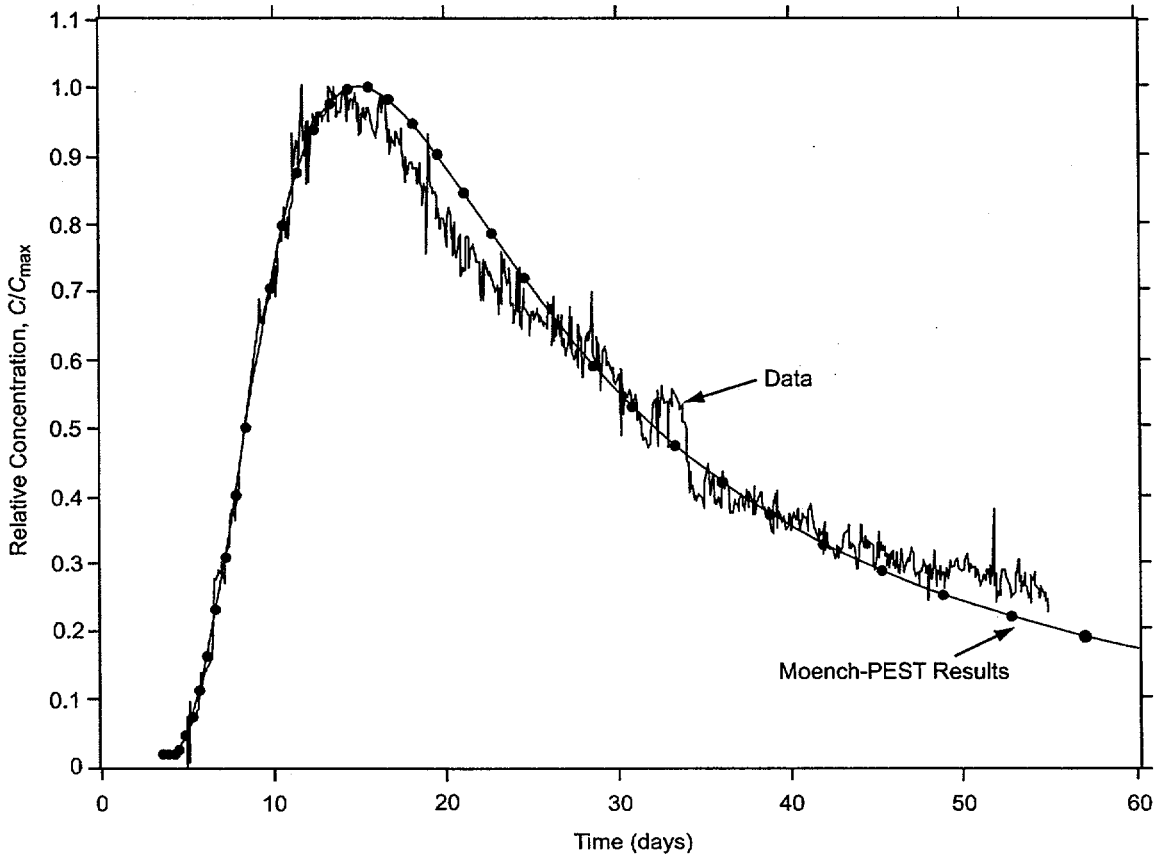

NOTE: The breakthrough curve was matched by the PEST program with initial estimates from a manual match. The optimal PEST results, with 95% confidence intervals in parentheses, are Pe = 15.7954 (15.4998–16.091), R = 1.0, σ = 1.87763 (1.65457–2.10068), and γ = 0.117934 (0.01741397–0.218454), and the other estimated parameters are dispersivity α_L = 1.83 m (6.01 ft), flow porosity ϕ_f = 7.2%, and matrix porosity ϕ' = 14.6%.

Figure 52. Breakthrough Curve for January 10, 1997, DFBA Tracer Test

Breakthrough occurred on March 27, 1997, 56.3 days after injection. The concentration of pyridone continued to increase, but at a gradually-decreasing rate until the end of the test (the test was terminated before a clear peak was observed). The maximum concentration of Pyridone reached was 0.210 µg/L (parts per billion (ppb)), or 210 parts per trillion (ppt).

The precision of the pyridone concentration values varies. For concentrations less than 100 ppt, errors exceeded ±10%, based on replicate sample analyses. Concentrations of pyridone less than 100 ppt are shown as open-circles on Figure 53. The filled-circles indicate concentrations of pyridone greater than 100 ppt and those samples with replicate errors less than or equal to ±10%.

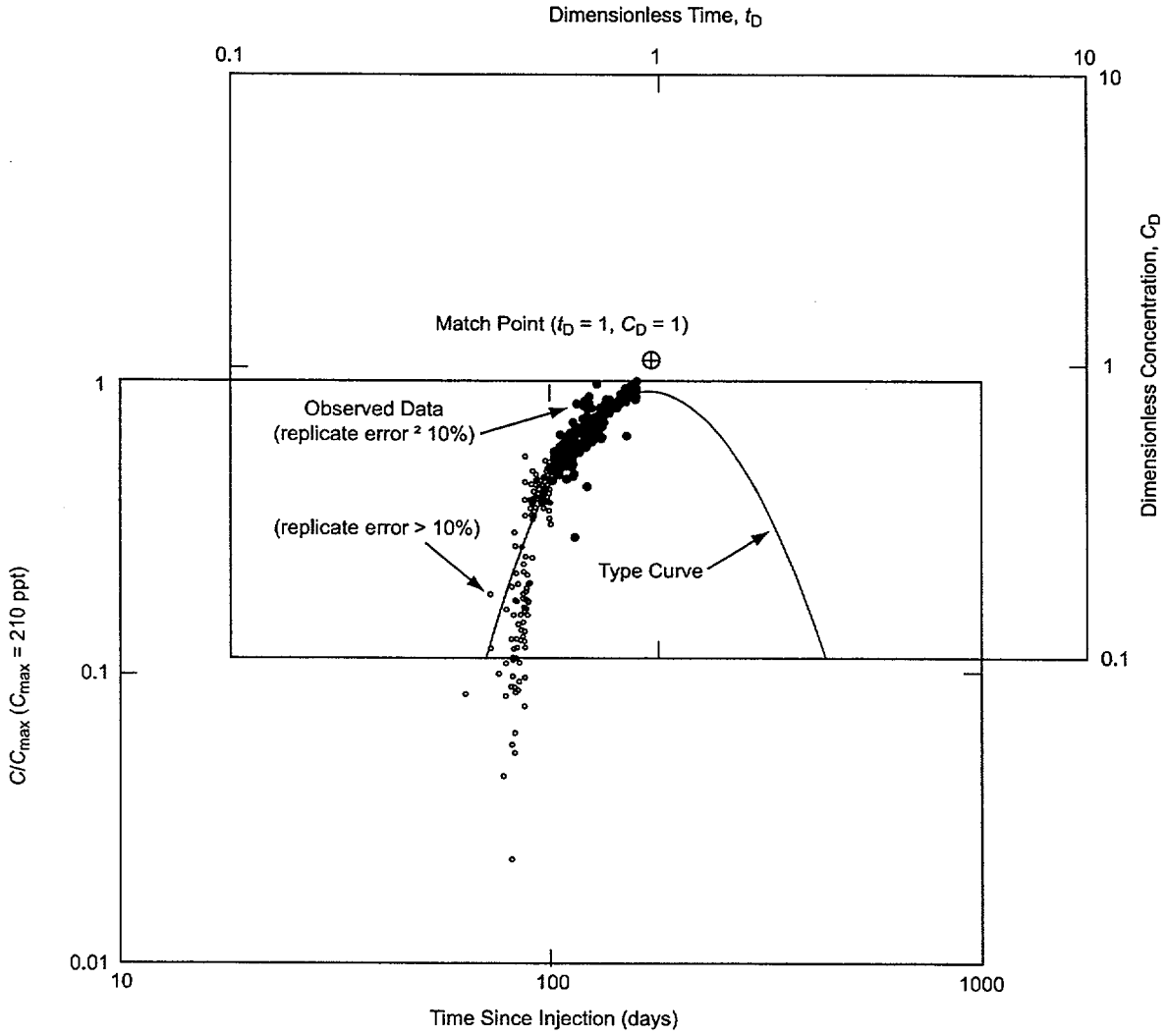

NOTE: The Peclet number Pe = 11.

Figure 53. Type Curve for Pyridone Injection in UE-25 c#1

3.1.1.3.1 Interpretation of Test

Because the pyridone test was prematurely terminated, only the rising limb part of the test was analyzed. The type curve depicted in Figure 53 fits these points well but is limited in that the test was terminated before a clear peak was observed. Assuming that the 0.210 µg/L concentration of pyridone is the maximum for the BTC, the dual-porosity (Moench 1995) analytical solution with a Peclet number of 11 matches the pyridone dimensionless concentration against the dimensionless time curve (Figure 53). (The single-porosity analytical solution (Moench 1989) would have produced a similar result if used to fit the rising limb because the matrix diffusion effects do not manifest themselves until the falling-limb phase of the test.)

3.1.1.4 PFBA and Iodide Tracer Tests in the Lower Bullfrog Interval

In cooperation with the USGS, LANL conducted two "pilot" tracer tests, each involving the injection of a single conservative tracer in the Lower Bullfrog interval during 1996. These tests were conducted primarily to determine which well, C#1 or C#2, would serve as a better injection well for the planned multiple-tracer test. The primary motivation was the concern that the responses of both sorbing and colloid tracers might be highly attenuated or excessively delayed relative to conservative tracers, which could make test durations impractically long. Thus, it was desirable to determine which potential injection well yielded the quickest and highest-concentration responses at the production well, C#3. It was not taken for granted that the best response would be from C#2, the injection well closest to C#3, because C#1 and C#3 are more closely aligned with the predominant fracture strike direction at the C-wells than C#2 and C#3.

The first pilot tracer test involved the injection of approximately 10 kg of PFBA into the lower Bullfrog interval in well C#2 on May 15, 1996. This same interval in C#3 was pumped continuously at about 575 L/min throughout the test (starting on May 8, 1996, prior to tracer injection). The PFBA was dissolved in ~1000 L of groundwater. The test was conducted under partial recirculation conditions with about 20 L/min of the water produced from C#3 (~3.5% of production rate) being continuously reinjected into C#2. The recirculation was initiated approximately 24 hr before tracer injection to establish a steady flow field, and it was continued for 23 days after injection. The tracer solution was plumbed into the recirculation loop such that there were no flow interruptions during injection.

The second pilot test involved the injection of about 12.7 kg of iodide (~15 kg of sodium iodide dissolved in ~1000 L of groundwater) into the Lower Bullfrog interval in C#1. It was conducted in a manner very similar to the PFBA pilot test and was initiated on June 18, 1996. The recirculation rate in this test was about 15 L/min (~2.6% of production rate), and recirculation continued for ~16 days after injection. Production from C#3 was maintained at ~575 L/m throughout the test.

It was clear a few days after the injection of iodide into C#1 that the PFBA response from C#2 was much more conducive to multiple-tracer testing than the iodide response from C#1. The results of the PFBA test are relevant to the interpretation of the multiple-tracer test conducted in the Lower Bullfrog interval, so they are discussed in Section 3.5 of this report along with the results of the multiple-tracer test. The iodide response between C#1 and C#3 is shown in Figure 54. This response is complicated by the initially high and gradually declining iodide background concentrations, which are attributed to the residual iodide in the aquifer from the February 13, 1996, injection of iodide into the Bullfrog Tram interval in C#2. However, there is clear evidence of a peak occurring about 2 months after injection. The estimated iodide recovery from the C#1 injection by October 1, 1996, (after correcting for the declining background) was 6 to 10% of the injected iodide mass. In contrast, the PFBA recovery from C#2 was about 72% on October 1, 1996. Neither the PFBA nor the iodide pilot tracer tests were quantitatively interpreted.

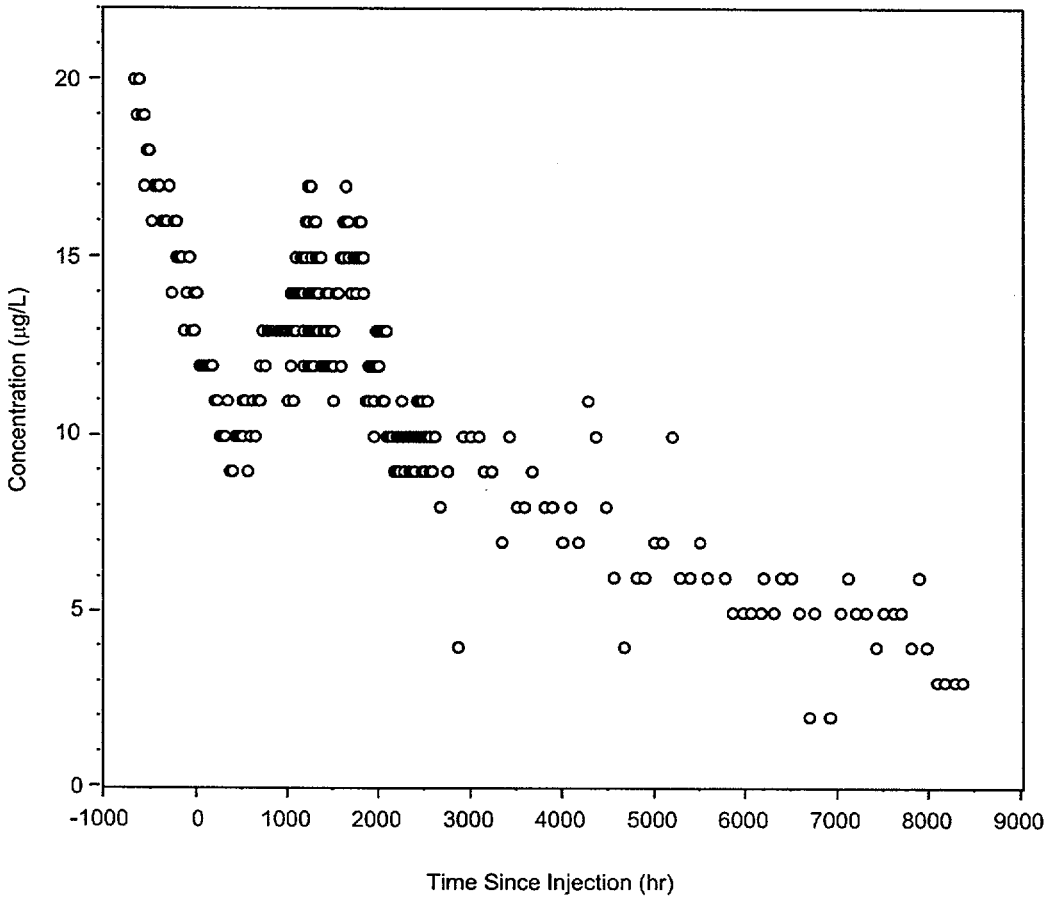

NOTE: The breakthrough curve is a result of injection of ~12.7 kg of iodide into UE-25 c#1 on June 18, 1996; the declining background prior to and immediately after injection is due to recovery of iodide from a February 1996 iodide injection into UE-25 c#2; and the estimated recovery from UE-25 c#1 accounting for UE-25 c#2 background was between 6 and 10% through June 1, 1997.

Figure 54. Breakthrough Curve for Iodide Injection in UE-25 c#1

3.2. PROW PASS FORMATION

3.2.1 2,4,5 Trifluorobenzoic Acid and Iodide Test from C#3 to C#2

On June 17, 1998, a partial-recirculation conservative tracer test was initiated from C#3 to C#2 by injecting approximately 14.83 kg of 2,4,5 trifluorobenzoic acid (TFBA) and 12.26 kg of iodide (in the form of sodium iodide) into the Prow Pass interval of C#3 while C#2 was pumped at the rate of approximately 4.35 gpm (0.33 L/s). The concentration of 2,4,5 TFBA was 14,239 ppm in the injected slug and that of iodide 14,307 ppm. Of the 4.35 gpm (0.33 L/s) pumped from C#2, 1.25 gpm (0.095 L/s) was continuously reinjected into the Prow Pass interval of C#3.

Approximately 40 hours after the injection, breakthrough of the tracers occurred in C#2. The peak for the 2,4,5 TFBA BTC occurred 6.74 days after injection, and the peak for iodide at 7 days after injection (Figure 55).

The iodide and 2,4,5 TFBA BTCs were analyzed using the single- and dual-porosity analytical solutions of the advection-dispersion equation as given in Moench (1989; 1995). These solutions were used, as is, for a hypothetical purely convergent flow field, and they were also lagged and superposed to obtain the solution for the actual partial-recirculation flow field. The curves were first analyzed assuming Moench's single-porosity solution for both the convergent and the partially recirculating flow-field assumptions, using the entire curves for the fits, to obtain the flow porosity and longitudinal dispersivity. In this case, the aquifer is considered to be an equivalent porous medium made up of a network of fractures, some of them continuous, and some discontinuous with connecting segments of matrix (Fahy 1997). The porosity of this network of fractures and connecting segments of matrix, through which flow of solutes occurs, is referred to herein as "flow porosity" (Fahy 1997). The curves were then analyzed assuming a dual-porosity system, also using the entire curves for the fit. In addition to the above network of fractures and connecting segments of matrix, the dual-porosity medium is conceptualized as having a storage component consisting of dead-end fractures and the part of the matrix not contributing to the flow network.

The flow porosity and longitudinal dispersivity are different for each of the solutions presented. The retardation coefficient used for all solutions was 1.0, indicating that iodide and 2,4,5 trifluorobenzoic acid are considered conservative with respect to the Prow Pass Tuff. All the solutions used the following input parameters:

- pumping rate of 0.33 L/s (5.23 gpm; represents the average rate for the test)
- aquifer thickness of 61 m (200.14 ft)
- distance between injection and pumping wells of 29 m (95.15 ft)
- radii of injection and pumping wells of 13.97 cm (5.5 in.)
- borehole mixing length of 30.5 m (100.07 ft; assumed, as discussed below).

3.2.1.1 Single-Porosity, Purely Convergent Interpretation

The single-porosity, purely convergent solution is obtained directly from the Moench (1989) solution to the advection-dispersion equation. The single-porosity solution for fitted flow porosity and longitudinal dispersivity values of 0.07% and 1.45 m, respectively, is presented in Figure 56, along with the iodide and 2,4,5 TFBA BTCs. All BTCs, such as the ones in Figure 56, were normalized by dividing the measured concentrations by the maximum concentration, C_{max}, rather than by the concentration of the injected mass slug, C_0. Longitudinal dispersivity is a measure of the media's ability to disperse a solute along streamlines. Transverse dispersivity, which represents the media's ability to disperse a solute in a direction perpendicular to streamlines, is not obtainable from this analysis method and flow geometry. The longitudinal dispersivity of 1.45 m and the 29-m flow length correspond to a Peclet number of 20,

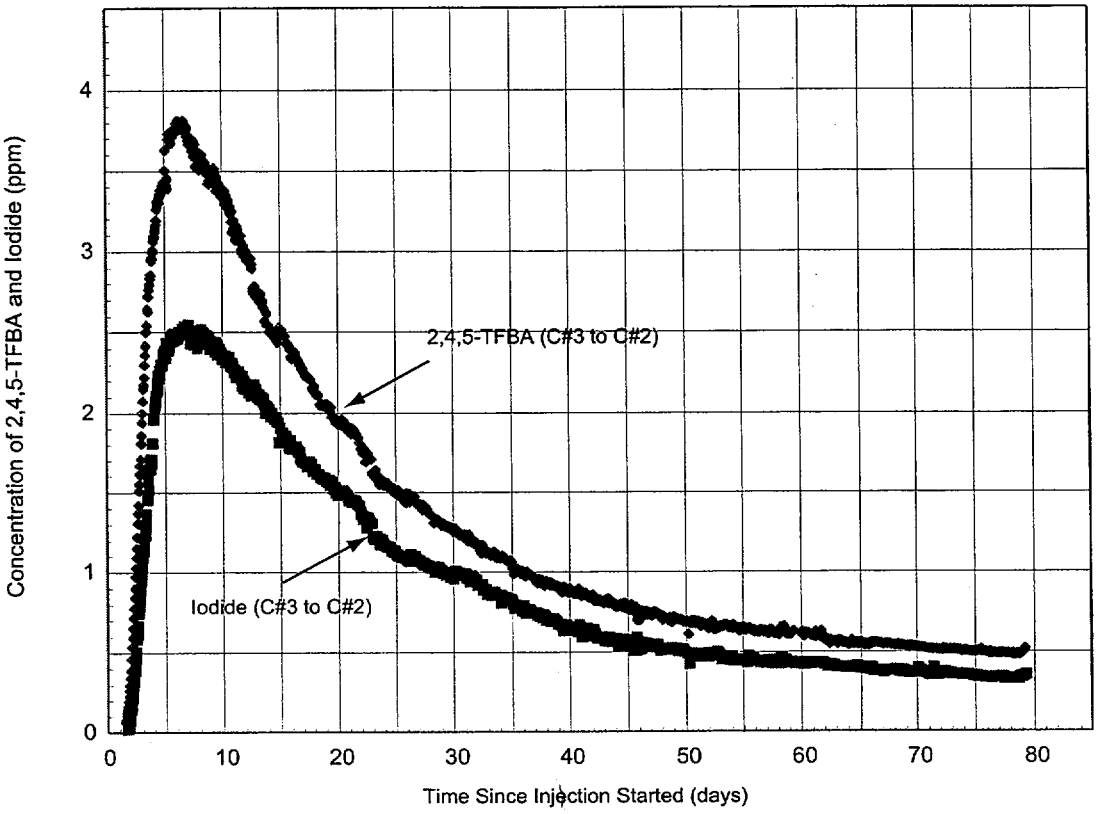

NOTE: C#2 and C#3 refer to UE-25 c#2 and UE-25 c#3, respectively.

Figure 55. Breakthrough Curves for 2,4,5 TFBA and Iodide Tracer Test from UE-25 c#3 to UE-25 c#2

where the Peclet number is a dimensionless parameter formed in Moench (1989; 1995) by dividing the distance between injection and pumping wells by the longitudinal dispersivity.

The fitted values of longitudinal dispersivity and flow porosity may be sensitive to the mixing lengths assumed for the injection and pumped wells. The mixing lengths represent those lengths within the boreholes through which the tracer enters or exits the aquifer. The 30.5-m mixing length assumed for all solutions is based on the thickness of the transmissive interval within the packed-off Prow Pass interval and is consistent with the hydrogeology of the interval.

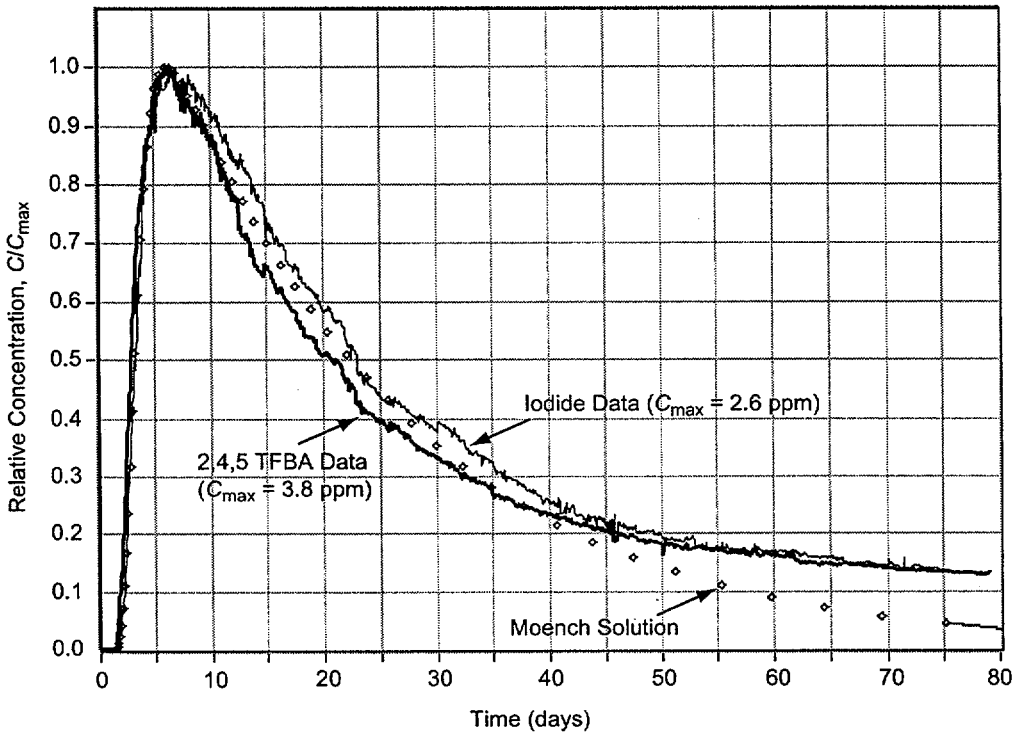

NOTE: Flow porosity = 0.0007, storage porosity was not applicable because a single-porosity medium was assumed, and longitudinal dispersivity = 1.45 m.

Figure 56. Breakthrough Curve for June 17, 1998, 2,4,5 TFBA and Iodide Tracer Test Matched by the Single-Porosity, Purely Convergent Moench Solution

The residence time of the tracer slug within the borehole is directly proportional to the mixing length. Data collected during the tracer injection indicate that the borehole was flushed in 8.5 hrs (the concentration in the injected interval was measured in the field and found to rise from below detection limit to 2,721 ppm and then back to below detection limit in 8.5 hrs). When the mixing length is reduced to 0.3 m and only the rising limb of the actual BTC is matched to the theoretical BTC from the single-porosity solution of Moench (1989; assuming minimal diffusion during the rising limb), a longitudinal dispersivity value of 4.27 m and a flow porosity value of 0.0016 are obtained as fitting parameters. Changing the mixing length from 30.5 m to 0.3 m constitutes a two-orders-of-magnitude change in this parameter. Corresponding to this change in the assumed mixing length, the estimates of longitudinal dispersivity and flow porosity change from 1.45 m and 0.0007 (for a 30.5-m mixing length) and to 4.3 m and 0.0016 (for a 0.3-m mixing length). This is a three-fold change of longitudinal dispersivity and a two-fold change of flow porosity, both less than one order of magnitude. The estimated parameters, therefore, are not very sensitive to the mixing length.

The above porosity value of 0.07% is in the range of 0.001% to 1% cited in the literature to represent fracture porosity (see, for example, Freeze and Cherry 1979, p. 408). This implies that the flow network for this test in the Prow Pass Tuff is composed predominately of only fractures.

3.2.1.2 Single-Porosity, Partially Recirculating Interpretation

When the purely convergent flow field of Figure 56 is replaced by a partially recirculating flow field, the resulting solution to the advection-dispersion equation changes from the curve labeled "Moench solution" in Figure 56 to the curve labeled "Modified Moench solution" shown in Figure 57. The difference between the two solutions reflects the difference in flow field representation and in the fitted values of longitudinal dispersivity and flow porosity used (or implied) for each solution. Two elements of partial recirculation are represented in this solution. Rather than straight converging rays into the pumped well, the partially recirculating flow field streamlines that are within the capture zone of the pumped well emanate from the injection well and curve towards the pumped well (Figure 58a). The streamlines shown in Figure 58a are lines of equal stream function values, in which the stream function of the partial-recirculation field is calculated as the sum of the stream functions of a 0.33 L/s sink and a 0.095 L/s source, 29 m apart. The volume of rock between pairs of these curved streamlines constitute distinct pathways for the solute (tracer) to take from the injection to the pumped well. Three such inter-streamline pathways (Figure 58a) are assumed for the partial-recirculation analysis in this section. The Moench (1989) single-porosity, purely convergent solution is viewed as the solution of the advection-dispersion equation along a single straight pathway (Figure 58b). This solution for a particular longitudinal dispersivity value and flow porosity is applied to each of the above three distinct pathways. A proper delay factor is added to account for the differences in lengths, or swept volumes, of these pathways relative to the straight purely convergent pathway.

The solutions from Moench (1989) for a particular longitudinal dispersivity value, flow porosity, and an instantaneous-slug injection are then superimposed with appropriate delay factors to obtain what is considered to be the system's unit response function. The summed curve represents what is seen at the pumped well in response to an instantaneous input function at the injection well in a partial-recirculation flow field.

The second element of partial recirculation is that the reinjected water contains a small amount of tracer; therefore, the tracer is continuously reintroduced into the aquifer. For the calculations presented here, it was assumed that this lag duration is approximately 1 hr. The injection concentration curve is then convolved (Levenspiel 1972) with the unit response function to produce the calculated partial-recirculation BTC at the pumped well.

Using the parameter-fitting process above, a longitudinal dispersivity of 0.27 m and a flow porosity of 0.00045 were selected as optimal for the single-porosity, partial-recirculation case. These parameters result in the calculated partial-recirculation BTC presented in Figure 57.

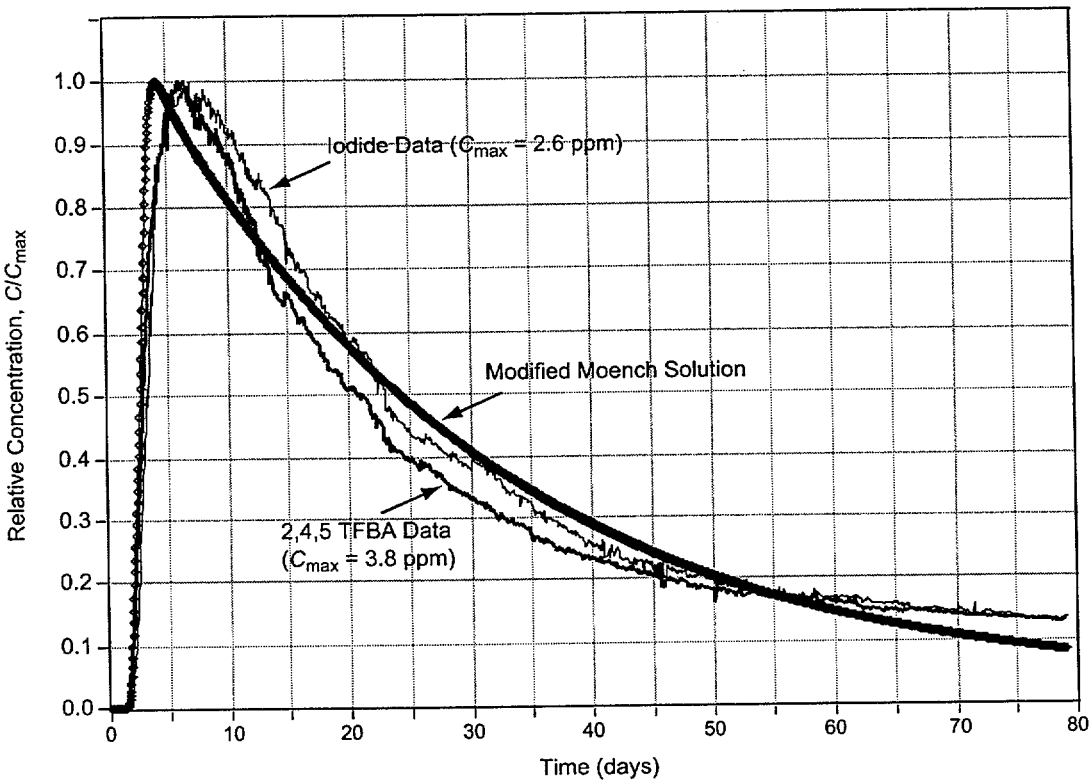

NOTE: Three inter-streamline pathways were assumed with delay factors of 1.01 days, 2.99 days, and 3.11 days. The "initial" flow porosity = 0.00045, storage porosity was not applicable because a single-porosity solution was assumed, and longitudinal dispersivity = 0.27 m.

Figure 57. Breakthrough Curve for June 17, 1998, 2,4,5 TFBA and Iodide Tracer Test Matched by the Single-Porosity, Partial-Recirculation Solution Derived from Moench

The delay factors for the three inter-streamline pathways inherent in the calculation of the BTC of Figure 57 were initially assumed to be 1.83 days for the first pathway, 3.5 days for the second, and 7.5 days for the third (these are the advective travel times calculated from the volume of rock of each pathway, the assumed porosity, and the flow rate within the pathway). However, use of these delay factors produced a calculated BTC that did not fit the actual BTC. The fit was substantially improved by changing the delay factors to 2.01 days, 2.99 days, and 3.11 days, which resulted in the calculated BTC of Figure 57. Because these three delay factors are not the ones indicated by the volumes of rock calculated for the three inter-streamline pathways, they are interpreted to represent the uncertainty in either the single-flow porosity value or in the assumed streamline pattern and resulting rock volumes.

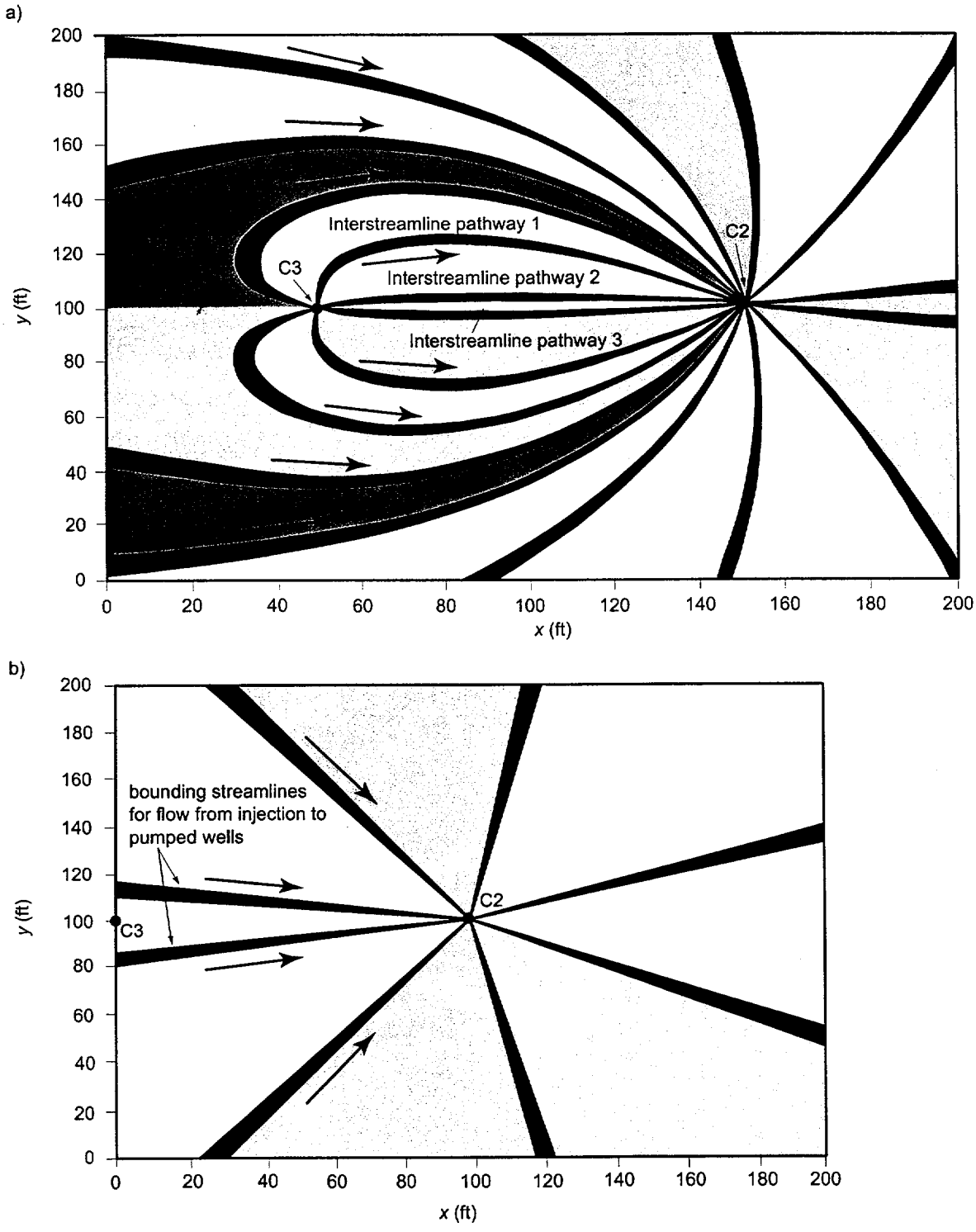

Figure 58. Streamlines for a) Partial-Recirculation Flow Field and b) Purely Convergent Flow Field

The results shown in Figures 56 and 57 indicate that if the BTCs of 2,4,5 TFBA and iodide are analyzed as if they result from a purely-convergent flow field, ignoring that the real flow field is partially recirculating, some error in the derived parameters results. A longitudinal dispersivity of 1.45 m is obtained when purely-convergent conditions are assumed, five times the 0.27 m obtained when the partial- recirculation flow field is recognized. The flow porosity of 0.0007 obtained for purely-convergent conditions is 56% higher than the flow porosity of 0.00045 obtained for partial recirculation.

3.2.1.3 Dual-Porosity, Partially Recirculating Interpretation

In the dual-porosity case, the medium is comprised of flow and storage components. The flow component is conceptualized as a flow network of (1) continuous fractures and (2) discontinuous fractures with interconnecting segments of matrix. The porosity of the flow component of the medium is referred to as the "flow porosity." The storage component is assumed to consist of dead-end fractures and the part of the matrix not contributing to the flow network. The porosity of the storage component of the medium is referred to as the "storage porosity" (within Section 3 of this report, "matrix porosity" means the same thing as "storage porosity"). The flow network is represented by a longitudinal dispersivity and a flow porosity, and the storage component is represented by a storage porosity and a dimensionless matrix diffusion coefficient.

The calculated dual-porosity solution is predicated upon the single-porosity, partial-recirculation solution presented earlier, i.e., a longitudinal dispersivity of 0.27 m and a flow porosity of 0.00045. Two calculated BTCs obtained for a storage porosity of 0.001 and two dimensionless matrix diffusion coefficients (Gamma), namely 0.0001 and 0.001, are presented in Figure 59 along with the actual BTCs of 2,4,5 TFBA and iodide.

The free-water molecular diffusion coefficients of 2,4,5 TFBA and iodide are 8.0×10^{-6} cm^2/s and 18.0×10^{-6} cm^2/s, respectively (Bowman 1984; Skagius and Neretnieks 1986). When a solution is placed in a porous medium and it diffuses into the matrix, the extent of matrix diffusion is represented by the dimensionless matrix diffusion parameter, Gamma, defined in Moench (1995, Table 1, p. 1826). It can be shown that for two tracers traveling in the same medium under the same testing configuration, the ratio of the dimensionless matrix diffusion parameter, Gamma, for the two tracers is the same as the ratio of their free-water molecular diffusion coefficients.

Figure 59 shows the effects on matrix diffusion, as represented by the two calculated BTCs, of changing the free-water diffusion coefficient by a factor of 10 for a fixed storage porosity of 0.001 and the fixed flow rate of the test. The effect of increasing the free-water diffusion coefficient, which increases Gamma, is a delay of the calculated BTC for higher Gamma relative to the BTC for lower Gamma. This "differential matrix diffusion delay" is seen as a horizontal offset between the two calculated BTCs in Figure 59 and later figures. The bigger the difference in Gamma between the two curves, the bigger the differential matrix diffusion delay.

In addition, it is seen from a comparison of Figures 59 and 60 that this differential matrix diffusion delay for a particular pair of free-water diffusion coefficients (or Gamma values) increases with increasing storage porosity. Figure 60, which uses the same pair of Gamma

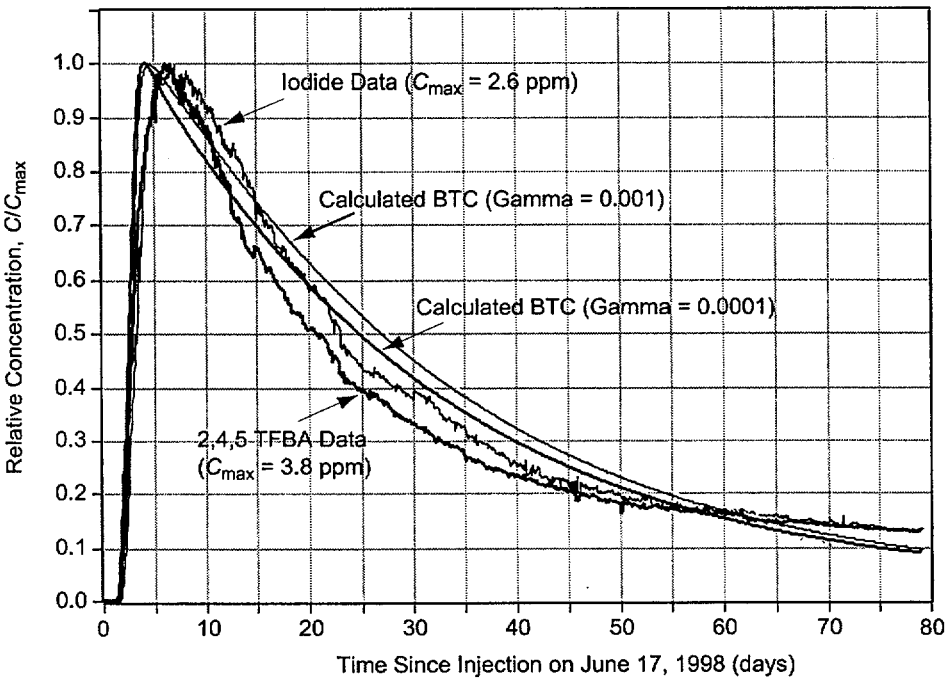

NOTE: The breakthrough curves were matched by the dual-porosity, partial-recirculation solution derived from Moench (1995) with storage porosity of 0.001 and dimensionless diffusion coefficients, Gamma, of 0.0001 and 0.001. Three inter-streamline pathways were assumed with delay factors of 2.01 days, 2.9 days, and 3.11 days. The "initial" flow porosity = 0.00045, and longitudinal dispersivity = 0.27 m.

Figure 59. Breakthrough Curve for June 17, 1998, 2,4,5 TFBA and Iodide Tracer Test Matched with a Lower Storage Porosity and a Lower Diffusion Coefficient

values used in Figure 59, shows that when the storage porosity is increased from the 0.001 value of Figure 59 to 0.01, the differential matrix diffusion delay is markedly larger than what it is in Figure 59.

The 10 to 1 ratio of the free-water diffusion coefficient used for the two calculated BTCs shown in Figures 59 and 60 is larger than the ratio of 18 to 8 (i.e., 2.25 to 1) of the free-water diffusion coefficient of iodide relative to that of 2,4,5 TFBA. When the ratio in free-water diffusion coefficients of the two calculated BTCs is fixed at that of iodide and 2,4,5 TFBA, i.e., 2.25 to 1 (Gamma ratio of 0.001 to 0.000444), the results shown in Figures 61 and 62 are obtained. Figure 61 shows two calculated BTCs with Gamma values of 0.001 and 0.000444 for a storage porosity of 0.001, and Figure 62 shows two BTCs with the same Gamma values but for a storage porosity of 0.01. As in Figures 59 and 60, the effects of matrix diffusion, seen as the differential

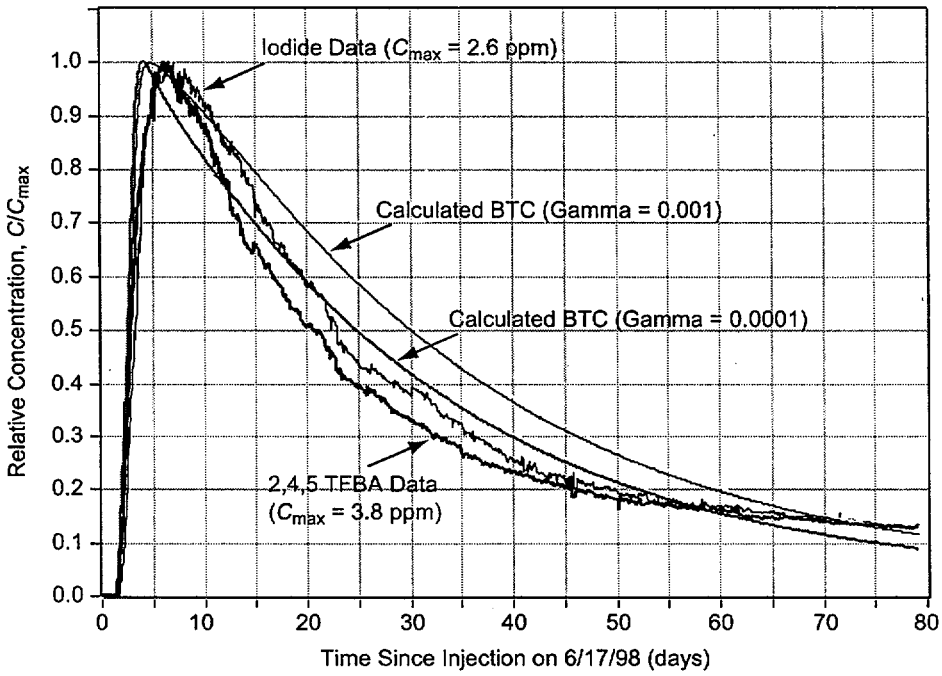

NOTE: The breakthrough curves were matched by the dual-porosity, partial-recirculation solution derived from Moench (1995) with storage porosity of 0.01 and dimensionless diffusion coefficients, Gamma, of 0.0001 and 0.001. Three inter-streamline pathways were assumed with delay factors of 2.01 days, 2.9 days, and 3.11 days. The "initial" flow porosity = 0.00045, and longitudinal dispersivity = 0.27 m.

Figure 60. Breakthrough Curve for June 17, 1998, 2,4,5 TFBA and Iodide Tracer Test Matched with a Higher Storage Porosity and a Lower Diffusion Coefficient

matrix diffusion delay between calculated BTCs, increase with increasing storage porosity for the same pair of water-diffusion-coefficient values, or Gamma values. In contrast to Figures 59 and 60, the calculated BTCs in Figures 61 and 62 show smaller differential matrix diffusion delays for a particular storage porosity because of the smaller difference in the free-water diffusion coefficients, or in Gamma values, used for the two curves in each figure.

The differential matrix diffusion delay between calculated BTCs in Figure 62 is similar to that between the actual 2,4,5 TFBA and iodide, suggesting a storage porosity value of approximately 0.01. This result is combined with earlier ones to indicate a dual-porosity medium with a flow porosity of 0.00045 (which may represent three inter-streamline pathways of flow porosities ranging from 0.0002 to 0.0005), a storage porosity of 0.01, and a longitudinal dispersivity of 0.27 m. The flow porosity and longitudinal dispersivity characterize a flow network within this medium comprised of (1) continuous fractures and (2) discontinuous fractures with interconnecting segments of matrix. The storage fractures with interconnecting segments of matrix. The storage porosity characterizes a storage component of the conceptualized dual-porosity medium consisting of dead-end fractures and the part of the matrix not contributing to the flow network.

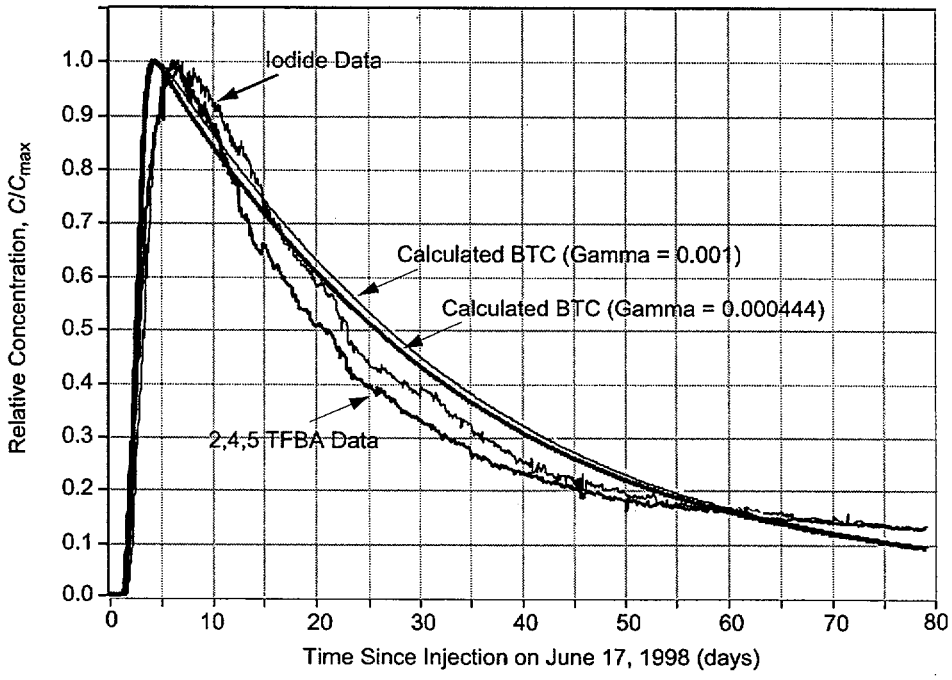

NOTE: The breakthrough curves were matched by the dual-porosity, partial-recirculation solution derived from Moench (1995) with storage porosity of 0.001 and dimensionless diffusion coefficients, Gamma, of 0.000444 and 0.001. Three inter-streamline pathways were assumed with fracture porosities of 0.0005, 0.0004, and 0.0002. The longitudinal dispersivity = 0.27 m (0.9 ft).

Figure 61. Breakthrough Curve for June 17, 1998, 2,4,5 TFBA and Iodide Tracer Test Matched with a Lower Storage Porosity and a Higher Diffusion Coefficient

3.2.2 2,3,4,5 Tetrafluorobenzoic Acid Test from C#1 to C#2

On July 31, 1998, the conservative tracer 2,3,4,5 tetrafluorobenzoic acid (2,3,4,5 TFBA) was injected in the Prow Pass interval of C#1 while C#2 continued to be pumped at the rate of approximately 4.35 gpm (0.33 L/s). Breakthrough of this tracer occurred on August 17, 1998 in the water pumped out of C#2, and the concentration eventually rose to a maximum of around 90 ppb, approximately 65 days after tracer injection (Figure 63). This tracer test has not yet been analyzed.

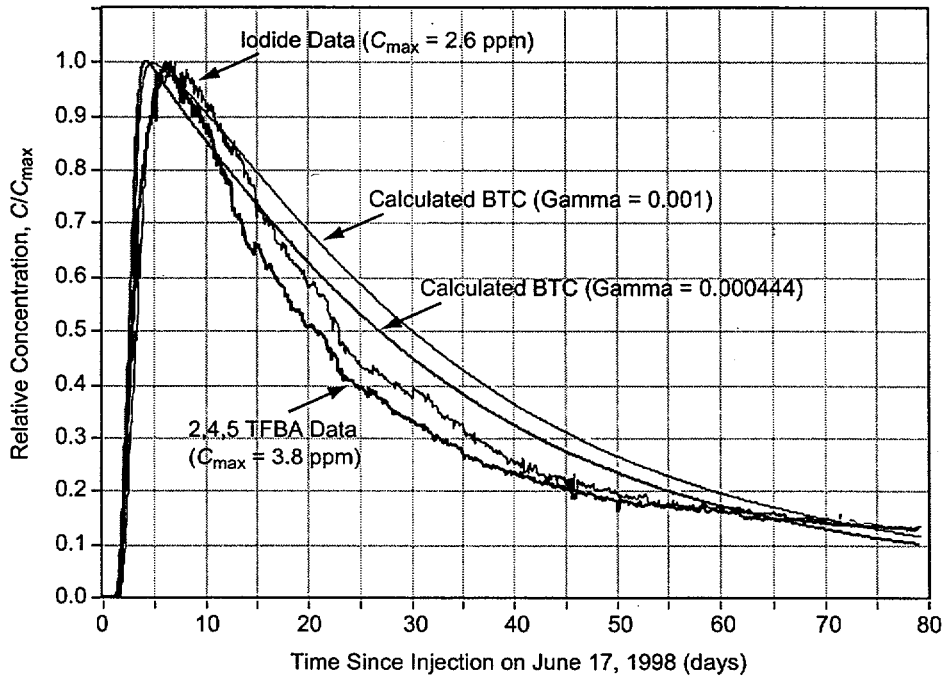

NOTE: The breakthrough curves were matched by the dual-porosity, partial-recirculation solution derived from Moench (1995) with storage porosity of 0.01 and dimensionless diffusion coefficients, Gamma, of 0.000444 and 0.001. Three inter-streamline pathways were assumed with delay factors of 2.01 days, 2.9 days, and 3.11 days. The "initial" flow porosity = 0.00045, and longitudinal dispersivity = 0.27 m.

Figure 62. Breakthrough Curve for June 17, 1998, 2,4,5 TFBA and Iodide Tracer Test Matched with a Higher Storage Porosity and a Higher Diffusion Coefficient

3.3 FLOW ANISOTROPY AT THE C-WELLS FROM CONSERVATIVE TRACER RESPONSES

The comparisons of tracer responses resulting from injections into well C#1 and into either well C#2 or C#3 (while pumping the other well) provided some insights into flow heterogeneity/ anisotropy at the C-wells. Table 12 lists the ratios of peak response times or first arrival times for conservative tracers between C#1 and the production well (either C#2 or C#3) and between C#2 and C#3 for all tests in which a comparison was possible. For a homogeneous, isotropic medium, the response times under radial flow conditions are expected to vary as R^2, the distance squared between injection and production well. The ratios of R^2 values corresponding to each case are also listed in Table 12. Note that the ratios of tracer response times and R^2 values are in reasonably good agreement in all three cases, suggesting that flow anisotropy at the C-wells may be relatively small despite the apparent orientation of the fracture network in the general direction of C#1 to C#2 (Geldon 1993).

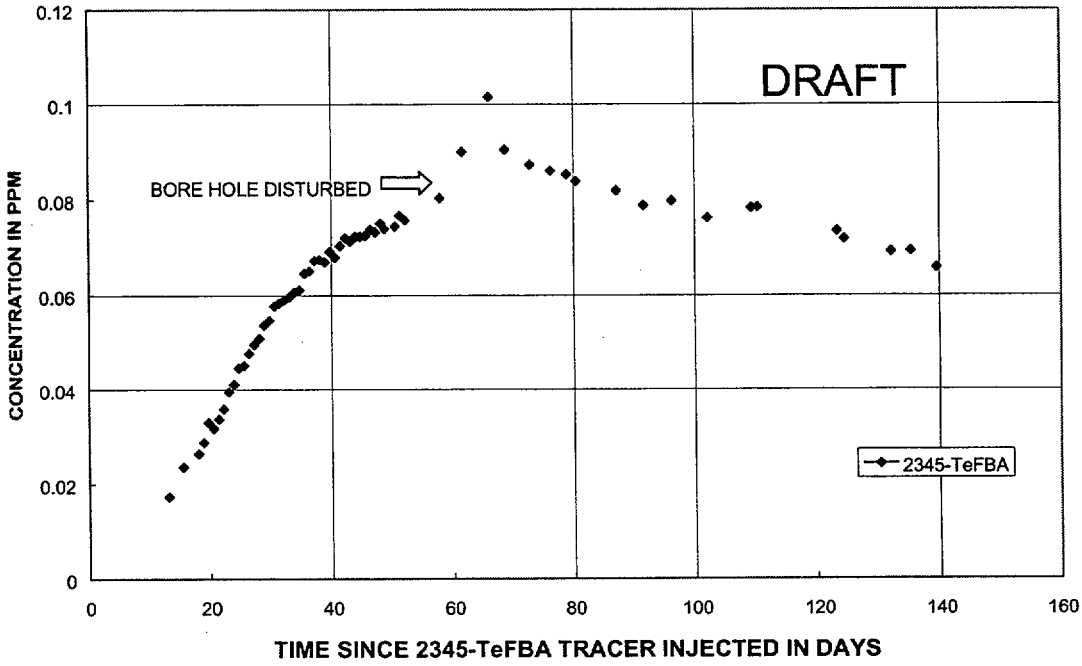

Figure 63. Breakthrough Curve for 2,3,4,5 TeFBA Tracer Test in Prow Pass from UE-25 c#1 to UE-25 c#2

Table 12. Ratios of Observed Tracer Arrival Times and Distances Squared for C-wells Tests

Tests	$Time_{C\#1}/Time_{C\#2\text{-}C\#3}$	$R^2_{C\#1}/R^2_{C\#2\text{-}C\#3}$
Bullfrog: PFBA (C#2) and iodide (C#1)[a]	6	7.4
Bullfrog: 2,6-DFBA (C#2) and pyridone (C#1)[b]	10	7.4
Prow Pass: iodide and 2,4,5-TFBA (C#3) and 2,3,4,5-TeFBA (C#1)[c]	10	8.3

NOTES: C#1, C#2, and C#3 are abbreviations for boreholes UE-25 c#1, UE-25 c#2, and UE-25 c#3. R^2 is the distance squared.

(a) Both tests conduced with 2.5 to 3.5% recirculation into injection well. Peak tracer arrivals compared.

(b) Both tests conduced with no recirculation. First tracer arrivals compared.

(c) C#3-to-C#2 test conduced with 30% recirculation; C#1-to-C#2 test conducted with no recirculation. Peak tracer arrivals compared.

3.4 SUMMARY OF CONCEPTUAL MODELS AND PARAMETERS

Uncertainty in the values of longitudinal dispersivity, flow porosity, and matrix porosity result from physical processes, such as the scale-dependence of dispersivity (when comparing tracer tests conducted from borehole C#1 to those conducted between boreholes C#2 and C#3), as well as from variability in the transport characteristics of the tracer materials. However, there is good agreement in dispersivity values obtained from tracer tests conducted between boreholes C#2 and C#3 in the Bullfrog and Tram intervals. Peclet numbers range from 11 to 15; therefore, the longitudinal dispersivities are similar (Table 13).

The breakthrough times are identical for the iodide and the DFBA tracer tests (Table 13), and the advective travel times are within 10 percent. Therefore, the inferred flow porosities are similar, which implies that similar flow pathways are used by the tracers in those tests. These differences can be explained by the different thicknesses of the zones tested: the iodide tracer test was conducted in the combined Bullfrog Tram zone, and the DFBA tracer test was conducted in the Lower Bullfrog zone.

The parameter estimates are robust because the visual-graphic fit is close to the PEST fit (which is based on the dual-porosity analytical model.) The differences are less than 5% for all parameters except matrix porosity, and these estimates vary by only 0.03 porosity units.

The estimated flow porosities suggest that the pathways between boreholes C#2 and C#3 in the Bullfrog and Tram intervals are not well-connected. This possibility is supported by the interpretation of the higher-than-expected flow porosities for the Bullfrog and Tram Tuffs. The microsphere responses (Section 3.5) are consistent with this interpretation. The arrival of the microspheres at the recovery borehole indicates the existence of a connected pathway, somewhere, with an aperture at least 0.36 μm wide. However, the small recovery of the microspheres (Section 3.5) also suggests poorly-connected/tortuous pathways or dead-ended flow pathways.

Table 13. Summary of Results and Transport Properties for the Bullfrog and Tram Tuffs

	Iodide test from C#2 to C#3 in Bullfrog-Tram	DFBA test from C#2 to C#3 in Lower Bullfrog	Pyridone test from C#1 to C#3 in Lower Bullfrog
Breakthrough (days)	5.07	5.07	56.3
Peak concentration (μg/L)	99.5	251	0.210 (current value)
Peclet number	11	12–15	11
Dispersivity (m)	2.6	2.4–1.9	6.2
Flow porosity, ϕ_f (%)	8.6	9.9–7.2	NA
Matrix (or storage) porosity, ϕ (%)	19	8.8–13.2	NA

NOTES: NA: the value is not available.

C#1, C#2, and C#3 are abbreviations for boreholes UE-25 c#1, UE-25 c#2, and UE-25 c#3, respectively.

The estimates of flow porosity cannot be separated from the parameter h, which represents a uniform aquifer thickness. In conducting tracer tests in isolated, permeable intervals in fractured rock, it is difficult to identify a meaningful thickness because transport occurs through an interconnected network of fractures. For this report, we have assumed that the appropriate thickness is the effective thickness as previously reported in Geldon (1996).

This report presents the first unequivocal testing from borehole C#1 to C#3 in the Lower Bullfrog test, and to C#2 in the Prow Pass test. The preliminary results suggest that the arrival time from C#1 to C#3, 56.3 days, is consistent with the arrival time from C#2 to C#3, 5.07 days, because, as implemented in the Moench solution, the arrival time is directly proportional to the square of the distance between injection and pumping wells.

Tracer testing in the Prow Pass interval (Table 14) showed different transport characteristics than those obtained in the Bullfrog and Tram intervals. The flow porosity was found to be 0.045% in the Prow Pass as opposed to 7.2 to 9.9% in the Bullfrog and Tram Tuffs (Table 13). This result indicates that the flow network in the Prow Pass is dominated by interconnected fractures (fracture porosity is in the range from 0.001% to 1%), whereas in the Bullfrog and Tram, it was dominated by discontinuous fractures with interconnecting segments of matrix.

Longitudinal dispersivity in the Prow Pass Tuff testing at the scale of the distance between C#2 and C#3 was calculated as 0.27 m, whereas it was 1.9 to 2.6 m in the Bullfrog and Tram intervals at the same scale. A relatively small dispersivity is consistent with a flow network dominated by interconnected fractures (Prow Pass), and a relatively large dispersivity is consistent with a flow network dominated by discontinuous fractures with interconnecting segments of matrix (Bullfrog and Tram) because the more the actual microscopic flow pathways are different from the macroscopic, averaged, flow pathway, the larger is the longitudinal dispersivity. Clearly, a flow network dominated by discontinuous fractures with interconnecting segments of matrix (Bullfrog and Tram) would have more microscopic flow pathways than a flow network dominated by interconnected fractures (Prow Pass).

The storage porosity (or matrix porosity) calculated for the Prow Pass Tuff was 1% (Table 14) whereas it was 8.8 to 19% for the Bullfrog and Tram (Table 13). A small storage porosity is consistent with a dual-porosity medium dominated by interconnected fractures (Prow Pass). In such a medium, the storage component, which is assumed to consist of dead-end fractures and the part of the matrix not contributing to the flow network, would be dominated by fractures, which have very small porosities. Similarly, a large storage porosity is consistent with a dual-porosity medium dominated by discontinuous fractures with interconnecting segments of matrix (Bullfrog and Tram). In such a medium, the porosity of the storage component (dead-end fractures and the part of the matrix not contributing to the flow network) would be dominated by the large porosity of the matrix component of storage.

Table 14. Summary of Results and Transport Properties in a Partly Recirculating Tracer Test from Boreholes C#3 to C#2 and from Boreholes C#1 to C#2, Prow Pass Tuff

Parameter	2,4,5 TFA & Iodide: C#3 to C#2	2,3,4,5 TeFBA: C#1 to C#2	Single-Porosity, Partial-Recirc. Solution: 2,4,5 DFBA: C#3 to C#2	Dual-Porosity, Partial-Recirc. Solution: 2,4,5 DFBA: C#3 to C#2
Breakthrough (days)	1.67	17		
Peak concentration (ppm)	TFBA : 3.7 Iodide : 2.7	0.09		
Longitudinal dispersivity (m)	(last 2 columns)		0.27	0.27
Peclet number	(last 2 columns)		107.4	107.4
Flow porosity, ϕ_f (%)	(last 2 columns)		0.045	0.045
Gamma (dimensionless matrix diffusion coefficient)	(last column)			0.000444–0.001
Storage porosity, ϕ (%)	(last column)			1.0

NOTE: C#1, C#2, and C#3 are abbreviations for boreholes UE-25 c#1, UE-25 c#2, and UE-25 c#3, respectively.

3.5 MULTIPLE TRACER TESTS AT THE C-WELLS

3.5.1 Introduction and Objectives

This section describes the conduct and interpretation of two cross-hole tracer tests between C#2 and C#3 in which multiple solute tracers and colloid tracers (carboxylate-modified latex microspheres) were simultaneously injected. One test was conducted in the Lower Bullfrog Tuff and the other was conducted in the Prow Pass Tuff (referred to as the Bullfrog test and the Prow Pass test, respectively). The objectives of the multiple-tracer tests in the fractured tuffs at the C-wells included the following.

- Testing/validating the applicability of a dual-porosity conceptual transport model (see next section) in the saturated, fractured volcanic tuffs that underlie Yucca Mountain
- Obtaining estimates of key transport parameters in the flow system, including parameters for colloid transport
- Assessing the applicability of laboratory-derived tracer transport parameters to field-scale transport predictions.

The latter objective is important because radionuclides cannot be tested in the field, so favorable comparisons of laboratory- and field-scale transport of nonradioactive tracers can lend credibility to the practice of using laboratory-derived radionuclide transport parameters in field-scale predictive simulations.

This section also summarizes laboratory experiments that were conducted to support the C-wells field test interpretations and to provide the comparisons between laboratory-derived transport

parameters and field-scale transport parameters. Special emphasis is given to the sorption behavior of the lithium ion, which was used as a sorbing tracer in the field tracer tests.

3.5.2 Dual-Porosity Conceptual Transport Model

A consistent observation in all hydrogeologic units below the water table at the C-wells is that bulk permeabilities (determined from aquifer tests) exceed matrix permeabilities (determined from laboratory core measurements) by 2 to 6 orders of magnitude (Geldon 1993; Geldon 1996). This ratio of bulk to matrix permeabilities suggests that flow in the Miocene tuffs at the C-wells occurs predominantly in fractures. However, matrix porosities in the C-wells range from about 0.10 to 0.35 (Geldon 1993), so most of the water in these rocks is stored in the pores of the matrix. Radionuclide and tracer transport in fractures, therefore, could be attenuated by diffusive mass transfer between the fractures and the rock matrix, a process known as matrix diffusion. Matrix diffusion in fractured systems has been discussed and modeled at length by Neretnieks (1980), Grisak and Pickens (1980), Tang et al. (1981), Maloszewski and Zuber (1984; 1985), and Moench (1995). A system exhibiting fracture and matrix flow frequently is called a "dual-porosity, dual-permeability" system. When the matrix permeability is small compared to the fracture permeability (e.g., smaller by a factor of 100 or more), the matrix permeability can be assumed to be negligible in transport calculations, and the system is often referred to as simply a "dual-porosity" system. It has been suggested elsewhere that the saturated zone in the vicinity of Yucca Mountain should behave as a dual-porosity system (Robinson 1994). This concept has important transport implications, particularly for sorbing radionuclides, because it suggests that solutes moving through fractures will have access to a very large surface area for sorption once they diffuse out of fractures and into adjacent matrix pores.

3.5.3 Tracer Testing Strategy

To accomplish all of the test objectives mentioned in Section 3.5.1 in a reasonable time, cross-hole, forced-gradient tracer tests were conducted in which three different solute tracers having different physical and chemical properties were simultaneously injected into the lower Bullfrog and Prow Pass flow systems. By dissolving the tracers in the same solution and simultaneously introducing them, it was ensured that they all experienced the same flow field and, hence, followed identical flow pathways through the system. This assurrance is especially important in field tests where it can be extremely difficult to reproduce exactly flow conditions for different tracer injections because of equipment problems and possible irreversible changes in the system (e.g., well development, biofouling, unsteady drawdown, etc.). The test interpretations were then based on comparing the responses of the different tracers. The tracers used in each test included two nonsorbing solutes having different diffusion coefficients (bromide and penta-fluoro-benzoate) and a weakly-sorbing, ion-exchanging solute (lithium ion). Carboxylate-modified-latex polystyrene microspheres were also injected in both tests to serve as colloid tracers. These microspheres have negatively charged hydrophilic surfaces at pH > 5, which tends to minimize their attachment to rock surfaces (Reimus 1995). The properties of all tracers are summarized in Table 15 along with the injection masses and concentrations used in the tracer tests.

Table 15. Tracer Characteristics, Injection Masses, and Injection Concentrations in the Two Multiple-Tracer Tests

Solute Tracers			
Parameters	**PFBA**	**Bromide**	**Lithium**
Free water diffusion coefficient, D_f (cm^2/sec)[a]	7.2×10^{-6} [b]	2.1×10^{-5} [c]	1.0×10^{-5} [c]
Sorption	None	None	Weak (ion exchange)
Bullfrog test injection mass (kg)	12.1	165.6	14.34
Bullfrog test injection concentration (mg/L)[d]	1000	13800	1200
Prow Pass test injection mass (kg)	12.0	30.6	16.0[e]
Prow Pass test injection concentration (mg/L)[f]	2000	5100	2670

Caboxylate-Modified Polystyrene Latex (CML) Microsphere Tracers			
Tracer	**Test**	**Injection Amount**	**Injection Concentration**
0.36-µm CML microspheres (yellow)	Bullfrog	3.5×10^{14} spheres	5.8×10^{10} spheres/L
0.64-µm CML microspheres (blue)[g]	Prow Pass	3.0×10^{14} spheres	5.1×10^{10} spheres/L
0.28-µm CML microspheres (orange)[g]	Prow Pass	2.1×10^{14} spheres	3.5×10^{10} spheres/L
0.28-µm CML microspheres (yellow)	Prow Pass	2.1×10^{14} spheres	3.5×10^{10} spheres/L

NOTES: (a) Callahan et al. (2000) found that diffusion coefficients in rock matrices had the same ratio as free water diffusion coefficients for PFBA and bromide.

(b) Benson and Bowman (1994; 1996).

(c) Newman (1973); based on ionic conductances at infinite dilution.

(d) Tracers were dissolved in ~12,000 L of groundwater.

(e) Lithium was injected as 33.3 kg LiBr and 80.8 kg LiCl.

(f) Tracers were dissolved in ~6,000 L of groundwater.

(g) These microspheres were injected 2 days prior to solute tracers in the Prow Pass test.

The rationale for using multiple solute tracers in cross-hole tests is illustrated in Figure 64. The left plot of this figure shows hypothetical solute tracer responses (log normalized concentration versus log time) for a cross-hole tracer test with a short injection pulse in a single-porosity system. Note that there is no distinction between nonsorbing tracers with different diffusion coefficients in this plot because there is no secondary porosity for the tracers to diffuse into and, hence, no separation of their responses. The sorbing tracer response is delayed in time and lower in concentration than the nonsorbing tracers. In contrast, the right plot of Figure 64 shows hypothetical solute tracer responses for a test in a dual-porosity system. In this case, there is a separation between nonsorbing tracers with different diffusion coefficients, with the higher diffusivity tracer exhibiting a lower peak concentration and a longer tail than the lower diffusivity tracer. This separation occurs because the higher-diffusivity tracer diffuses more readily into the matrix than the lower-diffusivity tracer, resulting in a lower recovery at early times but a longer tail due to subsequent diffusion back out of the matrix after the tracer pulse has passed. Figure 64 also shows two possible responses for a sorbing tracer: (1) one with sorption occurring in the matrix and (2) one with sorption occurring in the fractures and the matrix (if the fractures have sorptive mineral coatings or are filled with sorptive granular material). Note that in the matrix-only case, the sorbing tracer response is attenuated in peak

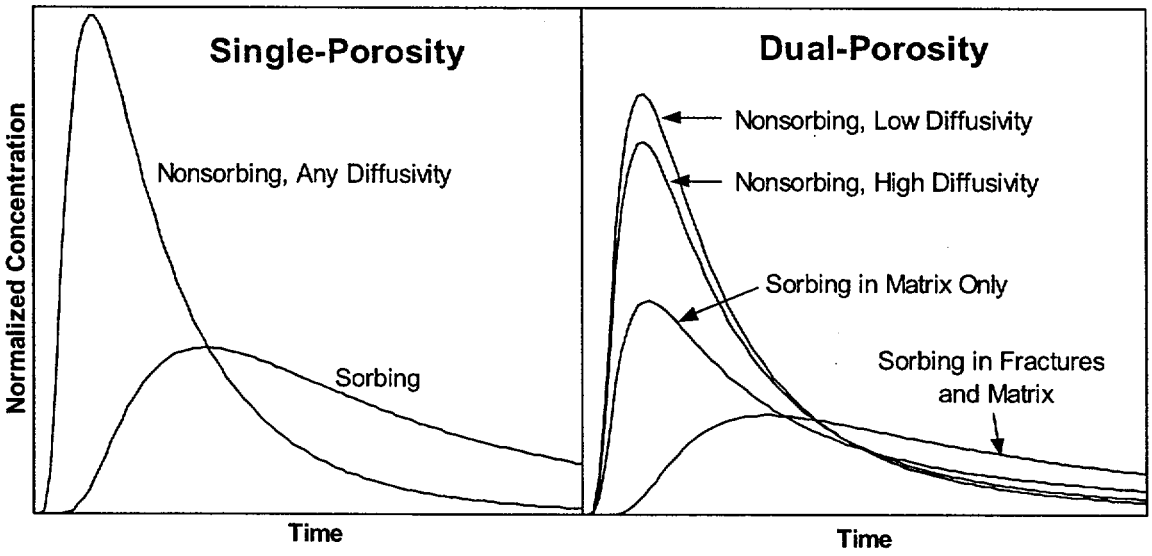

NOTE: The figure illustrates how multiple tracers can be used to distinguish between the two types of systems, that is, systems with single- and dual-porosity media. As cross-hole travel times increase, the lower peaks begin to arrive later than the higher peaks.

Figure 64. Hypothetical Cross-hole Responses of Tracers with Different Physical and Chemical Characteristics in Single- and Dual-Porosity Media

concentration but not significantly in time relative to the nonsorbing tracers, whereas in the latter case both a concentration and a time attenuation are apparent. The minimal time attenuation of the sorbing tracer relative to the nonsorbing tracers in the matrix-only sorption case is primarily a result of the relatively short duration of a typical cross-hole tracer test; as travel times increase, the time and concentration attenuation of a sorbing tracer relative to nonsorbing tracers should increase.

The hypothetical responses in Figure 64 suggest that a multiple tracer test involving the simultaneous injection of nonsorbing solute tracers with different diffusion coefficients and a sorbing tracer should allow qualitative discrimination between a single-porosity system and a dual-porosity system. That is, if nonsorbing tracers of different diffusion coefficients have different responses and/or if a sorbing tracer has a peak concentration that occurs at about the same time as a nonsorbing tracer but with a lower concentration, then a dual-porosity system is suggested. This approach was taken by Maloszewski et al. (1999), although they used only multiple nonsorbing tracers in a fractured sandstone/quartzite/slate system. Furthermore, if a dual-porosity response is observed and one knows the relative diffusion coefficients of the two nonsorbing tracers, it should be possible to determine how much of the apparent dispersion in the responses is due to true hydrodynamic dispersion and how much is due to matrix diffusion. Both of these processes have the effect of broadening the response curves/increasing the tailing of the tracers, but only matrix diffusion can cause a separation of the responses of the two tracers. The magnitude of the separation can be used to distinguish quantitatively between the effects of

matrix diffusion and hydrodynamic dispersion, resulting in unambiguous estimates of mean residence times, dispersion coefficients, and matrix diffusion parameters in a tracer test.

Effective sorption parameters associated with the response of a simultaneously injected sorbing tracer can then be estimated by assuming that the sorbing tracer experiences the same mean residence time, longitudinal dispersivity, and matrix diffusion (subject to its diffusion coefficient) as the nonsorbing tracers. In this case, only the sorption parameter(s) need be adjusted to obtain a model fit/match to the sorbing tracer response. Likewise, colloid filtration/attachment and detachment parameters can be obtained by assuming that the CML microspheres experience the same mean residence times and longitudinal dispersivities as the nonsorbing solute tracers. For the colloid tracers, matrix diffusion is assumed to be negligible because of their large size and small diffusivity relative to the solutes.

3.5.4 Conduct of Tracer Tests

The cross-hole tracer tests were conducted between wells C#2 and C#3, which are separated by about 30 m at the surface (Figure 1). C#2 was used as the tracer injection well and C#3 as the production well in the lower Bullfrog Tuff. In the Prow Pass Tuff, C#3 was the injection well, and C#2 was the production well. The natural gradient at the C-wells site, though quite flat, is believed to be oriented in the direction from C#3 to C#2 (Figure 1), so tracer movement in the Bullfrog test was against the gradient, and in the Prow Pass test, it was with the gradient. Prior to injecting tracers, a weak-dipole flow field was established in each test by reinjecting a fraction of the water pumped from the production well into the injection well. The production and reinjection flow rates are summarized in Table 16. The weak-dipole flow configuration was chosen over a convergent flow configuration (no recirculation) to ensure that tracers were "flushed" out of the injection wellbore instead of relying on the flow field induced by pumping the production well to draw tracers out of the wellbore. Pressure transducers continuously monitored pressures between the packers, above the upper packer, and below the lower packer in each well during the tests. Because of the drastic differences in transmissivity of the two test intervals, the water level drawdown in the Prow Pass interval (62 m) was over an order of magnitude greater than in the Bullfrog interval (5 m) despite the fact that the production rate in the Bullfrog test was ~30 times greater than in the Prow Pass test.

After establishing a reasonably steady weak-dipole flow field, as indicated by stable water levels in the packed-off intervals, the recirculation of produced water into the injection well was replaced by the injection of a groundwater solution containing the three solute tracers. The tracer solution was injected at the same flow rate as the recirculation and without any interruption to the flow, and when the injection was complete, recirculation was immediately resumed without interruption. Thus, there were no pressure or flow transients introduced to the system as a result of tracer injection. Recirculation of produced water was discontinued after 40 days in the Bullfrog test, but it was maintained throughout the Prow Pass test. The Bullfrog test was conducted for 337 days, and the Prow Pass test was conducted for 127 days.

Table 16. Average Production and Recirculation Rates During the Bullfrog and Prow Pass Tracer Tests and Summary of Flow Interruptions During the Prow Pass Test

Test	Production rate (L/min)	Recirculation rate (L/min)	Recirculation Ratio
Bullfrog	568	19 (zero after 40 days)	0.033
Prow Pass	19	5.7	0.3
Prow Pass Test Flow Interruptions:			
Interruption	**Flow Shut Off**	**Flow Turned On**	**Duration (hr)**
1	11/14/98, ~9:00 am	11/14/98, ~11:00 pm	~14
2	11/23/98, ~9:00 am	11/30/98, ~4:00 pm	~175
3	12/21/98, ~9:00 am	1/4/99, ~11:00 pm	~337

The Prow Pass test featured three different flow interruptions (two intentional) during the tailing portion of the test. The times and durations of these interruptions are summarized in Table 16. The first interruption was unplanned and occurred as a result of a diesel generator failure. The latter two interruptions were intentional and coincided with the Thanksgiving and Christmas-New Year's holiday breaks, respectively. In addition to the practical consideration of not staffing the remote field site over the holidays, these flow interruptions offered the opportunity to obtain independent confirmation of matrix diffusion in the flow system. If a flow interruption is introduced during the tailing portion of a tracer test in a dual-porosity medium when tracers are diffusing back out of the matrix, then an increase in tracer concentrations should result when flow is resumed.

Water samples were collected at the production well throughout both tests using an automatic sampler. The sampling interval was gradually increased as the tests progressed. Sampling of the injection interval was not possible in the Bullfrog test, but a sampling loop that was designed to continuously mix the injection interval in C#3 was implemented in the Prow Pass test. Unfortunately, the submersible pump used to bring water to the surface generated more heat than could be efficiently removed from the loop, so the use of the loop for mixing had to be abandoned to prevent overheating of the downhole instrumentation. However, the loop was used 40 days into the Prow Pass test to obtain samples over a 10-hr period to assess how well the injection wellbore had been purged of tracers by the reinjection of production water.

Groundwater samples were analyzed for bromide (Br^-) by liquid chromatography (with a conductivity detector) and for lithium (Li^+) by inductively-coupled-plasma, atomic-emission-spectroscopy (ICP-AES) at LANL. Pentafluorobenzoate (or PFBA) was analyzed by HPLC (with a UV absorbance detector), also at Los Alamos.

3.5.5 Tracer Test Results

Figure 65 shows the normalized concentrations of the three solute tracers at the production well as a function of time during the Bullfrog test. All concentrations are normalized to the injection masses of tracers (μg/L-kg injected or $L^{-1} \times 10^9$). The axes in Figure 65 have logarithmic scales so that the details of the BTCs can be seen throughout the entire test. The fractional recoveries of the tracers were 0.69 for both bromide and PFBA, and 0.39 for lithium. Figure 66 shows the response of the 360-nm diameter CML microspheres relative to the PFBA response in the

Bullfrog tracer test. It is apparent that while the microspheres arrived slightly earlier than the PFBA, they were significantly attenuated relative to the PFBA throughout the test. The fractional recovery of microspheres during the test was 0.15.

The most striking feature of the tracer BTCs (Figures 65 and 66) is their bimodal shape. It is believed that the double-peak responses were the result of at least two distinct fracture-flow pathways between the injection and production wells that were located at different depths within the relatively long (~100 m) test interval. The flow survey information in Figure 2 suggests that there were probably two principal zones of outflow during tracer injection and recirculation in C#2 (see the triangles indicating percentages of flow during open-hole pumping). Because of the lack of mixing in the injection interval, the tracer solutions, which were injected directly below the top packer and were ~2% more dense than the groundwater, probably sank rapidly to the bottom of the interval. Under these conditions, the majority of the tracer mass would be expected to exit C#2 from the lower flow zone; and, indeed, the majority of the tracer mass (60%) was associated with the second tracer peak. The first peak was apparently the result of a small percentage (~12%) of the tracer mass exiting C#2 from the upper flow zone. This zone was apparently more conductive (as suggested by the greater percentage of flow during open-hole pumping) and much better connected hydraulically to C#3 than the lower zone, as the travel time between the wells in this zone was much shorter. Additional evidence to support this hypothesis is obtained by comparing the PFBA response of Figure 65 with the response of the same tracer injected into C#2 six months prior to the start of the multiple tracer test. Figure 67 shows that the PFBA BTC in the earlier test was a more conventional single-peak response with a peak arrival time that coincided with the arrival time of the second peak in the latter test. The earlier test was conducted in the same interval between C#2 and C#3 and under the same flow conditions as the multiple-tracer test. The only noteworthy difference between the two tests, besides the additional tracers in the second test, was that only ~1000 L of tracer solution was injected in the first test, whereas ~12,000 L was injected in the second. The larger volume in the second test was due to the large mass of LiBr that was dissolved to ensure a quantifiable response of lithium ion. Given that the volume of the injection interval (volume between the two packers) was ~4300 L, it seems logical that the ~1000 L of tracer solution injected in the first test would have sunk rapidly and exited the borehole via only the lower flow zone. In contrast, the ~12,000 L of tracer solution injected in the second test (approximately 3 interval volumes) would have eventually "filled up" the interval, and a small fraction of the tracer mass apparently accessed the upper flow zone.

PFBA concentrations in the earlier test were monitored for just over 3000 hr with a total fractional recovery of 0.73; at 3000 hr into the second test, the total PFBA fractional recovery was 0.58. Thus, the tracer recovery in the former test was actually higher than in the latter test despite the early tracer arrival in the latter test. This observation, plus the fact that the shapes of the common peaks of the two tests are different, suggest that a considerable fraction of the mass injected in the latter test followed additional pathways that were not accessed in the first test.

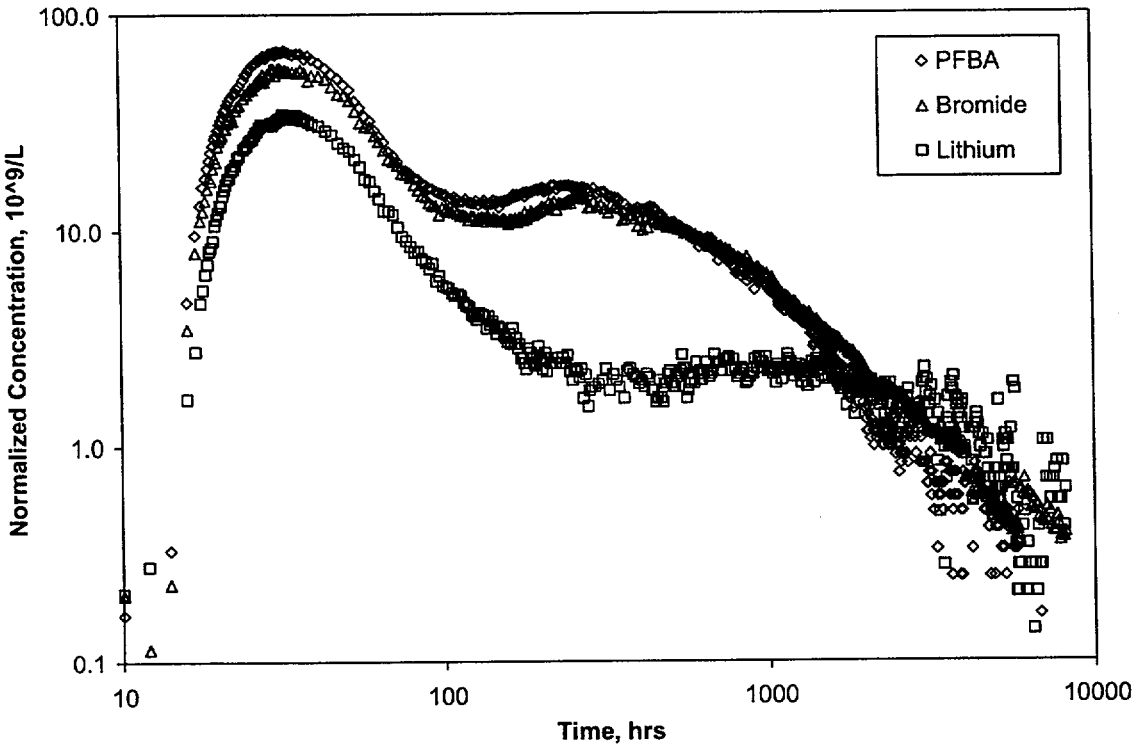

NOTE: Log-log scales are used for the axes so that the bimodal nature of the tracer responses can be seen more clearly.

Figure 65. Normalized Tracer Concentrations Versus Time in the Bullfrog Tuff Tracer Test Conducted from October 1996 to September 1997

Figure 68 shows the normalized concentrations of the three solute tracers at the production well as a function of time during the Prow Pass test. In contrast to the Bullfrog test, the responses in this test had a more conventional single-peak shape. Figure 68 also shows that there was indeed an increase in the tracer concentrations upon resumption of flow after each of the three interruptions. The fractional recoveries of the solute tracers were 0.52 for PFBA, 0.43 for bromide, and 0.19 for lithium ion. Note that the axes in Figure 68 have a linear scale as opposed to the logarithmic scale used in Figure 65 for the Bullfrog test.

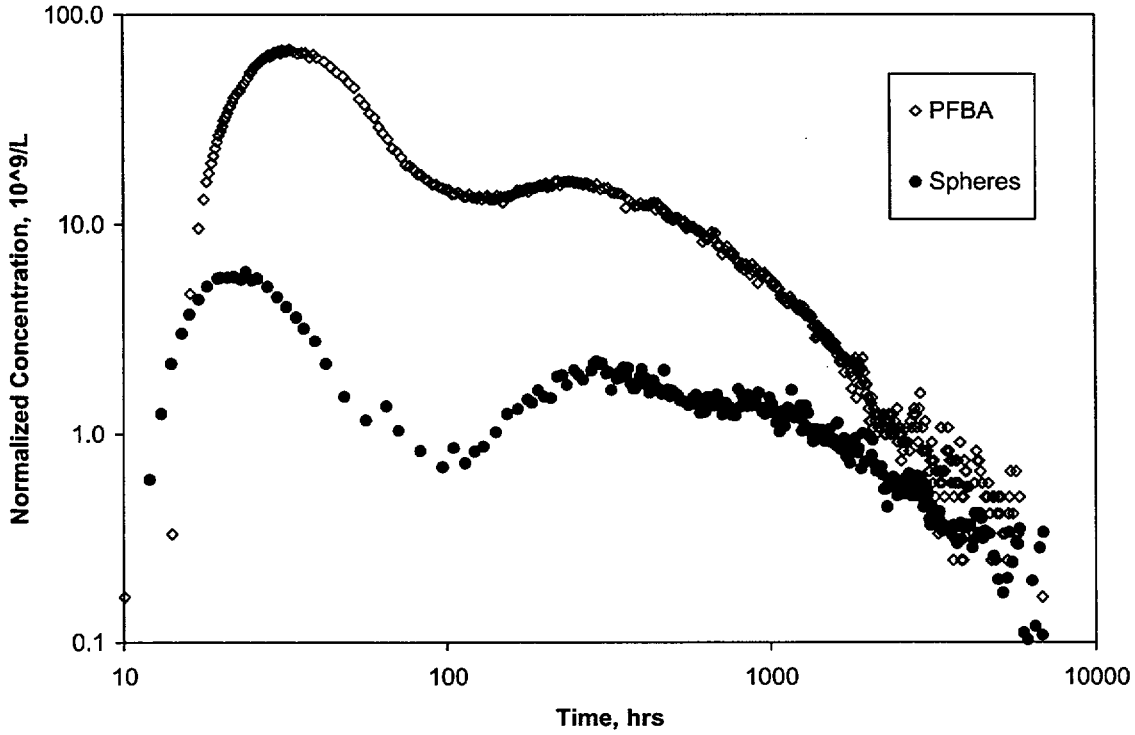

NOTE: Log-log scales are used for the axes so that the bimodal nature of the tracer responses can be seen more clearly.

Figure 66. Normalized Concentrations of PFBA and 360-nm-Diameter Carboxylate-Modified Polystyrene Latex Microspheres in the Bullfrog Tuff Tracer Test

It is apparent in both Figures 65 and 68 that there is considerable separation between the peak normalized concentrations of bromide and PFBA in the two tracer tests, with PFBA always having a higher normalized concentration in each peak. It is also apparent that the tails of the responses of these two tracers converge, with a suggestion of a crossover at late times. However, the appearance of a second peak in the Bullfrog test precluded a crossover after the first peak, and the Prow Pass test was not conducted long enough to see a definitive crossover. Referring to Figure 64, these BTC features are qualitatively consistent with a dual-porosity transport system. The lithium responses in the first peak of the Bullfrog test and in the Prow Pass test are highly attenuated in normalized concentration compared to the nonsorbing tracers, although they are not significantly attenuated in time. Again referring to Figure 64, these responses are qualitatively consistent with a dual-porosity transport system in which most of the sorption is occurring in the matrix (after diffusive mass transfer from the fractures), with possibly a small amount of sorption also occurring on fracture surfaces. In the case of the second peak in the Bullfrog test, the lithium response is attenuated both in concentration and in time, which is consistent with sorption occurring in both the matrix and on fracture surfaces.

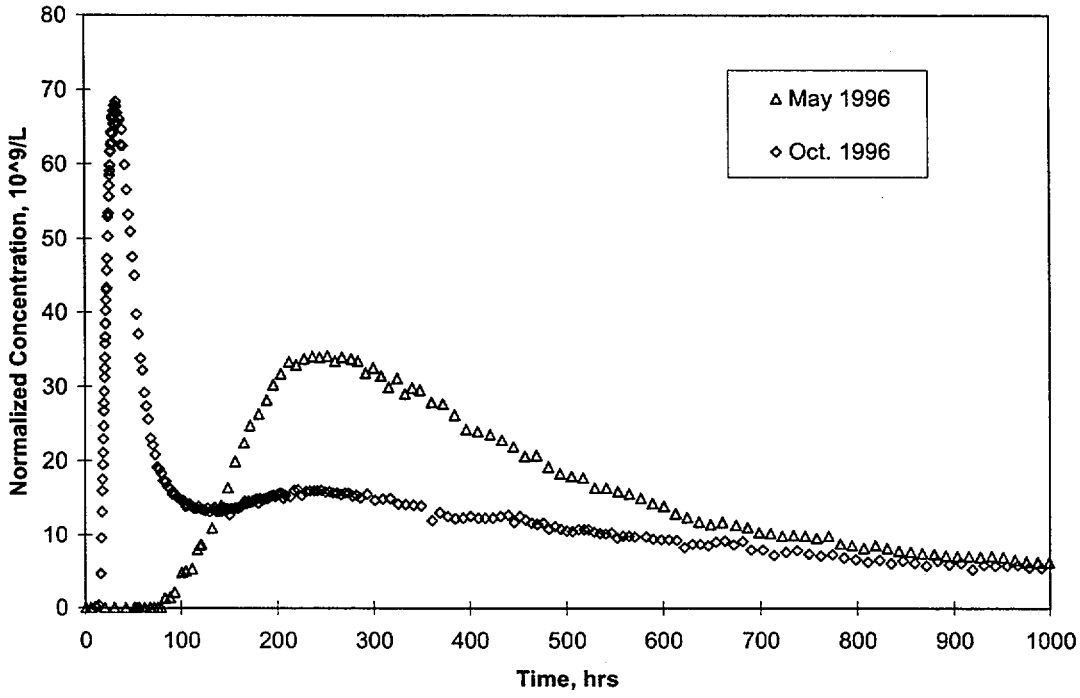

NOTE: The test conditions were the same in both tests, but the injection solution volume was ~1000 L in the May test and ~12,000 L in the October test.

Figure 67. Comparison of Normalized PFBA Responses in the Bullfrog Tuff Resulting from Tracer Injections in May 1996 and October 1996

The responses of the CML microspheres relative to PFBA in the Prow Pass test are shown in Figure 69, which has a logarithmic normalized concentration axis because of the very low normalized concentrations of the microspheres. The fractional recoveries of microspheres in this test were 0.0033 for the 640-nm-diameter spheres, 0.0012 for the 280-nm-diameter orange spheres, and effectively zero for the 280-nm-diameter yellow spheres. The response of the yellow spheres is not shown in Figure 69 because these microspheres effectively never arrived at the production well. The orange and blue microspheres were injected 2 days before the solutes, whereas the yellow microspheres were injected simultaneously with the solutes. It is likely that the high ionic strength of the injection solution (~0.4 M) caused the yellow microspheres to attach to rock surfaces much more readily than the other microspheres, which were injected in untraced groundwater (ionic strength = ~0.003 M). It is also interesting to note that the peak concentrations of blue and orange microspheres occurred at about the same time that solutes began arriving at C#2, and then the spheres rapidly decreased in concentration as the solute concentrations increased. This behavior may be purely coincidental, or it may hint that the increased ionic strength associated with the solutes caused the remaining spheres to attach more readily to rock surfaces. The microsphere "spikes" occurring at about 1000 hr into the test

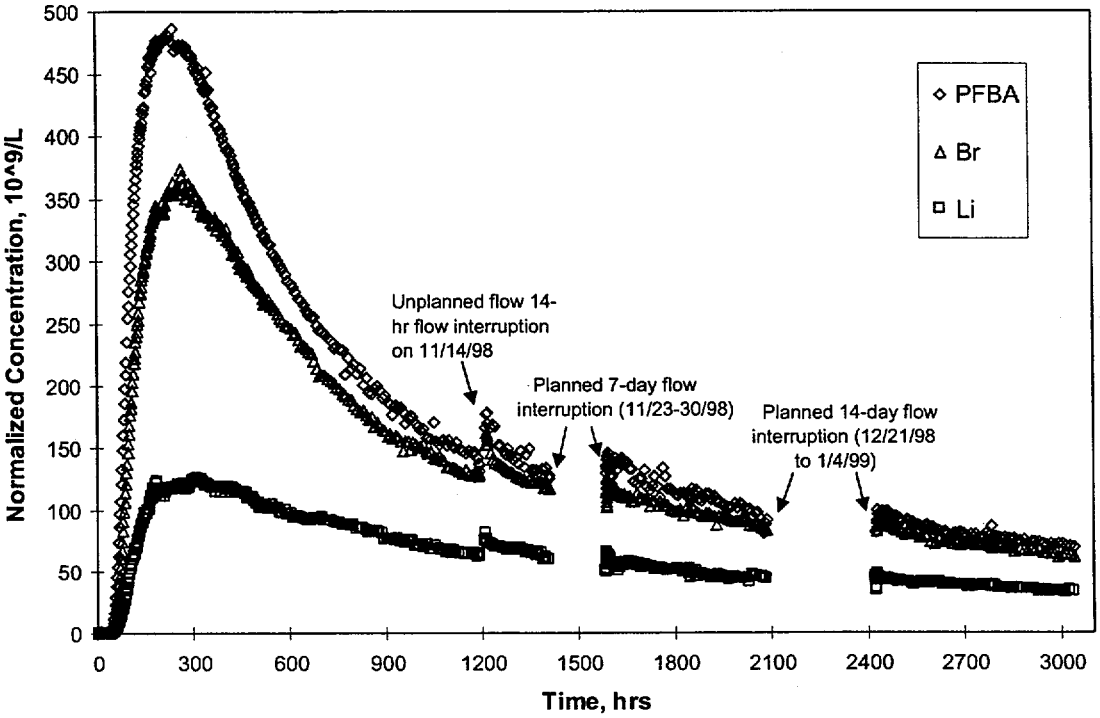

Figure 68. Normalized Tracer Concentrations Versus Time in the Prow Pass Tracer Test Conducted from September 1998 to January 1999

(Figure 69) actually correspond to a few days after the C#3 mixing/sampling loop was run, which suggests that the pressure and flow transients caused by the mixing may have mobilized/detached some microspheres. The timing of this response was consistent with the arrival time of the spheres after injection into C#3 on September 23, 1998. A second spike in sphere concentrations occurred the day after the unplanned flow interruption on November 14, 1998 (Figure 69), which further supports the hypothesis that flow and pressure transients may have resulted in microsphere detachment.

The sampling loop in C#3 in the Prow Pass test afforded the opportunity to see how well tracers had been "flushed" from the injection borehole after the test had been running for ~40 days. The sampling loop was run for ~11 hr, and over 50 samples were collected at the surface during this time. The "responses" from the injection interval are shown in Figure 70. These responses clearly indicate that there was a "slug" of concentrated tracer solution remaining in the interval and that this slug circulated around the sampling loop/borehole several times during the 11 hr of loop operation, dispersing as it circulated (indicated by the lowering and broadening of tracer peaks). Interestingly, the microspheres appear to precede the solutes each time the tracers cycle through the loop, which suggests that there was some as yet unexplained spatial separation of spheres and solutes in the borehole. The total mass of any given tracer associated with the slugs was less than 0.1% of the mass that was injected, so the injection interval had been reasonably well purged of all tracers. This result is important because it shows that the unaccounted-for

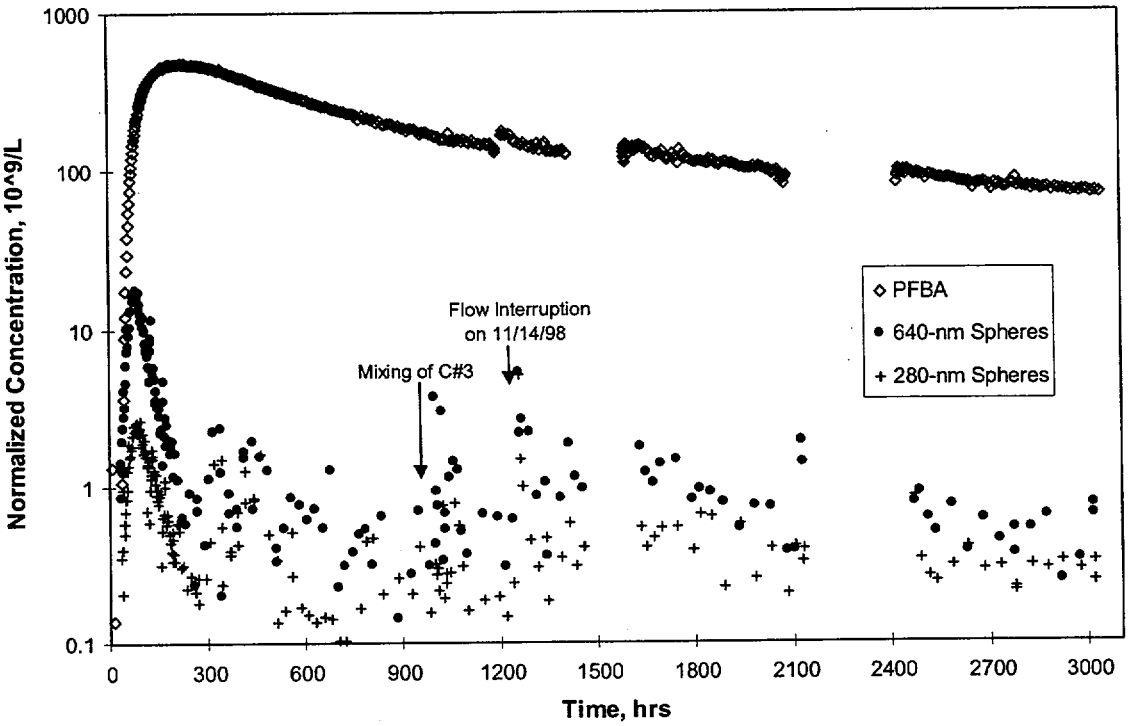

NOTE: The 280-nm-diameter spheres are the orange-dyed ones injected two days prior to the solutes. The yellow-dyed spheres that were injected with the solutes were not recovered.

Figure 69. Normalized Concentrations of PFBA and Carboxylate-Modified Polystyrene Latex Microspheres in the Prow Pass Tracer Test

tracer mass in the overall test is not the result of mass being left behind in the injection borehole, but rather it is mass that is being "lost" by other means (e.g., flow into the matrix that never makes it to the production borehole, stagnation points, losses due to density-driven flow). Given the flow rate through the sampling loop and the volumes of the injection interval and piping, the timing of the slug(s) suggested that they had been near the bottom of the interval where the pump intake was located. This result is consistent with the expectation that some of the dense tracer solution would have sunk to the bottom of the interval and remained there if there was no flow to push it out.

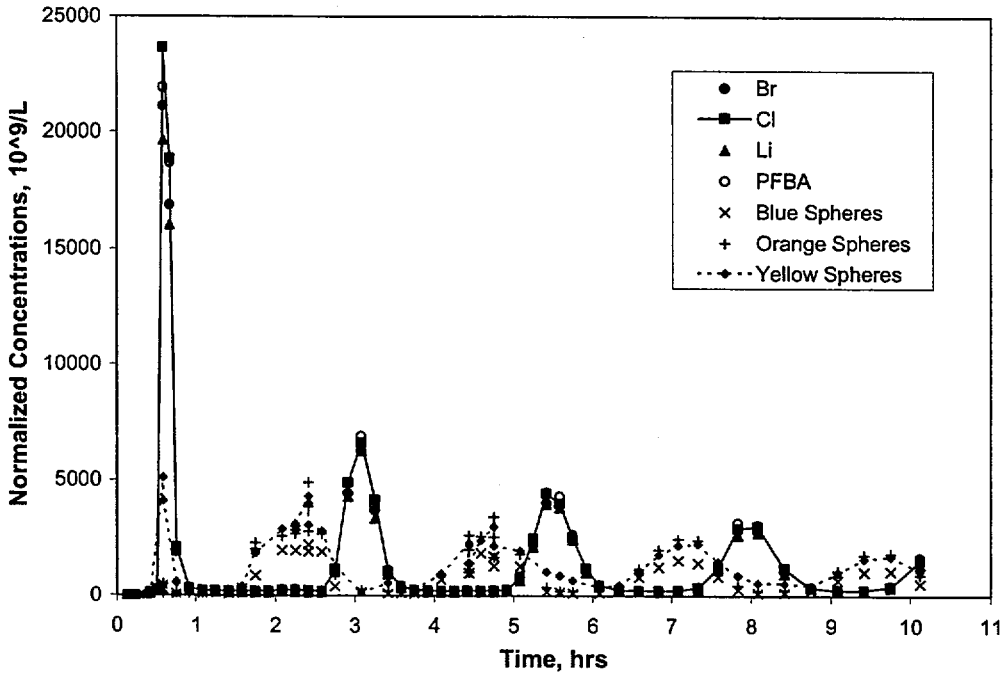

NOTE: The tracers remaining in the injection interval were apparently highly stratified, probably at the bottom of the interval. Total masses remaining in the injection interval were less than 0.1% of the total injection mass of each tracer.

Figure 70. Tracer Concentrations Mixing Loop 40 Days After Tracer Injection in UE-25 c#3 in the Prow Pass Tracer Test

3.5.6 Tracer Test Interpretive Modeling Approach

3.5.6.1 Solute Tracers

To obtain estimates of solute transport parameters in the flow system, the semi-analytical dual-porosity transport model RELAP (REactive transport LAPlace transform inversion computer code) was used to fit simultaneously the solute tracer responses. RELAP, which is described in detail by Reimus and Haga (1999), essentially combines the Laplace-domain dual-porosity transport equations derived by Maloszewski and Zuber (1984; 1985) (modified to account for linear sorption) with Laplace-domain transfer functions that describe a finite-pulse injection, wellbore mixing, and recirculation. Similar approaches have been used by others (Moench, 1989, 1995; Becker and Charbeneau 2000). Maloszewski and Zuber (1984; 1985) assumed that tracer transport in fractures was described by the one-dimensional (1-D) advection-dispersion equation with 1-D diffusion occurring into the surrounding matrix perpendicular to the flow direction in fractures. This simplified flow-system geometry assumed by RELAP is shown in Figure 71. The model assumes parallel-plate fractures of constant aperture and constant spacing, no concentration gradients across the fracture aperture, and a steady flow rate in fractures.

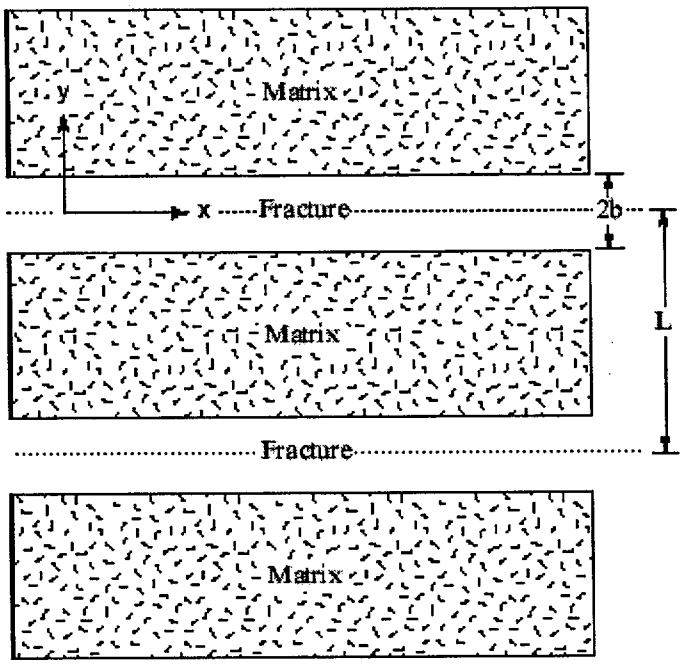

Figure 71. System Geometry Assumed in the RELAP and MULTRAN Codes

The equations describing dual-porosity transport under these conditions are the following (based on Maloszewski and Zuber (1984).

Fracture:

$$R_f \frac{\partial C_f}{\partial t} + v_f \frac{\partial C_f}{\partial x} - D_f \frac{\partial^2 C_f}{\partial x^2} - \frac{\phi D_m}{b\eta} \frac{\partial C_m}{\partial y}\bigg|_{y=b} = 0 \qquad \text{(Eq. 5)}$$

Matrix:

$$R_m \frac{\partial C_m}{\partial t} - D_m \frac{\partial^2 C_m}{\partial y^2} = 0 \qquad \text{(Eq. 6)}$$

subject to the following initial and boundary conditions

$$C_f(x,0) = 0 \qquad \text{(Eq. 5a)}$$

$$C_f(x,0) = C_i \text{ from } t = 0 \text{ to } t = t_{pulse} \text{ (i.e., Pulse Input)} \qquad \text{(Eq. 5b)}$$

$$C_f(\infty,t) = 0 \qquad \text{(Eq. 5c)}$$

$$C_m(y,x,0) = 0 \qquad \text{(Eq. 6a)}$$

$$C_m(b,x,t) = C_f(x,t) \qquad \text{(Eq. 6b)}$$

$$\frac{\partial C_m}{\partial y}\bigg|_{y=\frac{L}{2}} = 0 \qquad \text{(Eq. 6c)}$$

where

C_f = tracer concentration in solution in fractures, $\mu g/cm^3$

C_m = tracer concentration in solution in matrix, $\mu g/cm^3$

v_f = fluid velocity in fractures, cm/sec

D_f = dispersion coefficient in fractures, cm^2/sec

D_m = molecular diffusion coefficient in matrix, cm^2/sec

R_f = retardation factor in fractures = $1 + A_{sp} k_A$ (or $1 + \frac{2}{b} k_A$ for parallel-plate fractures)

R_m = retardation factor in matrix = $1 + \frac{\rho_B}{\phi} K_d$

K_d = sorption partition coefficient = mass of tracer sorbed per unit mass of aquifer material divided by solution concentration of tracer at equilibrium, cm^3/g

$k_A = K_d/A_{sp}$ surface-based sorption partition coefficient , cm^3/cm^2

A_{sp} = surface area per unit mass of material in fractures or on fracture walls, cm^2/g

ρ_f = bulk density in fractures, g/cm^3

ρ_B = bulk density in matrix, g/cm^3

η = porosity within fractures

ϕ = matrix porosity

b = fracture half aperture, cm

L = spacing between centerlines of adjacent fractures, cm.

The transformation of Equations 5 and 6 to the Laplace domain and their subsequent solution in the Laplace domain and inversion of the solution back to the time domain are described by Reimus and Haga (1999). Note that Equations 5 and 6 reduce to a single-porosity system if the matrix porosity, ϕ, (or the matrix diffusion coefficient, D_m) is set equal to zero. RELAP provides a simultaneous least-squares fit to up to four tracer data sets by automatically adjusting the following model parameters (which arise from the dimensionless forms of the governing equations):

- the mean fluid residence time in fractures (τ)
- the Peclet number ($Pe = L/\alpha$, where L = distance between wells, m, and α = dispersivity in fractures, m)
- the mass fraction of tracers participating in the test (f)
- a matrix diffusion mass-transfer coefficient, $\frac{\phi}{b}\sqrt{D_m}$

- the characteristic fracture spacing, L
- the fracture retardation factor, R_f
- the matrix retardation factor, R_m.

The fractional mass participation (f) is used as an adjustable parameter because low mass recoveries are frequently observed in field tracer tests in fractured rock (e.g., Reimus and Haga 1999; Reimus et al. 2001), presumably due to (1) dense tracer solutions "sinking" out of the zone of influence of pumping, (2) a significant volumetric flow of tracer solution into the matrix within the injection wellbore (this tracer mass will not make it to the production well during the tracer test because of the very low flow velocities in the matrix), or (3) the loss of tracer mass due to stagnation points induced either by recirculation or by the superposition of the induced flow field on the ambient flow field. Although these phenomena can affect absolute tracer responses, they should not, in principle, affect the relative responses of different tracers that are injected simultaneously.

The interpretation of the tracer responses in each test involved first fitting the two nonsorbing tracer responses by simultaneously adjusting all of the parameters listed above with the constraint that the matrix diffusion coefficient, D_m, for bromide was three times that of PFBA (and therefore the matrix diffusion mass transfer coefficient, $\frac{\phi}{b}\sqrt{D_m}$, was ~1.7 times that of PFBA). This factor-of-three difference is based on literature data (Newman 1973; Benson and Bowman 1994; 1996) and the experimental diffusion cell results discussed in Section 3.9. R_f and R_m were held equal to 1 for the two nonsorbing tracers. This fitting procedure implicitly assumed that both tracers had exactly the same mean residence time, Peclet number, mass fraction participation, and characteristic fracture spacing during the tracer tests, which is justified because the tracers were injected simultaneously and, thus, should have experienced the same flow system and same flow conditions.

For the Bullfrog test, the two sets of tracer peaks were fitted sequentially with the second peak being fitted after accounting for the contribution of the tail from the first peak. The model parameters were allowed to vary independently for each peak, as the peaks were assumed to represent different flow pathways with different transport characteristics. Although the tracer injection duration in the Bullfrog test was about 10 hr, it was assumed that for the first peak there was a delay of 4 hr followed by a 6-hr injection of tracer into the pathways that resulted in the first peak. The rationale for this assumption was that there was no early peak in the earlier PFBA test (Figure 67), which involved an injection of less than one hour, so it seemed logical to assume that the earliest injected tracer solution did not follow the earliest-arriving pathways. A 4-hr delay time was chosen because the injected-tracer-solution volume exceeded the injection-interval volume by this time, and it was felt that this was a reasonable criterion for when at least a portion of the tracer solution should have begun moving through the early arriving pathways.

In contrast to the Bullfrog test, the fitting procedure for the Prow Pass test was very straightforward, as only one set of tracer peaks was observed. However, because RELAP is based on a semi-analytical Laplace transform inversion method, it was not capable of simulating the flow transients associated with the flow interruptions during the latter part of the test. To

simulate these transients, the code MULTRAN (multicomponent transport) was used. MULTRAN is an implicit alternating-direction, two-dimensional (2-D), finite-difference code that accounts for cation exchange (involving up to three exchanging cations), charge balance, and multicomponent diffusion in a dual-porosity transport system (see Section 3.10.2.2 for details). The best-fitting transport parameters obtained from RELAP fits to the tracer data up until the time of the flow interruptions were used in MULTRAN to extend the simulations throughout the entire test.

Once best simultaneous fits to the nonsorbing tracer responses in both tests were obtained, the lithium responses associated with each distinct tracer peak were fitted with RELAP by adjusting R_f and R_m while holding all other parameters equal to the values that provided the best fits to the nonsorbing tracers. However, D_m for lithium was assumed to be half that of bromide (and ~1.5 times that of PFBA), based on ionic conductances at infinite dilution (Newman 1973). Rate-limited sorption was not considered in the field tests because the response times were all quite long relative to typical rates of ion exchange.

RELAP provided a good match to the lithium response associated with the second peak in the Bullfrog test and also to the lithium response in the Prow Pass test. However, in the case of the first peak in the Bullfrog test, RELAP consistently overestimated the normalized concentrations in the lithium tail when the leading edge of the lithium response was fitted well. The inability to fit the response of an ion-exchanging tracer using a linear equilibrium sorption model (K_d model) had been previously encountered when trying to fit cation responses from both laboratory-scale fracture-transport experiments (Section 3.10.2) and crushed-rock column experiments (Section 3.10.1). In these previous studies, it was observed that cation-exchanging tracers transport more conservatively than K_d models predict when the tracer injection concentration is high relative to the ionic strength of the groundwater (that is, when the total cation equivalents in the system are dominated by the cation tracer). Under these conditions, some of the cation tracer mass tends to elute with the anion tracers to maintain local charge balance in the system. When tracer concentrations are sufficiently dilute, local charge balance can be maintained by exchanging cations, and a K_d model tends to approximate more closely the observed transport behavior. In the Bullfrog test, the injection concentration of lithium was ~0.1 M, whereas the ionic strength of the C-wells groundwater was ~0.003 M; therefore, the conditions of a very high cation injection concentration relative to the groundwater ionic strength were met. MULTRAN provided much better predictions of cation transport data in laboratory-scale dual-porosity systems under these conditions than RELAP because it explicitly accounts for ion-exchange reactions, multicomponent diffusion, and local charge balance (see Section 3.10.2.2). For this reason, MULTRAN was employed to match the lithium data in the first peak of the Bullfrog test using the mean residence time, Peclet number, and matrix-diffusion, mass-transfer coefficient obtained from the best RELAP fit to the conservative tracer data and allowing the lithium ion-exchange parameters to be varied to fit the lithium data. Lithium was assumed to exchange with sodium and calcium ions based on the results of cation exchange capacity (CEC) measurements conducted on C-wells tuffs (Section 3.8.2).

It should be noted that the relatively low tracer concentrations observed at the production well in the Bullfrog test do not necessarily reflect the concentrations that existed in the fractures in which transport occurred; it is very likely that a significant amount of dilution occurred in the production borehole. Thus, concentrations could have remained quite high in the fractures that

conducted tracers, satisfying conditions for quasi-conservative transport of the lithium ion. For the second lithium peak of the Bullfrog test and for the Prow Pass test, concentrations in the fractures apparently were dilute enough during the much longer residence times associated with these responses that the lithium transport behavior could be reasonably approximated by a K_d model.

3.5.6.2 Colloid Tracers (Microspheres)

As with the solutes, the microsphere responses in the tracer tests were interpreted using the RELAP code to fit the data. The differential equations used to describe microsphere transport were:

$$\frac{\partial C}{\partial t} + V\frac{\partial C}{\partial x} - D\frac{\partial^2 C}{\partial x^2} + k_{filt}C - k_{res}S = 0 \qquad \text{(Eq. 7)}$$

$$\frac{1}{b}\frac{\partial S}{\partial t} - k_{filt}C + k_{res}S = 0 \qquad \text{(Eq. 8)}$$

where

C = colloid concentration in solution, no./L

S = colloid concentration on surfaces, no./cm^2

V = flow velocity in fractures, cm/sec

D = dispersion coefficient, cm^2/sec

k_{filt} = filtration rate constant (1/sec) = λV, where λ = filtration coefficient (1/cm)

k_{res} = resuspension rate constant, 1/cm-sec

x, t = independent variables for distance and time, respectively.

These equations assume that microspheres are confined to fractures because they are too large to diffuse significantly into the porous rock matrix. The RELAP semi-analytical model is capable of representing Equations 7 and 8 by making use of its rate-limited sorption features and setting the matrix porosity equal to zero (to eliminate matrix diffusion). It was assumed that the mass fractions, mean residence times, and Peclet numbers that provided the best fits to the nonsorbing solute responses also applied to the microspheres. Thus, the only adjustable parameters in the analysis were a forward first-order filtration-rate constant and a first-order reverse-filtration-rate constant (also called a resuspension or detachment-rate constant).

Initially, attempts to fit the microsphere response associated with the first peak in the Bullfrog test were made by assuming only irreversible filtration with no resuspension/detachment. Although this approach was capable of fitting the timing and normalized concentration of the first microsphere peak, it resulted in a much shorter tail than the data indicated. Therefore, to account for the tail, a small fraction of the filtered microspheres was assumed to detach. A fit to the tail was obtained by adjusting both the fraction of spheres detaching and the detachment rate constant (only a single-forward filtration-rate constant was assumed for all the microspheres in the first peak).

A fit to the second microsphere peak in the Bullfrog test was obtained in the same manner. However, in this case, the forward filtration rate constant had to be adjusted large enough so that essentially all of the microspheres were filtered as they moved through the system. This approach was necessary because any microspheres moving through the system without being filtered were predicted to arrive too early to match the observed response (note that the second microsphere peak occurred after the second nonsorbing solute peaks; see Figure 66). Unfiltered spheres moving through the second set of pathways were predicted to arrive at about the same time as the low point in concentration between the two peaks. Thus, to account for the second microsphere peak, it was necessary to assume that a substantial fraction of the spheres in the second set of pathways were reversibly filtered. Unlike the first peak, however, it was not possible to fit the entire second peak using a single-detachment-rate constant. The peak itself was fit by assuming a fraction of the microspheres experienced one detachment rate, and the tail was fit by assuming a separate fraction experienced another detachment rate. The remaining microspheres were assumed to not detach at all. The forward rate constant associated with each of these mass fractions was set equal to the minimum rate constant necessary to ensure that nearly all of the microspheres were filtered before making it through the system.

In the Prow Pass test, only a single filtration and detachment-rate constant were needed to fit the responses of each microsphere, provided the "spikes" associated with the flow transients could be ignored. No attempt was made to fit these spikes.

3.5.7 Tracer Test Interpretations

3.5.7.1 Solute Tracers

The best RELAP/MULTRAN fits to the solute tracer BTCs in the Bullfrog test are shown in Figure 72. As discussed above, RELAP was used to fit the nonsorbing tracer responses and the lithium response in the second peak, and MULTRAN was used to fit the lithium response in the first peak (MULTRAN fits to the bromide and PFBA data are also shown for the first peak in Figure 72). The RELAP fits were obtained assuming a constant production rate of 568 L/min and a constant recirculation rate of 19 L/min (3.3% of production), despite the fact that recirculation in the field test was stopped after 40 days. Both tracer peaks occurred well before recirculation was terminated, so the only portion of the test that was incorrectly modeled was the latter tailing portion of the second peak. Separate simulations comparing the results of MULTRAN runs with and without recirculation after 40 days indicated that the assumption of continued recirculation after 40 days had negligible effect on the fits or the values of the fitted model parameters.

The best-fitting model parameters from RELAP for the Bullfrog test are listed in Table 17. Note that separate estimates of τ and Pe are provided, depending on whether linear flow (constant flow velocity between injection and production well) or radial flow (flow velocity inversely proportional to distance from production well) is assumed to occur in the test interval. RELAP is capable of providing estimates for these parameters under either assumption (the quality of the fits and the other model parameters are not affected). For radial flow, Equation 5 is converted to radial coordinates and solved in Laplace space using a method outlined by Becker and Charbeneau (2000). In a heterogeneous, confined aquifer, the flow velocity to a single

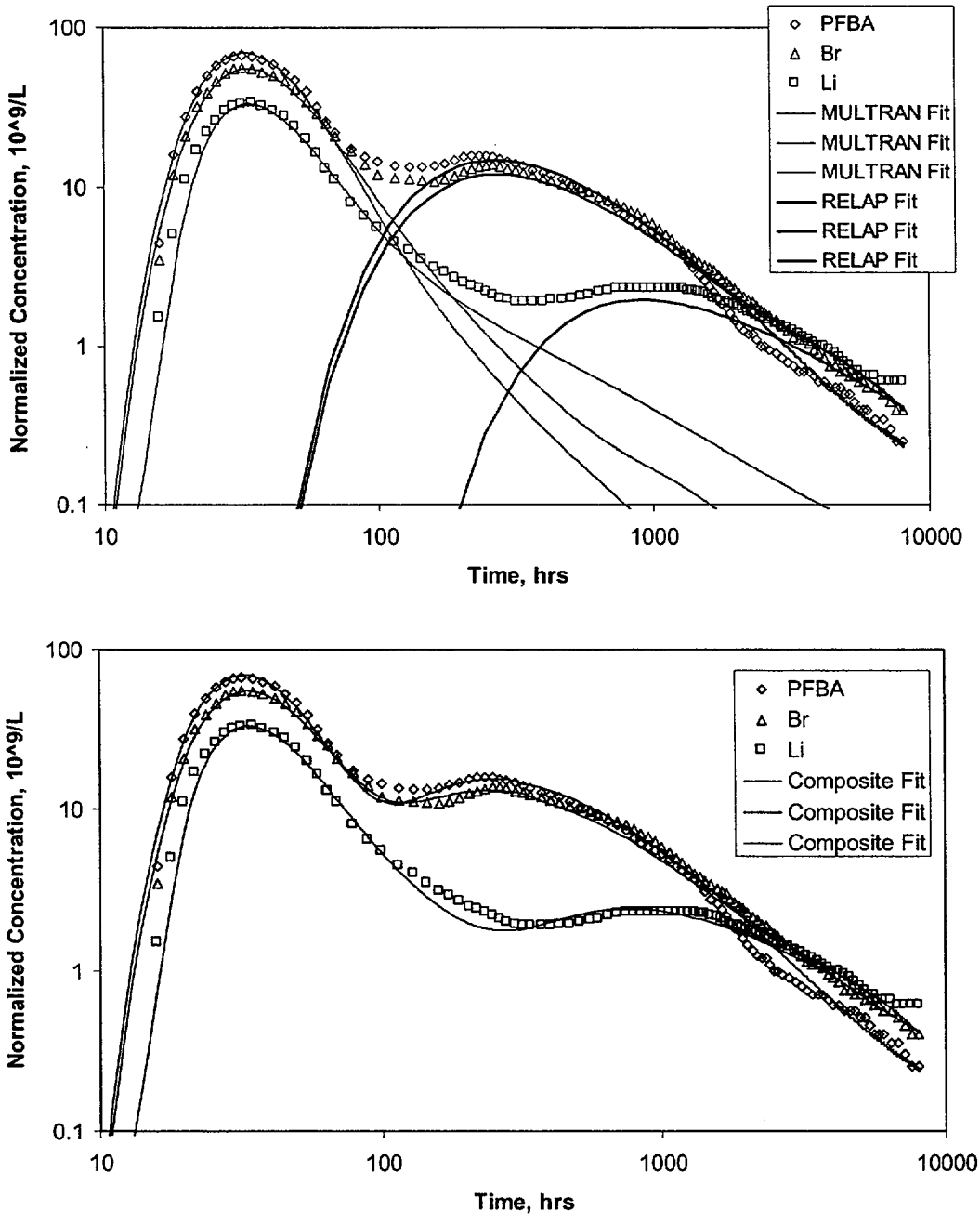

NOTE: The upper plot shows individual fits to first and second tracer peaks (MULTRAN and RELAP, respectively), and the lower plot shows composite fits. For clarity, the data points shown are a subset of the actual data. The best-fitting model parameters are provided in Table 17.

Figure 72. RELAP and MULTRAN Fits to the Tracer Response Curves in the Bullfrog Tuff Tracer Test

Table 17. RELAP Model Parameters Providing the Best Fits to the Bullfrog Tracer Test Data

Parameter	Pathway 1	Pathway 2
Mass fraction, f	0.115	0.60
Linear flow τ (hr)	36	1020
Peclet number, *Pe*, for linear flow	6.5	1.6
Radial flow τ (hr)	30	630
Peclet number, *Pe*, for radial flow	9.3	2.8
$\frac{\phi}{b}\sqrt{D_m}$ for bromide ($sec^{-1/2}$) [a]	0.0015	0.000469
Fracture spacing (cm)	∞ (2.4) [b]	4.4
Lithium fracture retardation factor	1	3
Lithium matrix retardation factor	7.5[c]	33

NOTES: Pathway 1 and Pathway 2 are associated with the first and second tracer peaks, respectively. The fits are shown in Figure 72 (MULTRAN was used to fit first lithium peak in Figure 72).

(a) The mass transfer coefficient, $MTC = \frac{\phi}{b}\sqrt{D_m}$, for PFBA is 0.577 times that for bromide.

(b) The number in parentheses is the minimum fracture spacing that yields the same results as an infinite fracture spacing.

(c) Lithium response associated with first tracer peak was poorly fitted by RELAP, so MULTRAN was used to obtain a better fit, which is shown in Figure 72.

production well with no recirculation into an injection well is expected to vary between linear and radial (National Research Council 1996). Thus, if it is assumed that the test interval was reasonably confined, presenting the two values of τ and *Pe* in Table 17 is a rough way of bounding these model parameter estimates as a result of flow-field uncertainty. Although the Bullfrog flow system was not perfectly confined, this approach should still yield reasonable bounds for τ and *Pe*, as the flow velocities in pathways carrying tracers from C#2 to C#3 should have started out relatively high due to the recirculation into C#2, gone through a minimum, and then increased again in the vicinity of C#3. Thus, the weak dipole should have resulted in a flow pattern that was intermediate between linear and radial flow.

Figure 73 shows the best RELAP/MULTRAN fits to the Prow Pass solute tracer test data, and Table 18 gives the best-fitting RELAP model parameters (obtained by simulating the first 1200 hr of the test, prior to the first flow interruption). MULTRAN was used after the first flow interruption to model the remainder of the test using the best-fitting parameters from RELAP to extend the simulations. Because the tracer concentrations were significantly higher in this test than in the Bullfrog test, it was possible to determine the responses of the cations (sodium and calcium) that exchanged with lithium during the test. (The background concentrations of the exchanging cations were too high relative to their signals in the Bullfrog test to determine their responses.) Figure 74 shows the responses of lithium, sodium, and calcium ions in the Prow Pass test, expressed as meq/L versus time. MULTRAN fits to the data are also included in Figure 74. Although not shown here, it was confirmed that the total cation and anion charges balanced each other, as they must, throughout the test.

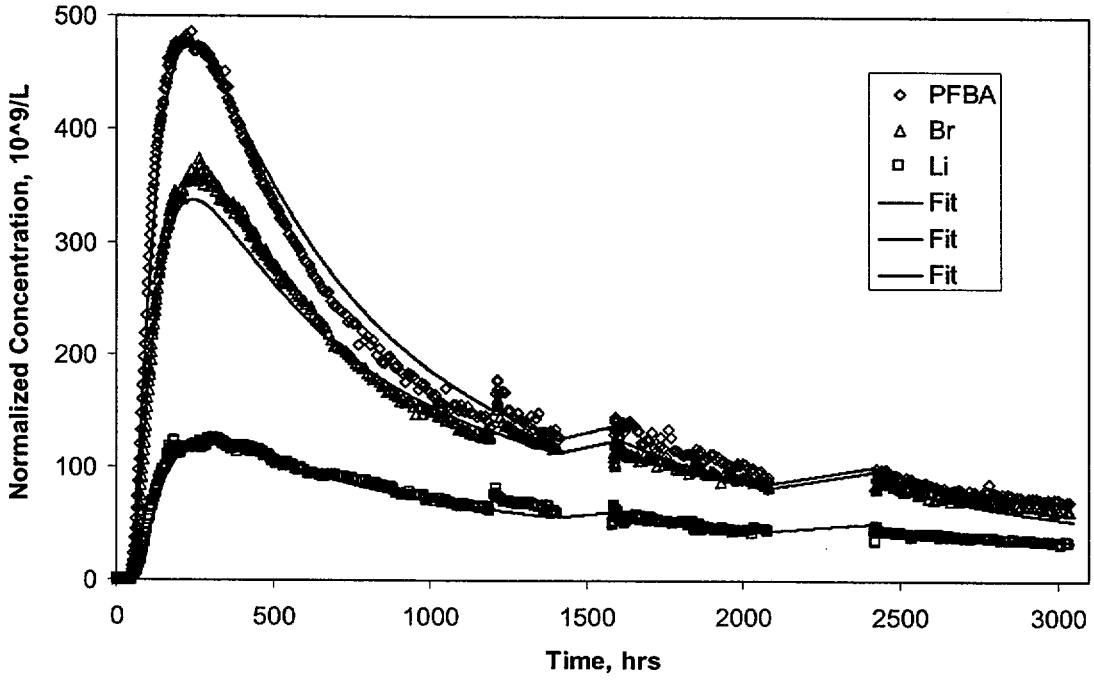

NOTE: The best-fitting model parameters are provided in Table 18.

Figure 73. RELAP/MULTRAN Fits to the Tracer Response Curves in the Prow Pass Tuff Tracer Test

3.5.7.2 Colloid Tracers (Microspheres)

The fit(s) to the Bullfrog test microsphere data are shown in Figure 75. The "pathways" labeled 1A and 1B represent the nondetaching and detaching fractions, respectively, of the microspheres following the pathway(s) that resulted in the first solute peak. Pathways 2A, 2B, and 2C in Figure 75 represent the nondetaching and the two detaching fractions of the microspheres following the pathway(s) that resulted in the second solute peak. The fitted mass fractions and filtration parameters associated with the "subpathways" in Figure 75 are given in Table 19.

Note that the predicted first arrival of microspheres precedes their actual first arrival by 2 to 3 hr. This result can be attributed to the fact that a 4-hr delay was not assumed for the injection of microspheres into the pathways that resulted in the first tracer peaks (as it was for the solutes). No delay was assumed for the microspheres because the microsphere injection began about 3.5 hr after the solutes were injected. If the solutes did not begin entering the pathways resulting in the first tracer peaks until after the microspheres were injected, then it would be reasonable to assume that the microspheres should have entered those pathways at the same time as the solutes.

Table 18. RELAP Model Parameters Providing the Best Fits to the First 1200 Hours of Prow Pass Tracer Test Data

Parameter	Parameter Value
Mass fraction, f	0.72
Linear flow τ (hr)	1210
Peclet number, *Pe*, for linear flow	1.3 [(a)]
Radial flow τ (hr)	610
Peclet number, *Pe*, for radial flow	4.8 [(a)]
$\frac{\phi}{b}\sqrt{D_m}$ for bromide ($sec^{-1/2}$) [(b)]	0.00095
Fracture spacing (cm)	∞ (6.4) [(c)]
Lithium fracture retardation factor	1
Lithium matrix retardation factor	11.5

NOTES: The fits (extended by MULTRAN simulations) are shown in Figure 73.

(a) The Peclet numbers were adjusted to correct for the theoretical dispersion caused by the partial recirculation flow field (see text). Peclet numbers obtained directly from RELAP were 0.9 (linear flow) and 1.9 (radial flow).

(b) The mass transfer coefficient, $MTC = \frac{\phi}{b}\sqrt{D_m}$, for PFBA is 0.577 times that for bromide.

(c) The number in parentheses is the minimum fracture spacing that yields the same results as infinite fracture spacing.

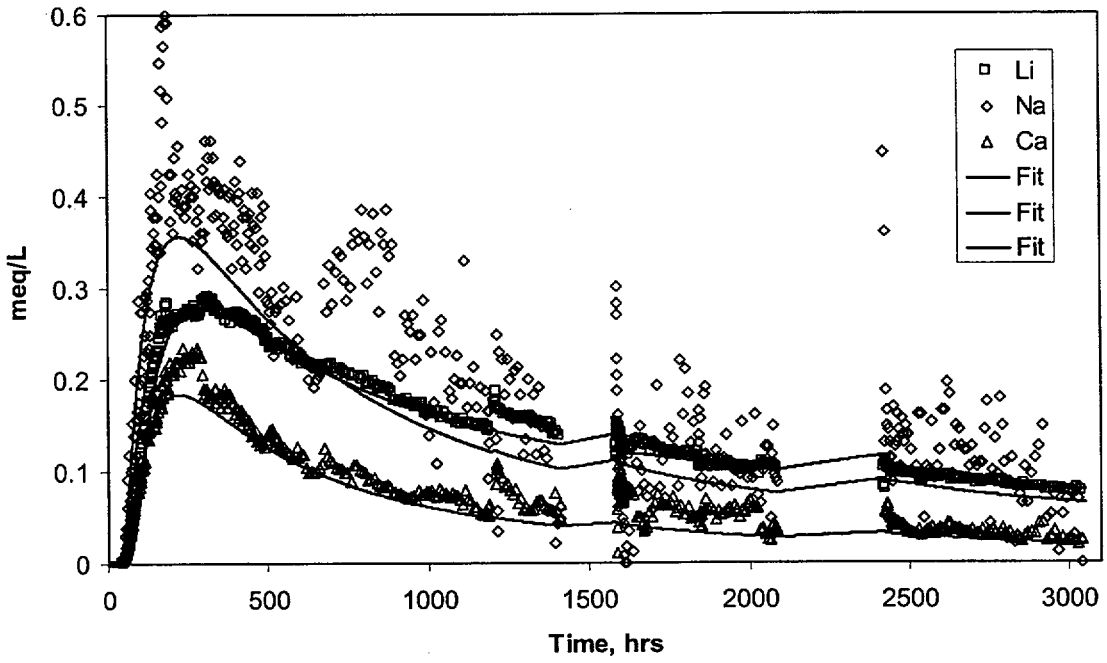

NOTE: Scatter for sodium is due to the background, which has been subtracted, being large relative to the signal.

Figure 74. MULTRAN Fits to Cation Responses in the Prow Pass Tracer Test

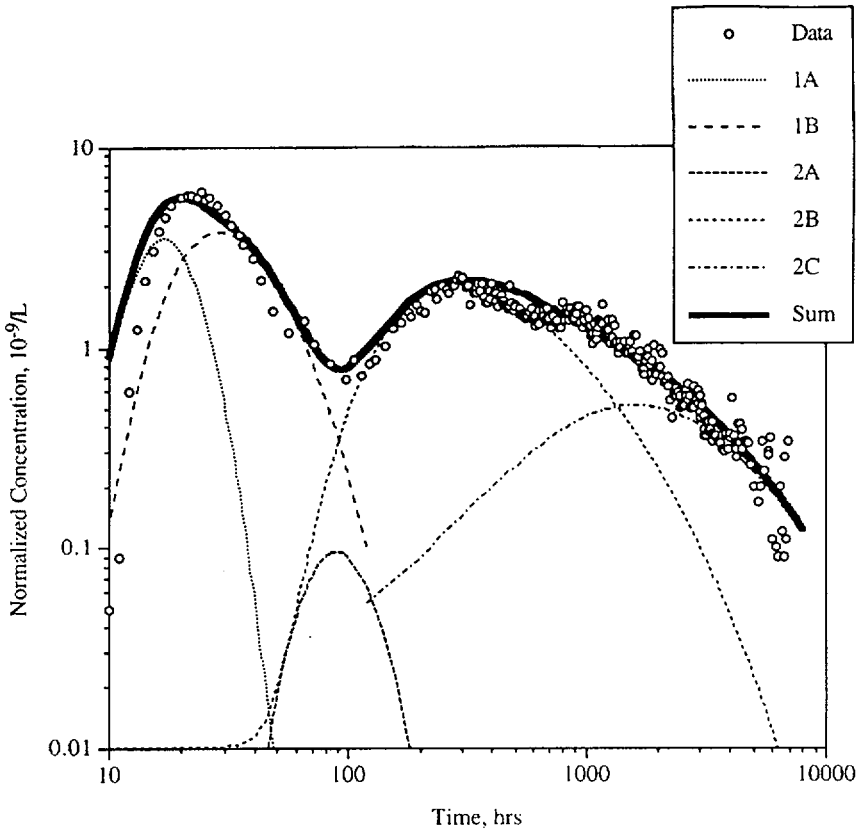

Figure 75. RELAP Fits to Carboxylate-Modified Polystyrene Latex Microsphere Response in Bullfrog Tuff Tracer Test

Table 19. Microsphere Filtration and Detachment Parameters Associated with the Fits Shown in Figure 75

Parameter	Path 1A	Path 1B	Path 2A	Path 2B	Path 2C
Mass fraction, f	0.115	0.005	0.423	0.067	0.1
k_{filt} (1/hr)	0.2	0.2	0.04	0.04	0.04
λ^a (1/cm)	0.00247	0.00247	0.0133	0.0133	0.0133
$bk_{res}{}^b$ (1/cm-hr)	0.00025[c]	3.33	0.000404[c]	0.4	0.008

NOTE: Other transport parameters used to obtain the fits are given in Table 17. Note that subpathways 1A and 1B represent a mass fraction split of Pathway 1 from Table 17, and subpathways 2A, 2B, and 2C represent a mass fraction split of Pathway 2 from Table 17.

(a) λ calculated as k_{filt}/V, where V = average linear velocity determined from mean fluid residence time.

(b) b = fracture half aperture in cm. The fitted detachment rate constant is this lumped parameter.

(c) Maximum detachment rate constant; cannot distinguish between this value and zero.

However, if the microspheres experienced a delay similar to the solutes, then their predicted first arrival would actually be slightly later than the observed first arrival. In fact, in this case, the first arrival would coincide almost exactly with the first arrival of solutes. Thus, the uncertainty associated with when the microspheres actually began entering the flow system causes uncertainty in the predicted first arrival of the microspheres.

The fits to the Prow Pass test microsphere data are shown in Figure 76, and the corresponding best-fitting filtration and detachment rate constants are listed in Table 20. The fits suggest that the small peaks in this test were the result of a very small fraction of spheres that moved through the flow system unfiltered, and the long tails were the result of small detachment rate constants. The filtration-rate constant listed in Table 20 for the yellow 280-nm-diameter microspheres was not obtained from fitting, but rather it was the smallest filtration coefficient that resulted in a peak concentration of spheres that was at or below detection limits. This number can be considered a lower-bound estimate of the yellow-sphere filtration coefficient because any larger value will result in more filtration and an even lower recovery. Unlike the Bullfrog test, only a single filtration and detachment rate constant were needed to effectively fit the microsphere responses in the Prow Pass test. As mentioned in Section 3.5.6.2, no attempt was made to fit the "spikes" in microsphere concentration that occurred after flow transients.

It should be pointed out that the interpretations of the microsphere responses presented in the preceding paragraphs, particularly for the Bullfrog test, are by no means unique. First, it is quite likely that there exists a continuous distribution of filtration and detachment rate constants rather than a few discrete ones, as assumed in the above analyses. Such a distribution could arise from a distribution of colloid surface properties and/or physical and chemical heterogeneities in fracture surfaces. It is also possible that colloid filtration and detachment are not linear first-order processes as assumed in Equations 7 and 8. Rather, they might be better described as nonlinear and/or stochastic processes (Dabros and Van de Ven 1982; 1983). Finally, as mentioned above, the interpretation of the microsphere response relative to the solutes is complicated by the fact that, with the exception of the yellow microspheres in the Prow Pass test, the sphere injections were not started at exactly the same times as the solute injections. In addition to causing uncertainty as to when the microspheres actually began moving into flow pathways (relative to the solutes), the differences in injection times may have resulted in the microspheres not being distributed into flow pathways in exactly the same proportion as the solutes (i.e., a different source term). If different assumptions were made about the distribution of spheres between the two major sets of pathways in the Bullfrog test, different filtration parameters would be obtained.

3.5.8 Discussion of Field Tracer Test Results

Estimates of transport parameters that can be used directly in solute transport models were derived from the best-fitting model parameters in Tables 17 and 18. These parameter estimates are presented in Table 21 as ranges of values that are consistent with the tracer test interpretation(s). Additional discussion of these ranges and how they were derived is provided in the following sections. This parameter estimation exercise has several important implications for radionuclide transport in fractured volcanic tuffs near Yucca Mountain.

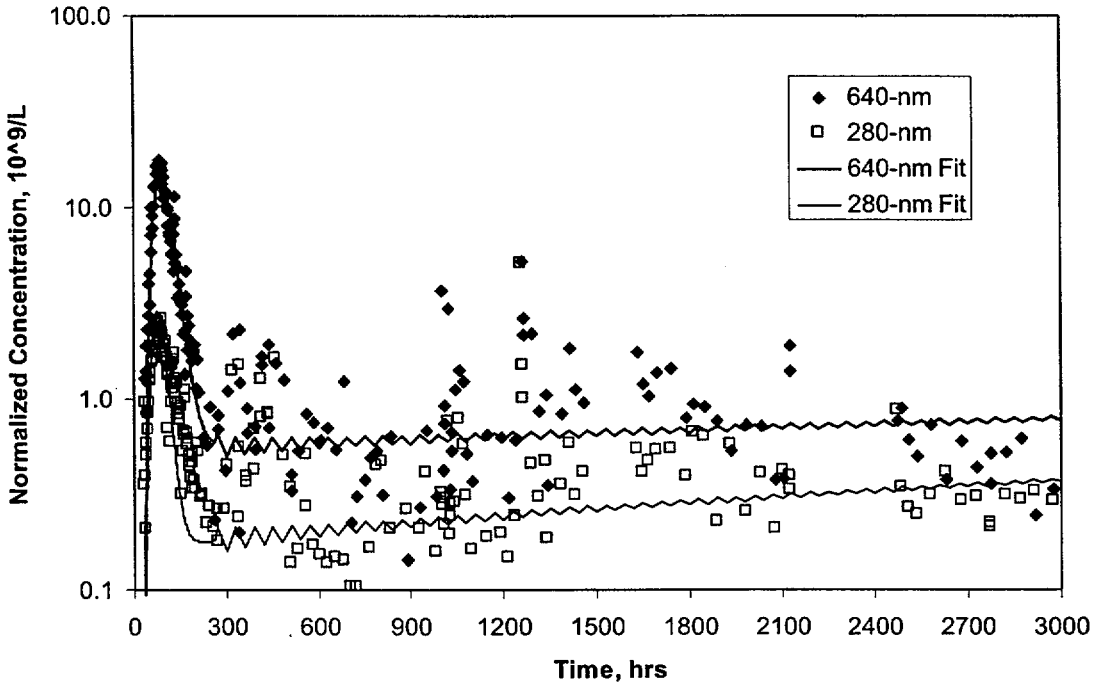

NOTE: Jagged appearance of the fits starting at ~300 hr is the result of instabilities in the Laplace transform inversion algorithm of RELAP.

Figure 76. RELAP Fits to the Carboxylate-Modified Polystyrene Latex Microsphere Responses in the Prow Pass Tracer Test

Table 20. Filtration and Detachment Rate Constants for the Carboxylate-Modified Polystyrene Latex Microspheres in the Prow Pass Tuff Tracer Test

	Microspheres		
Parameter	**640-nm Blue**	**280-nm Orange**	**280-nm Yellow**
k_{filt} (1/hr)	0.043	0.07	0.2[(a)]
λ (1/cm)	0.017	0.028	0.08
bk_{res}[(b)] (1/hr)	0.000154	0.000251	0.001

NOTE: Mass fractions are assumed to be the same as for solutes (Table 18).

(a) Minimum value that is consistent with the lack of appearance of these spheres at the production well. The actual filtration rate constant could be much higher.

(b) Maximum values; cannot distinguish between these values and zero. See also footnote (b) of Table 19.

Table 21. Transport Parameter Estimates Deduced from the Bullfrog and Prow Pass Multiple-Tracer Tests

Parameter	Prow Pass		Bullfrog	
	Lower Bound	Upper Bound	Lower Bound	Upper Bound
Effective flow porosity	0.003	0.006	0.003[1]	0.034 [a]
Longitudinal dispersivity, m [b]	6.3	61.5	3.2	62.5
$\frac{\phi}{b}\sqrt{D_m}$ for radionuclides ($sec^{-1/2}$) [c]	0.00054	0.00095	0.00027	0.0015
Fracture aperture (cm)	0.18	1.06	0.085	1.28
Fracture spacing (cm)	6.4	∞	2.4	∞
Ratio of stagnant to flowing water volumes	1.8–10.2	∞	0.3–15.2	∞

NOTE: These values above are provided as ranges of values; see text for explanations.

(a) These estimates assume that 75% of the production flow was associated with flow pathways that resulted in the first tracer peak and 25% was associated with the second tracer peak (based on flow survey information).

(b) Lower bounds assume Peclet numbers for radial flow and 30-m travel distance; upper bounds assume Peclet numbers for linear flow and interval thicknesses as travel distances.

(c) Assumes that bromide and PFBA effectively bound sizes and diffusion coefficients of radionuclide solution species.

3.5.8.1 Conceptual Transport Model

Even without quantitative parameter estimation, it is clear that the tracer responses in both the Bullfrog and Prow Pass tests are consistent with a dual-porosity conceptual transport model for the fractured volcanic tuffs. It is simply not possible to account for the differences in the bromide and PFBA responses or the relatively small time attenuation but significant concentration attenuation of the lithium response relative to the nonsorbing tracers (in the Prow Pass test and the first peak of the Bullfrog test) without invoking diffusion between flowing fractures and stagnant matrix water. Some diffusion into stagnant water within fractures (e.g., dead-end fractures or along rough fracture walls) cannot be ruled out. However, if the stagnant water were primarily in fractures, the surface area for sorption would be limited, and it is unlikely that there would be as much concentration attenuation of lithium relative to the nonsorbing solutes as observed in the tracer tests. The large surface-area-to-volume ratio necessary to result in the large observed concentration attenuation of lithium seems plausible only if a significant fraction of the stagnant water is in matrix pores.

The quantitative estimates of the lumped mass transfer parameter $\frac{\phi}{b}\sqrt{D_m}$ for bromide in Tables 17 and 18 are based on the assumption that bromide has a diffusion coefficient that is a factor of three greater than PFBA. This assumption is based on matrix diffusion coefficients measured in laboratory diffusion cell tests, which are discussed in Section 3.9. It is worth noting that RELAP simulations in which a finite matrix was assumed (i.e., a finite spacing between fractures) offered a slightly better fit to the tracer responses associated with the second peak of the Bullfrog test than simulations assuming an infinite matrix. This result suggests that tracer molecules may

have diffused far enough into the matrix to begin encountering molecules from neighboring fractures; that is, the spacing between fractures may have been small enough that the tracers were able to diffuse to the middle of matrix blocks separating fractures. For the first peak in the Bullfrog test and for the Prow Pass test, a finite matrix offered no better fits to the tracer data than an infinite matrix. In these cases, it can only be stated that the fracture spacing must have exceeded some threshold value below which the tracer responses would have been significantly different than observed. The applicable threshold values for the first Bullfrog test peak and for the Prow Pass test were estimated by adjusting the fracture spacing in RELAP until the simulated tracer responses began to differ significantly from the simulated responses assuming an infinite matrix. The results are presented in Tables 17, 18, and 21 as lower bounds for fracture spacing.

The tracer responses and the qualitative and quantitative conclusions about matrix diffusion that can be drawn from them illustrate very clearly the advantages of using multiple nonsorbing tracers with different diffusion coefficients in tracer tests to distinguish between alternative conceptual transport models. The individual responses of either bromide or PFBA could have been fit reasonably well assuming no matrix diffusion at all. Only when the responses of these tracers are considered together is it obvious that diffusive mass transfer must be invoked to explain the test results. Even long tails that plot linearly on log-log plots of tracer responses (power-law behavior), which are often said to infer matrix diffusion when single tracer responses are analyzed (Haggerty et al. 2000), do not unequivocally substantiate diffusive mass transfer. Such responses can also be attributed to hydrodynamic dispersion that scales with residence time (due to the recirculating flow field or effects of density-driven flow), stagnation points, and/or source-term effects (e.g., the slow release of tracers from the injection borehole). Furthermore, the fact that the lithium responses were significantly retarded in concentration but not in time supports the concept that a significant amount of diffusion occurred into the matrix pores and not simply into stagnant water within the fracture network. This conclusion is very important for Yucca Mountain performance assessment because mass transfer between flowing fractures and the true matrix implies that a large amount of surface area will be available for sorption of radionuclides in the saturated, fractured tuffs.

3.5.8.2 Fracture Apertures

An estimate of the average fracture aperture ($2b$) experienced by the tracers in the Bullfrog and Prow Pass tests can be obtained from the estimate of the lumped, diffusive, mass-transfer parameter, $\frac{\phi}{b}\sqrt{D_m}$, provided independent estimates of matrix porosity, ϕ, and matrix diffusion coefficients, D_m, are available. Using estimates of ϕ determined from laboratory measurements and D_m for bromide and PFBA from diffusion cell tests (Section 3.9), estimates of $2b$ range from 0.085 to 1.28 in the Bullfrog Tuff and from 0.18 to 1.06 in the Prow Pass Tuff, as listed in Table 21. Because the long tracer test intervals in each test both included more than one major lithology (Figure 2), it was necessary to estimate $2b$ for each major lithologic unit in each interval. The fact that there is a positive correlation between matrix porosity and matrix diffusion coefficient results in a relatively large range of aperture estimates. If it is assumed that the flow pathways associated with the first tracer peak in the Bullfrog test were in the central Bullfrog unit and the pathways associated with the second tracer peak were in the lower Bullfrog unit, then the aperture estimates in these two units correspond to the two extremes listed in Table 21. These aperture estimates based on tracer responses should be distinguished from friction loss

or cubic-law aperture estimates that are obtained from hydraulic responses (Tsang 1992), although they should be the most appropriate aperture estimates to use for transport calculations.

3.5.8.3 Ratios of Stagnant Water to Flowing Water Volumes

Estimates of the ratio of stagnant water volume to flowing water volume in the flow system(s) can be calculated from estimates of fracture spacings, matrix porosities, and fracture apertures discussed in the previous two sections (ratio = $\phi L/2b$ - b). Ranges of these estimates are listed in Table 21. The ranges are rather large because the estimates of fracture aperture and fracture spacing have large ranges. The upper-bound ratios for both tracer tests are listed as infinite because all tracer responses could be fitted reasonably well, assuming infinite fracture spacing. The ranges listed as lower bounds in Table 21 were obtained from the combinations of fracture apertures and fracture spacings that resulted in the highest and lowest ratios (excluding infinity). These ratios plus one can be considered physical retardation factors for nonsorbing species in the flow system when flow rates are low enough that there is ample time for solutes to diffuse throughout the stagnant water in the system (Robinson 1994).

3.5.8.4 Lithium Sorption Behavior

Tables 17 and 18 list the best-fitting values of the lithium fracture and matrix retardation factors (R_f and R_m, respectively) for the Bullfrog and Prow Pass tests. Note that the R_f values are 1 for both the Prow Pass test and for the first peak in the Bullfrog test, implying negligible retardation within the fractures and sorption only in the matrix. Note that a fracture retardation factor of 1 does not necessarily imply that sorption did not occur on fracture surfaces; it merely suggests that the majority of the lithium sorption occurred after a diffusive mass-transfer step to sorptive surfaces in the matrix. For the second peak in the Bullfrog test, the lithium response was best fitted with $R_f = 3$ and $R_m = 33$, implying some sorption in fractures and a large amount of sorption in the matrix.

Matrix K_d values were deduced from the fitted matrix retardation factors by simple rearrangement of the expression defining the retardation factor:

$$K_d = \frac{\phi}{\rho_B}(R_m - 1) \qquad \text{(Eq. 9)}$$

Because the K_d values depend on the matrix porosity, values are listed in Table 22 for each lithologic unit that transport may have occurred in for each test (matrix porosities from Section 3.9 were used in Equation 9). For a given retardation factor, the corresponding K_d value is always higher in a unit with higher matrix porosity. The R_m value associated with the first lithium peak in the Bullfrog test (Table 17) was obtained by fitting the rising limb of the lithium response using RELAP. However, because it was necessary to use MULTRAN to achieve a reasonable fit to the tail of the response (see above), the K_d value for this peak was estimated from the ion-exchange parameters that yielded the best fit to the lithium data (see Section 3.10.1.3) rather than from the R_m value obtained from RELAP. The best-fitting, ion-exchange parameters suggested a highly nonlinear sorption isotherm for lithium in the matrix; hence, K_d values are reported in Table 22 for lithium concentrations of both 100 mg/L (low K_d value) and

Table 22 Lithium Partition Coefficients Derived from Field Tracer Tests and Laboratory Measurements

Parameter	Field K_d	Laboratory K_d [(a)]
Prow Pass matrix K_d assuming Central Prow Pass Tuff	0.66	0.13 (0.26 at infinite dilution)
Prow Pass matrix K_d assuming Lower Prow Pass Tuff	1.65	0.084 (0.44 at infinite dilution)
Bullfrog matrix K_d in Pathway 1 assuming Central Bullfrog Tuff [(b)]	0.13–12.6 (nonlinear)[(c)]	0.19 (0.44 at infinite dilution)
Bullfrog matrix K_d in Pathway 1 assuming Lower Bullfrog Tuff [(b)]	0.50–48.8 (nonlinear)[(c)]	0.32 (1.64 at infinite dilution)
Bullfrog matrix K_d in Pathway 2 assuming Central Bullfrog Tuff [(b)]	1.36	0.19 (0.44 at infinite dilution)
Bullfrog matrix K_d in Pathway 2 assuming Lower Bullfrog Tuff [(b)]	5.27	0.32 (1.64 at infinite dilution)

NOTE: These lithium partition coefficients (K_d values) were derived from field tracer tests assuming transport in different lithologies within the test intervals; the corresponding laboratory measurements of K_d values in these intervals were taken from Anghel et al. (2000).

(a) Values at "infinite dilution" obtained from slopes of Langmuir isotherm fits to the data (asymptotic slope at very low concentrations (i.e., $K_L S_{max}$). Other values obtained from a simple linear fit to the entire range of data.

(b) "Pathway 1" refers to pathways that resulted in the first tracer peak in the Bullfrog reactive tracer test, and "Pathway 2" refers to pathways that resulted in the second peak in this test. K_d values were calculated from the smallest matrix retardation factors obtained from alternative interpretations of the test.

(c) The first number corresponds to a K_d value calculated at 100 mg/L Li^+ using the three-component cation exchange model parameters yielding the best fit to the first lithium peak (see Section 3.10.1.3 for description of three-component model); the second number corresponds to a K_d value calculated at 1 mg/L Li^+ concentration using the same model parameters.

1 mg/L (high K_d value). This range of concentrations should reasonably bound the concentrations experienced in the field test.

Laboratory batch measurements of lithium sorption onto crushed tuff from C-wells cores indicated a dependence of K_d values on both lithium concentrations and the mineralogy associated with the different lithologies (see Section 3.8). The concentration dependence in each case could be represented by a classic nonlinear isotherm in which K_d values decreased as lithium solution concentrations increased. There was also a strong dependence of lithium K_d values on the smectite and zeolite content of the tuffs (Anghel et al. 2000). The range of laboratory-derived K_d values associated with each unit that could have participated in the Bullfrog and Prow Pass tests is listed in Table 22 next to each corresponding field-derived K_d value.

The lithium K_d values deduced from the field tracer tests (assuming any given lithologic unit) are consistently higher than the corresponding K_d values measured at the lowest lithium concentrations in the laboratory. The only possible exception is that the field K_d value may be somewhat lower than the laboratory K_d value in the flow pathways resulting in the first peak in the Bullfrog test (especially if these pathways were located in the central Bullfrog Tuff). However, in general, these results suggest that the use of laboratory-derived K_d values to predict

sorbing species transport in the saturated fractured tuffs near the C-wells location would tend to underpredict the amount of sorption experienced by the species. The fact that the field K_d values tended to be greater than the laboratory K_d values suggests that lithium may have come in contact with alteration minerals in the field that were not present or were depleted in the lab rock samples. Any loosely adhering alteration minerals (e.g., clays) that may have been present in the core samples would very likely have been lost during crushing and sieving of the material when it was prepared for the batch sorption experiments.

3.5.8.5 Effective Flow Porosity

Contaminant transport predictions are generally very sensitive to assumed flow porosities because transport rates are directly proportional to the specific discharge divided by flow porosity. The effective flow porosity in a cross-hole tracer test without recirculation can be estimated from the following equation, which assumes a confined, homogeneous, isotropic flow system:

$$\phi = \frac{Q\tau}{\pi L^2 T} \qquad \text{(Eq. 10)}$$

where

ϕ = effective flow porosity
Q = production flow rate, m^3/hr
τ = mean residence or travel time, hr
L = distance between wells, m
T = formation thickness (assumed to be interval length).

With recirculation, the situation is complicated by the fact that there is a hypothetical stagnation point; hence, the mean tracer residence time theoretically approaches infinity. However, the interpretive method described in this report allows for incomplete tracer mass recoveries that could result from stagnation, so a finite estimate of the mean tracer residence time can always be obtained. Guimera and Carrera (2000) discuss an alternative method of estimating effective flow porosity from peak, rather than mean, tracer arrival times in tests with partial recirculation. However, their method was derived for system Peclet numbers (L/α) ranging from 10 to 100, which are considerably larger than the Peclet numbers obtained in the C-wells tests; therefore, their method was not applied here.

For the mean and peak tracer arrival times and flow conditions in the C-wells tracer tests, Table 21 gives the effective flow porosities calculated using Equation 10 for the Bullfrog and Prow Pass tests. The upper and lower bounds given in Table 21 were calculated using the mean tracer residence times calculated assuming linear and radial flow, respectively (values in Tables 17 and 18). Also, in the Bullfrog test, it was assumed that 75% of the total production flow rate was associated with the first tracer peak and 25% was associated with the second tracer peak (based on flow survey information suggesting that a large amount of flow occurred in the upper part of the injection interval in C#2; see Figure 2).

The relatively large effective porosity estimates obtained from Equation 10 could be due to heterogeneities in the flow field. Flow is undoubtedly not radial, as assumed in the above

equations, but rather it very likely follows tortuous pathways between the injection and production wells. Furthermore, it is conceivable that a single high-conductivity feature such as a large, open fracture or fault could transmit the vast majority of the flow to the production well. If this feature does not pass near the injection well, the effective flow rate drawing tracers to the production well will be greatly reduced relative to what would occur in a radial flow field. Numerical modeling experiments will be conducted in the future to investigate the effects of fracture flow field heterogeneities on travel times in cross-hole tracer tests.

3.5.8.6 Longitudinal Dispersivity

Longitudinal dispersivity estimates from cross-hole tracer tests generally have considerable uncertainty due to (1) uncertainty in the actual tracer transport distance (the actual flow pathways followed by tracers are unknown), (2) whether the flow field is radial, linear, or some combination, (3) the amount of apparent dispersion caused by nonidealities such as a poorly mixed injection wellbore or density/buoyancy effects, and (4) the amount of apparent dispersion caused by recirculation or the ambient flow field. It is beyond the scope of this report to address in detail the possible effects of each of these uncertainties on the longitudinal dispersivity estimates provided in Table 21. These estimates can be considered "upper and lower bounds" that were obtained as follows.

1. The maximum transport distance was assumed to be the distance from the top of one packed-off interval to the bottom of the other (80 to 100 m) while the minimum transport distance was assumed to be the linear distance between the wells (~30 m).

2. The radial and linear Peclet numbers were used to obtain estimates of the dispersivity for the two cases above ($\alpha = L/Pe$), and the most extreme values were used for the upper and lower bounds.

3. The RELAP code simulated a gradual release of tracer from the borehole to the formation by assuming a well-mixed interval, resulting in an exponential decay in tracer concentration in the wellbore. The decay time constant was determined from the volume of the packed-off interval divided by the injection/recirculation rate. Thus, the slow release of tracers from the injection well did not bias the dispersivity (or mean residence time) estimates.

4. An attempt to "subtract out" the apparent dispersion caused by recirculation in the Prow Pass test was made by the following.

    a. Obtaining a simulated tracer response for a cross-hole test with the appropriate amount of recirculation in a homogeneous, isotropic medium using a particle-tracking code developed by Reimus (1996).

    b. Calculating the variance of the particle residence times in (1).

    c. Calculating the variance of tracer response in the actual field test from $\sigma^2 = 2\frac{\tau^2}{Pe}$ where σ^2 is the variance.

d. Subtracting the variance in (2) from the variance in (3) to obtain the variance due to "true hydrodynamic dispersion" in the flow system (this assumes that the variance due to recirculation and the variance due to true dispersion are additive, which assumes that the two processes giving rise to the total variance are independent).

e. Rearranging the above expression to obtain the Peclet number and, hence, dispersivity, that represents true hydrodynamic dispersion; i.e., $Pe = 2\frac{\tau^2}{\sigma^2}$.

Corrections for dispersion caused by recirculation in the Bullfrog test were calculated to be negligible. No attempt was made to account for density/buoyancy effects or the effects of the ambient flow field on the longitudinal dispersivity estimates.

3.5.8.7 Colloid Transport

The microsphere filtration and detachment rate constants deduced from the Bullfrog and Prow Pass tracer tests can potentially be used as estimates of filtration and detachment rate constants for natural colloids that could facilitate the transport of radionuclides that are strongly adsorbed to colloids. However, it must be kept in mind that the CML microspheres do not have the same physical and chemical properties as natural inorganic colloids. At the time this report was written, experiments were in progress to compare the transport behavior of 330-nm-diameter CML microspheres and 100-nm-diameter silica spheres in fractured media. Preliminary results from these experiments indicated that the microspheres transported with the same attenuation or less attenuation through the fractures than the silica spheres, suggesting that microsphere filtration and detachment rate constants should be conservative if used to predict silica colloid transport in fractured media. However, it is emphasized that these results must be considered preliminary at this time.

Perhaps of greater importance than the microsphere filtration and detachment rate constants derived from the field tests is the fact that the microsphere responses qualitatively indicate that (1) colloid detachment from fracture surfaces is a process that clearly occurs in fractured tuffs, and (2) colloid detachment is apparently enhanced by flow transients. These qualitative results suggest that it is not sufficient to consider only colloid filtration when assessing colloid-facilitated radionuclide transport, but that colloid detachment and its dependence on other variables must also be considered and could actually dominate the transport behavior of colloids.

3.6 LIMITATIONS AND UNCERTAINTIES ASSOCIATED WITH TRACER TESTS

Several factors contributed to the uncertainty in transport parameters derived from tracer test interpretations. First, there are data uncertainties, which are related to the accuracy and precision of the tracer chemical analyses, including both random and systematic errors. Random errors were estimated to be small because the BTC data are not widely scattered and show well-defined trends. The most significant sources of systematic errors would have been day-to-day differences in analytical instrument operation and in analytical standard preparation. However, repeat measurements on separate days indicate that these errors were also minimal.

During the iodide tracer test in the Bullfrog-Tram interval, the pump gradually failed, resulting in a decreasing flow rate during the test, which changed from 139 gpm at the beginning to 98 gpm at the end. This violated one of the assumptions in the Moench (1989) semi-analytic method employed to analyze the tracer test results. This source of uncertainty was eliminated for subsequent tests by replacing the pump.

There was uncertainty regarding the extent to which the tracers were evacuated from the injection intervals to the aquifer in each test. The very long injection intervals (ranging from 75 to almost 200 m) and the lack of down-hole mixing contributed to this uncertainty. Slow release of tracers from the injection intervals could have contributed to tailing in the tracer responses that would have been interpreted as dispersion or matrix diffusion. Attempts to reduce this uncertainty in the Prow Pass tests were made by deploying a down-hole system capable of mixing the tracer solution after its injection into the borehole. Although the down-hole mixing system worked only marginally, it is believed that stratification of tracer concentration in the borehole was minimized. Also, recirculation of 30% of the water produced from C#2 during the Prow Pass test should have served to help "flush" tracers out of the injection interval.

The influence of the natural gradient that exists at the C-wells on tracer recovery at the pumped well is a source of uncertainty. Determinations of the capture zone of the pumped well, and how it is altered by the existence of a natural gradient, depend on the assumptions made regarding flow heterogeneity and anisotropy. Mass that is not recovered by the pumped well is potentially the result of pathways other than the postulated radially convergent or partially recirculating streamlines toward the pumped well.

When estimating flow porosity and longitudinal dispersivity using a semi-analytical solution to the advection-dispersion equation, such as the Moench (1989) solution or the RELAP model employed in this study, several assumptions are made. The medium is assumed to be homogeneous and isotropic, and the flow regime is assumed to be strictly radial (i.e., in the two horizontal dimensions without a vertical component). Then, based on these assumptions, flow porosity and dispersivity (Peclet number) are determined by fitting the BTCs. Uncertainty associated with assuming either radial or linear flow (when the actual nature of the flow field could be somewhere in between) was addressed in the multiple tracer test interpretations by reporting mean residence times and Peclet numbers for both radial and linear flow assumptions.

When assuming a dual-porosity medium, as was done in this study, non-uniqueness of tracer test interpretations is an issue. For instance, long tails in tracer responses can be interpreted as being the result of either large longitudinal dispersion or significant matrix diffusion. In the conservative tracer tests, nonuniqueness was addressed by using PEST to obtain optimal transport parameter estimates and to estimate confidence intervals associated with the parameters. In the multiple tracer tests, nonuniqueness of interpretations was minimized by simultaneously fitting the tracer responses using known ratios of diffusion coefficients as constraints on the relative amount of matrix diffusion that could occur for different tracers.

Uncertainties associated with alternative interpretive methods were addressed indirectly by using two different interpretive approaches for the conservative and multiple tracer tests. Differences in the flow porosities, dispersivities, and matrix diffusion parameters estimated from these tests

reflect, in part, the different methodologies and assumptions used to obtain the estimates. Highlights of the differences in the two methods are discussed below.

(1) The first method (Section 3.1) involves normalizing tracer concentrations to the maximum (peak) tracer concentration, whereas the second method (Section 3.5.6) involves normalizing tracer concentrations to the injection mass. The first approach results in matching the shapes of breakthrough curves (or differences in shapes when there are multiple tracers), while the second is aimed at matching not only shapes, but also peak concentrations and total recoveries (as well as differences in heights and recoveries). Thus, the second method has some additional fitting constraints that result in different transport parameter estimates compared to the first method.
(2) Both methods use essentially the same mathematical model to account for the tracer residence time in the injection borehole (i.e., a well-mixed interval with an exponential decay in tracer concentration). However, the mean residence time was allowed to be much larger when running simulations using the first method (Section 3.1) compared to the second method (Section 3.5.6). A larger residence time in the injection borehole effectively adds dispersion to the simulated response curves, which results in a smaller flow system dispersivity when the tracer data are fitted. Thus, the longitudinal dispersivity estimates from the first method tend to be somewhat lower than from the second method.

A limitation of all tracer tests conducted at the C-wells is that they produce estimates only of longitudinal dispersivity, not transverse dispersivity. In addition, the estimation of flow porosity has the uncertainty of an unknown travel distance between source and sink. The probability that the travel distance is a straight-line distance between source and sink is remote. This unknown quantity can affect the flow porosity calculation.

3.7 CONCLUDING REMARKS ABOUT FIELD TRACER TESTS

It is recognized that the tracer-test interpretations using primarily semi-analytical solution methods that assume an idealized geometry and steady flow rates is a considerable simplification of reality. Numerical models could certainly be used to account for greater system heterogeneity. Also, more sophisticated semi-analytical representations of dual-porosity systems, such as the multirate-diffusion model of Haggerty and Gorelick (1995), could be applied. However, the information available to support these more sophisticated representations of the flow and transport system is sparse to nonexistent. Furthermore, the agreement between the relatively simple semi-analytical models (either the Moench model or RELAP) and the tracer responses are considered to be very good. The only additional model complexity needed to explain any portion of the tracer-test data sets was the multicomponent transport and ion exchange capabilities of the MULTRAN model needed to match the lithium response in the first peak of the Bullfrog tracer test. Although the introduction of additional model complexity could improve the agreement between model and data, it appears that all of the critical features of the tracer responses were effectively captured, and the introduction of additional complexity, especially in light of the minimal information to support it, is not justified.

One must also keep in mind that the tracer-test results are intended to support predictive calculations that span much larger time and distance scales than represented by the test. With this in mind, it is desirable to capture the important transport processes with as concise a model

as possible so that others can incorporate a relatively simple model on a local scale into a more sophisticated flow model that captures the important hydraulic features of the larger-scale flow system. It is believed that the C-wells tracer tests and their interpretations presented in this report accomplish this objective.

3.8 BATCH TESTING OF LITHIUM SORPTION TO C-WELLS TUFFS

3.8.1 Materials and Methods

The batch lithium sorption experiments were conducted as follows.

- C-wells core from a stratigraphic unit of interest was crushed, pulverized, and passed through a 500-μm sieve but retained on a 75-μm sieve.
- A specified amount of crushed tuff was added to polycarbonate (polyallomer) Oak Ridge centrifuge tubes. In some experiments, the tuff and centrifuge tubes were autoclaved prior to contacting the tuff with the lithium solution.
- The tuff was preconditioned with filter-sterilized (0.2-μm filter) J-13 water.
- A specified amount of lithium-bearing water (either from well J-13 or well C#3) was added to the preconditioned tuff, and the mixture was continuously shaken for 24 to 72 hr at either 25°C or 38°C to achieve equilibration between solid and solution.
- After equilibration, the tubes were centrifuged and a portion of the supernate was filtered (0.2- or 0.4-μm filter) for tracer analysis to determine the tracer concentration remaining in solution. Lithium was analyzed by inductively-coupled plasma-atomic emission spectrometry (ICP-AES).
- The mass of tracer sorbed to the tuff was determined by mass balance, with corrections, if necessary, to account for sorption to the container walls, which was measured in control experiments in which tuff was omitted.
- All measurements were made in duplicate or triplicate.

Sorption isotherms were determined under several different experimental conditions:

- 1:1 solution:solid ratio in J-13 water at 25°C
- 1:1 solution:solid ratio in J-13 water at 38°C
- 2:1 solution:solid ratio in J-13 water at 25°C
- 4:1 solution:solid ratio in C-3 water at 38°C
- 4:1 solution:solid ratio in J-13 water at 25°C
- 4:1 solution:solid ratio in J-13 water at 38°C.

The two temperatures were intended to span the range of conditions under which sorption would occur in either the laboratory or the field (the average groundwater temperature in the Bullfrog Tuff at the C-wells is about 38°C).

At the time of these studies, groundwater from the C-wells complex was not consistently available, so groundwater from well J-13, located 4 km southeast of the C-wells complex, was used as a surrogate in most tests. J-13 water is well-characterized and has become a *de facto* standard groundwater for use in Yucca Mountain sorption studies (Harrar et al. 1990, pp. 6.6 to 6.7; Triay et al. 1997, pp. 11, 16, 45). A comparison of J-13 and C-wells groundwater chemistry shows that the two waters are both sodium bicarbonate dominated and, in all regards, quite similar (Table 23). Lithium solutions for sorption tests were prepared by dissolving reagent-grade lithium bromide in either C#3 or J-13 water. All solutions were filter-sterilized before use.

Table 23. Comparison of J-13 and C-wells Groundwater Chemistry

Species	Concentration (µg/mL)	
	J-13	C-Wells
Al	< 0.03	
B	0.13	
Ba	< 0.001	
Ca	11.3	11
Cl	7	7
Fe	0.02	
K	5	2
Li	0.040	0.11
Mg	< 0.010	0.38
Mn	0.01	
Na	44	55
Si	30	25
Sr	0.040	0.044
PO_4	< 2.5	
SO_4	19	22
HCO_3	124	142
pH	7.2	7.8

Source: Fuentes et al. (1989, p. 15).

A few tests were conducted in a sodium bicarbonate solution having the same ionic strength as J-13 water but without the calcium and other cations present in J-13 water. Lithium sorption in this solution was noticeably greater than in J-13 water, presumably because of the absence of cations that compete with lithium for sorption sites (primarily calcium). The results of these experiments are not reported here.

Ion-exchange theory suggests that the actual ion-exchange process is rapid and will reach equilibrium quickly; in natural systems, apparent equilibration rates are limited by diffusion of ions through the solution to the mineral surface (Bolt et al. 1978, pp. 54 to 90). In a well-mixed system, such as a shaken centrifuge tube, diffusion is not limiting, and equilibration should be achieved quickly. A previous study of lithium sorption to the Prow Pass member of the Crater Flat Tuff found that sorption equilibrium was reached within 1 hr, confirming this hypothesis (Newman et al. 1991). For consistency with other sorption studies and for scheduling convenience, a minimum equilibration period of 24 hr was adopted for these studies.

Tuffs from seven different lithologies were tested, including two samples of the same unit (the central Bullfrog Tuff) from two different holes (C#1 and C#2) to allow an assessment of spatial heterogeneity in lithium-sorption parameters. The experimental matrix of tuffs, groundwaters, temperatures, and solid-solution ratios is summarized in Table 24. Figure 77 shows the sampling locations of the C-wells core used in the experiments. This figure is essentially identical to Figure 2 except that the triangles indicating flow zones in the wells have been replaced with triangles identifying locations of core samples used in the batch experiments.

Table 24. Summary of C-wells Experimental Batch Lithium Sorption Test Matrix

Tuff*	Water	Solution: Solid (mL:g)	Temperature (°C)
Central Bullfrog, C#1, 715 m (1)	J-13	2:1	25
	J-13	2:1	38
Central Bullfrog, C#2, 734 m (2)	J-13	1:1	25
	J-13	1:1	38
	C#3	4:1	38
Lower Bullfrog, C#1, 795 m (3)	J-13	4:1	25
	J-13	4:1	38
	J-13	2:1	25
Upper Prow Pass, C#2, 533 m (4)	J-13	4:1	25
	J-13	4:1	38
	J-13	2:1	25
Central Prow Pass, C#2, 553 m (5)	J-13	4:1	25
	J-13	4:1	38
	J-13	2:1	25
Lower Prow Pass, C#1, 573 m (6)	J-13	4:1	25
	J-13	4:1	38
	J-13	2:1	25
Bedded Prow Pass, C#2, 643 m (7)	J-13	4:1	25
	J-13	4:1	38
	J-13	2:1	25
Upper Tram, C#2, 839 m (8)	J-13	4:1	25
	J-13	4:1	38
	J-13	2:1	25

NOTE: *Lithology, borehole, and depth from land surface are in meters. The numbers in parentheses correspond to the numbers in Figure 77 (the locations where core was collected from the C-wells).

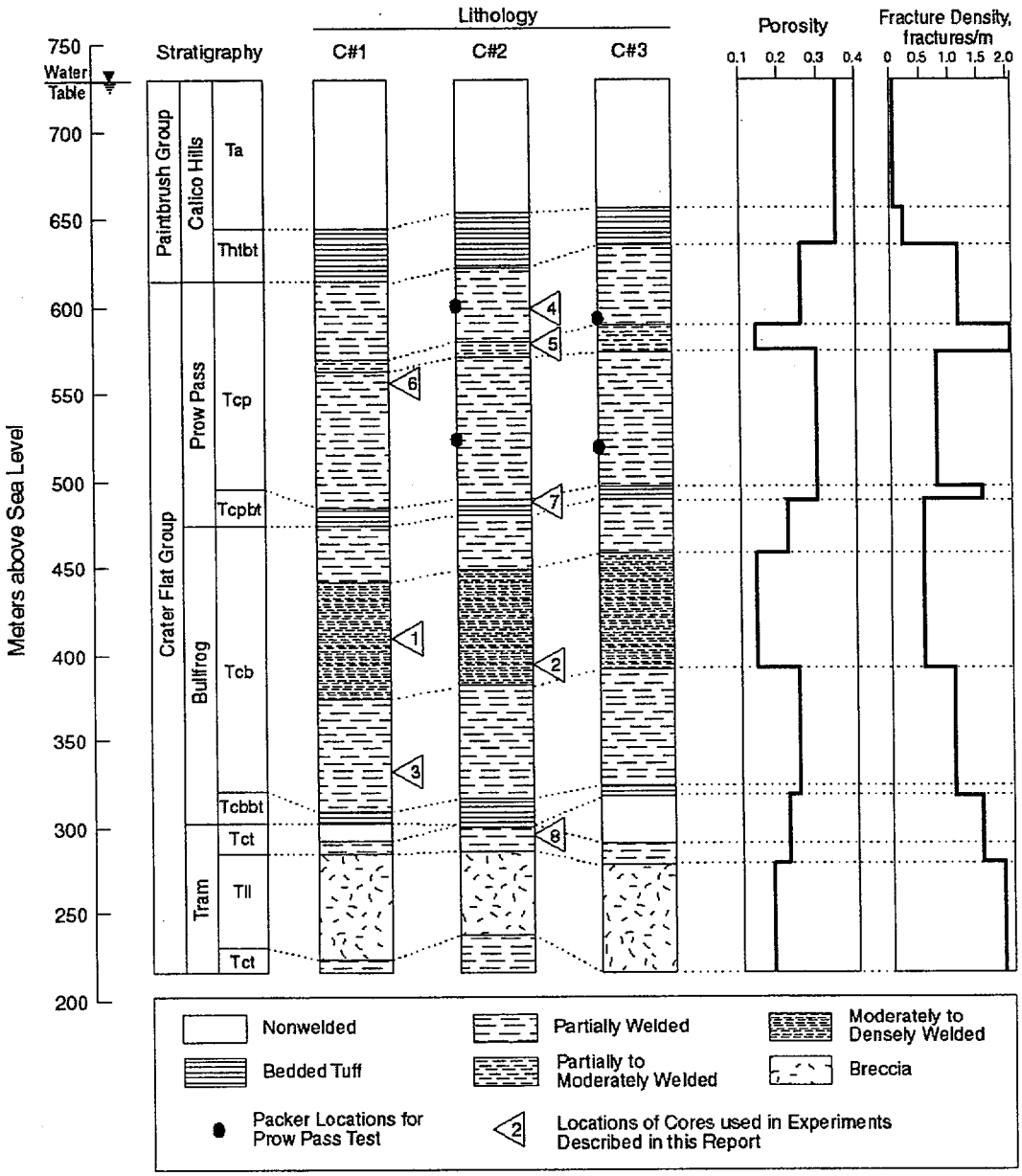

Source: Geldon 1993.

NOTE: The numbers in the figure correspond to the numbers in Table 24. Also shown are approximate locations of packers for the multiple tracer test in the Prow Pass Tuff.

Figure 77. C-wells Hydrogeology Showing Sampling Locations of All Core Used in the Laboratory Experiments Described in Sections 3.8, 3.9, and 3.10

Table 25. X-Ray Diffraction Results for Tuffs from Prow Pass, Bullfrog, and Tram Units

Tuff	Depth (m)	Concentration (wt %)				
		Smectite	Clinoptilolite	Mordenite	Analcime	Calcite
Central Bullfrog, C#1	715	$2^{\pm}1$	—	—	—	$2^{\pm}1$
Central Bullfrog, C#2	734	$5^{\pm}2$	—	—	—	—
Lower Bullfrog, C#1	795	$9^{\pm}3$	$4^{\pm}1$	$3^{\pm}1$	$12^{\pm}1$	$4^{\pm}1$
Upper Prow Pass, C#2	533	—	—	—	—	Trace
Central Prow Pass, C#2	553	$2^{\pm}1$	—	—	—	$2^{\pm}1$
Lower Prow Pass, C#1	573	$2^{\pm}1$	—	—	—	—
Bedded Prow Pass, C#2	643	—	—	$20^{\pm}4$	$39^{\pm}2$	—
Upper Tram, C#2	839	$1^{\pm}1$	—	—	—	—

NOTE: C#1, C#2, and C#3 are abbreviations for boreholes UE-25 c#1, UE-25 c#2, and UE-25 c#3, respectively.

Trace: trace abundance of < 0.5 wt%.

Only the main sorptive fractions are listed; the balance of the tuffs was mostly quartz and feldspar with small amounts of hematite, mica/illite, and/or kaolinite.

Batch-sorption experiments were also conducted on each of the tuffs to determine whether PFBA and bromide sorbed to them. The bromide experiments were actually conducted simultaneously with the lithium experiments, as lithium was added to the solutions as lithium bromide. The starting bromide concentrations ranged from ~10 ppm to ~1000 ppm. The PFBA experiments were conducted at a single concentration (1 ppm). These experiments were conducted on each rock type at 25°C. There was no measurable sorption of PFBA or bromide on any of the tuffs.

The mineralogy of the tuffs used in the batch-sorption experiments is listed in Table 25. The mineralogy was determined from quantitative X-ray diffraction (XRD) analyses. The tuffs differ primarily in their smectite and zeolite (clinoptilolite and mordenite) content, both of which have high cation-exchange capacities and would be expected to sorb lithium quite strongly compared to other minerals present in the rocks.

A Li-specific CEC method was developed to quantify the Li affinity for the selected tuffs. The method involved two steps: saturation of the exchange sites with Li, followed by displacement of the Li and other cations with Cs. The mineralogical composition of the samples was preserved as close as possible to the field conditions; therefore, no pretreatment was applied to remove carbonate or organic matter. The method involved the following steps.

- The tuff samples were crushed and wet-sieved with J-13 water to a particle-size range between 75 to 500 μm. Then ~5 g of each tuff was weighed into a 50-mL centrifuge Teflon tube. Each tuff sample was tested in triplicate.

- The samples were saturated three times with 30 mL of 0.8 N LiBr–0.2 N LiOAc solution to ensure replacement of cations present on mineral surface sites with Li. The pH of the solution was maintained at ~8.2 to prevent dissolution of calcite. After each LiBr addition, the tubes were sonicated to disperse the centrifuged sediment, and then the samples were shaken for 30 min.

- The samples were centrifuged at 10,000 rpm for 15 minutes to achieve a good separation of solids and solution. The supernatant from each Li-sorption step was combined and analyzed for Na, K, Ca, and Mg.

- After the Li-sorption steps, the tuff present in each centrifuge tube was washed three times with 30 mL of 1 N CsCl to remove the sorbed Li. The combined supernate from centrifuging was analyzed for Li, Na, Ca, K, and Mg. Residual Li saturating solution remaining in the centrifuge tubes was discounted by analyzing for Br and making the appropriate correction. Cs has more affinity for zeolites, and it should, therefore, displace more cations than Li. In many cases, Cs sorption gives a measure of the total CEC (Li measurements of the aliquots give the CEC for Li-Cs exchange).

The method described yields two different CEC results: (1) *CEC-Li*$_T$, the total CEC available to Li, estimated from the total cations displaced by Li in the saturation step, and (2) *CEC-Cs*$_T$, the total CEC available to Cs, estimated from the total cations displaced by Cs in the displacement step. *CEC-Cs*$_T$ can be further subdivided into CEC-*Cs*$_{Li}$, based on the Li displaced by Cs, and *CEC-Cs*$_{Nat}$, based on the native cations (Na, K, Ca, Mg) displaced by Cs. Each of these results is expressed in milliequivalents per 100 g of dry tuff.

3.8.2 Results and Discussion

During the course of the experiments, it became apparent that lithium sorption was essentially independent of solution:solid ratio, temperature, and water composition (J-13 or C#3) over the range of conditions studied. Therefore, the data sets for a given tuff lithology were combined to estimate sorption parameters. Three common isotherm models, defined as follows, were fitted to the data for each tuff.

(1) *Linear Isotherm:*

$$S = K_d C \qquad \text{(Eq. 11)}$$

where

S = equilibrium sorbed concentration (μg/g)
C = equilibrium solution concentration (μg/mL)
K_d = linear distribution coefficient (mL/g).

(2) *Freundlich Isotherm:*

$$S = K_F C^n \qquad \text{(Eq. 12)}$$

where

K_F = Freundlich coefficient (mL/μg)^n(μg/g)
n = Freundlich exponent (dimensionless).

(3) *Langmuir Isotherm:*

$$S = \frac{K_L S_{max} C}{1 + K_L C} \qquad \text{(Eq. 13)}$$

where

K_L = Langmuir coefficient (mL/μg)
S_{max} = maximum solid sorption capacity (μg/g).

Figures 78 to 84 show the experimental data for each tuff plotted as log-equilibrium-sorbed concentration (μg/g) versus log-solution concentration (μg/mL). A Langmuir isotherm consistently yielded better visual fits to the data than the other isotherms, so a fitted Langmuir isotherm is also shown in each figure. The Langmuir isotherm is the only isotherm that captures the curvature of the data when graphed on log-log axes. Furthermore, only the Langmuir isotherm recognizes the finite sorptive capacity of the solid matrix; the other models imply potential infinite sorption. A previous study of lithium sorption to the Prow Pass member of the Crater Flat Tuff also revealed Langmuir behavior (Newman et al. 1991). The Langmuir, Freundlich, and linear isotherm parameters associated with the data in Figures 78 to 84 are given in Table 26. It is concluded that a Langmuir isotherm provides the best representation of lithium sorption onto C-wells tuffs. However, a detailed statistical analysis to quantify how much better this representation is relative to the other isotherms (or whether it is statistically better) was not conducted. Statistical analyses were not conducted to determine whether there were significant isotherm differences as a function of temperature, solid-solution ratio, or core taken from different locations in the same lithological unit (i.e., the central Bullfrog Tuff from C#1 or C#2). However, it appears from Figures 78 to 84 that any of these differences should have been minimal.

The error bounds shown in Figures 78 to 84 reflect uncertainty due to analytical errors in determining lithium concentrations in solution. The error bounds were calculated assuming a 5% relative standard deviation in the lithium concentration measurements (typical for ICP-AES analyses). Errors increase as concentrations increase because there is a lower percentage of lithium sorbing at higher concentrations and, hence, a smaller relative difference between measured initial and final solution concentrations. It is apparent that the scatter in the data sets often exceeds the analytical error bounds, suggesting other sources of error besides analytical errors. These other potential sources of error have not been systematically identified.

The fitted Langmuir isotherms corresponding to all seven C-wells tuff lithologies are plotted together in Figure 85. By comparing Figure 85 to the XRD results of Table 25, it is apparent that the two tuffs demonstrating the greatest affinity for lithium (Bedded Prow Pass and Lower Bullfrog) are also the tuffs that have the greatest smectite and/or zeolite contents. A quantitative relationship between lithium sorption and tuff mineralogy is discussed further below.

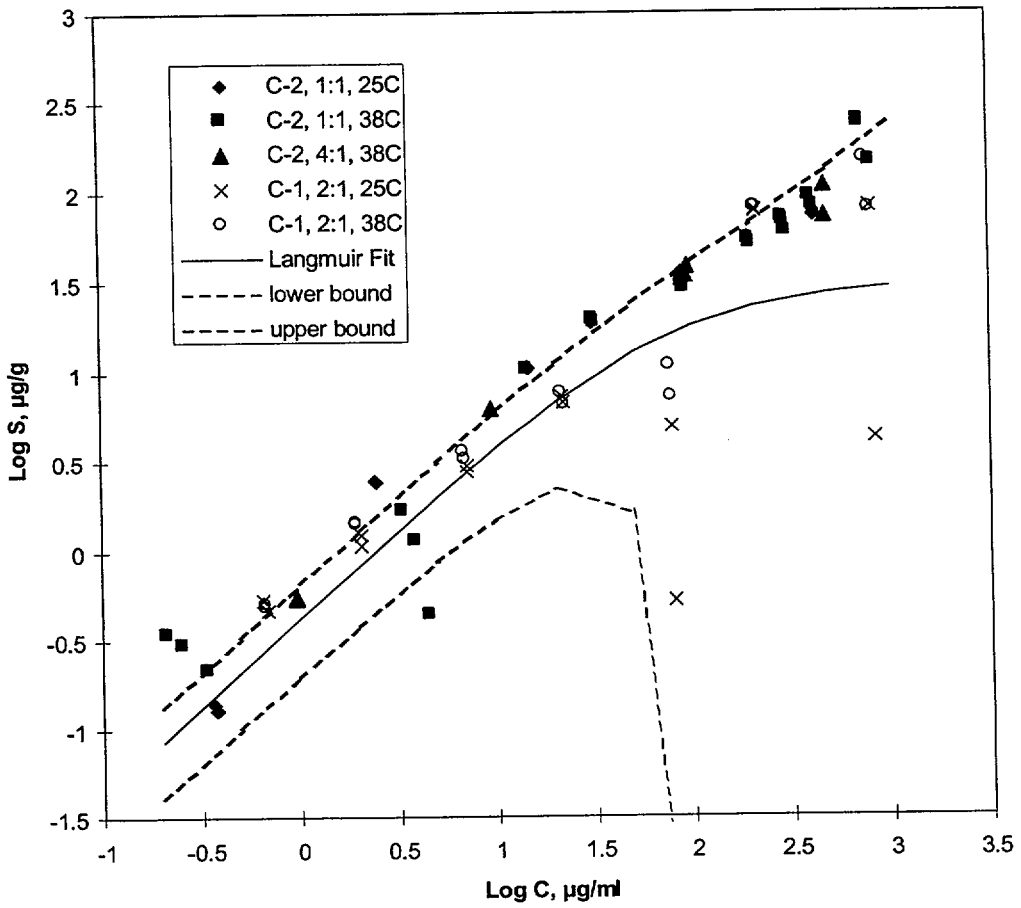

NOTE: C-1 and C-2 refer to UE-25 c#1 and c#2, respectively. The legend indicates the borehole (C-1 or C-2) from which the tuff came, the solution:solid ratio (mL:g), and the temperature of the experiments. The dashed lines are error bars associated with 5% analytical measurement error. J-13 water was used in all experiments except for "C-2, 4:1, 38C." Water from C#3 was used for "C-2, 4:1, 38C." The lithium concentration range in the Bullfrog Tuff field test spanned from less than 0.1 µg/mL up to 1200 µg/mL.

Figure 78. Lithium Sorption Data and Fitted Langmuir Isotherm for the Central Bullfrog Tuff

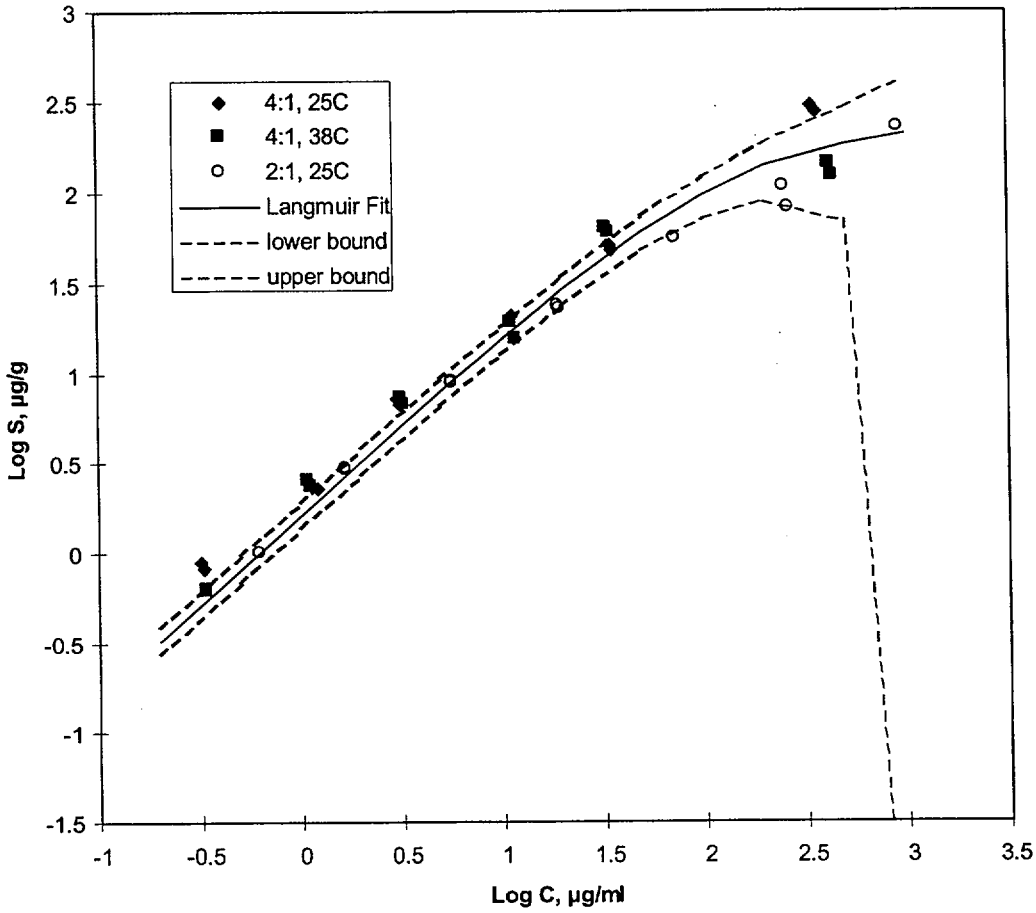

NOTE: The legend indicates the solution:solid ratio (mL:g) and the temperature of the experiments. The dashed lines are error bars associated with 5% analytical measurement error. J-13 water was used in all experiments. The lithium concentration range in the Bullfrog Tuff field test spanned from less than 0.1 µg/mL up to 1200 µg/mL.

Figure 79. Lithium Sorption Data and Fitted Langmuir Isotherm for the Lower Bullfrog Tuff

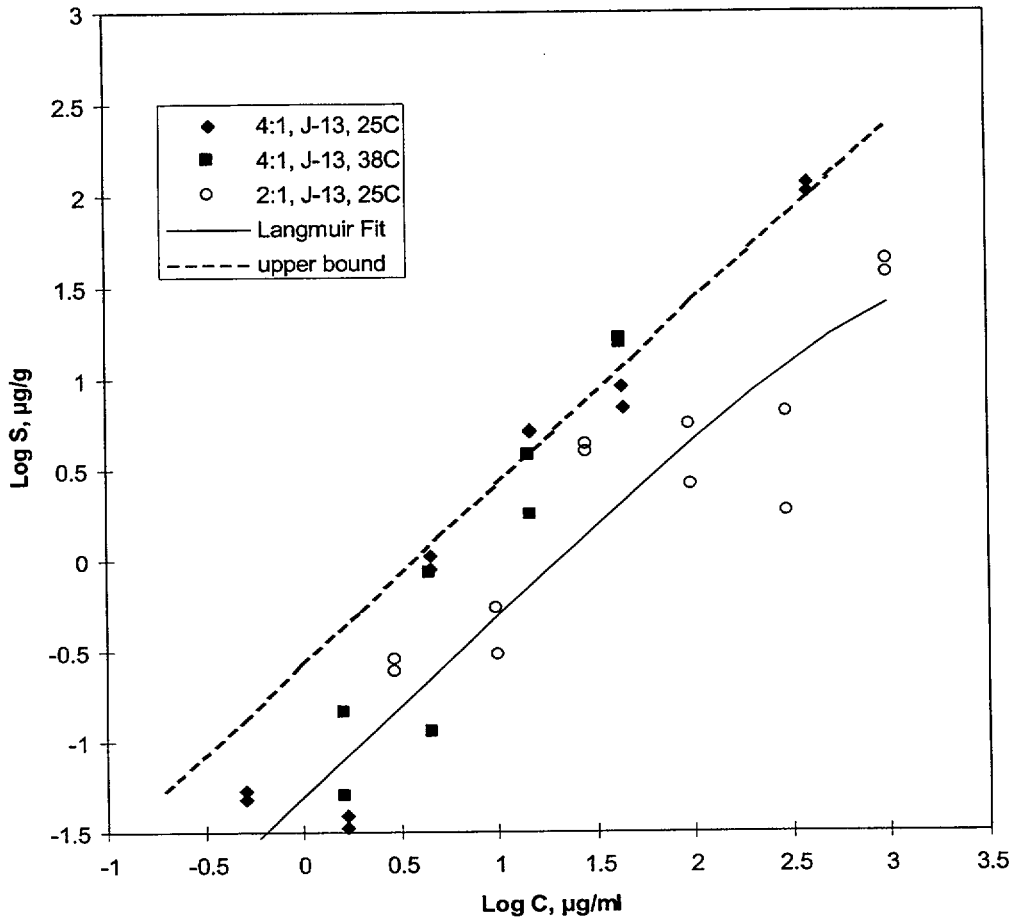

NOTE: The legend indicates the solution:solid ratio (mL:g) and the temperature of the experiments. The dashed lines are error bars associated with 5% analytical measurement error (lower error bound is off-scale over entire range of data). J-13 water was used in all experiments. The lithium concentration in the Prow Pass Tuff field test ranged from less than 0.1 µg/mL up to 2700 µg/mL.

Figure 80. Lithium Sorption Data and Fitted Langmuir Isotherm for the Upper Prow Pass Tuff

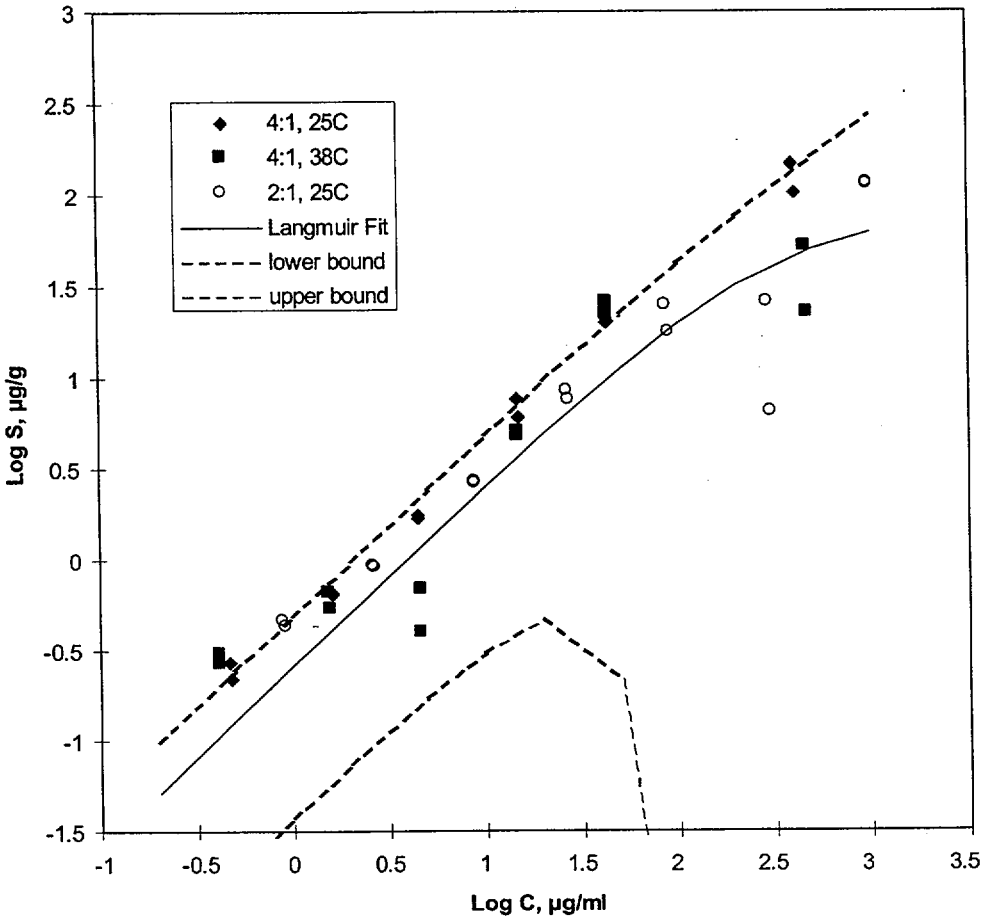

NOTE: The legend indicates the solution:solid ratio (mL:g) and the temperature of the experiments. The dashed lines are error bars associated with 5% analytical measurement error. J-13 water was used in all experiments. The lithium concentration in the Prow Pass Tuff field test ranged from less than 0.1 µg/mL up to 2700 µg/mL.

Figure 81. Lithium Sorption Data and Fitted Langmuir Isotherm for the Central Prow Pass Tuff

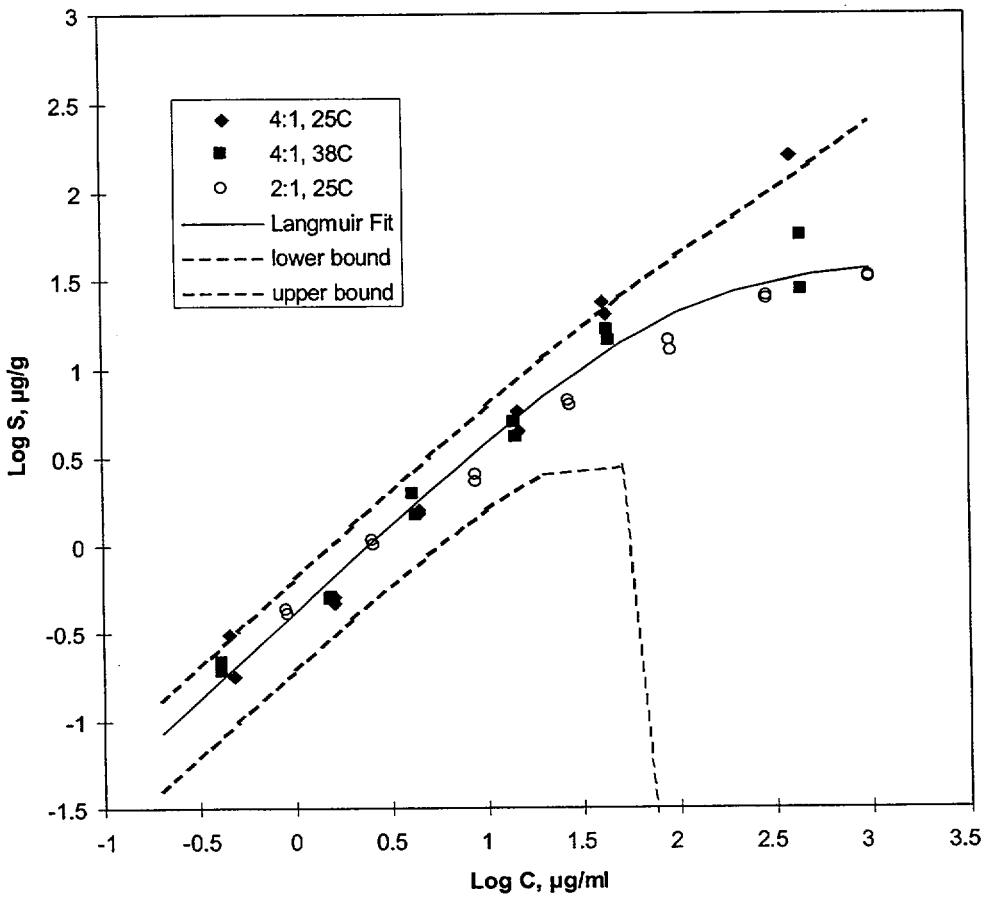

NOTE: The legend indicates the solution:solid ratio (mL:g) and the temperature of the experiments. The dashed lines are error bars associated with 5% analytical measurement error. J-13 water was used in all experiments. The lithium concentration in the Prow Pass Tuff field test ranged from less than 0.1 µg/mL up to 2700 µg/mL.

Figure 82. Lithium Sorption Data and Fitted Langmuir Isotherm for the Lower Prow Pass Tuff

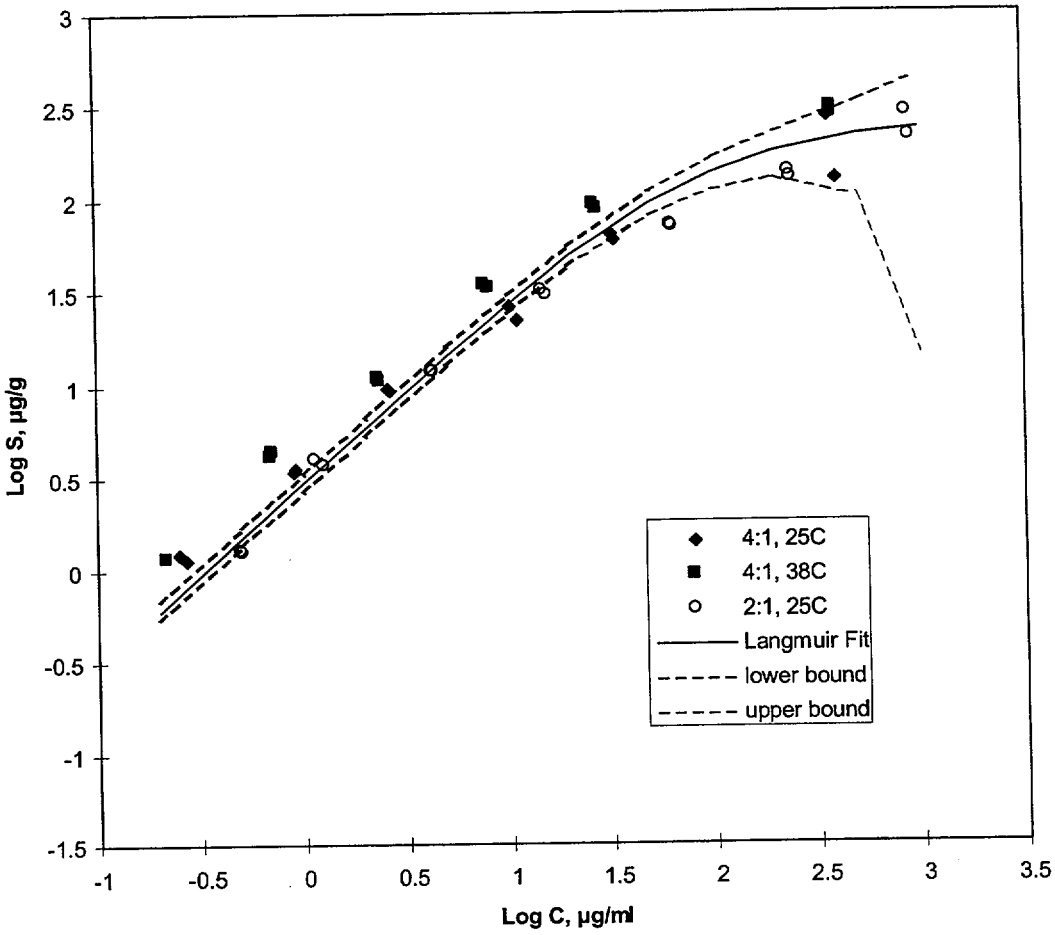

NOTE: The legend indicates the solution:solid ratio (mL:g) and the temperature of the experiments. The dashed lines are error bars associated with 5% analytical measurement error. J-13 water was used in all experiments.

Figure 83. Lithium Sorption Data and Fitted Langmuir Isotherm for the Bedded Prow Pass Tuff

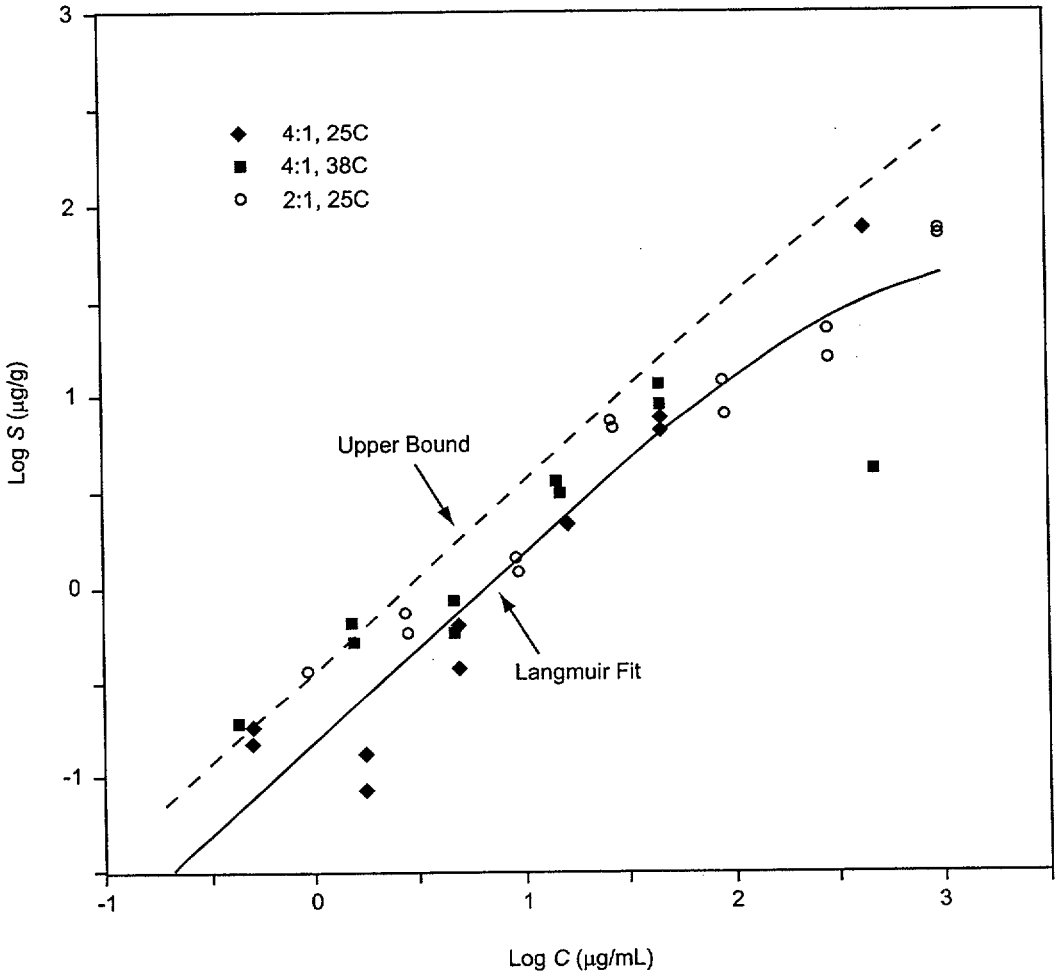

NOTE: The legend indicates the solution:solid ratio (mL:g) and the temperature of the experiments. The dashed lines are error bars associated with 5% analytical measurement error (lower error bound is off-scale over entire range of data). J-13 water was used in all experiments.

Figure 84. Lithium Sorption Data and Fitted Langmuir Isotherm for the Upper Tram Tuff

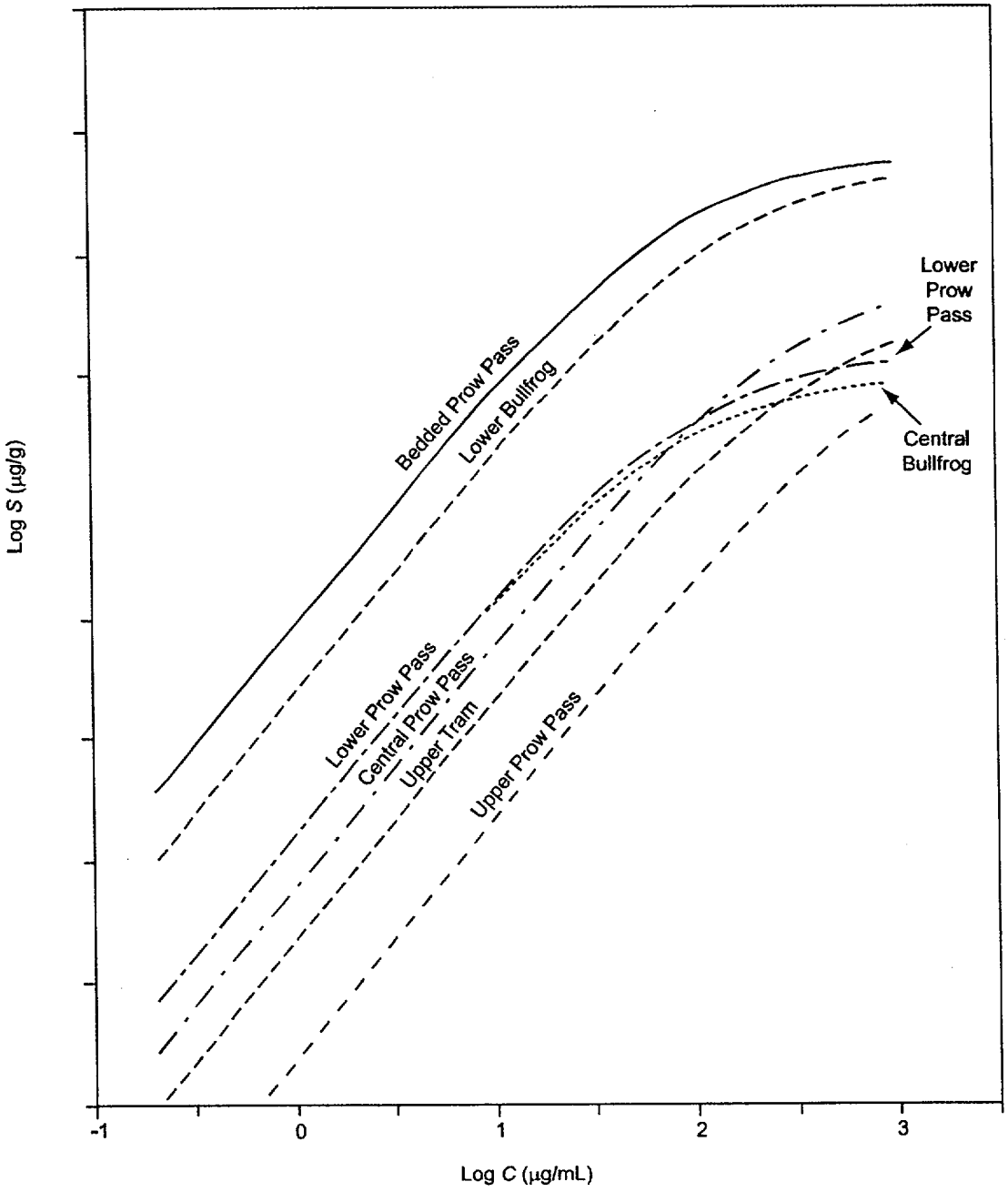

NOTE: The lithium concentration range in the field test in the central and lower Bullfrog Tuff spanned from less than 0.1 µg/mL up to 1200 µg/mL. The concentration range in the Prow Pass Tuff field test ranged from less than 0.1 µg/mL up to 2700 µg/mL.

Figure 85. Fitted Langmuir Isotherms for the Seven C-wells Tuffs

Table 26. Lithium Sorption Isotherm Parameters Associated with the Different C-wells Tuffs

Unit	Langmuir		Freundlich		Linear
	K_L (L/mg)	S_{max} (µg/g)	K_F	N	K_d (mL/g)
Central Bullfrog, C#1 + C#2 [(a)]	0.014	31.4	0.69	0.79	0.186
Lower Bullfrog, C#1	0.0070	233.9	2.26	0.75	0.321
Upper Prow Pass, C#2	0.00094	53.1	0.075	1.03	0.068
Central Prow Pass, C#2	0.0031	83.3	0.48	0.80	0.131
Lower Prow Pass, C#1	0.011	39.8	0.48	0.78	0.084
Bedded Prow Pass, C#2	0.012	254.9	4.17	0.69	0.383
Upper Tram, C#2	0.0026	59.8	0.27	0.78	0.072

NOTE: C#1 and C#2 are abbreviations for boreholes UE-25 c#1 and UE-25 c#2, respectively.

(a) Sorption data from C#1 and C#2 tuffs lumped together to obtain parameter estimates.

Results of the four CEC measurements on the seven tuff samples are presented in Figure 86 and Table 27. In all cases, the total CEC available to Cs ($CEC\text{-}Cs_T$) exceeds that available to Li ($CEC\text{-}Li_T$). This result is not surprising; the hydrated ionic radius of Cs (0.33 nm) is smaller than that of Li (0.38 nm) (Israelachvili 1992), which permits Cs access to internal exchange sites in zeolites that are not available to Li. More surprising is the consistent observation that Cs displaces more Li during the displacement step than Li displaced other cations during initial saturation (i.e., $CEC\text{-}Cs_{Li} > CEC\text{-}Li_T$). This phenomenon, a "lithium excess" during the displacement step, was also reported by Eckstein et al. (1970). They attributed this Li excess to a separate process that occurs in addition to normal cation exchange: selective and specific adsorption of Li, particularly to amorphous silicates and to edges and broken bonds of non-expanding clay minerals. They state that "it [is] difficult or even doubtful that a 'true' value for the exchange capacity can be given for any specific clay." They further conclude that "the sum of cations replaced by Li will usually give a better value for the exchange capacity than the amount of Li retained and replaced by $Ca(OAc)_2$."

Inspection of the mineralogy of the samples, presented in Table 25, indicates that the primary minerals likely to participate in cation exchange include smectite and the zeolite minerals clinoptilolite and mordenite. (Although analcime has a high theoretical CEC [Ming and Mumpton 1989] kinetic factors prevent significant cation exchange at normal environmental temperatures, [Vaughn 1978].) To test whether a simple two-mineral model could explain the observed measurements, a multivariable linear regression was conducted on the CEC results, using measured smectite and (clinoptilolite + mordenite) fractions (f_{smec}, $f_{clin/mord}$) as independent variables, and three CEC estimates as the dependent variables. In all cases, the model yielded excellent results.

$$CEC\text{-}Li_T = 106\pm8 \text{ meq/100g}\cdot f_{smec} + 99\pm3 \text{ meq/100g}\cdot f_{clin/mord} + 1.5\pm0.3 \text{ meq/100g}, r^2 = 0.997.$$

$$CEC\text{-}Cs_{Li} = 103\pm13 \text{ meq/100g}\cdot f_{smec} + 95\pm5 \text{ meq/100g}\cdot f_{clin/mord} + 6.1\pm0.5 \text{ meq/100g}, r^2 = 0.990.$$

$$CEC\text{-}Cs_T = 90\pm13 \text{ meq/100g}\cdot f_{smec} + 199\pm5 \text{ meq/100g}\cdot f_{clin/mord} + 7.7\pm0.5 \text{ meq/100g}, r^2 = 0.997.$$

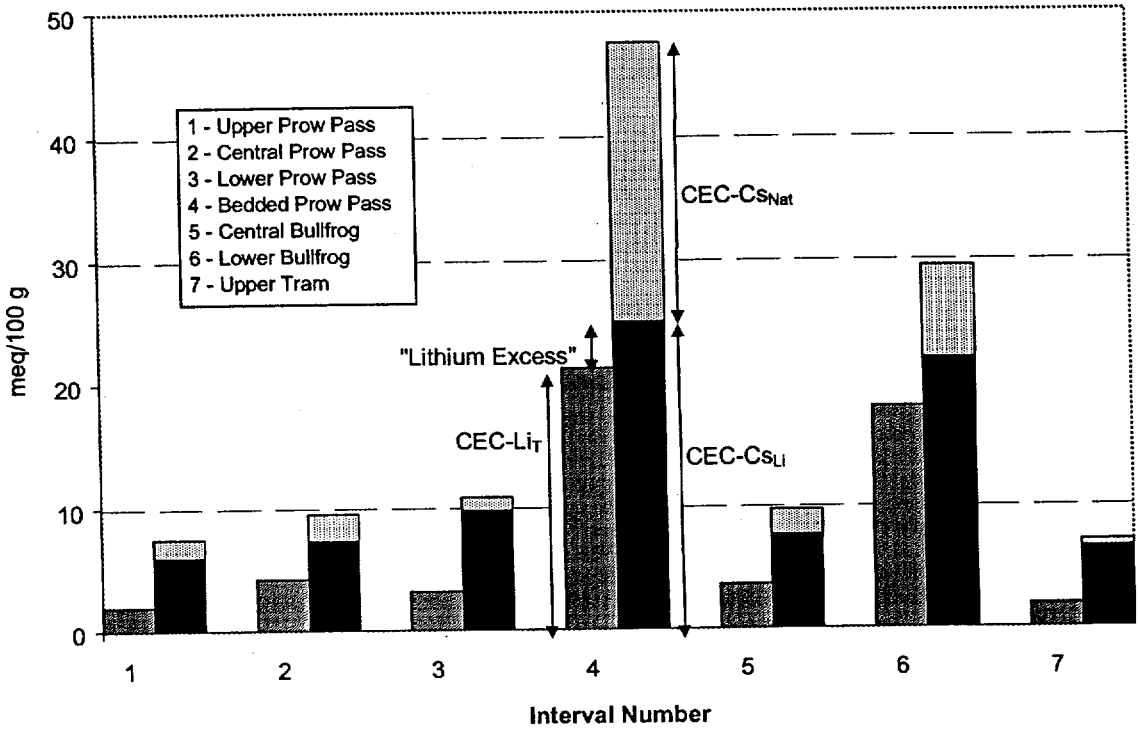

Figure 86. Cation Exchange Capacity Results for the Seven Different C-wells Tuff Intervals

Table 27. Cation Exchange Capacity Measurements for C-wells Tuffs

Sample	Cation Exchange Capacity (meq/100g)				
	CEC-Li$_T$	*CEC-Cs$_{Nat}$*	*CEC-Cs$_{Li}$*	*CEC-Cs$_T$*	Li Excess
Upper Prow Pass	2.0 ± 0.5	1.5 ± 0.1	6.1 ± 0.8	7.5	4.1
Central Prow Pass	4.3 ± 0.1	2.1 ± 0.0	7.4 ± 0.4	9.5	3.1
Lower Prow Pass	3.2 ± 0.4	1.0 ± 0.9	9.8 ± 1.9	10.8	6.6
Bedded Prow Pass	21.3 ± 0.1	22.5 ± 0.4	25.0 ± 1.4	47.5	3.8
Central Bullfrog [(a)]	3.7 ± 0.1	2.0 ± 0.5	7.7 ± 0.6	9.7	4.1
Lower Bullfrog	18.0 ± 0.2	7.5 ± 0.4	21.9 ± 0.2	29.5	4.0
Upper Tram	1.9 ± 0.1	0.5 ± 0.2	6.6 ± 0.5	7.1	4.7

NOTE: Range shown is ± one standard deviation. Refer to text for definitions.

(a) Only the Central Bullfrog Tuff from C#1 was analyzed for CEC.

The exchange factors for the individual minerals can be compared to literature values of 110 ± 23 meq/100 g for smectite (Borchardt 1989) and 220 meq/100 g for both clinoptilolite and mordenite (Ming and Mumpton 1989). Starting with the model for $CEC\text{-}Li_T$, we see that the specific exchange capacity for smectite matches previously reported values, whereas the modeled capacity for the zeolite minerals is less than half that reported elsewhere. This discrepancy is consistent with the inaccessibility of some of the internal zeolite exchange sites to the relatively large Li ion. The $CEC\text{-}Li_T$ model includes a relatively small constant term, indicating that almost all of the observed behavior can be explained by smectite and clinoptilolite/mordenite cation exchange. Comparing this model to the $CEC\text{-}Cs_{Li}$ model, we see that the major difference lies in the constant term; the larger constant term in the second model reflects the observed Li excess. The similarity of the other two terms demonstrates that the Li-excess effect is not a result of exchange onto either smectite or clinoptilolite/mordenite; additional correlation analysis shows that the Li excess is not proportional to any of the mineral phases identified by quantitative x-ray diffraction (QXRD). These observations, combined with the overall uniformity of the Li excess among these widely varying tuff samples, lead one to agree with Eckstein et al. (1970) and attribute the Li excess to a noncation exchange sorption process.

The final model for $CEC\text{-}Cs_T$ reveals a similar specific CEC for smectite as found in the literature and the previous models but shows a much higher specific CEC for the zeolite minerals, which is more in line with published values. This demonstrates the accessibility to the smaller Cs ion of internal exchange sites that were apparently unavailable to Li.

To a first approximation, it can be seen that the two samples that sorb Li most strongly have the highest isotherms in Figure 86 and the largest K_d and K_F values in Table 26. These two rocks also showed the highest CEC values. To quantify the sorption relationships more rigorously, the linearization of the nonlinear Freundlich isotherm was undertaken, and K_{lin} was calculated. K_{lin} is an effective distribution coefficient with uniform units, identical to those of K_d. For this purpose, the equal-area linearization of van Genuchten et al. (1977) was used:

$$K_{lin} = \frac{2K_F C_{max}^{n-1}}{n+1} \qquad \text{(Eq. 14)}$$

where C_{max} is the maximum concentration of interest; in this case, 1000 mg/L. Using the same multivariate linear regression methods described above, K_{lin} can be modeled as a function of smectite and clinoptilolite/mordenite content:

$$K_{lin} = 1.70\pm0.71 \text{ L/kg}\cdot f_{smec} + 1.87\pm0.29 \text{ L/kg}\cdot f_{clin/mord} + 0.06\pm0.03 \text{ L/kg}, r^2 = 0.924.$$

This model does not fit the data as well as the CEC models described above but, nevertheless, demonstrates that Li sorption can be estimated fairly accurately for these tuffs, given smectite, clinoptilolite, and mordenite concentrations. The small constant term in the model indicates that the contribution of other minerals to Li sorption is quite low.

3.8.3 Conclusions from Batch Lithium Sorption Studies

Lithium ion sorption onto devitrified tuffs from the saturated zone near Yucca Mountain follows nonlinear isotherm behavior. Both the lithium sorption parameters and the lithium-specific

cation exchange capacities of the tuffs are highly correlated with the clay (smectite) content and the zeolite (clinoptilolite + mordenite) content of the tuffs. Multiple linear regression analyses shows that these two classes of minerals account for the majority of the observed lithium exchange. Regression of cesium cation-exchange data yields results that are consistent with the accessibility of the smaller cesium ion to internal zeolite exchange sites that lithium cannot access. The cesium CEC data also suggest that some of the lithium sorption to the tuffs can be attributed to a noncation exchange process. The results of this study support the development and use of mineralogy-based models for predicting cation sorption in the saturated zone near Yucca Mountain.

3.9 DIFFUSION CELL EXPERIMENTS

3.9.1 Materials and Methods

Six diffusion cell experiments were conducted to determine diffusion coefficients of PFBA and bromide ion in five different C-wells tuff matrices. Estimates of matrix diffusion coefficients are important because they can greatly reduce uncertainty in interpreting and predicting both field-scale and laboratory-scale tracer experiments. One of the tests was a repeat experiment using a different core from the same interval as another test (the lower Prow Pass Tuff). This test was conducted to determine the reproducibility and variability of the experiments. The five different intervals tested in the diffusion cell experiments represented all of the major lithologies in either the Bullfrog field tracer test or the Prow Pass field tracer test.

A schematic drawing of the experimental diffusion cell apparatus is illustrated in Figure 87. The apparatus consists of two Plexiglas reservoirs, one large and one small, separated by a "pellet" of tuff, which is cut/cored from C-wells core and incorporated into either a flat epoxy cast or an RTV (room-temperature vulcanizing) silicone cast of the same thickness as the pellet. After saturating the tuff, experiments were initiated by carefully pouring a solution containing PFBA and LiBr into the large reservoir and tracer-free solution into the small reservoir. The pressures in the two reservoirs were kept approximately equal to minimize advective flow through the tuff, thus ensuring that tracer movement through the tuff was by diffusion only. The small reservoir was kept well mixed with a magnetic stir bar and flushed continuously at a relatively low flow rate. The flush water was collected in an automatic fraction collector, and fractions were analyzed for tracers to establish BTCs through the tuff from which diffusion coefficients could be estimated. As in the other laboratory experiments, PFBA and bromide were analyzed by liquid chromatography, and lithium was analyzed by ICP-AES. Filtered J-13 water or synthetic J-13 water (a sodium/calcium bicarbonate solution having the same ionic strength as J-13 water) were used in all experiments.

The porosities of the tuffs were measured by subtracting dry weights from saturated weights of intact tuff samples and dividing by the volumes of the samples (measured by water displacement). Porosity measurements were used to obtain unambiguous estimates of diffusion coefficients in the tuff matrices (see equations below). Hydraulic conductivities/permeabilities of the tuffs were also measured by imposing a known head difference across the tuff pellets, either before or after a diffusion experiment was conducted. The flow through the pellets at the imposed head difference was measured by weighing the water that flowed through the pellet over a specified amount of time.

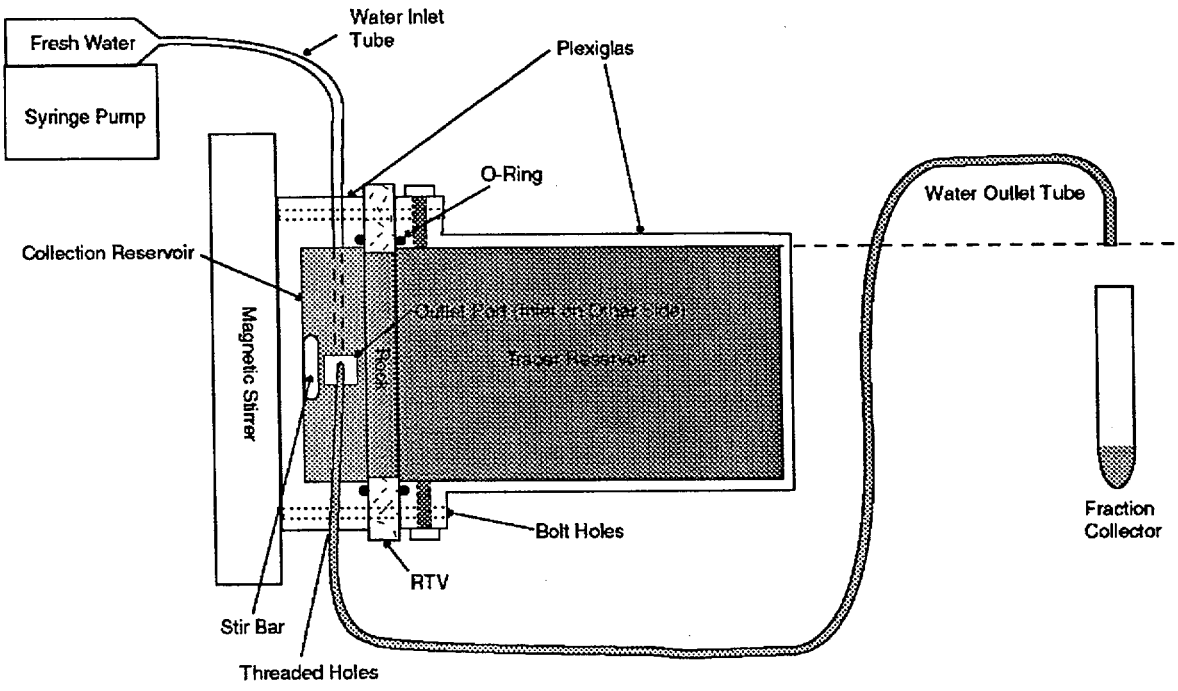

Figure 87. Diffusion Cell Experimental Apparatus

Hydraulic conductivities were then calculated from the following equation:

$$K = -\frac{Q L}{A \Delta H} \qquad \text{(Eq. 15)}$$

where

K = hydraulic conductivity, cm/sec
ΔH = water height (head) difference across pellet, cm
A = surface area of pellet, cm^2
Q = volumetric flow rate through pellet, ml/sec
L = thickness of pellet, cm.

Permeabilities were calculated from hydraulic conductivities using the following well-known formula (Freeze and Cherry 1979, pp. 26 to 30):

$$k = \left(1.013 \times 10^{11}\right)\frac{K \mu}{\rho g} \qquad \text{(Eq. 16)}$$

where

k = permeability, millidarcys (mD)
μ = water viscosity, g/cm-sec
ρ = water density, g/cm^3
g = acceleration due to gravity, cm/sec^2
and the constant 1.013 x 10^{11} has units of mD/cm^2.

To estimate diffusion coefficients, it was assumed that the tracers moved according to 1-D diffusive transport through the tuff pellets. The 1-D diffusion equation is:

$$\frac{\partial c}{\partial t} = \frac{D}{R}\frac{\partial^2 c}{\partial x^2} \qquad \text{(Eq. 17)}$$

where

c = tracer concentration, µg/mL
D = diffusion coefficient, cm^2/sec
R = retardation factor (1 for nonsorbing solutes),
x = distance, cm
t = time, sec.

Although analytical solutions to this simple partial differential equation exist for simple boundary conditions (Jenson and Jeffreys 1977, pp. 291 to 295), the time-dependent concentration boundary conditions at the inlet and outlet reservoirs in the diffusion cell experiments demand a numerical solution. Thus, Equation 17 was solved using an implicit finite-difference technique. The equations describing the tracer concentrations in the inlet and the outlet reservoirs (the first and last finite difference nodes), respectively, were:

$$\frac{\partial c_i}{\partial t} = \frac{\phi \pi r^2 D}{V_i}\left.\frac{\partial c}{\partial x}\right|_{x=0} \qquad \text{(Eq. 18)}$$

$$\frac{\partial c_o}{\partial t} = -\frac{\phi \pi r^2 D}{V_o}\left.\frac{\partial c}{\partial x}\right|_{x=L} - \frac{Q}{V_o}c_o \qquad \text{(Eq. 19)}$$

where

c_i = tracer concentration in inlet reservoir, µg/mL
c_o = tracer concentration in outlet reservoir, µg/mL
V_i = volume of inlet reservoir, mL
V_o = volume of outlet reservoir, mL
Q = flush rate of outlet reservoir, mL/sec
ϕ = porosity of tuff
r = radius of tuff "pellet", cm
L = thickness of tuff "pellet", cm.

The numerical solution of Equations 17, 18, and 19 was obtained using computer code DIFFCELL. This code allows the user to specify changes in the flush rate, Q, with time, which was necessary to simulate the manner in which the experiments were conducted.

3.9.2 Results and Discussion

Figures 88 through 93 show the BTCs of the bromide and PFBA in each of the six diffusion cells along with "fits" to the data obtained using DIFFCELL. The "fits" are not actual least-squares fits; rather, they were obtained by manual adjustment of the diffusion coefficients until a reasonable match to the data was obtained. The apparent discontinuities in some of the data sets and the corresponding model predictions are a consequence of changes in the flush rate through the outlet reservoirs. A decrease in concentration occurs when the flush rate is increased and vice-versa.

The resulting estimates of tracer diffusion coefficients in each diffusion cell are given in Table 28 (measured tuff porosities, pellet thicknesses, and tuff permeabilities are also listed in this table). It is apparent that there is about an order of magnitude range of diffusion coefficients in the various tuff lithologies. Figures 94 and 95 show the bromide diffusion coefficients in the tuff matrices as a function of porosity and permeability, respectively, for the five different C-wells tuffs. Although the diffusion coefficients are not well correlated with porosity, they are quite well correlated with permeability (on a log-log scale). This result suggests that permeability may be a good predictor of matrix diffusion coefficients. Such correlations could prove useful for estimating matrix diffusion coefficients, as diffusion coefficients are typically more difficult to measure than matrix properties such as permeabilities.

Table 28 shows that excellent agreement was obtained between the two diffusion cell experiments conducted for the same lithology (the lower Prow Pass Tuff). This result suggests that the experiments have reasonably good reproducibility, although certainly more experiments should be conducted in the same lithologies before measurement uncertainty and tuff variability can be properly assessed.

It is interesting to note that although the PFBA and bromide diffusion coefficients are significantly different in the different tuffs, the ratios of the diffusion coefficients are approximately the same in each tuff. This result suggests that advection through the tuff pellets was successfully eliminated, as any advection would result in different ratios in different tests. The factor of ~3 difference in the diffusion coefficients of the PFBA and bromide is the basis for assuming a factor of 3 difference in all of the field and laboratory tracer-test interpretations in this report.

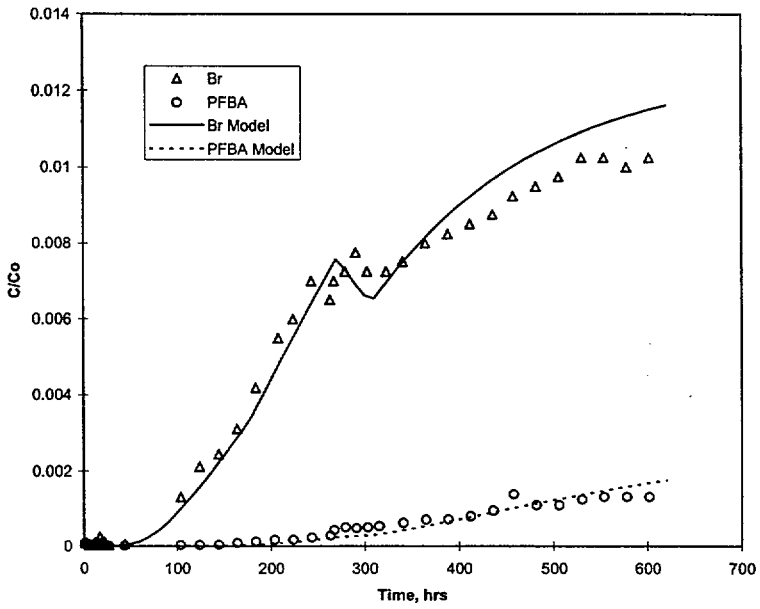

NOTE: Diffusion coefficients are given in Table 28.

Figure 88. Diffusion Cell Data and DIFCEL Model Fits for Bromide and PFBA in the Central Bullfrog Tuff

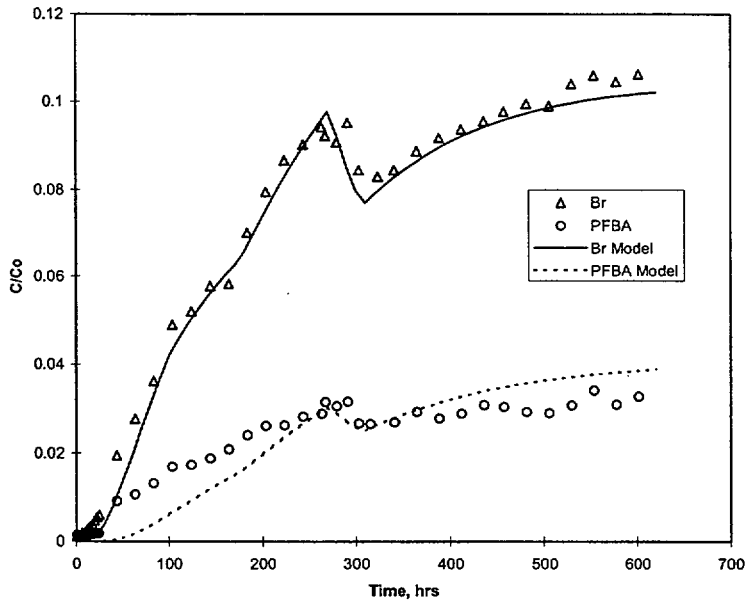

NOTE: Diffusion coefficients are given in Table 28.

Figure 89. Diffusion Cell Data and DIFCEL Model Fits for Bromide and PFBA in the Lower Bullfrog Tuff

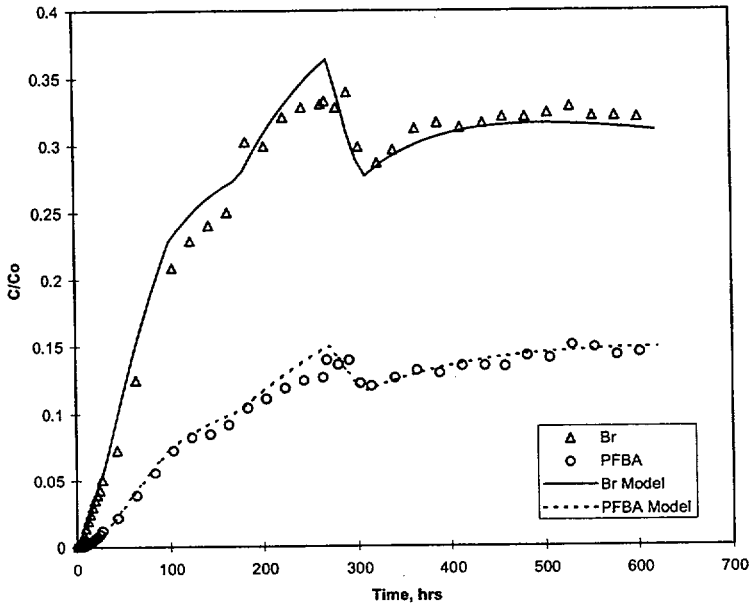

NOTE: Diffusion coefficients are given in Table 28.

Figure 90. Diffusion Cell Data and DIFCEL Model Fits for Bromide and PFBA in the Upper Prow Pass Tuff

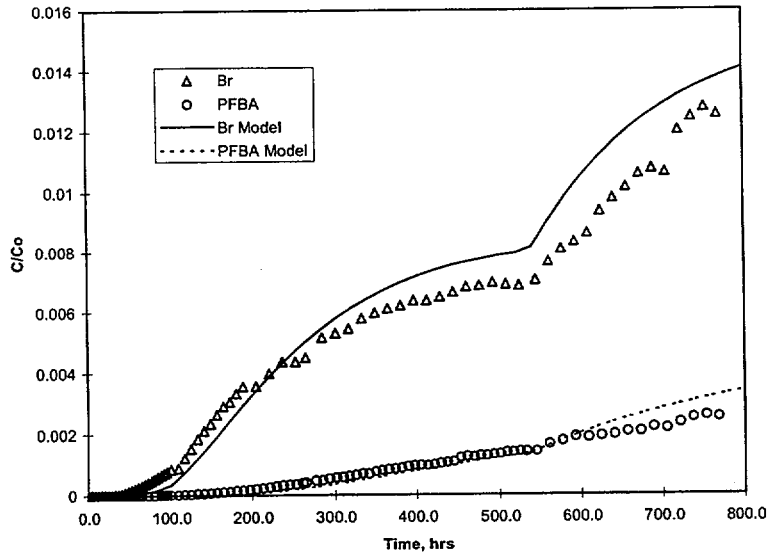

NOTE: Diffusion coefficients are given in Table 28.

Figure 91. Diffusion Cell Data and DIFCEL Model Fits for Bromide and PFBA in the Central Prow Pass Tuff

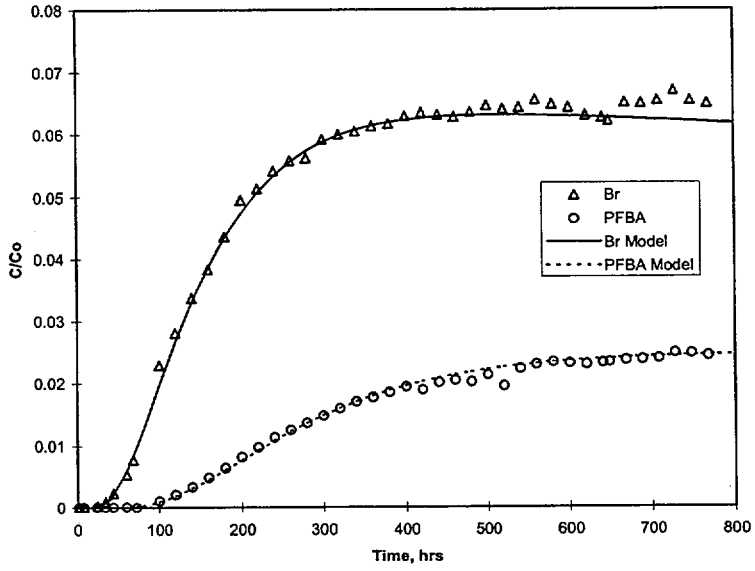

NOTE: Diffusion coefficients are given in Table 28.

Figure 92. First Diffusion Cell Data and DIFCEL Model Fits for Bromide and PFBA in the Lower Prow Pass Tuff

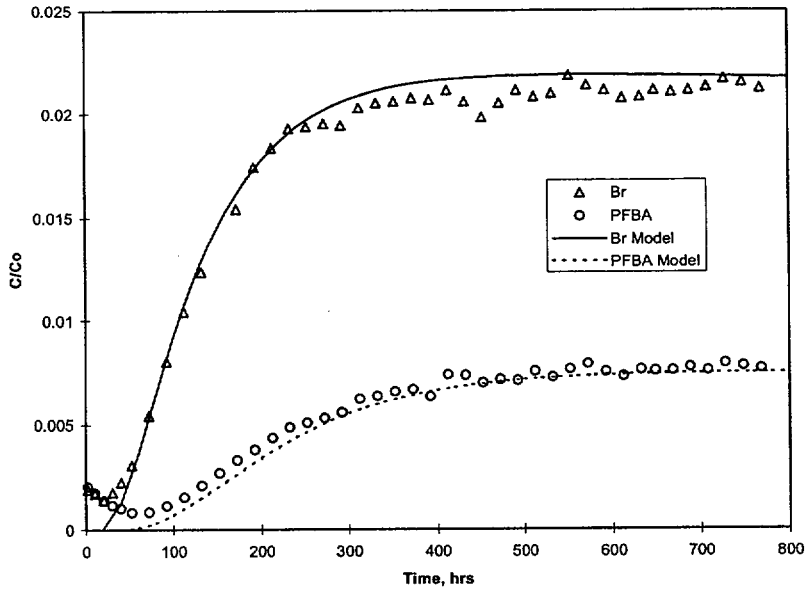

NOTE: Diffusion coefficients are given in Table 28.

Figure 93. Second Diffusion Cell Data and DIFCEL Model Fits for Bromide and PFBA in the Lower Prow Pass Tuff

Table 28. Measured Porosities, Permeabilites, and Matrix Diffusion Coefficients of Bromide and PFBA in C-wells Tuffs

Tuff [a]	Porosity	Permeability (mDarcy)	Thickness [b] (cm)	Diffusion Coefficient ($cm^2/s \times 10^6$)		
				Br	PFBA	Br/PFBA
Central Bullfrog (1)	0.094	0.00107	1.16	0.45	0.13	3.46
Lower Bullfrog (3)	0.298	0.0949	0.84	1.0	0.35	2.86
Upper Prow Pass (4)	0.272	4.72	0.91	6.0	1.9	3.16
Central Prow Pass (5)	0.138	0.000786	1.23	0.4	0.13	3.08
Lower Prow-1 (6)	0.288	0.455	2.27	3.0	1.1	2.73
Lower Prow-2 (6)	0.288	0.455	1.82	3.0	1.0	3.0

NOTE: Synthetic J-13 water was used for the experiments involving the first three tuffs. Filtered J-13 water was used in the other three experiments.

(a) Numbers in parentheses correspond to numbers in Figure 77 (locations where core was collected from the C-wells) and in Table 24 (where actual depths associated with the cores are listed).

(b) Thickness, *L*, of tuff wafer.

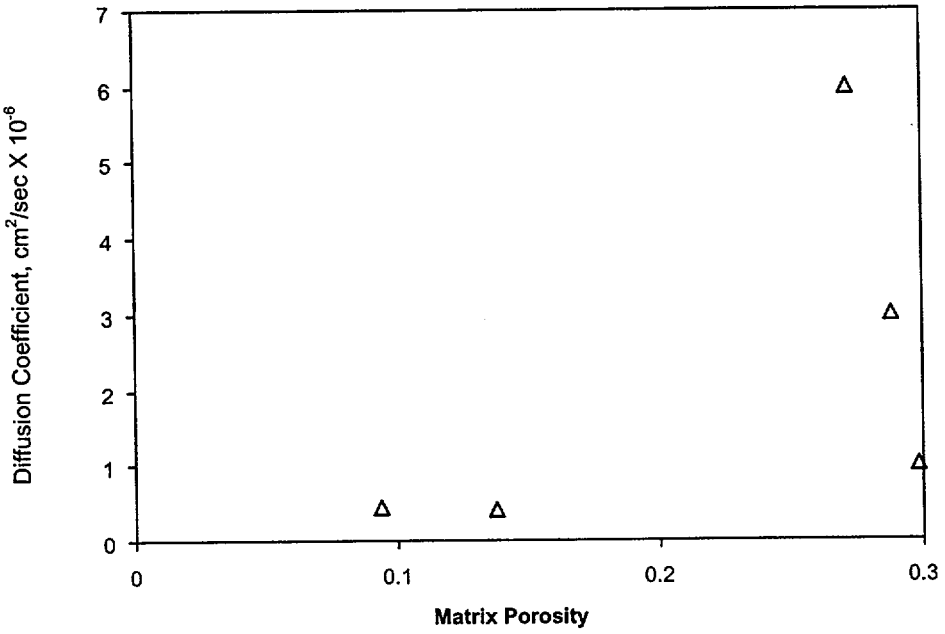

NOTE: Porosity and diffusion coefficient for bromide are listed in Table 28.

Figure 94. Bromide Diffusion Coefficients Versus Tuff Porosity for all C-wells Diffusion Cell Experiments

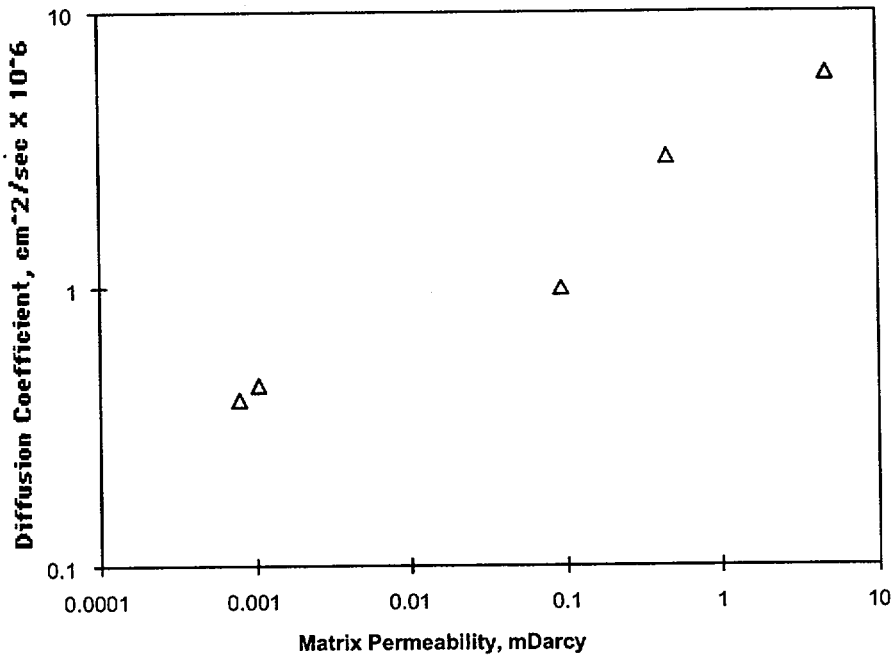

NOTE: Permeability and diffusion coefficient are listed in Table 28.

Figure 95. Bromide Diffusion Coefficients Versus Tuff Permeability for all C-wells Diffusion Cell Experiments

3.10 LABORATORY STUDIES OF LITHIUM TRANSPORT IN TUFF COLUMNS AND FRACTURES

Several laboratory transport experiments were conducted to study lithium transport under flowing conditions in both columns packed with crushed C-wells tuff and fractured C-wells cores. The crushed-tuff column experiments were conducted to compare lithium sorption parameters under flowing conditions to batch-sorption measurements. The fractured-core experiments were conducted to study lithium transport under more realistic fracture flow conditions where matrix diffusion and sorption in the matrix should also influence transport. The crushed-tuff experiments are described in Section 3.10.1, and the fractured-core experiments are described in Section 3.10.2.

3.10.1 Crushed-Tuff Column Experiments

3.10.1.1 Experimental Methods

A series of transport experiments was conducted in plexiglass columns 91.44 cm in length and 0.62 cm in diameter. The columns were packed with crushed central Bullfrog Tuff (from location number 2 in Figure 77) that had been wet-sieved to a size range between 75 and 500 μm. A wet slurry technique was used to pack the columns. Column porosity was measured at ~57%, and dry bulk density was calculated at 1.14 g/mL by assuming a mineral density of 2.65 g/mL, which are typical values for columns prepared in this fashion (e.g., Treher and Raybold 1982, pp. 8 to 9; Thompson 1989). Three columns were prepared identically. The column apparatus included a constant-rate pump, a valve to switch between a reservoir containing J-13 "background" water and a solution of lithium bromide in J-13 water, and an automatic fraction collector at the downstream end of the column. Each experiment began by pumping approximately 180 mL (roughly 12 pore volumes) of J-13 water through the column at a specified flow rate to equilibrate the tuff with the groundwater. The input was then switched to a lithium bromide solution, which was maintained for approximately three pore volumes before being switched back to tracer-free groundwater. Effluent samples were analyzed for lithium and bromide using liquid chromatography (detection limits were 0.10 mg L^{-1} for Li^+ and 0.005 mg L^{-1} for Br^-). Bromide was used as a nonsorbing tracer to determine mean residence times and dispersivities in the columns as well as to serve as a conservative tracer against which lithium retardation could be gauged.

A total of five experiments was conducted in the three columns, with the tracer concentrations and flow rate both being varied. In three of the five column experiments, the responses of Li^+ and Br^- were monitored until concentrations returned to background levels; in the other two experiments, concentrations were monitored only until they leveled off at the inlet concentrations. The experimental conditions are summarized in Table 29. The different tracer concentrations were intended to investigate potential effects of lithium sorption nonlinearity, and the different flow rates were intended to reveal rate-limited effects such as sorption nonequilibrium or diffusion-controlled sorption rates. All tests were conducted at 25°C.

3.10.1.2 Interpretive Methods

The bromide responses in the experiments were interpreted using the RELAP model to obtain estimates of mean residence times and dispersivities/Peclet numbers in the columns. RELAP was also used to fit the rising limbs of the lithium responses in each experiment to obtain an estimate of the lithium retardation factor in the columns. The rate-limited sorption features of RELAP were also used to obtain an estimate of the rate constant (k_f) describing lithium sorption onto the column packing material. The rate constants were obtained by relaxing the equilibrium sorption assumption and adjusting the rate constants for each data set until the RELAP fits were optimized. Damkohler numbers ($k_f\tau$), which represent the ratio of reaction rate to advection rate in the columns, were calculated for each experiment. Damkohler numbers significantly greater than one indicate a system that can be treated as being at equilibrium locally (Valocchi 1985).

It was apparent that while RELAP could fit the arrival of lithium, it could not fit the tails of the lithium responses when concentrations were monitored until they returned to background levels. The tails exhibited a behavior suggesting that a portion of the lithium eluted with the bromide as if it were a nonsorbing tracer. This behavior can occur when an ion-exchanging cation such as lithium comprises the majority of the cation equivalents in the tracer solution, which was certainly the case in the higher-concentration LiBr experiments. Essentially, if the CEC of the tuff and the exchange equilibria are not sufficient to exchange all of the lithium injected into a column, then some of the lithium must elute with the bromide to maintain charge balance in the solution exiting the column. Thus, for the tests in which the lithium was fully eluted from the columns, the MULTRAN model, which is capable of explicitly modeling cation exchange and maintaining solution charge balance, was used to interpret the lithium responses (see Section 3.10.2.2 for description of the model).

Table 29. Using RELAP to Fit Rising Limbs of Lithium and Bromide Breakthrough Curves in Crushed Tuff Columns

Column	Figure	Flow Rate (mL/hr)	Li Conc. (mg/L)	τ (hr)	*Pe*	R_F	k_f (1/hr)	*Da*
1*	97	2.2	23.5	8.2	300	2.0	2.2	18
1	98	1.6	23.5	11	300	1.9	3.6	40
2*	99	9.7	20.1	1.9	400	1.8	14	27
3*	100	2.2	5.9	8.0	400	2.3	18	140
3	101	1.6	5.9	11	400	2.2	14	160

NOTE: *Denotes experiments in which tracer concentrations were monitored until background levels were reached.

In this table, τ is residence time; *Pe* is the Peclet number; R_f is the retardation factor; k_f is the rate constant for sorption onto the column material; and *Da* is the Damkohler number ($=k_f\tau$), which represents the ratio of reaction rate to advection rate in the columns

3.10.1.3 Results and Interpretations

The rising limbs of the BTCs for the five experiments along with the RELAP fits to the data are shown in Figures 96 through 100. The best-fitting model parameters are listed in Table 29. Although significant improvements to the RELAP fits were obtained by assuming finite sorption rates, the relatively large Damkohler numbers listed in Table 29 suggest that the local equilibrium assumption is reasonably valid in the columns. Furthermore, this assumption should be even more valid in field experiments where tracer residence times are much longer than in the columns. Figure 96 shows the results of fitting the lithium response curve from one of the experiments assuming a nonlinear (Langmuir) sorption isotherm with parameters obtained from batch sorption testing (K_L = 0.0053 mL/µg and Smax = 110 µg/g for the Bullfrog Tuff from C#2 used in these columns). It is apparent that the model fits are not improved by assuming a nonlinear isotherm. The RETRAN model (Reimus and Haga 1999) was used for the nonlinear simulations.

Table 29 shows that lithium retardation factors (R_Fs) for the tests with lower tracer concentrations ranged from 2.2 to 2.3, with a mean of 2.25; whereas R_Fs for the higher concentration tests ranged from 1.7 to 2.0, with a mean of 1.87. The observed decreased R_F at higher concentrations is consistent with a nonlinear sorption isotherm. For the Langmuir isotherm, the R_F can be shown to be (Fetter 1993, pp. 122 to 123):

$$R_F = 1 + \frac{\rho_B}{\theta}\left(\frac{K_L S_{max}}{(1+K_L C)^2}\right) \qquad \text{(Eq. 20)}$$

where

ρ_B is the dry bulk density of the medium (g/mL)

θ is the volumetric moisture content, or porosity for a saturated medium.

By solving Equation 20 with the batch Langmuir parameters (K_L = 0.0053 mL/µg and S_{max} = 110 µg/g) and column values for ρ_B and θ, retardation factor predictions of 2.11 are obtained for the lower concentration tests and 1.95 for the higher concentration tests. Overall these predictions match the R_F values of Table 29 very well, differing by 7% or less for both concentration levels. The MULTRAN fits to the full data sets for the three experiments in which tracer concentrations were monitored until they returned to background levels are shown in Figures 101 to 103. The K_1 and K_2 values listed in these figures correspond to the "selectivity coefficients" (Q_1 and Q_2, respectively) for the following cation exchange reactions:

$$Li^+ + NaX \leftrightarrow LiX + Na^+ \quad Q_1 = \frac{[LiX][Na^+]}{[NaX][Li^+]} \qquad \text{(Eq. 21)}$$

$$2Li^+ + CaX_2 \leftrightarrow 2LiX + Ca^{2+} \quad Q_2 = \frac{[LiX]^2[Ca^{2+}]}{[CaX_2][Li^+]^2} \qquad \text{(Eq. 22)}$$

where X = a negatively charged surface site.

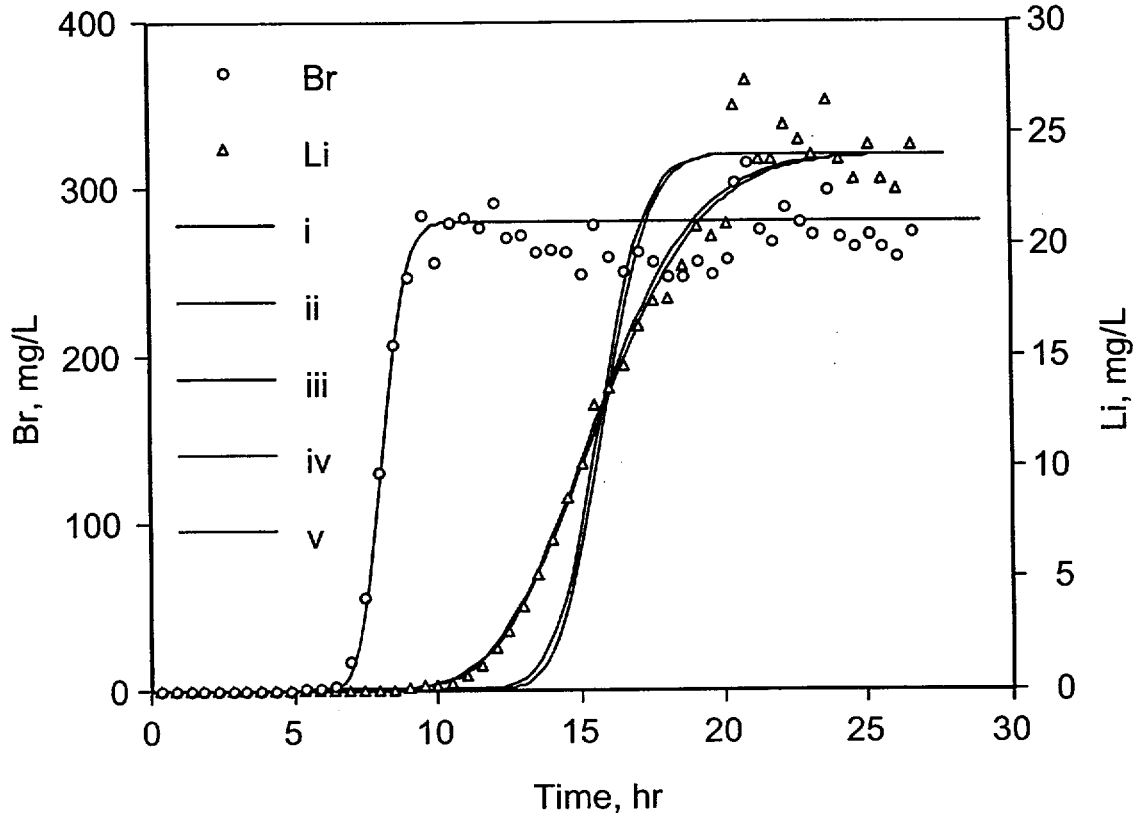

NOTE: The curves above are numbered as follows: (i) fit to bromide data with a Peclet number of 300, (ii) fit to lithium data assuming linear isotherm (R_F = 2.0) with equilibrium sorption, (iii) fit to lithium data assuming linear isotherm with a forward rate constant of 2.2 1/hr, (iv) fit to lithium data assuming a Langmuir isotherm with equilibrium sorption, and (v) fit to lithium data assuming a Langmuir isotherm with a forward rate constant of 2.2 1/hr.

Langmuir isotherm parameters: K_L = 0.0053 mL/µg and S_{max} = 110 µg/g (batch isotherm values obtained for lithium on central Bullfrog Tuff from UE-25 c#2).

Figure 96. Bromide and Lithium Breakthrough Curves in Column 1 at a Flow Rate of 2.2 mL/hr and corresponding RELAP and RETRAN Fits to Data

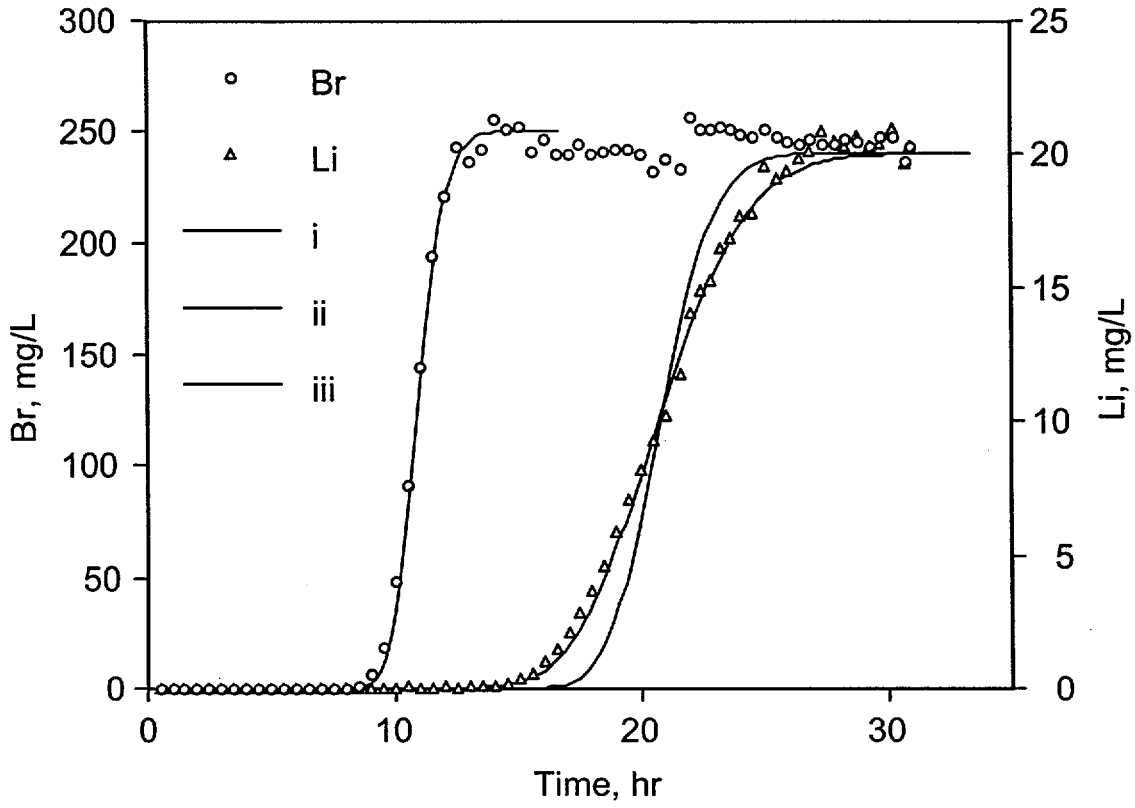

NOTE: The curves above are numbered as follows: (i) fit to bromide data with a Peclet number of 300, (ii) fit to lithium data assuming linear isotherm (R_F = 1.9) with equilibrium sorption, and (iii) fit to lithium data assuming linear isotherm with a forward rate constant of 3.6 1/hr.

Figure 97. Bromide and Lithium Breakthrough Curves in Column 1 at a Flow Rate of 1.6 mL/hr and Corresponding Fits to Data

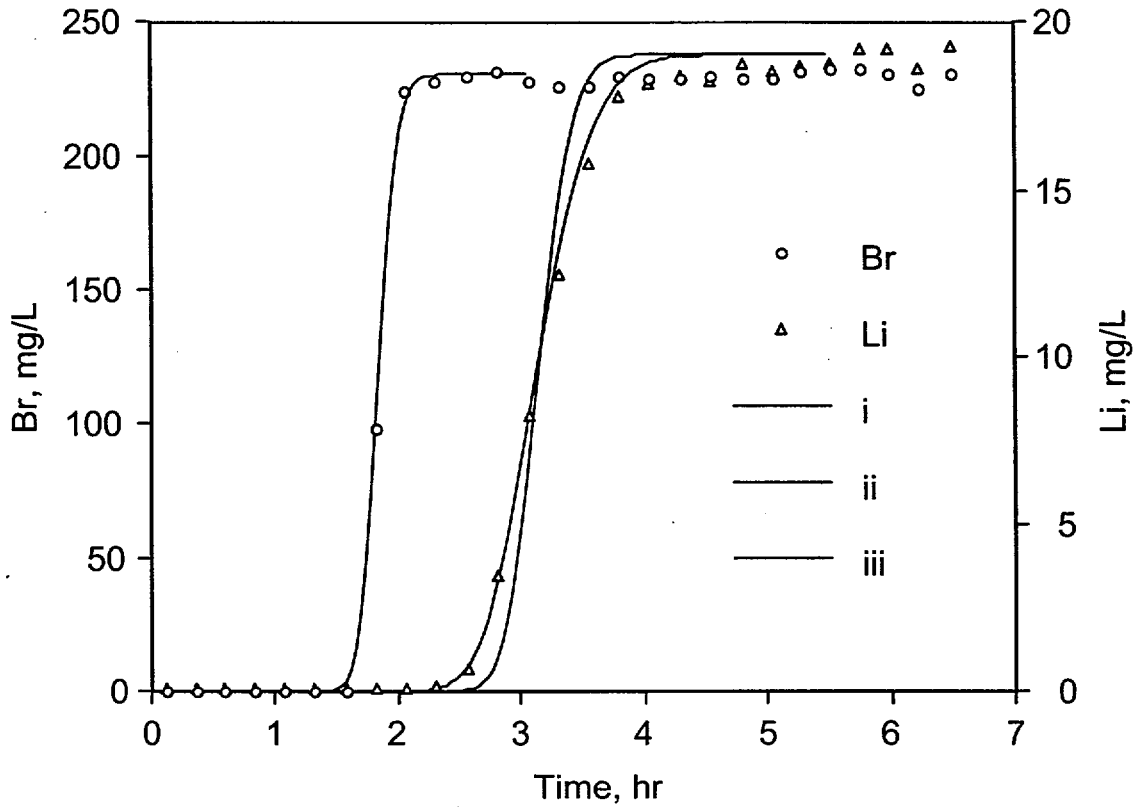

NOTE: The curves above are numbered as follows: (i) fit to bromide data with a Peclet number of 400, (ii) fit to lithium data assuming linear isotherm (R_F = 1.7) with equilibrium sorption, and (iii) fit to lithium data assuming linear isotherm with a forward rate constant of 14 1/hr.

Figure 98. Bromide and Lithium Breakthrough Curves in Column 2 at a Flow Rate of 9.7 mL/hr and Corresponding Fits to Data

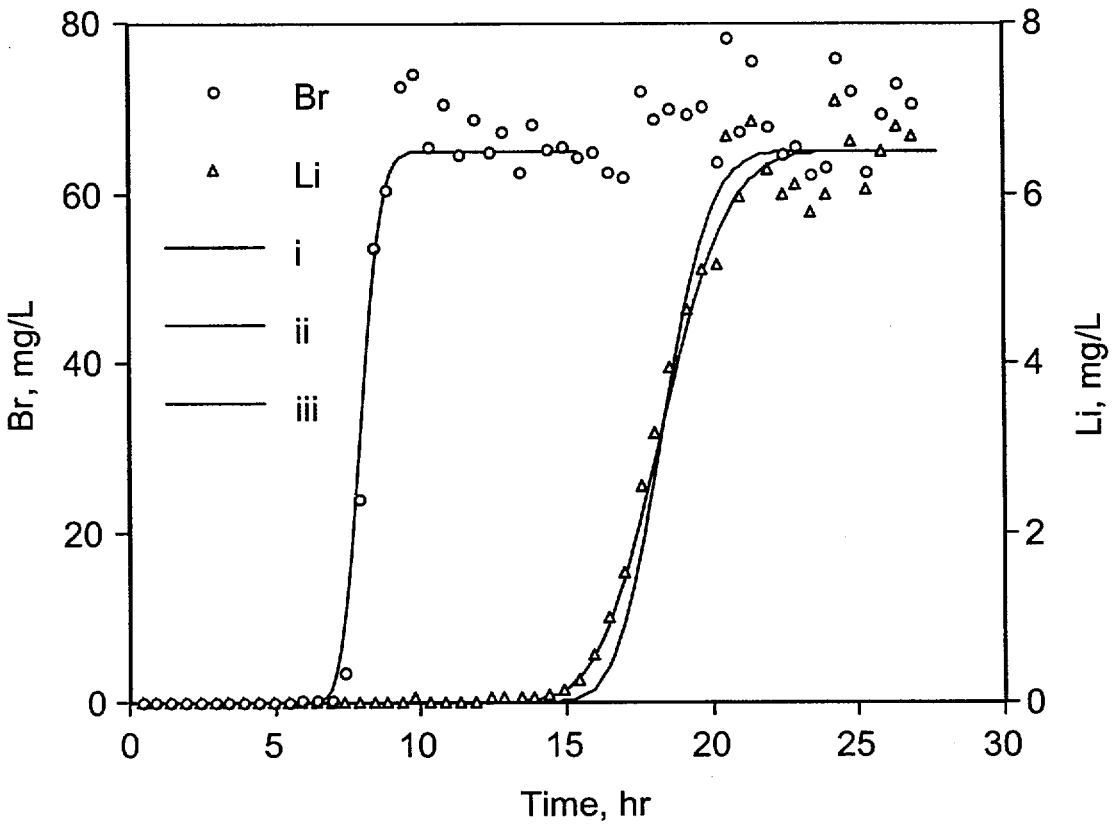

NOTE: The curves above are numbered as follows: (i) fit to bromide data with a Peclet number of 400, (ii) fit to lithium data assuming linear isotherm (R_F = 2.3) with equilibrium sorption, and (iii) fit to lithium data assuming linear isotherm with a forward rate constant of 18 1/hr.

Figure 99. Bromide and Lithium Breakthrough Curves in Column 3 at a Flow Rate of 2.2 mL/hr and Corresponding Fits to Data

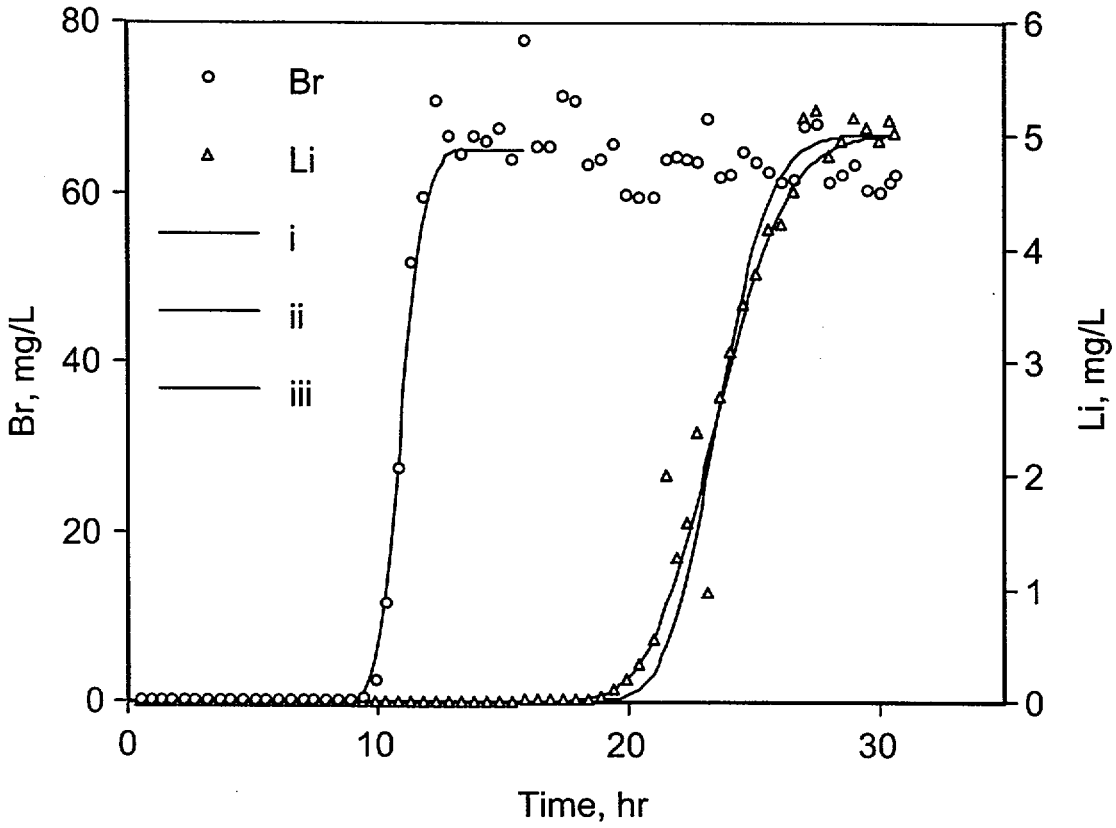

NOTE: The curves above are numbered as follows: (i) fit to bromide data with a Peclet number of 400, (ii) fit to lithium data assuming linear isotherm (R_F = 2.2) with equilibrium sorption, and (iii) fit to lithium data assuming linear isotherm with a forward rate constant of 14 1/hr.

Figure 100. Bromide and Lithium Breakthrough Curves in Column 3 at a Flow Rate of 1.6 mL/hr and Corresponding Fits to Data

In addition to these reactions, MULTRAN also accounts for the exchange between sodium and calcium ions, and it solves the surface cation-exchange balance equation for a three-component system:

$$2Na^+ + CaX_2 \leftrightarrow 2NaX + Ca^{2+} \quad \frac{Q_2}{Q_1^2} = \frac{[NaX]^2[Ca^{2+}]}{[CaX_2][Na^+]^2}, \qquad \text{(Eq. 23)}$$

$$CEC = \frac{\rho_B}{\phi}([LiX] + [NaX] + 2[CaX_2]) \qquad \text{(Eq. 24)}$$

The measured CEC for the Bullfrog Tuff (Section 3.8.2) was used as the CEC value in the model simulations, and the selectivity coefficients Q_1 and Q_2 were adjusted to fit the lithium data. However, without sodium and calcium concentration data, it was not possible to obtain a unique

fit to the lithium responses. In fact, the lithium responses could be fit equally well assuming lithium exchange with only sodium or only calcium. Thus, the K_1 and K_2 values presented in Figures 101 through 103 should be considered as only one of many possible combinations that could fit the lithium data equally well. However, it is not the values of these parameters that are important but rather the recognition that cation-exchange equilibria must be explicitly accounted for to explain the observed transport behavior of the lithium. For comparison, a RELAP "fit" to the data from Figure 101 is shown in Figure 104. It is clear that the single-component equilibrium K_d-model fit cannot capture the tailing behavior of the lithium. These results could have important implications for field tracer tests conducted in porous media that have a small sorption capacity for cation-exchanging tracers.

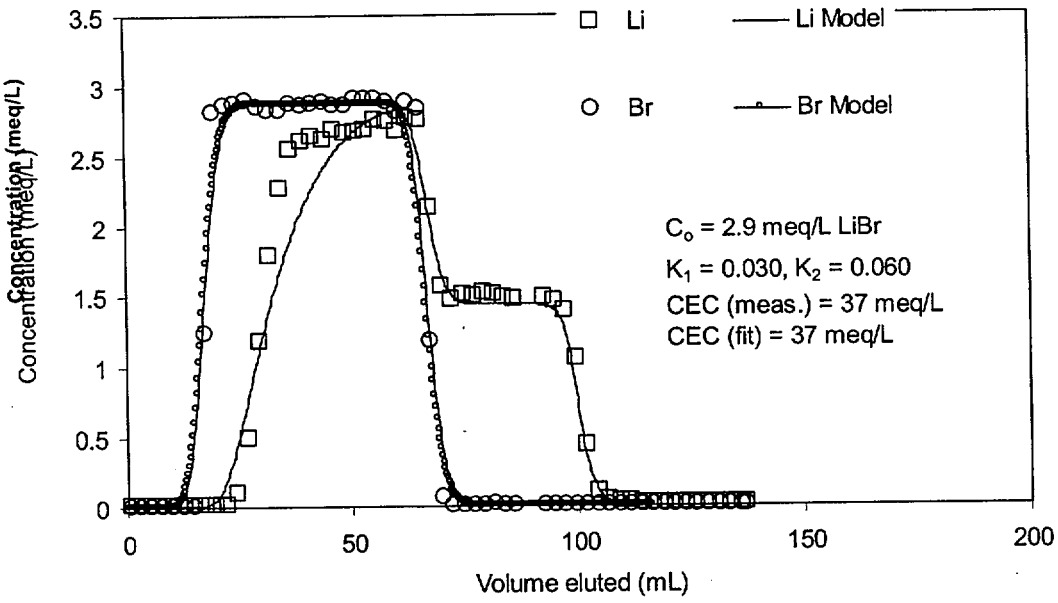

Figure 101. MULTRAN Fits to Complete Bromide and Lithium Breakthrough Curves From Experiment Conducted at 9.7 mL/hr in Column 2 (Figure 98)

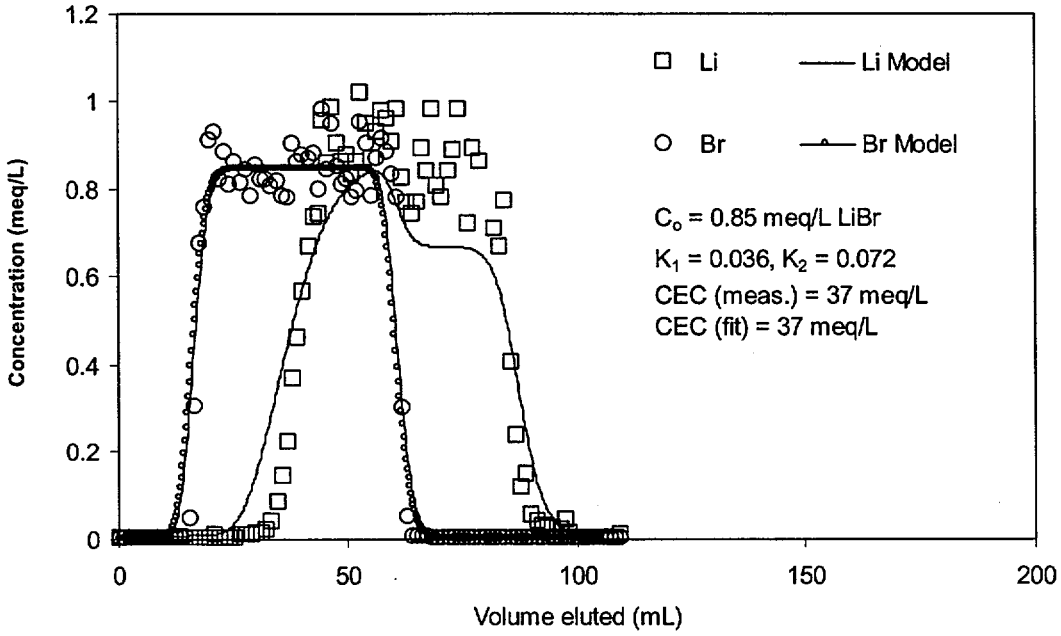

Figure 102. MULTRAN Fits to Complete Bromide and Lithium Breakthrough Curves from Low-Concentration Experiment Conducted in Column 3 (Figure 99)

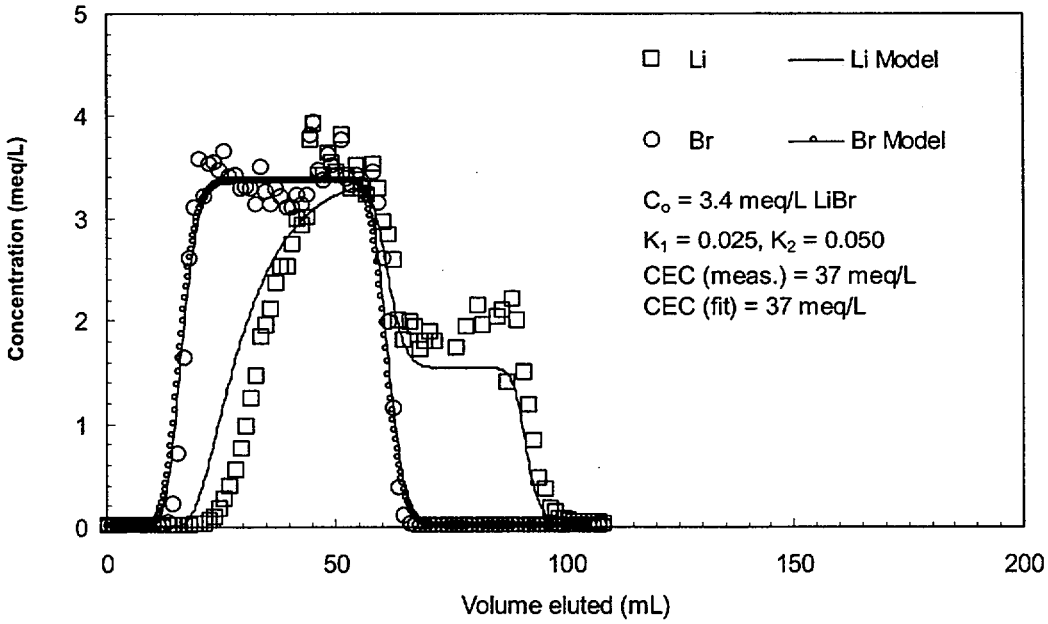

Figure 103. MULTRAN Fits to Complete Bromide and Lithium Breakthrough Curves from High-Concentration Experiment Conducted in Column 3 (Figure 99)

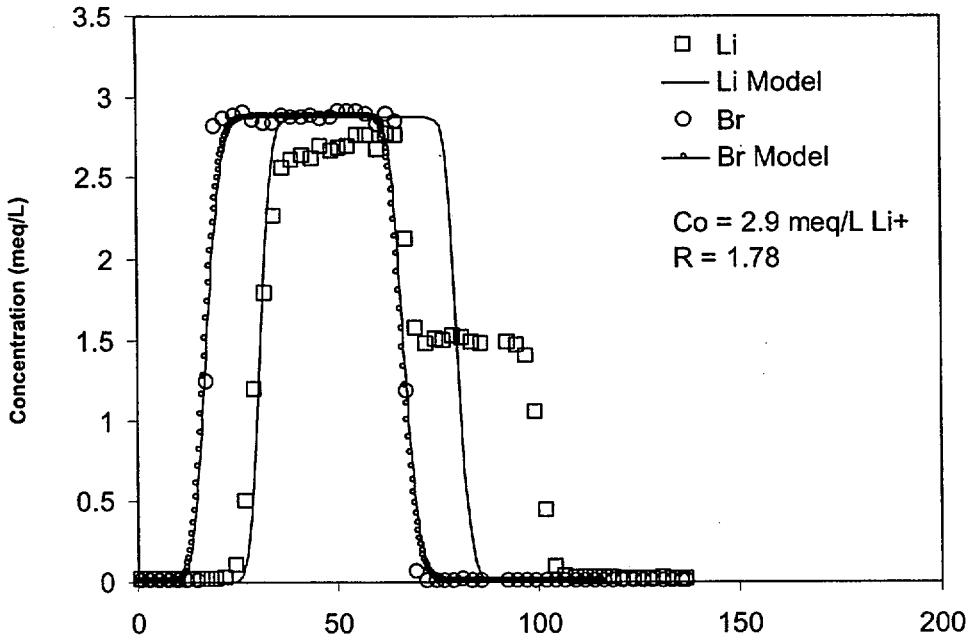

Figure 104. RELAP Fits to Complete Bromide and Lithium Breakthrough Curves from Experiment Conducted at 9.7 mL/hr in Column 2 (Figure 101 shows the MULTRAN fits)

3.10.2 Fractured-Core Experiments

3.10.2.1 Experimental Methods

Fractured-core transport experiments were conducted on four separate cores obtained from the C-wells following the procedure of Callahan et al. (2000). The cores were obtained from locations 3, 4, 5, and 6 in Figure 77. In the following discussion, the cores from the upper, central, and lower flow zones of the Prow Pass Tuff (locations 4, 5, and 6, respectively) will be referred to as cores 1, 2, and 3, respectively. The core from the lower flow zone of the Bullfrog Tuff will be referred to as core 4. The mineralogy of the cores is given in Table 20. Core 4 (lower flow zone of the Bullfrog Tuff) contained the highest percentage of clay and zeolite minerals, 9 ± 3 wt. % smectite, 4 ± 1 wt % clinoptilolite, and 13 ± 1 wt. % analcime. A single fracture was mechanically induced in each of the four cores. The cores were laid on a cement floor and a four-pound hammer and chisel were used to induce an axial fracture running the length of the core. The cores were then encased in an epoxy and Plexiglas column apparatus following the procedure of Callahan et al. (2000). Figure 105 shows a schematic illustration of a column apparatus.

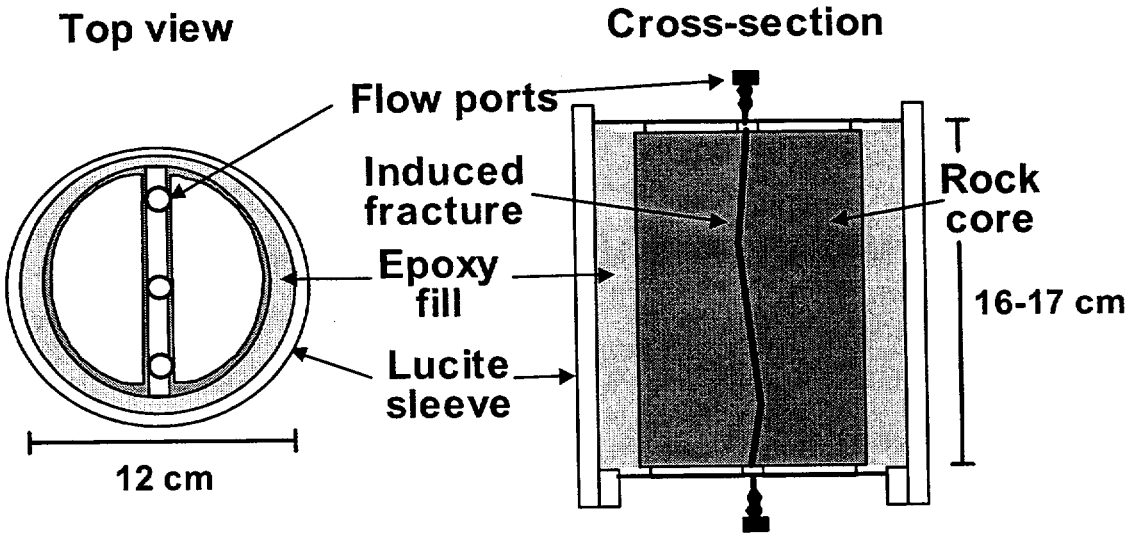

NOTE: Three flow ports on each end of the core allowed access to the inlet and outlet regions; the central flow ports were used to connect the cores to a syringe pump and fraction collector via a 0.8-mm diameter tubing. The lengths of the cores varied, but the diameters of all cores were 9.5 cm.

Figure 105. Schematic Illustration of a Fractured Rock Core Apparatus

The tracer experiments conducted in each core are summarized in Tables 30 through 35. As described by Callahan et al. (2000), cores 1 and 2 each featured three experiments in which iodide was used as a conservative tracer at three different flow rates. The objective of these experiments was to obtain estimates of matrix-diffusion, mass-transfer parameters in the cores by using RELAP to fit simultaneously the iodide responses at each flow rate. All four cores also featured at least two multiple-tracer experiments that were conducted and interpreted very similarly to the C-wells field tracer tests. Each experiment involved the injection of a pulse containing PFBA, lithium bromide (LiBr), and, in some cases, sodium iodide (NaI). Five multiple-tracer experiments were conducted in core 1 (two intended to be replicates), and two were conducted in each of the other three cores. The flow rate in at least one of the multiple-tracer experiment in each core was approximately an order of magnitude lower than the flow rate(s) in the other multiple-tracer experiment(s). Flow rates were varied over this large range so that the effect of experiment time scale on matrix diffusion processes could be assessed in fracture systems of constant geometry.

A steady-state flow field was established in each core by continuously injecting degassed, filtered groundwater obtained from well J-13 (see Table 18). A pulse of tracer solution (tracers dissolved in J-13 water) was then injected. After injection of the tracer pulse, continuous injection of tracer-free J-13 well water was resumed. The effluent was monitored for the tracer ions as well as for Na^+ and Ca^{2+} using ion chromatography (IC) for Br^- and PFBA and ICP-AES for analysis of Li^+, Na^+, and Ca^{2+}. Iodide was analyzed either using an ion-selective electrode or IC. The quantitative detection limits were 0.05 mg/L for Li^+, Na^+, and Ca^{2+}, 0.04 mg/L for Br^-, 0.02 mg/L for I^-, and 0.02 mg L^{-1} for PFBA. Na^+ and Ca^{2+} were analyzed so that cation

exchange equilibria could be more rigorously quantified than in the crushed-tuff column experiments described in Section 3.10.1. In some of the tests (Tables 31 through 35), flow was interrupted for a time after the tracer concentrations had been tailing to verify diffusive mass transfer in the cores (Brusseau et al. 1997; Callahan et al. 2000). This strategy was similar to that used in the Prow Pass multiple-tracer field test (Section 3.5.4).

Table 30. Experimental Conditions for the Iodide Fracture Transport Tests, Upper Prow Pass Tuff Core (Core 1)

Experimental Parameters			
Core length, L (m)		0.161	
Core width, w (m)		0.095	
Matrix porosity, n_m		0.272	
Hydraulic aperture, B_h (m) [a]		0.14×10^{-3}	
Iodide tests:	**Test 1**	**Test 2**	**Test 3**
Volumetric flow rate, Q (mL/hr)	2.01	20.11	8.30
Injection duration, t_p (hr)	29.92	2.87	7.26
Injection concentration, C_o (mg/L)	1000	1000	1000
Flow interruption period, time since start of injection (hr)	N/A [b]	N/A [2]	N/A [b]
Flow rate after restart, Q (mL/hr)	N/A [b]	N/A [2]	N/A [b]
Mass recovery (%)	86	96	94

NOTE: (a) Determined from a constant head permeameter method.

(b) N/A: Not applicable; flow was not interrupted during these tests.

3.10.2.2 Interpretive Methods

The RELAP code was used to interpret the nonsorbing iodide, bromide, and PFBA tracer responses. For the iodide-only experiments conducted in cores 1 and 2, the responses at the three different flow rates were simultaneously fitted, assuming the same Peclet number and matrix diffusion mass transfer coefficient ($MTC = \frac{\phi}{b}\sqrt{D_m}$) in each test, and a mean residence time (τ) that was inversely proportional to flow rate. This procedure assumes that the MTC and Peclet number have no flow rate or time scale dependence.

For the multiple-tracer tests, the bromide and PFBA responses were simultaneously fitted, assuming that bromide had a matrix diffusion coefficient a factor of three greater than PFBA (this same assumption was used in the field tracer-test interpretations). However, because of the difficulties encountered in fitting the lithium responses in the crushed-tuff column experiments, and the fact that Na^+ and Ca^{2+} were analyzed in addition to Li^+ in the fractured-core experiments, it was decided to use the MULTRAN model (described below) rather than RELAP to interpret the lithium responses. The values of τ, Pe, and MTC that provided the best RELAP fits to the bromide and PFBA responses were used as inputs to MULTRAN (note that for tests conducted at different flow rates in the same core, τ was adjusted such that it was inversely proportional to

flow rate and *Pe* was held constant for all tests). The parameters Q_1 and Q_2 were then adjusted to fit the Li^+, Na^+, and Ca^{2+} data while holding the CEC values equal to the measured CEC values.

MULTRAN is a 2-D numerical model that employs an implicit-in-time, alternating-direction, finite-difference method to solve the equations describing multicomponent transport of sorbing and nonsorbing solutes in a single- or dual-porosity medium. Figure 106 illustrates the assumed model domain and shows an example spatial discretization. Advective transport, simulated by solving the advection-dispersion equation, is assumed to occur only in the x-direction in Region I. The first and last nodes in the x-direction in this region are modeled as well-mixed regions that simulate either boreholes in field experiments or flow manifolds in laboratory experiments. Reinjection of part or all of the solution entering the last node back into the first node can be specified to simulate recirculating conditions in tracer experiments. Only diffusive transport is assumed to occur in the y-direction in both regions I and II, with the model having the capability to simulate different diffusion coefficients in the different regions. Finally, within each region, additional diffusive transport can be simulated into "grains," which are assumed to be spherical. These grains can be assigned a lognormal distribution of diameters with specified mean and variance. The user can control the spatial discretization within each region and within the grains.

The user also can eliminate certain portions of the model domain shown in Figure 106 simply by specifying that they have zero porosity. For instance, if one wishes to simulate a single-porosity medium, it is only necessary to specify a zero porosity for region II and zero porosity for the grains in region I. This approach was taken to simulate the crushed-tuff column transport experiments described in Section 3.10.1 because the columns were packed with a relatively uniform material that had no apparent secondary porosity. Reducing the model effectively to a 1-D system (region I) greatly simplifies numerical computations.

Table 31. Experimental Conditions for the Multiple-Tracer Fracture Transport Tests, Upper Prow Pass Tuff Core (Core 1)

Experimental Parameters	Test 1	Test 2
Volumetric flow rate, Q (mL/hr)	3.96	3.99
Injection duration, t_p (hr)	14.97	15.22
Injection concentration, C_o (mg/L)	192 (Li^+) 0 (Na^+) 0 (Ca^{2+}) 1728 (Br^-) 300 (I^-) 635 (PFBA)	192 (Li^+) 0 (Na^+) 0 (Ca^{2+}) 1728 (Br^-) 300 (I^-) 635 (PFBA)
Background groundwater concentration, C_i (mg/L)	0.64 (Li^+) 46.7 (Na^+) 12.8 (Ca^{2+}) 3.63 (Br^-) 1.8 (I^-) 1.11 (PFBA)	1.79 (Li^+) 45.4 (Na^+) 12.8 (Ca^{2+}) 10.7 (Br^-) 0.55 (I^-) 3.86 (PFBA)
Flow interruption period, time since start of injection (hr)	87.3–137.3	87.1–137.2
Flow rate after restart, Q (mL/hr)	3.96	3.99
Mass recovery (%)	89 (Li^+) 89 (Br^-) 92 (I^-) 95 (PFBA)	89 (Li^+) 89 (Br^-) 86 (I^-) 95 (PFBA)

Experimental Parameters	Test 3	Test 4	Test 5
Volumetric flow rate, Q (mL hr^{-1})	0.53	8.46	6.39
Injection duration, t_p (hr)	151.1	19.2	11.53
Injection concentration, C_o (mg/L)	159 (Li^+) 394 (Na^+) 0 (Ca^{2+}) 1870 (Br^-) 296 (I^-) 641 (PFBA) 145 (Cu^{2+}) 699 (EDTA [b])	1010 (Li^+) 59.1 (Na^+) 0 (Ca^{2+}) 11400 (Br^-) N/A [a] (I^-) 766 (PFBA)	216 (Li^+) 250 (Na^+) 0 (Ca^{2+}) 2528 (Br^-) N/A [a] (I^-) 766 (PFBA) 192 (Cu^{2+}) 1131 (EDTA [b])
Background groundwater concentration, C_i (mg/L)	0.08 (Li^+) 51.8 (Na^+) 13.2 (Ca^{2+}) 10.87 (Br^-) < 0.4 (I^-) 2.07 (PFBA)	0.08 (Li^+) 45 (Na^+) 13.3 (Ca^{2+}) < 0.02 (Br^-) < 0.4 (I^-) < 0.005 (PFBA)	0.53 (Li^+) 45 (Na^+) 13.3 (Ca^{2+}) 0.98 (Br^-) < 0.4 (I^-) < 0.005 (PFBA)
Flow interruption period, time since start of injection (hr)	689–904	19.8–21.2, 49.9–64.2	44.0–64.0
Flow rate after restart, Q (mL/hr)	0.53	8.05, 8.04	6.46
Mass recovery (%)	83 (Li^+) 94 (Br^-) 82 (I^-) 94 (PFBA)	89 (Li^+) 89 (Br^-) N/A [a] (I^-) 95 (PFBA)	89 (Li^+) 89 (Br^-) N/A [a] (I^-) 95 (PFBA)

NOTE: (a) N/A: not applicable; iodide was not injected in these tests.

(b) EDTA: ethylenediamine tetraacetic acid.

Table 32. Experimental Conditions for the Iodide Fracture Transport Tests, Central Prow Pass Tuff Core (Core 2)

Experimental Parameters			
Core length, L (m)	0.173		
Core width, w (m)	0.095		
Matrix porosity, n_m	0.138		
Hydraulic aperture, B_h (m) [a]	0.13×10^{-3}		
	Test 1	**Test 2**	**Test 3**
Volumetric flow rate, Q (mL/hr)	19.93	49.59	11.74
Injection duration, t_p (hr)	4.0	1.5	6.2
Injection concentration, C_o (mg/L)	1000	1000	1000
Flow interruption period, time since start of injection (hr)	N/A [b]	N/A [b]	N/A [b]
Flow rate after restart, Q (mL/hr)	N/A [b]	N/A [b]	N/A [b]
Mass recovery (%)	89	98	84

NOTES: (a) Determined from a constant head permeameter method.

(b) N/A: not applicable; flow was not interrupted during these tests.

Table 33. Experimental Conditions for the Multiple-Tracer Fracture Transport Tests, Central Prow Pass Tuff Core (Core 2)

Experimental Parameters	Test 1	Test 2
Volumetric flow rate, Q (mL/hr)	5.96	0.44
Injection duration, t_p (hr)	11.94	168.13
Injection concentration, C_o (mg/L)	216 (Li^+) 205 (Na^+) 0 (Ca^{2+}) 2528 (Br^-) N/A[a] (I^-) 766 (PFBA) 192 (Cu^{2+}) 1131 (EDTA[b])	159 (Li^+) 301 (Na^+) 0 (Ca^{2+}) 1870 (Br^-) 296 (I^-) 641 (PFBA) 145 (Cu^{2+}) 699 (EDTA[b])
Background groundwater concentration, C_i (mg/L)	0.08 (Li^+) 45 (Na^+) 13.3 (Ca^{2+}) < 0.02 (Br^-) < 0.4 (I^-) < 0.005 (PFBA)	0.55 (Li^+) 75.1 (Na^+) 10.0 (Ca^{2+}) 1.97 (Br^-) 0.9 (I^-) 0.98 (PFBA)
Flow interruption period, time since start of injection (hr)	42.9–62.9	799–999
Flow rate after restart, Q (mL/hr)	5.95	0.44
Mass recovery (%)	84 (Li^+) 90 (Br^-) N/A[a] (I^-) 95 (PFBA)	68 (Li^+) 97 (Br^-) 97 (I^-) 102 (PFBA)

NOTES: (a) N/A: not applicable; iodide was not injected in these tests.

(b) EDTA: ethylenediamine tetraacetic acid.

Table 34. Experimental Conditions for the Multiple-Tracer Fracture Transport Tests, Lower Prow Pass Tuff Core (Core 3)

Experimental Parameters		
Core length, L (m)	0.116	
Core width, w (m)	0.095	
Matrix porosity, n_m	0.288	
Hydraulic aperture, B_h (m)[(a)]	0.16×10^{-3}	
	Test 1	**Test 2**
Volumetric flow rate, Q (mL/hr)	11.4	0.47
Injection duration, t_p (hr)	14.4	168.1
Injection concentration, C_o (mg/L)	159 (Li^+) 331 (Na^+) 1.2 (Ca^{2+}) 1870 (Br^-) 296 (I^-) 641 (PFBA) 145 (Cu^{2+}) 699 (EDTA[(b)])	165 (Li^+) 310 (Na^+) 0 (Ca^{2+}) 1930 (Br^-) 299 (I^-) 681 (PFBA) 150 (Cu^{2+}) 699 (EDTA[(b)])
Background groundwater concentration, C_i (mg/L)	0.08 (Li^+) 44.6 (Na^+) 13.3 (Ca^{2+}) < 0.02 (Br^-) < 0.35 (I^-) < 0.005 (PFBA)	4.41 (Li^+) 67.2 (Na^+) 16.4 (Ca^{2+}) 60.1 (Br^-) 9.49 (I^-) 16.2 (PFBA)
Flow interruption period, time since start of injection (hr)	43.6–68.6	792–992
Flow rate after restart, Q (mL/hr)	11.4	0.47
Mass recovery (%)	97.2 (Li^+) 95.7 (Br^-) 98.4 (I^-) 99.3 (PFBA)	72.4 (Li^+) 87.3 (Br^-) 84.2 (I^-) 80.1 (PFBA)

NOTES: (a) Determined from a constant head permeameter method.

(b) EDTA: ethylenediamine tetraacetic acid.

Table 35. Experimental Conditions for the Multiple-Tracer Fracture Transport Tests, Lower Bullfrog Tuff core (Core 4)

Experimental Parameters	Test 1	Test 2
Volumetric flow rate, Q (mL/hr)	4.92	0.47
Injection duration, t_p (hr)	35.0	344.7
Injection concentration, C_o (mg/L)	165 (Li^+) 342 (Na^+) 0 (Ca^{2+}) 1930 (Br^-) 299 (I^-) 681 (PFBA) 150 (Cu^{2+}) 699 (EDTA*)	192 (Li^+) 0 (Na^+) 0 (Ca^{2+}) 1728 (Br^-) 300 (I^-) 635 (PFBA)
Background groundwater concentration, C_i (mg/L)	0.04 (Li^+) 51.1 (Na^+) 11.0 (Ca^{2+}) 0.14 (Br^-) 0.07 (I^-) 0.14 (PFBA)	4.41 (Li^+) 67.2 (Na^+) 16.4 (Ca^{2+}) 60.1 (Br^-) 9.49 (I^-) 16.2 (PFBA)
Flow interruption period, time since start of injection (hr)	67.2–87.2	79–992
Flow rate after restart, Q (mL/hr)	5.05	0.47
Mass recovery (%)	57 (Li^+) 96 (Br^-) 86 (I^-) 99 (PFBA)	85 (Li^+) 103 (Br^-) 86 (I^-) 91 (PFBA)

NOTE: *EDTA: ethylenediamine tetraacetic acid.

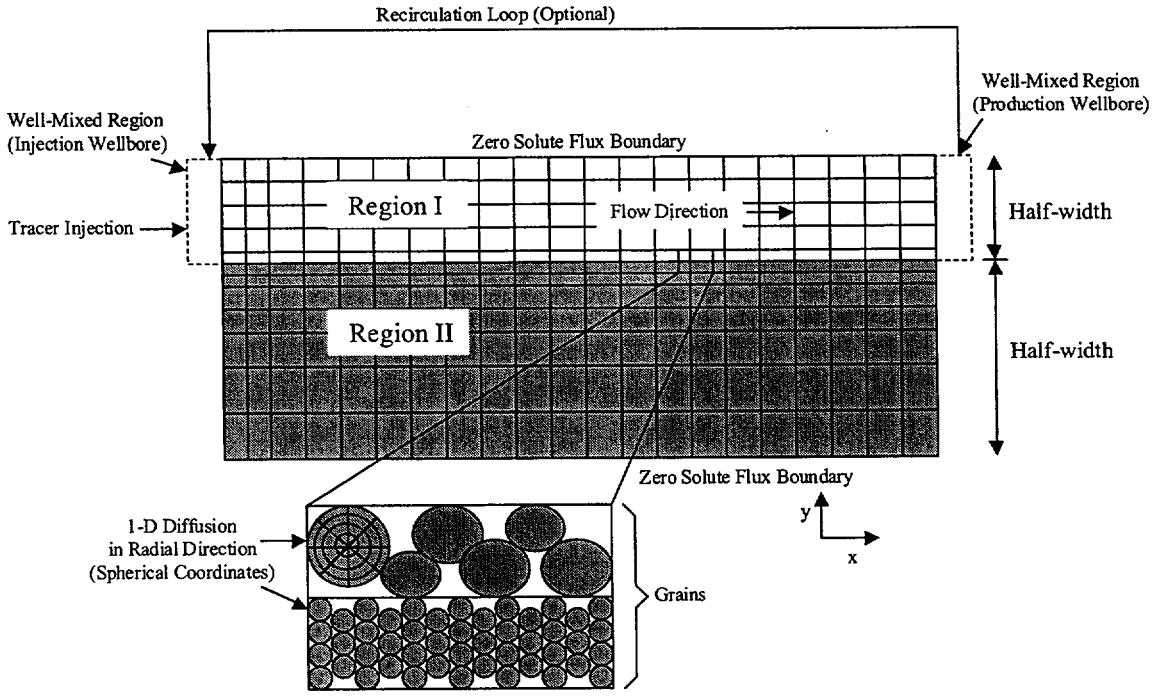

NOTE: Blocks are finite-difference cells that are solved at their midpoints. Region I is the high-permeability layer (advective transport in *x*-direction, diffusive in *y*-direction); region II is the low-permeability layer (diffusive transport in *y*-direction only).

Figure 106. Schematic Illustration of MULTRAN Model Domain

Each time-step of a MULTRAN simulation is broken into four computational segments that are conducted sequentially, as follows.

(1) Solution of the advection-dispersion equation in the *x*-direction in region I

$$\frac{\partial c}{\partial t} = -V\frac{\partial c}{\partial x} + D\frac{\partial^2 c}{\partial x^2} \qquad \text{(Eq. 25)}$$

where

c = molar concentration, moles/L

V = velocity in x direction, cm/sec

D = dispersion coefficient, cm^2/sec ($D = \alpha V$, α = dispersivity).

(2) Solution of the multicomponent diffusion equation(s) and the local electroneutrality equation in the *y*-direction in regions I and II (coupled)

a. *Multicomponent diffusion equation for all species except species n (Newman 1973):*

$$\frac{\partial c_i}{\partial t} = D_i \nabla^2 c_i - \sum_j \frac{z_j}{z_i}\left(D_j - D_n\right)\nabla \cdot (t_i \nabla c_i) \qquad \text{(Eq. 26)}$$

where

c_i = molar concentration of species i, moles/L

D_i = diffusion coefficient of species i, cm^2/sec

∇ = del operator

∇^2 = Laplacian operator

$t_i = \dfrac{z_i^2 u_i c_i}{\sum_j z_j^2 u_j c_j}$ = transference number of species i

z_i = charge of species i

$u_i = \dfrac{D_i}{RT}$ = mobility of species i, where R = gas constant and T = temp (K).

b. *Electroneutrality equation for species n:*

$$z_n c_n = -\sum_{j \neq n} z_j c_j \qquad \text{(Eq. 27)}$$

(3) Solution of the multicomponent diffusion equation(s) and the local electroneutrality equation in the radial direction in the grains of both regions I and II (same as step 2, but using spherical coordinates).

(4) Chemical re-equilibration of the entire system with respect to cation exchange. This step is accomplished by solving Equations 21 through 24 at each node in the model domain to ensure that the equilibrium expressions and the surface cation balance are locally satisfied. The system is assumed to always be at chemical equilibrium (i.e., reaction kinetics assumed to be fast relative to transport rates). Slow-reaction kinetics may be considered in a future version of MULTRAN.

3.10.2.3 Results and Interpretations

The experimental data and modeling fits for the iodide-only tests conducted in cores 1 and 2 (three in each core) are shown in Figures 107 and 108, respectively. Tables 36 and 37 list the model parameters associated with the fits shown in these figures. It is apparent that RELAP offered good simultaneous fits to the three data sets. The experimental data and associated MULTRAN fits to the first two multiple-tracer tests conducted in core 1 and the first multiple-tracer test in core 2 are shown in Figures 109 through 111. Table 38 lists the model parameters associated with these fits. The first two tests in core 1 were intended to be replicates, and it is apparent that the transport behavior of the solutes was nearly identical in these two tests.

For test 1 in core 1, the best-fit values for Q_1 and Q_2 were 0.005 and 0.079, respectively; for test 2, Q_1 was 0.008, and Q_2 was 0.103. These parameter values obtained from MULTRAN are essentially the same due to the relative insensitivity of the model to Q_1 and Q_2. The MULTRAN fits were less sensitive to Q_2 than Q_1 because the ion exchange equilibria depend on $[Ca^{2+}]$ to a power half that of $[Na^+]$ and $[Li^+]$. The ion-exchange parameters Q_1 and Q_2 for test 1 in core 2 were 10.1 and 0.032, respectively. The model simulations show a good match to the Li^+ and Na^+ data; however the model did not match the Ca^{2+} data very well, as seen in the log-log plot of Figure 111. Sodium hydroxide (NaOH) was also added to the injection solution to adjust the pH to 7.8 (dissociation of the PFBA resulted in an initial pH of about 3). Therefore, ion exchange was dominated by exchange between Li^+ and Na^+ in this tracer test. On the other hand, in the first two experiments in core 1, Li^+ was the only cation added to the tracer solution (the pH of the tracer solutions for the core 1 tests was buffered using LiOH).

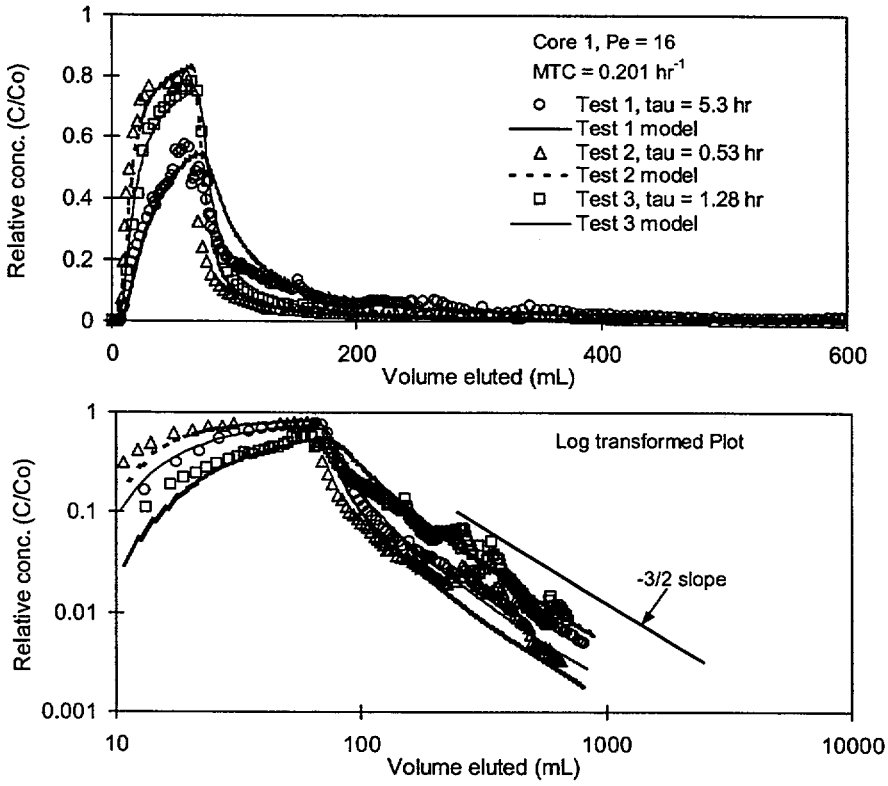

NOTE: All three data sets were used to simultaneously fit τ, *Pe*, and *MTC*. Concentrations are normalized to injection concentration. The –3/2 slope on the log-log plot is the expected slope for a system experiencing single-rate matrix diffusion.

Figure 107. Experimental and Modeling Results From the Three Iodide Transport Tests in Core 1

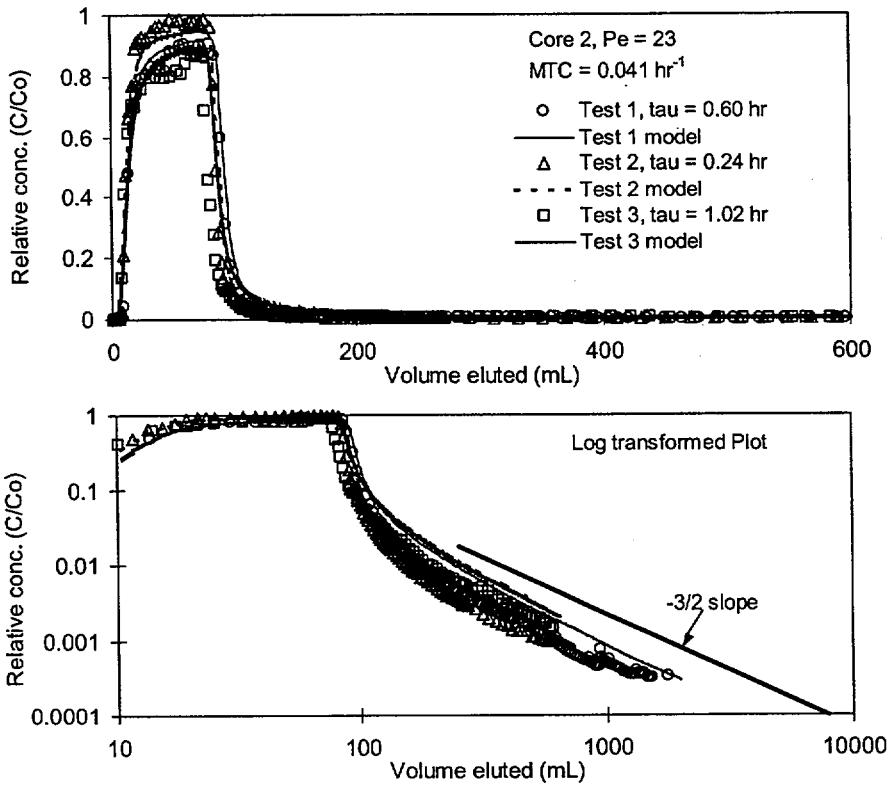

NOTE: All three data sets were used to simultaneously fit τ, *Pe*, and *MTC*. Concentrations are normalized to injection concentration. The –3/2 slope on the log-log plot is the expected slope for a system experiencing single-rate matrix diffusion.

Figure 108. Experimental and Modeling Results from the Three Iodide Transport Tests in Core 2

Table 36. Modeling Results for the Three Iodide Tracer Tests in Upper Prow Pass Tuff Core (Core 1)

Modeling Parameters [a]	Test 1	Test 2	Test 3
Solute mean residence time, τ (hr)	3.0	0.34	0.76
Peclet number, *Pe*		18	
Mass transfer coefficient, $MTC = \frac{\phi}{b}\sqrt{D_m}$ ($hr^{-0.5}$)		1.56 (I⁻)	
Fracture aperture, 2*b* (cm) [b]		0.044	
Dispersivity in fracture, $\alpha = \frac{L}{Pe}$ (cm)		0.89	
Matrix diffusion coefficient, D_m (x 10^{-10} m^2/s) [c]		4.5 (I⁻)	

NOTES: (a) The three I⁻ data sets were fit simultaneously assuming *Pe* was the same for the three tests and τ was inversely proportional to the volumetric flow rate. The Br^- and PFBA data were fit simultaneously by constraining the D_m ratio for Br^-:PFBA to 3:1.

(b) Based on the relationship $b = \frac{Q\tau}{Lw}$, where τ is the solute mean residence time.

(c) Determined from the *MTC* using the measured ϕ and the calculated *b*.

Table 37. Modeling Results for the Three Iodide Tracer Tests in Central Prow Pass Tuff Core (Core 2)

Modeling Parameters [a]	Test 1	Test 2	Test 3
Solute mean residence time, τ (hr)	0.48	0.19	0.84
Peclet number, *Pe*		24	
Mass transfer coefficient, $MTC = \frac{\phi}{b}\sqrt{D_m}$ ($hr^{-0.5}$)		0.518 (I⁻)	
Fracture aperture, 2*b* (cm) [b]		0.058	
Dispersivity in fracture, $\alpha = \frac{L}{Pe}$ (cm)		0.72	
Matrix diffusion coefficient, D_m (x 10^{-10} m^2/s) [c]		3.3 (I⁻)	

NOTE: (a) The three I⁻ data sets were fit simultaneously assuming *Pe* was the same for the three tests and τ was inversely proportional to the volumetric flow rate. The Br^- and PFBA data were fit simultaneously by constraining the D_m ratio for Br^-:PFBA to 3:1.

(b) Based on the relationship $b = \frac{Q\tau}{Lw}$, where τ is the solute mean residence time.

(c) Determined from the *MTC* using the measured ϕ and the calculated *b*.

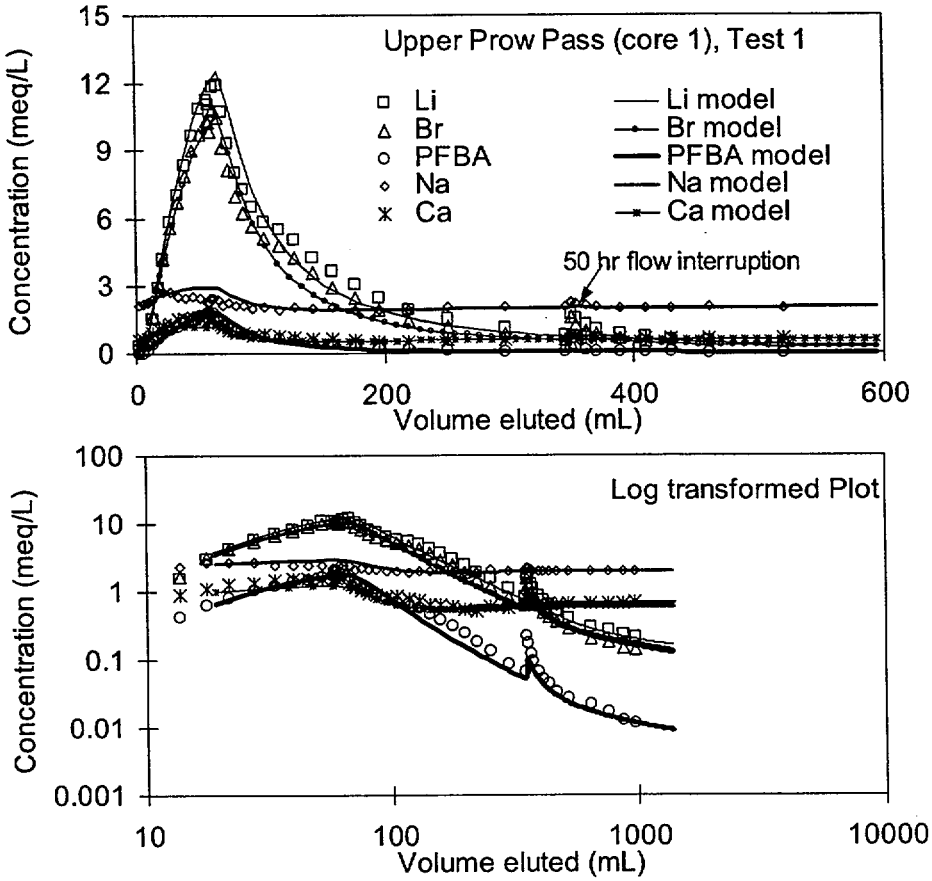

Figure 109. Experimental Data and MULTRAN Modeling Results for Multiple-Tracer Test 1 in Core 1

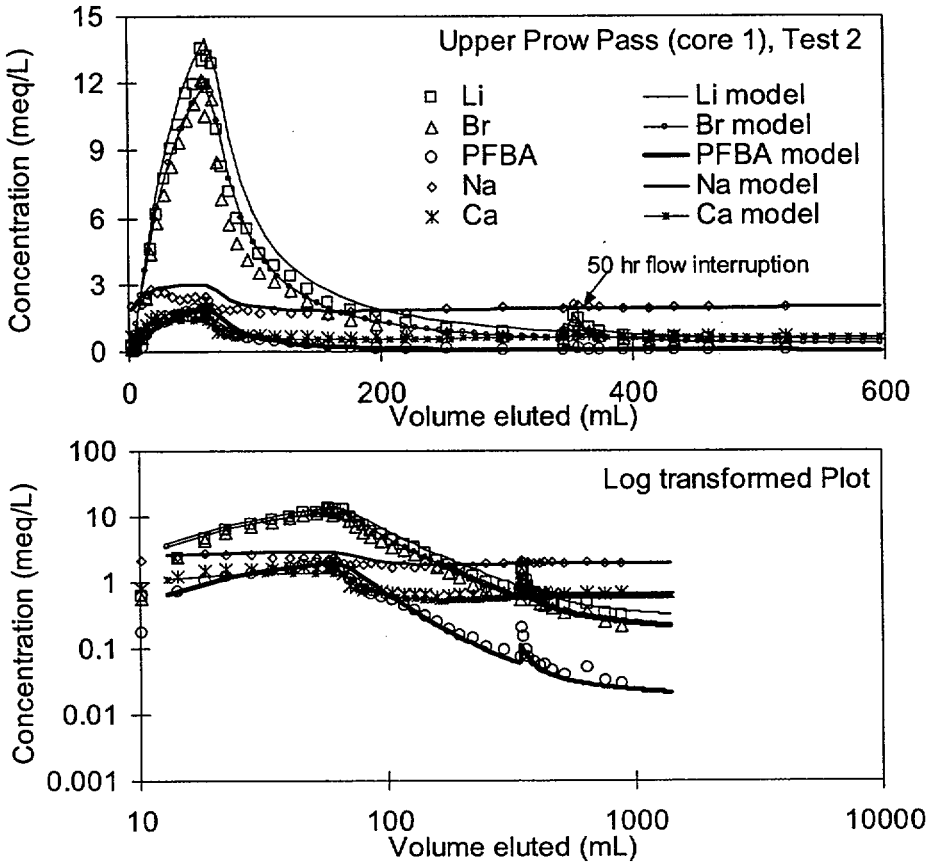

Figure 110. Experimental Data and MULTRAN Modeling Results for Multiple-Tracer Test 2 in Core 1

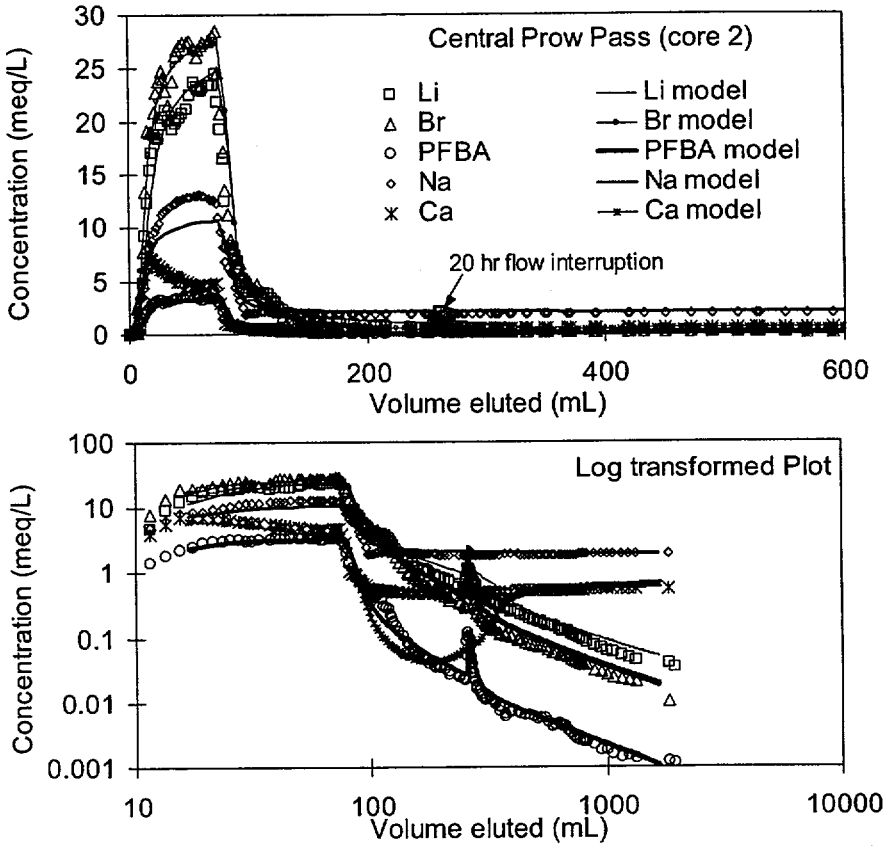

Figure 111. Experimental Data and MULTRAN Modeling Results for Multiple-Tracer Test 1 in Core 2

Table 38. Best-Fit Model Parameters for the Multiple-Tracer Tests Conducted in Cores 1 and 2

Modeling Parameters [a]	Core 1, Test 1	Core 1, Test 2	Core 2
Porosity of matrix	0.27	0.27	0.14
Solute mean residence time, τ (hr)	7.6	7.0	1.4
Peclet number, *Pe*	2.5	2.5	7
Dispersivity in fracture, $\alpha = \frac{L}{Pe}$ (cm)	6.4	6.4	2.5
Li^+ Retardation factor, *R* [b]	2.25	2.3	4.2
Li^+ Partition coefficient, K_d (L/kg)	0.17	0.18	0.19
Mass transfer coefficient, $MTC = \frac{\phi}{b}\sqrt{D_m}$ ($hr^{-0.5}$)	0.474 (Br^-) 0.274 (PFBA)	0.517 (Br^-) 0.299 (PFBA)	0.579 (Br^-) 0.335 (PFBA)
Fracture aperture, 2*b* (cm) [c]	0.188	0.178	0.05
Matrix diffusion coefficient, D_m (x 10^{-10} m^2/s) [d]	7.6 (Br^-) 2.5 (PFBA)	8.1 (Br^-) 2.7 (PFBA)	3.1 (Br^-) 1.0 (PFBA)
CEC (meq/kg), Measured	19.9	19.9	43.2
Q_1 [e]	0.005	0.008	10.1
Q_2 [e]	0.079	0.103	0.032

NOTES: Cores 1 and 2 are shown in Figures 109 through 111.

(a) The Br^- and PFBA data were fit simultaneously by constraining the D_m ratio for Br^-:PFBA to 3:1. The matrix diffusion coefficient for Li^+ was assumed to be 2/3 the value for Br^-.

(b) Calculated from the Li^+ transport data from the rising portion of the BTC using the Reactive Transport Laplace Transform Inversion code (RELAP) [Reimus and Haga (1999)].

(c) Based on the relationship $b = \frac{Q\tau}{Lw}$, where τ is the solute mean residence time.

(d) Determined from the *MTC* using the measured ϕ and the calculated *b*.

(e) Equilibrium ion exchange coefficients, determined from best fit to the Li^+, Na^+ and Ca^{2+} data for each test.

Figure 112 shows the experimental data and modeling fits for the first multiple-tracer test conducted in core 3. The best-fitting parameters are listed in Table 39. The ion-exchange parameters Q_1 and Q_2 were 0.029 and 0.036, respectively. The model fits matched the Li^+ and Na^+ data, but for the Ca^{2+} data, the model approximated the BTC pattern but was lower in magnitude. This result is similar to that for core 2.

Data obtained from the transport tests in core 4 indicated a higher sorption capacity for Li^+ relative to the other three rock types. The experimental data and best-fit model results for the first multiple-tracer test conducted in core 4 are shown in Figure 113. The best-fitting model parameters for this test are listed in the last column of Table 39. Figure 114 shows the model results from both the MULTRAN ion-exchange model and from the single-component RELAP model for Li^+ transport along with the Li^+ data in the first multiple-tracer test in core 4. This

core exhibited the most asymmetric Li^+ response, and it is apparent that MULTRAN was better able to capture the asymmetry than RELAP. This result is qualitatively consistent with the results obtained for the crushed-tuff column experiments (e.g., compare Figures 101 and 104), although the degree of asymmetry in the fractured cores is not as great as in the crushed-tuff columns. QXRD measurements on crushed samples of this rock type indicated 9 ± 3 wt. % smectite, 13 ± 3 wt. % analcime, and 4 ± 1 wt. % clinoptilolite (Table 20). The other rock types contained ≤ 2 ± 1 wt. % of these minerals.

The experimental data and the RELAP/MULTRAN fits for the final three multiple-tracer tests in core 1 and for the final multiple-tracer test in each of the other three cores are not presented in this report. The lower flow-rate experiments in each core were conducted primarily to investigate the effects of experiment time scale on matrix diffusion rather than to determine lithium-sorption/ion-exchange parameters at the lower flow rates. The results of these experiments were mixed, with the matrix diffusion MTC ($\frac{\phi}{b}\sqrt{D_m}$) decreasing at the lower flow rate in core 2 (relative to the higher flow rate), increasing at the lower flow rates in cores 1 and 4, and staying almost the same in core 3. Also, for all cores except core 2, a finite matrix offered a better fit to the tracer data than an infinite matrix, suggesting that the tracers may have reached diffusion boundaries in the cores. This result is not surprising given the relatively small diameter of the cores (~9.5 cm). A summary comparison of the value of MTC obtained from RELAP fits to the multiple-tracer test data in each core is given in Table 40. These results are discussed further in Section 3.11.2.

3.11 SCALE-DEPENDENCE OF TRANSPORT PARAMETERS IN FRACTURED TUFFS

3.11.1 Scale-Dependence of Longitudinal Dispersivity

A plot of the longitudinal dispersivity values as a function of test scale for several NTS fractured-rock, tracer-test programs is shown in Figure 115. The plot indicates that the longitudinal dispersivity increases with test scale that ranges from less than one meter to over 100 meters. Figure 116 shows the range of longitudinal dispersivities as a function of scale derived from the C-wells multiple-tracer tests (darkened area) superimposed on a plot of dispersivity versus scale prepared by Neuman (1990). Note that the lower end of the range of length scales associated with the darkened area corresponds to the interwell separation in the tracer tests, and the upper end corresponds to the test interval thickness (used as an upper bound for the transport distance).

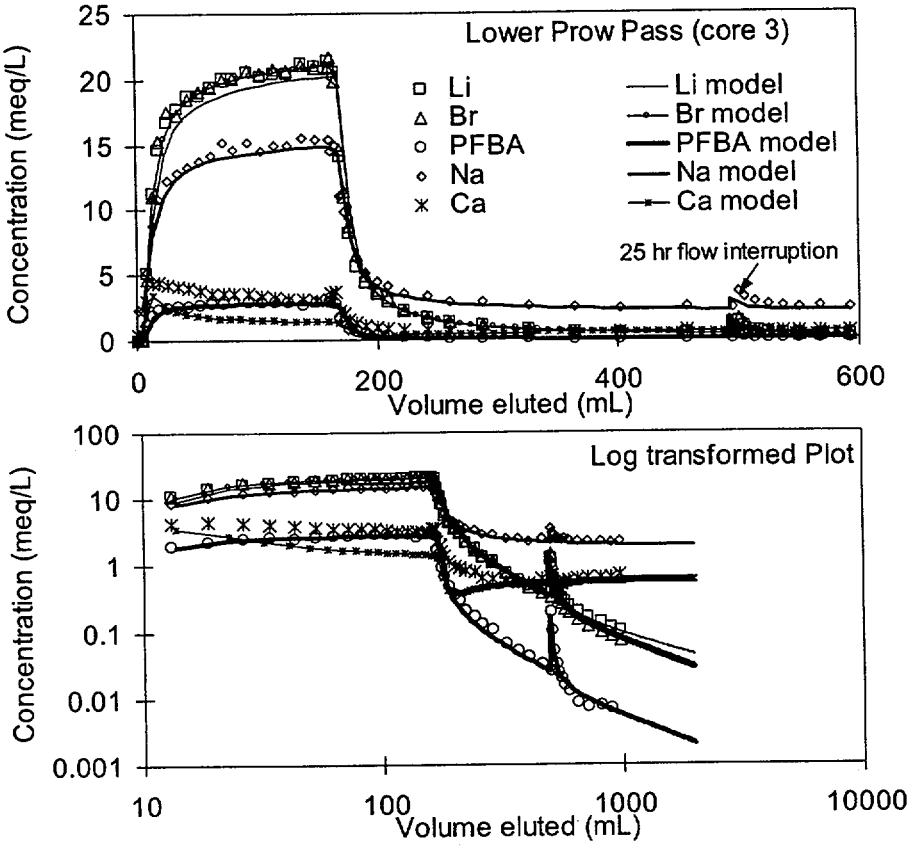

Figure 112. Experimental Data and MULTRAN Modeling Results for Multiple Tracer Test 1 in Core 3

Table 39. Best-Fit Model Parameters for the Multiple-Tracer Tests Conducted in Cores 3 and 4

Modeling Parameters [a]	Core 3	Core 4
Porosity of matrix	0.29	0.30
Solute mean residence time, τ (hr)	0.5	5.0
Peclet number, *Pe*	9.0	20
Dispersivity in fracture, $\alpha = \frac{L}{Pe}$ (cm)	1.29	1.09
Li^+ Retardation factor, *R* [b]	1.3	10.0
Li^+ Partition coefficient, K_d (L/kg)	0.046	1.46
Mass transfer coefficient, $MTC = \frac{\phi}{b}\sqrt{D_m}$ ($hr^{-0.5}$)	1.406 (Br^-) 0.811 (PFBA)	0.415 (Br^-) 0.239 (PFBA)
Fracture aperture, 2*b* (cm) [c]	0.052	0.122
Matrix diffusion coefficient, D_m (x 10^{-10} m^2/s) [d]	4.4 (Br^-) 1.5 (PFBA)	2.0 (Br^-) 0.67 (PFBA)
CEC (meq/kg), Measured	31.9	179.7
Q_1 [e]	0.029	9.1
Q_2 [e]	0.036	0.12

NOTE: Cores 3 and 4 are shown in Figures 112 and 113.

(a) The Br^- and PFBA data were fit simultaneously by constraining the D_m ratio for Br^-:PFBA to 3:1. The matrix diffusion coefficient for Li^+ was assumed to be 2/3 the value for Br^-.

(b) Calculated from the Li^+ transport data from the rising portion of the BTC using the Reactive Transport Laplace Transform Inversion code (RELAP) [Reimus and Haga (1999)].

(c) Based on the relationship $b = \frac{Q\tau}{Lw}$, where τ is the solute mean residence time.

(d) Determined from the *MTC* using the measured ϕ and the calculated *b*.

(e) Equilibrium ion exchange coefficients, determined from best fit to the Li^+, Na^+, and Ca^{2+} data for each test.

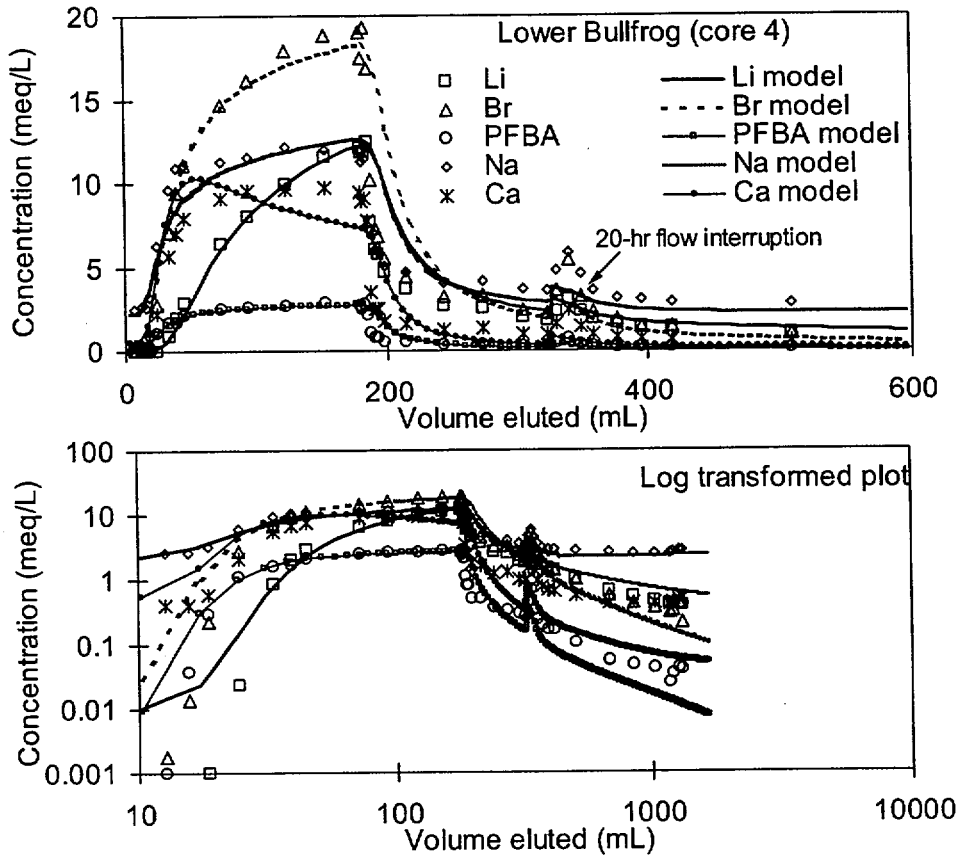

Figure 113. Experimental Data and MULTRAN Modeling Results for Multiple-Tracer Test 1 in Core 4

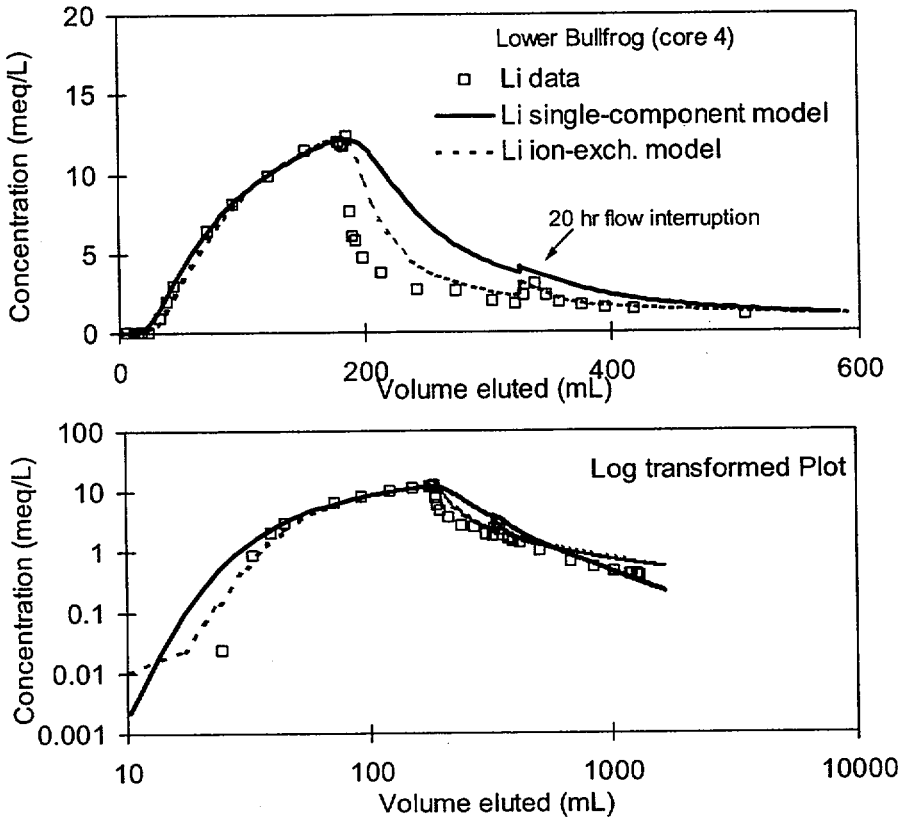

Figure 114. Comparison of the Fits of the MULTRAN Multicomponent Ion-Exchange Model and the Single-Component RELAP Model to the Lithium Transport Data in the First Multiple-Tracer Test in Core 4

Table 40. Model Parameters Obtained from RELAP for the Fractured-Rock Core Tests Conducted at Significantly Different Flow Rates in Cores 1 through 4

Experiment	τ(hr)	*Pe*	MTC (Br^-) ($hr^{-0.5}$)
Core 1, Test 1	7.6	2.5	0.46
Test 2	7.0	2.5	0.52
Test 3	52.0	2.5	0.75
Core 2, Test 1	1.4	7	0.58
Test 2	19.6	7	0.25
Core 3, Test 1	0.5	9	1.41
Test 2	11.0	9	1.42
Core 4, Test 1	5.0	20	0.42
Test 2	52.0	20	0.61

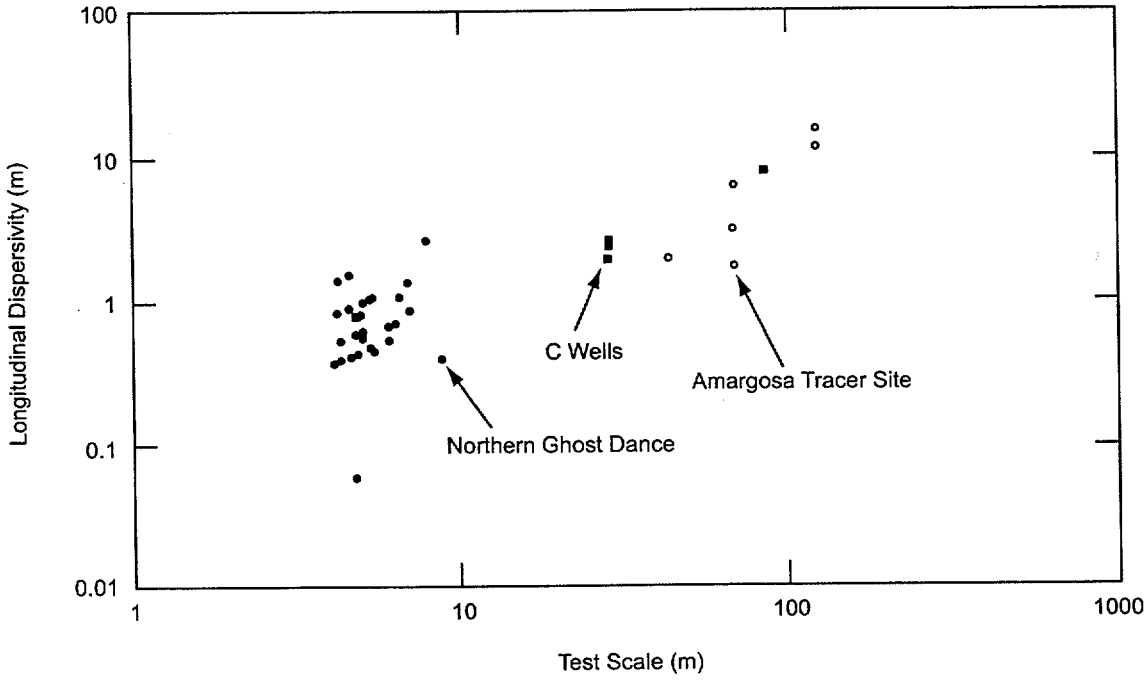

Source: Amargosa Tracer Site data taken from Leap and Belmonte (1992).

Figure 115. Longitudinal Dispersivity as a Function of Test Scale in Several Tracer Tests Conducted in the Vicinity of Yucca Mountain

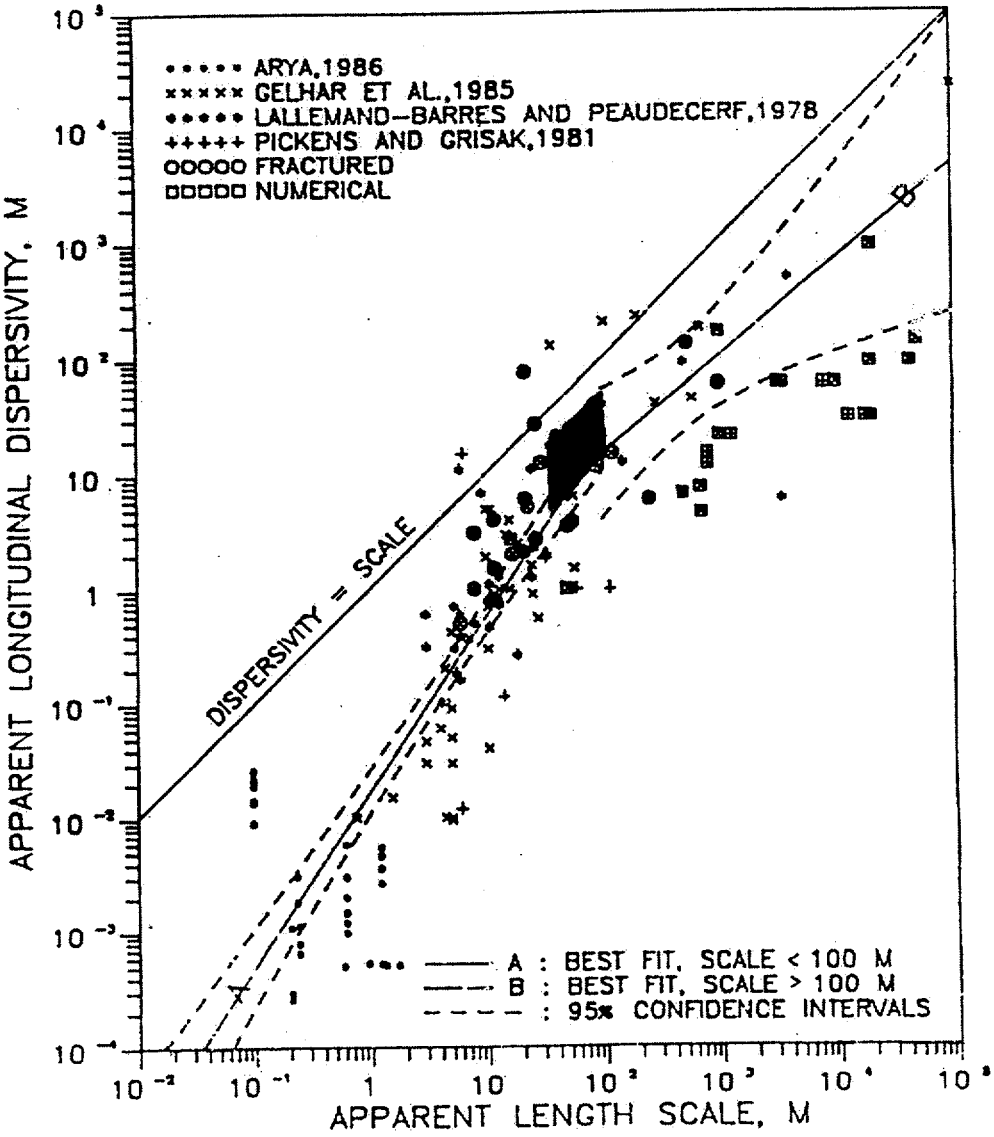

Source: Plot taken from Neuman (1990).

NOTE: The darkened box shows the range of values derived from the multiple-tracer tests. The right edge of the box corresponds to the interwell separation distance, and the left edge of the box corresponds to the test interval thickness (taken to be the upper limit of transport distance).

Figure 116. Plot of Longitudinal Dispersivity Versus Length Scale Showing the Range of C-wells Values Derived from Interpretations of the Prow Pass and Bullfrog Multiple-Tracer Tests

3.11.2 Scale-Dependence of Matrix Diffusion

As shown in Table 40, the *MTC* values obtained from RELAP fits to the bromide and PFBA data in the multiple-tracer tests in the fractured cores did not have a consistent trend as a function of flow rate. Also, the diffusion coefficients measured in the diffusion-cell tests were consistently smaller than those calculated from the fractured-core tests (Table 41).

Cussler (1984) and Hu (2000) state that molecular diffusion coefficients vary with concentration, and it should be noted that the tracer concentrations for the diffusion-cell and fractured-rock-core tests were generally within an order of magnitude. Assuming that the small difference in tracer concentration in the two types of tests did not drastically affect the diffusion process, the diffusion coefficients obtained from the diffusion-cell tests probably better reflect the true bulk values of diffusivity in the porous matrix of these rock types because diffusion through the porous medium was the only transport mechanism in these tests.

Callahan (2001) hypothesized that the diffusive *MTC* was larger for very short duration laboratory fractured-core tests because of free-water diffusion within the fractures during the short-term tests, which was interpreted as matrix diffusion. Free-water diffusion could take place within voids along the rough walls of the fracture surfaces or between flow channels and adjacent stagnant water within the fractures. This free-water diffusion should be less important at larger time scales, and *MTC* values determined at larger scales, therefore, should represent more accurately "true" matrix diffusion because solutes will access a larger volume of porous matrix relative to free water in the fractures at longer time scales. A transition from a free diffusion-dominated system to a matrix diffusion-dominated system could explain the significant decrease in MTC at the lower flow rate (longer residence time) in core 2 relative to the higher flow rate. However, the tracer transport behavior in the other cores did not follow this trend. In fact, the data for cores 1 and 4 suggest that there may have actually been a "skin" effect in these cores, with a lower effective matrix diffusion coefficient near the fracture-matrix interface than in the bulk matrix. Such a skin effect could come about as a result of microbial growth in pores along the fracture walls causing partial "clogging" of the pores.

Figure 117 shows the relationship between the *MTC* and residence time for both the laboratory and field multiple-tracer tests. A trend of decreased *MTC* with larger residence time is evident when comparing the lab data to the field data, although, as discussed above, the results are mixed for the lab data alone. The most-likely explanation for the observed trend is that the tracers experienced significantly larger average fracture apertures in the field than in the cores. Matrix diffusion coefficients would have to be about two orders of magnitude smaller in the field than in the lab to explain the trend of Figure 117 (if all other variables were held constant), which seems implausible. Similarly, matrix porosities would have to be smaller by about a factor of 10 in the field or fracture apertures larger by a factor of 10 to explain the observed trend. Although all of these variables are probably changing somewhat when going from lab to field scales, larger fracture apertures in the field seem the most likely explanation for the much smaller field *MTC* values. One would expect an asymptotic upper limit to be reached eventually for the *MTC*, given a long enough travel time or distance in fractured media. For the C-wells field system, the transport data suggest that this asymptotic value, if it exists, was not obtained for characteristic times of advection up to 1230 hrs or travel distances of ~30 m (Figure 117).

All of the test results discussed here are consistent with diffusive mass transfer having a strong influence on the migration of solutes in the fractured volcanic tuffs. However, at very short time scales, there may be a significant influence of diffusion into stagnant free water within the fractures in addition to "true" matrix diffusion. Also, Figure 117 shows that there was significantly more apparent matrix diffusion in the laboratory tests than in the field experiments. Thus, matrix diffusion parameters obtained from laboratory tracer experiments should be used cautiously when predicting contaminant migration at larger scales in fractured media.

Table 41. Comparison of Matrix Diffusion Coefficients Calculated from Fractured-Core Tracer Tests and from Diffusion-Cell Experiments

Experiment	τ (hr)	$2b$ (cm)	D_m (Br^-) [(a)] (m^2/s)	D_m^* (Br^-) [(b)] (m^2/s)
Core 1, Test 1	7.6	0.188	7.6×10^{-10}	6.0×10^{-10}
Test 2	7.0	0.178	8.1×10^{-10}	
Test 3	52.0	0.178	16.9×10^{-10}	
Core 2, Test 1	1.4	0.05	3.1×10^{-10}	0.4×10^{-10}
Test 2	19.6	0.05	0.58×10^{-10}	
Core 3, Test 1	0.5	0.052	4.4×10^{-10}	3.0×10^{-10}
Test 2	11.0	0.052	4.5×10^{-10}	
Core 4, Test 1	5.0	0.122	2.0×10^{-10}	1.0×10^{-10}
Test 2	52.0	0.122	4.2×10^{-10}	

NOTE: (a) Determined from *MTC* using the measured matrix porosity and from b, which was, in turn, determined from $b = Q\tau$ (third column in table).

(b) Molecular diffusion coefficients determined in diffusion cell tests (Table 23).

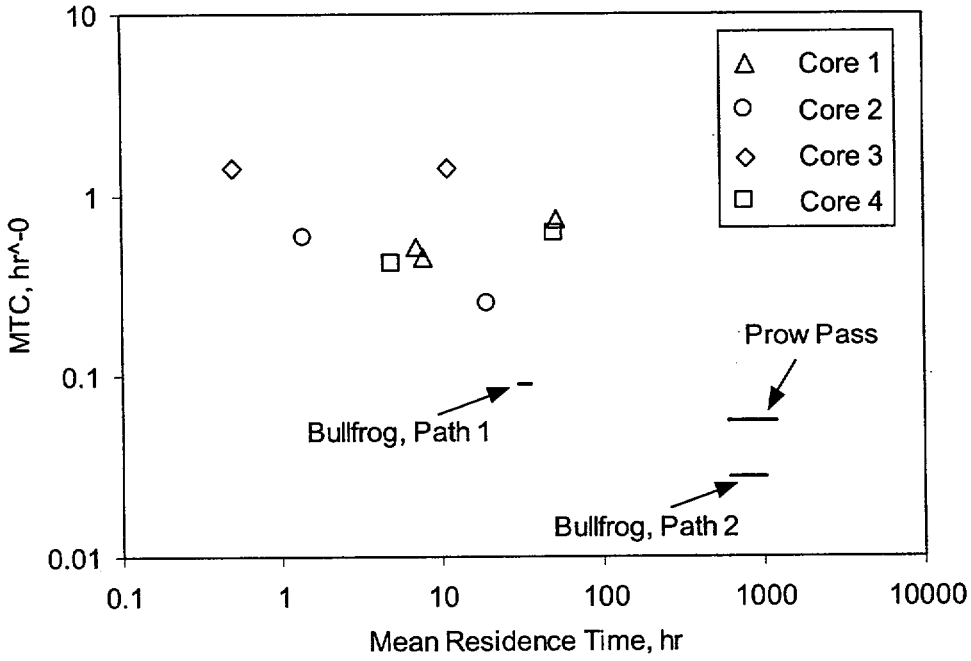

NOTE: The lines represent the field tests; endpoints of the lines reflect the uncertainty in the mean residence time depending on whether radial or linear flow is assumed.

The matrix diffusion mass transfer coefficient is defined as $\frac{\phi}{b}\sqrt{D_m}$.

The experimental time scale here is the mean residence time.

Figure 117. Matrix Diffusion Mass Transfer Coefficient as a Function of Experimental Time Scale in All of the C-wells Laboratory and Field Multiple-Tracer Tests

4. CONCLUSIONS

The most significant conclusions from in-situ testing in the saturated zone at the C-wells complex are the following.

- For flow modeling purposes, the saturated volcanic tuffs in the vicinity of Yucca Mountain can be treated as an equivalent porous medium (at least locally). The fracture networks in the tuffaceous rocks are apparently well-enough connected that hydraulic responses are similar to those observed in porous media. However, the flow system exhibits layered heterogeneity with layers of high permeability often associated with relatively narrow fractured intervals. Also, larger-scale hydraulic characteristics of the saturated tuffs are strongly influenced by structural features such as faults. Hydraulic parameters derived from cross-hole testing in the fractured volcanics are summarized in Tables 9 through 11.

- Solute tracer responses in cross-hole tracer tests at the C-wells were consistent with a dual-porosity conceptual transport model. In this model, solute migration occurs primarily in flowing fractures, but the solutes are effectively attenuated by diffusion into stagnant water in the porous rock matrix (matrix diffusion). Solute transport parameters derived from cross-hole tracer testing at the C-wells are summarized in Tables 17, 18, and 25.

- Apparent sorption of an ion-exchanging tracer (lithium) was generally greater in field tracer tests in the volcanic tuffs than in laboratory tests using the same materials. These results lend credibility to the practice of using laboratory-derived radionuclide sorption parameters in performance assessment simulations, as they suggest that laboratory parameters will tend to yield conservative predictions of radionuclide transport in the tuffs. Comparisons of field and laboratory lithium sorption parameters are provided in Table 17.

- Polystyrene microsphere responses in cross-hole tracer tests at the C-wells suggest that filtration processes effectively attenuate a large percentage of the microspheres over relatively short distances. However, some of the filtered microspheres later detach from fracture surfaces and continue to migrate. Also, flow transients appear to be capable of initiating detachment. Estimates of microsphere transport parameters derived from the C-wells tracer tests are provided in Tables 23 and 24.

- Longitudinal dispersivities derived from the C-wells field tracer tests were consistent with published correlations and data compilations of longitudinal dispersivity versus length scale.

- Matrix diffusion mass transfer coefficients derived from the C-wells field tracer tests were smaller than those derived from laboratory tests in fractured C-wells cores. This result is tentatively attributed to larger fracture apertures in the field than in the cores. The mass transfer coefficients from the field experiments fall well within the statistical distribution of mass transfer coefficients used in performance assessment simulations.

5. INPUTS AND REFERENCES

5.1 DOCUMENTS CITED

Anghel, I.; Turin, H.J.; and Reimus, P.W. 2000. *Lithium Sorption to Yucca Mountain Tuffs.* LANL Report LA-UR-00-2998. Los Alamos, New Mexico: Los Alamos National Laboratory.

Becker, M.W. and Charbeneau, R.J. 2000. "First-Passage-Time Transfer Functions for Groundwater Tracer Tests Conducted in Radially Convergent Flow." *Journal of Contaminant Hydrology, 40*, (4), 299-310. New York, New York: Elsevier.

Benson, C.F. and Bowman, R.S. 1994. "Tri- and Tetrafluorobenzoates as Nonreactive Tracers in Soil and Groundwater." *Soil Science Society of America Journal, 58*, (4), 1123-1129. Madison, Wisconsin: Soil Science Society of America.

Benson, C.F. and Bowman, R.S. 1996. "Erratum, Tri- and Tetrafluorobenzoates as Nonreactive Tracers in Soil and Groundwater." *Soil Science Society of America Journal, 60*, (4), 1780. Madison, Wisconsin: Soil Science Society of America.

Bolt, G.H.; Bruggenwert, M.G.M.; and Kamphorst, A. 1978. "Adsorption of Cations by Soil." *Soil Chemistry, A: Basic Elements*. Bolt, G.H. and Bruggenwert, M.G.M., eds. Pages 54-90. Amsterdam, The Netherlands: Elsevier Science.

Borchardt, G. 1989. "Smectites." In *Minerals in Soil Environments*, Chapter 14 of *Soil Science Society of America Book Series*. Dixon, J.B. and Weed, S.B., eds. Pages 675-727. Madison, Wisconsin: Soil Science Society of America.

Bowman, R.S. 1984. "Evaluation of Some New Tracers for Soil-Water Studies." *Soil Science Society of America Journal, 48*, (5), 987-993. Madison, Wisconsin: Soil Science Society of America.

Brusseau, M.L.; Hu, Q.; and Srivastava, R. 1997. "Using Flow Interruption to Identify Factors Causing Nonideal Contaminant Transport." *Journal of Contaminant Hydrology, 24*, (3-4), 205-219. New York, New York: Elsevier.

Callahan, T.J. 2001. *Laboratory Investigations and Analytical and Numerical Modeling of the Transport of Dissolved Solutes Through Saturated Fractured Rock.* Ph.D. dissertation. Socorro, New Mexico: New Mexico Institute of Mining and Technology.

Callahan, T.J.; Reimus, P.W.; Bowman, R.S.; and Haga, M.J. 2000. "Using Multiple Experimental Methods to Determine Fracture/Matrix Interactions and Dispersion in Saturated Fractured Volcanic Tuff." *Water Resources Research, 36*, (12), 3547-3558. Washington, D.C.: American Geophysical Union.

Carr, M.D.; Waddell, S.J.; Vick, G.S.; Stock, J.M.; Monsen, S.A.; Harris, A.G.; Cork, B.W.; and Byers, F.M., Jr. 1986. *Geology of Drill Hole UE-25 p #1: A Test Hole into Pre-Tertiary Rocks*

near Yucca Mountain, Southern Nevada. Open-File Report 86-175. Menlo Park, California: U.S. Geological Survey.

Cohen, A.J.B.; Najita, J.; Karasaki, K.; and Simmons, A. 1996. *Conceptual Model Development of Saturated Zone Flow in the Vicinity of C-holes, Yucca Mountain, Nevada*. Berkeley, California: Lawrence Berkeley National Laboratory.

Cooper, H.H., Jr. and Jacob, C.E. 1946. "A Generalized Graphical Method for Evaluating Formation Constants and Summarizing Well-Field History." *Transactions, American Geophysical Union, 27*, (IV), 526-534. Washington, D.C.: American Geophysical Union.

Craig, R.W. and Robison, J.H. 1984. *Geohydrology of Rocks Penetrated by Test Well UE-25 p #1, Yucca Mountain Area, Nye County, Nevada*. Water-Resources Investigations Report 84-4248. Denver, Colorado: U.S. Geological Survey.

Cussler, E. L. 1997. *Diffusion: Mass Transfer in Fluid Systems*. Second edition. New York, New York: Cambridge University Press.

D'Agnese, F.A.; Faunt, C.C.; Turner, A.K.; and Hill, M.C. 1997. *Hydrogeologic Evaluation and Numerical Simulation of the Death Valley Regional Ground-Water Flow System, Nevada and California*. Water-Resources Investigations Report 96-4300. Denver, Colorado: U.S. Geological Survey.

Dabros, T. and Van de Ven, T.G. 1982. "Kinetics of Coating by Colloidal Particles." *Journal of Colloid and Interface Science, 89*, (1), 232-244. Orlando, Florida: Academic Press.

Dabros, T. and Van de Ven, T.G. 1983. "On the Effects of Blocking and Detachment on Coating Kinetics." *Journal of Colloid and Interface Science, 93*, (2), 576-579. Orlando, Florida: Academic Press.

Day, W.C.; Potter, C.J.; Sweetkind, D.S.; Dickerson, R.P.; and San Juan, C.A. 1998. *Bedrock Geologic Map of the Central Block Area, Yucca Mountain, Nye County, Nevada*. Miscellaneous Investigations Series Map I-2601. Washington, D.C.: U.S. Geological Survey.

Dickerson, R.P. and Drake, R.M., II. 1998. "Structural Interpretation of Midway Valley, Yucca Mountain, Nevada." *High-Level Radioactive Waste Management, Proceedings of the Eighth International Conference, Las Vegas, Nevada, May 11-14, 1998*. Pages 254-256. La Grange Park, Illinois: American Nuclear Society.

Eckstein, Y.; Yaalon, D.H.; and Yariv, S. 1970. "The Effect of Lithium on the Cation Exchange Behaviour of Crystalline and Amorphous Clays." *Israel Journal of Chemistry, 8*, 335-342. Jerusalem, Israel: Laser Pages Publishing.

Erickson, J.R. and Waddell, R.K. 1985. *Identification and Characterization of Hydrologic Properties of Fractured Tuff Using Hydraulic and Tracer Tests—Test Well USW H-4, Yucca Mountain, Nye County, Nevada*. Water-Resources Investigations Report 85-4066. Denver, Colorado: U. S. Geological Survey.

Ervin, E.M.; Luckey, R.R.; and Burkhardt, D.J. 1994. *Revised Potentiometric-Surface Map, Yucca Mountain and Vicinity, Nevada.* Water-Resources Investigations Report 93-4000. Denver, Colorado: U.S. Geological Survey.

Fahy, M.F. 1997, written communication to CRWMS M&O.

Fahy, M.F. 1997. "Dual-Porosity Analysis of Conservative Tracer Testing in Saturated Volcanic Rocks at Yucca Mountain in Nye County, Nevada." *International Journal of Rock Mechanics and Mining Science, 34*, (3-4). Amsterdam, The Netherlands: Elsevier Science.

Farrell, D.A.; Armstrong, A.; Winterle, J.R.; Turner, D.R.; Ferrill, D.A.; Stamatakos, J.A.; Coleman, N.M.; Gray, M.B.; and Sandberg, S.K. 1999. *Structural Controls on Groundwater Flow in the Yucca Mountain Region.* San Antonio, Texas: Center for Nuclear Waste Regulatory Analyses.

Faunt, C.C. 1997. *Effect of Faulting on Ground-Water Movement in the Death Valley Region, Nevada and California.* Water-Resources Investigations Report 95-4132. Denver, Colorado: U.S. Geological Survey.

Ferrill, D.A.; Winterle, J.; Wittmeyer, G.; Sims, D.; Colton, S.; Armstrong, A.; and Morris, A.P. 1999. *Stressed Rock Strains Groundwater at Yucca Mountain, Nevada.* GSA Today, 9, (5), 1-8. Boulder, Colorado: Geological Society of America.

Fetter, C.W. 1993. *Contaminant Hydrogeology.* New York, New York: Macmillan Publishing Co.

Freeze, R.A. and Cherry, J.A. 1979. *Groundwater.* Englewood Cliffs, New Jersey: Prentice-Hall, Inc.

Frizzell, V.A., Jr. and Shulters, J. 1990. *Geologic Map of the Nevada Test Site, Southern Nevada.* Miscellaneous Investigations Series Map I-2046. Denver, Colorado: U.S. Geological Survey.

Fuentes, H.R.; Polzer, W.L.; Essington, E.H.; and Newman, B.D. 1989. *Characterization of Reactive Tracers for C-Wells Field Experiments I: Electrostatic Sorption Mechanism, Lithium.* LA-11691-MS. Los Alamos, New Mexico: Los Alamos National Laboratory.

Galloway, D. and Rojstaczer, S. 1988. "Analysis of the Frequency Response of Water Levels in Wells to Earth Tides and Atmospheric Loading." *Proceedings of the Fourth Canadian/American Conference on Hydrogeology: Fluid Flow, Heat Transfer, and Mass Transport in Fractured Rocks.* Hitchon, B. and Bachu, S., eds. Pages 100-113. Dublin, Ohio: National Water Well Association.

Geldon, A.L. 1993. *Preliminary Hydrogeologic Assessment of Boreholes UE-25c #1, UE-25c #2, and UE-25c #3, Yucca Mountain, Nye County, Nevada.* Water-Resources Investigations Report 92-4016. Denver, Colorado: U.S. Geological Survey.

Geldon, A.L. 1996. *Results and Interpretation of Preliminary Aquifer Tests in Boreholes UE-25c #1, UE-25c #2, and UE-25c #3, Yucca Mountain, Nye County, Nevada.* Water-Resources Investigations Report 94-4177. Denver, Colorado: U.S. Geological Survey.

Geldon, A.L.; Earle, J.D.; and Umari, A.M.A. 1997b. *Determination of Barometric Efficiency and Effective Porosity, Boreholes UE-25 c #1, UE-25 c #2, and UE-25 c #3, Yucca Mountain, Nye County, Nevada.* Water-Resources Investigations Report 97-4098. Denver, Colorado: U.S. Geological Survey.

Geldon, A.L.; Umari, A.M.A.; Earle, J.D.; Fahy, M.F.; Gemmell, J.M.; and Darnell, J. 1998. *Analysis of a Multiple-Well Interference Test in Miocene Tuffaceous Rocks at the C-Hole Complex, May-June 1995, Yucca Mountain, Nye County, Nevada.* Water-Resources Investigations Report 97-4166. Denver, Colorado: U.S. Geological Survey.

Geldon, A.L.; Umari, A.M.A.; Fahy, M.F.; Earle, J.D.; Gemmell, J.M.; and Darnell, J. 1997a. *Results of Hydraulic and Conservative Tracer Tests in Miocene Tuffaceous Rocks at the C-Hole Complex, 1995 to 1997, Yucca Mountain, Nye County, Nevada.* Milestone SP23PM3. Las Vegas, Nevada: U. S. Geological Survey.

Golder Associates. 2000. *Software Code: GoldSim.* 6.04.007. PC, Windows, NT> 10344-6.04.007-00.

Graves, R.P.; Tucci, P.; and O'Brien, G.M. 1997. *Analysis of Water-Level Data in the Yucca Mountain Area, Nevada, 1985-95.* Water-Resources Investigations Report 96-4256. Denver, Colorado: U.S. Geological Survey.

Grisak, G.E. and Pickens, J.F. 1980. "Solute Transport Through Fractured Media. 1. The Effect of Matrix Diffusion." *Water Resources Research, 16,* (4), 719-730. Washington, D.C.: American Geophysical Union.

Guimera, J. and Carrera, J. 2000. "A Comparison of Hydraulic and Transport Parameters Measured in Low-Permeability Fractured Media." *Journal of Contaminant Hydrology,* 41, (3-4), 261-281. New York, New York: Elsevier.

Haggerty, R. and Gorelick, S. 1995. "Multiple-rate Mass Transfer for Modeling Diffusion and Surface Reactions in Media with Pore-scale Heterogeneity." *Water Resources Research, 31,* (10), 2383-2400. Washington, D.C.: American Geophysical Union.

Haggerty, R.; McKenna, S.A.; and Meigs, L.C. 2000. "On the Late-time Behavior of Tracer Test Breakthrough Curves." *Water Resources Research, 36,* (12), 3467-3479. Washington, D.C.: American Geophysical Union.

Harr, M.E. 1987. *Reliability-Based Design in Civil Engineering.* New York, New York: McGraw-Hill Book Company.

Harrar, J.E.; Carley, J.F.; Isherwood, W.F.; and Raber, E. 1990. *Report of the Committee to Review the Use of J-13 Well Water in Nevada Nuclear Waste Storage Investigations.* UCID-21867. Livermore, California: Lawrence Livermore National Laboratory.

Hu, P. 2000. *Diffusion Coefficients of Hydrologic Tracers as Measured by a Taylor Dispersion Apparatus*. M.S. thesis. Socorro, New Mexico: New Mexico Institute of Mining and Technology.

Israelachvili, J.N. 1992. *Intermolecular and Surface Forces*. San Diego, CA: Academic Press.

Jenson, V.G. and Jeffreys, G.V. 1977. *Mathematical Methods in Chemical Engineering*. 2nd Edition. New York, New York: Academic Press.

Johnson, G. 1995. *Labview: Graphical Programming and Application Development*. New York, New York: McGraw-Hill.

Kruseman, G.P. and Deridder, N.A. 1979. *Analysis and Evaluation of Pumping Test Data*. Bulletin 11. Wageningen, The Netherlands: International Institute for Land Reclamation and Improvement.

Lahoud, R.G.; Lobmeyer, D.H.; and Whitfield, M.S., Jr. 1984. *Geohydrology of Volcanic Tuff Penetrated by Test Well UE-25b #1, Yucca Mountain, Nye County, Nevada*. Water-Resources Investigations Report 84-4253. Denver, Colorado: U.S. Geological Survey.

Leap, D.I. and Belmonte, P.M. 1992. "Influence of Pore Pressure on Apparent Dispersivity of a Fissured Dolomitic Aquifer." *Ground Water, 30*, (1), 87-95. Dublin, Ohio: Water Well Journal Publishing.

Levenspiel, O. 1972. *Chemical Reaction Engineering*, Second edition. New York, New York: John Wiley and Sons.

Lohman, S.W. 1979. *Ground-Water Hydraulics*. Professional Paper 708. Washington, D.C.: U.S. Geological Survey.

Luckey, R.R.; Tucci, P.; Faunt, C.C.; Ervin, E.M.; Steinkampf, W.C.; D'Agnese, F.A.; and Patterson, G.L. 1996. *Status of Understanding of the Saturated-Zone Ground-Water Flow System at Yucca Mountain, Nevada, as of 1995*. Water-Resources Investigations Report 96-4077. Denver, Colorado: U.S. Geological Survey.

Majer, E. 1993, written communication, Lawrence Berkeley National Laboratory.

Maloszewski, P. and Zuber, A. 1984. "Interpretation of Artificial and Environmental Tracers in Fissured Rocks with a Porous Matrix." *Isotope Hydrology 1983, Proceedings of an International Symposium on Isotope Hydrology in Water Resources Development, Vienna, Austria, September 12-16, 1983*. Vienna, Austria: International Atomic Energy Commission.

Maloszewski, P. and Zuber, A. 1985. "On the Theory of Tracer Experiments in Fissured Rocks with a Porous Matrix." *Journal of Hydrology, 79,* (3-4), 333-358. Amsterdam, The Netherlands: Elsevier Science Publishers B.V.

Maloszewski, P.; Herrmann, A.; and Zuber, A. 1999. "Interpretation of Tracer Tests Performed in Fractured Rock of the Lange Bramke Basin, Germany." *Hydrogeology Journal, 7,* (2), 209-218. Berlin, Germany: Springer-Verlag.

Ming, D.W. and Mumpton, F.A. 1989. "Zeolites in Soils, Minerals in Soil Environments." *Soil Science Society of America Book Series No. 1*, 873-911. Madison, Wisconsin: Soil Science Society of America.

Moench, A.F. 1989. "Convergent Radial Dispersion: A Laplace Transform Solution for Aquifer Tracer Testing." *Water Resources Research, 25*, (3), 439-447. Washington, D.C.: American Geophysical Union.

Moench, A.F. 1995. "Convergent Radial Dispersion in a Double-Porosity Aquifer with Fracture Skin: Analytical Solution and Application to a Field Experiment in Fractured Chalk." *Water Resources Research, 31*, (8), 1823-1835. Washington, D.C.: American Geophysical Union.

National Research Council. 1996. *Rock Fractures and Fluid Flow, Contemporary Understanding and Applications*. Washington, D.C: National Academy Press.

Neretnieks, I. 1980. "Diffusion in the Rock Matrix: An Important Factor in Radionuclide Retardation?" *Journal of Geophysical Research, 85*, (B8), 4379-4397. Washington, D.C.: American Geophysical Union.

Neuman, S. 1975. "Analysis of Pumping Test Data from Anisotropic Unconfined Aquifers Considering Delayed Gravity Response." *Water Resources Research, 11*, (2), 329-342. Washington, D.C.: American Geophysical Union.

Neuman, S.P. 1990. "Universal Scaling of Hydraulic Conductivities and Dispersivities in Geologic Media." *Water Resources Research, 26,* (8), 1754-1758. Washington, D.C.: American Geophysical Union.

Newman, B.D.; Fuentes, H.R.; and Polzer, W.L. 1991. "An Evaluation of Lithium Sorption Isotherms and Their Application to Ground-Water Transport." *Ground Water, 29,* (6), 818-824.

Newman, J.S. 1973. *Electrochemical Systems*. Englewood Cliffs, New Jersey: Prentice-Hall, Inc.

Nye County Nuclear Waste Repository Project Office. 1995. *Borehole UE-25 ONC #1 and USW NRG-4 Drilling and Instrumentation Report, Yucca Mountain, Nevada*. Pahrump, Nevada: Nye County Nuclear Waste Repository Program.

O'Brien, G.M.; Tucci, P.; and Burkhardt, D.J. 1995. *Water Levels in the Yucca Mountain Area, Nevada, 1992*. Open-File Report 94-311. Denver, Colorado: U.S. Geological Survey.

Reimus, P. W. 1996. *Predictions of Tracer Transport in Interwell Tracer Tests at the C-Hole Complex*. Milestone 4077, LA-13160-MS. Los Alamos, New Mexico: Los Alamos National Laboratory.

Reimus, P.W. 1995. *The Use of Synthetic Colloids in Tracer Transport Experiments in Saturated Rock Fractures*. Ph.D. dissertation, University of New Mexico. LA-13004-T. Los Alamos, New Mexico: Los Alamos National Laboratory.

Reimus, P.W. and Haga, M.J. 1999. *Analysis of Tracer Responses in the BULLION Forced-gradient Experiment at Pahute Mesa, Nevada*. LA-13615-MS. Los Alamos, New Mexico: Los Alamos National Laboratory.

Reimus, P.W.; Pohll, G.; Mihevc, T.; Chapman, J.; Haga, M.; Lyles, B.; Kosinski, S.; Niswonger, R.; and Sanders, P. 2001. *Testing and Parameterizing a Conceptual Model for Radionuclide Transport in a Fractured Granite Using Multiple Tracers in a Forced-Gradient Test*. LA-01-4108-UR. Los Alamos, New Mexico: Los Alamos National Laboratory.

Robinson, B.A. 1994. "A Strategy for Validating a Conceptual Model for Radionuclide Migration in the Saturated Zone Beneath Yucca Mountain." *Radioactive Waste Management and Environmental Restoration, 19*, (1-3), 73-96. Yverdon, Switzerland: Harwood Academic Publishers.

Skagius, K. and Neretnieks, I. 1986. "Porosities and Diffusivities of Some Nonsorbing Species in Crystalline Rocks." *Water Resources Research, 22*, (3), 389-398. Washington, D.C.: American Geophysical Union.

Stetzenbach, K.J. and Thompson, G.M. 1983. "A New Method for Simultaneous Measurement of Cl^-, Br^-, NO_3^-, SCN^-, and I^- at sub-ppm Levels in Ground Water." *Ground Water*, 21, (1), 36-41. Long Island City, New York: Pergamon Press.

Streltsova, T.D. 1988. *Well Testing in Heterogeneous Formations*. New York, New York: John Wiley and Sons, Inc.

Streltsova-Adams, T.D. 1978. "Well Testing in Heterogeneous Aquifer Formations." Volume 11 of *Advances in Hydroscience*. Chow, V.T., ed. Pages 357-423. New York, New York: Academic Press.

Tang, D.H.; Frind, E.O.; and Sudicky, E.A. 1981. "Contaminant Transport in Fractured Porous Media: Analytical Solution for a Single Fracture." *Water Resources Research, 17*, (3), 555-564. Washington, D.C.: American Geophysical Union.

Theis, C.V. 1935. "The Relation Between the Lowering of the Piezometric Surface and the Rate and Duration of Discharge of a Well Using Ground-Water Storage." *Transactions of the American Geophysical Union Sixteenth Annual Meeting, April 25 and 26, 1935, Washington, D.C.* Pages 519-524. Washington, D.C.: National Academy of Science, National Research Council.

Thompson, J.L. 1989. "Actinide Behavior on Crushed Rock Columns." *Journal of Radioanalytical and Nuclear Chemistry—Articles, 130* (2), 353-364. Lausanne, Switzerland: Elsevier Sequoia.

Treher, E.N. and Raybold, N.A. 1982. *The Elution of Radionuclides Through Columns of Crushed Rock from the Nevada Test Site.* LA-9329-MS. Los Alamos, New Mexico: Los Alamos National Laboratory.

Triay, I.R.; Meijer, A.; Conca, J.L.; Kung, K.S.; Rundberg, R.S.; Strietelmeier, E.A.; Tait, C.D.; Clark, D.L.; Neu, M.P.; and Hobart, D. E. 1997. *Summary and Synthesis Report on Radionuclide Retardation for the Yucca Mountain Site Characterization Project.* Eckhardt, R.C., ed. LA-13262-MS. Los Alamos, New Mexico: Los Alamos National Laboratory.

Tsang, Y. W. 1992. "Usage of 'Equivalent Apertures' for Rock Fractures as Derived from Hydraulic and Tracer Tests." *Water Resources Research, 28,* (5), 1451-1455. Washington, D.C.: American Geophysical Union.

Tucci, P. and Burkhardt, D.J. 1995. *Potentiometric-Surface Map, 1993, Yucca Mountain and Vicinity, Nevada.* Water-Resources Investigations Report 95-4149. Denver, Colorado: U.S. Geological Survey.

U.S. Geological Survey, National Earthquake Information Center. 1997, oral communication.

Valocchi, A.J. 1985. "Validity of the Local Equilibrium Assumption for Modeling Sorbing Solute Transport through Homogeneous Soils." *Water Resources Research, 21,* (6), 808-820. Washington, D.C.: American Geophysical Union.

van Genuchten, M.T.; Wierenga, P.J.; and O'Connor, G.A. 1977. "Mass Transfer Studies in Sorbing Porous Media: III. Experimental Evaluation with 2,4,5-T." *Soil Science Society of America Journal, 41,* 278-285. Madison, Wisconsin: Soil Science Society of America.

Vaughn, D.E.W. 1978. "Properties of Natural Zeolites." *Natural Zeolites, Occurrence, Properties, Use, A Selection of Papers Presented at Zeolite, 76, an International Conference on the Occurrence, Properties, and Utilization of Natural Zeolites, Tucson, Arizona, June 1976.* Sand, L.B. and Mumpton, F..A., eds. Pages 353-371. New York, New York: Pergamon Press.

Watermark Computing. 1994. *PEST, Model-Independent Parameter Estimation.* Oxley, Australia: Watermark Computing.

Whitfield, M.S., Jr.; Thordarson, W.; and Eshom, E.P. 1984. *Geohydrologic and Drill-Hole Data for Test Well USW H-4, Yucca Mountain, Nye County, Nevada.* Open-File Report 84-449. Denver, Colorado: U.S. Geological Survey.

Winterle, J.R. and La Femina, P.C. 1999. *Review and Analysis of Hydraulic and Tracer Testing at the C-Holes Complex Near Yucca Mountain, Nevada.* San Antonio, Texas: Center for Nuclear Waste Regulatory Analyses.

5.2 CODES, STANDARDS, REGULATIONS, AND PROCEDURES

40 CFR 197. 2001. Protection of Environment: Public Health and Environmental Radiation Protection Standards for Yucca Mountain, Nevada.

The staff will evaluate the following parts of the identification of events with probabilities greater than 10^{-8} per year, using the review methods and acceptance criteria in Sections 4.2.1.2.2.2 and 4.2.1.2.2.3:

- Definitions of events, such as faulting, seismicity, igneous activity, and criticality;
- The probability assigned to each event, and the technical bases used to support this assignment;
- Conceptual models evaluated or considered in determining the probabilities of events;
- Parameters used to calculate the probabilities of events; and
- Uncertainty in models and parameters used to calculate the probabilities of events.

4.2.1.2.2.2 Review Methods

Review Method 1 Event Definition

Evaluate whether the definitions for events (potentially beneficial or disruptive), applicable to the Yucca Mountain repository, are unambiguous; probabilities are estimated for the specific event; and event definitions are used consistently and appropriately in probability models.

Confirm that probabilities of intrusive and extrusive igneous events are calculated separately. Verify that definitions of faulting and earthquakes are derived from the historical record, paleoseismic studies, or geological analyses. Confirm that criticality events, for the purpose of initial screening of the features, events, and processes list, are calculated separately, only by location of the criticality event (e.g., in-package, near-field, and far-field).

Review Method 2 Probability Estimates

Evaluate whether the probability estimates for events applicable to Yucca Mountain are based on past patterns of natural events in the Yucca Mountain region, or are consistent with the design of the proposed repository system. Evaluate whether the U.S. Department of Energy interpretations of the likelihood of future occurrence of the events are compatible with current understandings of present and likely future conditions of the natural and engineered repository systems.

Verify that probability estimates for future igneous events are based on past patterns of igneous events in the Yucca Mountain region. Evaluate the adequacy and sufficiency of the U.S. Department of Energy characterization and documentation of past igneous activity. This should include uncertainties about the distribution, timing, and characteristics of past igneous activity. Confirm that, at a minimum, documentation of past igneous activity, since about 12 million years ago, encompasses the area within about 50 kilometers (30 miles) of the proposed repository site. Give particular attention to the documentation of the locations, ages, volumes, geochemistry, and geologic settings of less than 6-million-year-old basaltic igneous features, such as cinder cones, lava flows, igneous dikes, and sills. Verify that the

The staff will evaluate the following parts of the identification of events with probabilities greater than 10^{-8} per year, using the review methods and acceptance criteria in Sections 4.2.1.2.2.2 and 4.2.1.2.2.3:

- Definitions of events, such as faulting, seismicity, igneous activity, and criticality;
- The probability assigned to each event, and the technical bases used to support this assignment;
- Conceptual models evaluated or considered in determining the probabilities of events;
- Parameters used to calculate the probabilities of events; and
- Uncertainty in models and parameters used to calculate the probabilities of events.

4.2.1.2.2.2 Review Methods

Review Method 1 Event Definition

Evaluate whether the definitions for events (potentially beneficial or disruptive), applicable to the Yucca Mountain repository, are unambiguous; probabilities are estimated for the specific event; and event definitions are used consistently and appropriately in probability models.

Confirm that probabilities of intrusive and extrusive igneous events are calculated separately. Verify that definitions of faulting and earthquakes are derived from the historical record, paleoseismic studies, or geological analyses. Confirm that criticality events, for the purpose of initial screening of the features, events, and processes list, are calculated separately, only by location of the criticality event (e.g., in-package, near-field, and far-field).

Review Method 2 Probability Estimates

Evaluate whether the probability estimates for events applicable to Yucca Mountain are based on past patterns of natural events in the Yucca Mountain region, or are consistent with the design of the proposed repository system. Evaluate whether the U.S. Department of Energy interpretations of the likelihood of future occurrence of the events are compatible with current understandings of present and likely future conditions of the natural and engineered repository systems.

Verify that probability estimates for future igneous events are based on past patterns of igneous events in the Yucca Mountain region. Evaluate the adequacy and sufficiency of the U.S. Department of Energy characterization and documentation of past igneous activity. This should include uncertainties about the distribution, timing, and characteristics of past igneous activity. Confirm that, at a minimum, documentation of past igneous activity, since about 12 million years ago, encompasses the area within about 50 kilometers (30 miles) of the proposed repository site. Give particular attention to the documentation of the locations, ages, volumes, geochemistry, and geologic settings of less than 6-million-year-old basaltic igneous features, such as cinder cones, lava flows, igneous dikes, and sills. Verify that the